

PROCEEDINGS OF THE 2007 ANTENNA APPLICATIONS SYMPOSIUM  
Volume II of II

Daniel Schaubert, Editor

University of Massachusetts at Amherst  
Electrical and Computer Engineering  
100 Natural Resources Road  
Amherst MA 01003

Final Report

20 December 2007

APPROVED FOR PUBLIC RELEASE; DISTRIBUTION UNLIMITED



AIR FORCE RESEARCH LABORATORY  
Sensors Directorate  
Electromagnetics Technology Division  
80 Scott Drive  
Hanscom AFB MA 01731-2909

## NOTICE AND SIGNATURE PAGE

Using Government drawings, specifications, or other data included in this document for any purpose other than Government procurement does not in any way obligate the U.S. Government. The fact that the Government formulated or supplied the drawings, specifications, or other data does not license the holder or any other person or corporation; or convey any rights or permission to manufacture, use, or sell any patented invention that may relate to them.

This report was cleared for public release by the Electronic Systems Center Public Affairs Office for the Air Force Research Laboratory Electromagnetic Technology Division and is available to the general public, including foreign nationals. Copies may be obtained from the Defense Technical Information Center (DTIC) (<http://www.dtic.mil>).

AFRL-RY-HS-TR-2007-0037 HAS BEEN REVIEWED AND IS APPROVED FOR PUBLICATION IN ACCORDANCE WITH ASSIGNED DISTRIBUTION STATEMENT.



---

DAVID D. CURTIS  
Chief, Antenna Technology Branch



---

MICHAEL N. ALEXANDER  
Technical Advisor  
Electromagnetic Technology Division

This report is published in the interest of scientific and technical information exchange, and its publication does not constitute the Government's approval or disapproval of its ideas or findings.

This report is published in the interest of scientific and technical information exchange, and its publication does not constitute the Government's approval or disapproval of its ideas or findings.

REPORT DOCUMENTATION PAGE				Form Approved OMB No. 0704-0188	
Public reporting burden for this collection of information is estimated to average 1 hour per response, including the time for reviewing instructions, searching existing data sources, gathering and maintaining the data needed, and completing and reviewing this collection of information. Send comments regarding this burden estimate or any other aspect of this collection of information, including suggestions for reducing this burden to Department of Defense, Washington Headquarters Services, Directorate for Information Operations and Reports (0704-0188), 1215 Jefferson Davis Highway, Suite 1204, Arlington, VA 22202-4302. Respondents should be aware that notwithstanding any other provision of law, no person shall be subject to any penalty for failing to comply with a collection of information if it does not display a currently valid OMB control number. <b>PLEASE DO NOT RETURN YOUR FORM TO THE ABOVE ADDRESS.</b>					
1. REPORT DATE (DD-MM-YYYY) 20-12-2007		2. REPORT TYPE FINAL REPORT		3. DATES COVERED (From - To) 18 Sep 2007 - 20 Sep 2007	
4. TITLE AND SUBTITLE  Proceedings of the 2007 Antenna Applications Symposium, Volume II				5a. CONTRACT NUMBER F33615-02-D-1283	
				5b. GRANT NUMBER	
				5c. PROGRAM ELEMENT NUMBER	
6. AUTHOR(S)  Daniel Schaubert, Editor				5d. PROJECT NUMBER	
				5e. TASK NUMBER	
				5f. WORK UNIT NUMBER	
7. PERFORMING ORGANIZATION NAME(S) AND ADDRESS(ES) University of Massachusetts Amherst Electrical and Computer Engineering 100 Natural Resources Road Amherst, MA 01003				8. PERFORMING ORGANIZATION REPORT	
9. SPONSORING / MONITORING AGENCY NAME(S) AND ADDRESS(ES) Electromagnetics Technology Division Sensors Directorate Air Force Research Laboratory 80 Scott Drive Hanscom AFB MA 01731-2909				10. SPONSOR/MONITOR'S ACRONYM(S) AFRL-RY-HS	
				11. SPONSOR/MONITOR'S REPORT NUMBER(S) AFRL-RY-HS-TR-2007-0037	
12. DISTRIBUTION / AVAILABILITY STATEMENT APPROVED FOR PUBLIC RELEASE; DISTRIBUTION UNLIMITED					
13. SUPPLEMENTARY NOTES Volume I contains pages 1 – 271                      Public Affairs release Number ESC 07-1445, 18 DEC 2007 Volume II contains pages 272 – 561					
14. ABSTRACT  The Proceedings of the 2007 Antenna Applications Symposium is a collection of state-of-the art papers relating to antenna arrays, millimeter wave antennas, simulation and measurement of antennas, integrated antennas, and antenna bandwidth and radiation improvements.					
15. SUBJECT TERMS Antennas, phased arrays, digital beamforming, millimeter waves, antenna measurements, airborne antenna applications, Vivaldi antennas, waveguide antenna arrays, broadband arrays, electrically small antennas					
16. SECURITY CLASSIFICATION OF:			17. LIMITATION OF ABSTRACT  UU	18. NUMBER OF PAGES  300	19a. NAME OF RESPONSIBLE PERSON David D. Curtis
a. REPORT Unclassified	b. ABSTRACT Unclassified	c. THIS PAGE Unclassified			19b. TELEPHONE NUMBER (include area code) N/A





## Table of Contents

2007 ANTENNA APPLICATIONS SYMPOSIUM (Volumes I & II)  
18 - 20 September 2007, Monticello, Illinois

<b>Current Capabilities of Digital Beamforming</b> D.D. Curtis, D. Spendley and D.Q. Luu	<b>1</b>
<b>Flex Based L-Band Phased Array Antenna Demonstration</b> P. Buxa, T. Dalrymple, C. Lesniak and R. Neidhard	<b>34</b>
<b>Parameter Variation for Broadband Arrays of Irregular Polyomino Subarrays</b> R.J. Mailloux, S.C. Santarelli, T.M. Roberts and B.C. Kaanta	<b>46</b>
<b>Sub-Array Mirroring for Mediation of Second-Order Beams in Planar Edge Slot Waveguide Antenna Arrays</b> B.J. Herting, M.W. Elsallal and J.B. West	<b>65</b>
<b>Planar Edge Slot Waveguide Antenna Array Design using COTS EM Tools</b> M.W. Elsallal, B.J. Herting and J.B. West	<b>76</b>
<b>A Cross-Flux Method for Coupling Prediction of Two Installed Antennas</b> C.C. Lu	<b>90</b>
<b>Proposed Coincident Phase Center Orthogonal Dipoles</b> W.R. Pickles and W.M. Dorsey	<b>106</b>
<b>Scan Impedance for an Infinite Dipole Array: Hansen's Formulas vs. Ansoft HFSS Simulations</b> S.N. Makaorv	<b>125</b>
<b>High Performance Phased Arrays of Doubly Mirrored Balanced Antipodal Vivaldi Antenna (DmBAVA): Current Development and Future Considerations</b> M.W. Elsallal and D.H. Schaubert	<b>148</b>
<b>Miniaturization of Cavity-Backed Slot Antennas</b> M. Al-Joumayly and N. Behdad	<b>160</b>

<b>A Compact Ku/Ka Band Feed for Airborne Antenna Applications</b>	<b>169</b>
J.P. Creticos and D.H. Schaubert	
<b>UWB Tapered Slot Antenna Array Using SIW Technology</b>	<b>181</b>
S. Lin, S. Yang and A.E. Fathy	
<b>A Study of the Performance Properties of Small Antennas</b>	<b>193</b>
S.R. Best	
<b>Non-Foster Matching of a Lossy, Electrically-Small Antenna Over an Extended Frequency Range</b>	<b>220</b>
S.E. Sussman-Fort and R.M. Rudish	
<b>Microfluidic Reconfiguration of Antennas</b>	<b>241</b>
G.H. Huff, P. Bahukudumbi, W.N. Everett, A. Beskok, M.A. Bevan, D. Lagoudas and Z. Ounaies	
<b>Novel Reconfigurable Multi-Band Antennas for Wireless Receivers</b>	<b>259</b>
S. Yang, H.K. Pan, A.E. Fathy, S.M. El-Ghazaly and V.K. Nair	
<b>Performance Predictions for Linear Antennas with Offset Loading and Offset Excitation</b>	<b>272</b>
P.E. Mayes, P.W. Klock and S. Barot	
<b>Improvements on MF Ground Wave Antennas for the Global Maritime Distress and Safety System (GMDSS)</b>	<b>284</b>
T.R. Vogler, T.C. Kramer and W.A. Davis	
<b>A Compact, Wide Bandwidth UHF / L-Band Communications System Antenna for Ground-Based Applications</b>	<b>313</b>
T. Goodwin	
<b>Effects of Modulation Ratio on the Performance of 4 Arm MAW Spirals</b>	<b>328</b>
W.N. Kefauver, T.P. Cencich and D.S. Filipovic	
<b>Dual-Substrate Capacitive Loading Technique in Linearly and Circularly Polarized Shorted Annular Ring Antennas</b>	<b>347</b>
W.M. Dorsey, J. Valenzi and A.I. Zaghloul	

<b>A New Radio Direction Finder for Wildlife Research</b>	<b>384</b>
T.A. Borrowman, S.J. Franke and G.W. Swenson, Jr.	
<b>Challenges and Solutions for the Efficiency Measurement of an Electrically Small Antenna for Animal Tracking</b>	<b>395</b>
J.M. Martin, G.W. Swenson, Jr. and J.T. Bernhard	
<b>Transformational Element Level Arrays (TELA) Testbed</b>	<b>406</b>
T. Dalrymple, J. Buck, P. Buxa, J. McCann, R. Neidhard, G. Scalzi, C. Shreffler, D. Spendley and P. Watson	
<b>A Transportable VHF Ground Plane Antenna Range for Azimuthal Pattern Measurement</b>	<b>431</b>
A. Adrian and J.M. Huk	
<b>Exponentially Tapered and Folded Wideband TEM Horn Array for 20 KV of Impulse</b>	<b>447</b>
Y-J Ahn, J-S Lee, S-J Kim, F.J. Harackiewicz and B. Lee	
<b>Multipath Rejection by Virtue of a Choke Ring for a Broadband Droopy Turnstile Antenna</b>	<b>467</b>
S.N. Makarov and F. Scire Scappuzzo	
<b>Leaky Wave Antenna Research at AFRL</b>	<b>508</b>
D. Janning, J. McCann, M. Corwin, T. Dalrymple, L. Kempel, D. Killips, K. Pasala, R. Penno, J. Radcliffe, S. Schneider and K. Zeller	
<b>Scalar and Tensor Artificial Impedance Surface Conformal Antennas</b>	<b>526</b>
J.S. Colburn, D.F. Sievenpiper, B.H. Hong, J.J. Ottusch, J.L. Visher and P.R. Herz	
<b>Three-Dimensional Electronic Band Gap (3-D EBG) Structures for Advanced Conformal Antennas</b>	<b>541</b>
F. Scire Scappuzzo, J.P. Towle and M. Lazzaro	

## Identifiers for Proceedings of Symposia

The USAF Antenna Research and Development Program

<b>Year</b>	<b>Symposium No.</b>	<b>Identifier</b>
1951	First	_____
1952	Second	ADB870006
1953	Third	ADB283180
1954	Fourth	AD63139
1955	Fifth	AD90397
1956	Sixth	AD114702
1957	Seventh	AD138500
1958	Eighth	AD301151
1959	Ninth	AD314721
1960	Tenth	AD244388 (Vol. 1) AD319613 (Vol. 2)
1961	Eleventh	AD669109 (Vol. 1) AD326549 (Vol. 2)
1962	Twelfth	AD287185 (Vol. 1) AD334484 (Vol. 2)
1963	Thirteenth	AD421483
1964	Fourteenth	AD609104
1965	Fifteenth	AD474238L
1966	Sixteenth	AD800524L
1967	Seventeenth	AD822894L
1968	Eighteenth	AD846427L
1969	Nineteenth	AD860812L
1970	Twentieth	AD875973L
1971	Twenty-First	AD888641L
1972	Twenty-Second	AD904360L
1973	Twenty-Third	AD914238L

## Antenna Applications Symposium

<b>Year</b>	<b>Symposium No.</b>	<b>Technical Report No.</b>	<b>Identifier</b>
1977	First	_____	ADA955413
1978	Second	_____	ADA955416
1979	Third	_____	ADA077167
1980	Fourth	_____	ADA205907
1981	Fifth	_____	ADA205816
1982	Sixth	_____	ADA129356
1983	Seventh	_____	ADA142003; 142754
1984	Eighth	85-14	ADA153257; 153258
1985	Ninth	85-242	ADA166754; 165535
1986	Tenth	87-10	ADA181537; 181536
1987	Eleventh	88-160	ADA206705; 206704
1988	Twelfth	89-121	ADA213815; 211396
1989	Thirteenth	90-42	ADA226022; 226021
1990	Fourteenth	91-156	ADA237056; 237057
1991	Fifteenth	92-42	ADA253681; 253682
1992	Sixteenth	93-119	ADA268167; 266916
1993	Seventeenth	94-20	ADA277202; 277203
1994	Eighteenth	95-47	ADA293258; 293259
1995	Nineteenth	96-100	ADA309715; 309723
1996	Twentieth	97-189	ADA341737
1997	Twenty First	1998-143	ADA355120
1998	Twenty Second	1999-86	ADA364798
1999	Twenty Third	2000-008 Vol. I & II	ADA386476; 386477
2000	Twenty Fourth	2002-001 Vol. I & II	ADA405537; 405538
2001	Twenty Fifth	2002-002 Vol. I & II	ADA405328; 405327
2002	Twenty Sixth	2005-001 Vol. I & II	ADA427799; 427800
2003	Twenty Seventh	2005-005 Vol. I & II	ADA429122; 472514
2004	Twenty Eighth	2005-016 Vol. I & II	ADA431338; 431339
2005	Twenty Ninth	2005-039 Vol. I & II	ADM001873
2006	Thirtieth	2006-0047 Vol. I & II	ADA464058, 464059
2007	Thirty First	2007-0037 Vol. I & II	

## 2007 Author Index

Adrian, A.	431	Lazzaro, M.	541
Ahn, Y-J	447	Lee, B.	447
Al-Joumayly, M.	160	Lee, J-S	447
Anthony, T.K.	366	Lee, Y.M.	366
Bahukudumbi, P.	241	Lesniak, C.	34
Barot, S.	272	Lin, S.	181
Behdad, N.	160	Lu, C.C.	90
Bernhard, J.T.	395	Luu, D.Q.	1
Beskok, A.	241	Mailloux, R.J.	46
Best, S.R.	193	Makarov, S.N.	125, 467
Bevan, M.A.	241	Martin, J.M.	395
Borrowman, T.A.	384	Mayes, P.E.	272
Buck, J.	406	McCann, J.	406, 508
Buxa, P.	34, 406	Nair, V.K.	259
Cencich, T.P.	328	Neidhard, R.	34
Colburn, J.S.	526	Neidhard, R.	406
Corwin, M.	508	Ottusch, J.J.	526
Creticos, J.P.	169	Ounaies, Z.	241
Curtis, D.D.	1	Pan, H.K.	259
Dalrymple, T.	34, 406, 508	Pasala, K.	508
Davis, W.A.	284	Penno, R.	508
Dorsey, W.M.	106, 347	Pickles, W.R.	106
El-Ghazaly, S.M.	259	Radcliffe, J.	508
Elsallal, M.W.	65, 76, 148	Roberts, T.M.	46
Everett, W.N.	241	Rudish, R.M.	220
Fathy, A.E.	181, 259	Santarelli, S.G.	46
Filipovic, D.S.	328	Scalzi, G.	406
Franke, S.J.	384	Schaubert, D.H.	148, 169
Goodwin, T.	313	Schneider, S.	508
Harackiewicz, F.J.	447	Scire Scappuzzo, F.	467, 541
Herting, B.J.	65, 76	Shreffler, C.	406
Herz, P.R.	526	Sievenpiper, D.F.	526
Hong, B.H.	526	Spendley, D.	1, 406
Huff, G.H.	241	Sussman-Fort, S.E.	220
Huk, J.M.	431	Swenson, Jr., G.W.	384, 395
Janning, D.	508	Towle, J.P.	541
Kaanta, B.C.	46	Valenzi, J.	347
Kefauver, W.N.	328	Visher, J.L.	526
Kempel, L.	508	Vogler, T.R.	284
Killips, D.	508	Watson, P.	406
Kim, S-J	447	West, J.B.	65, 76
Klock, P.W.	272	Yang, S.	181, 259
Kramer, T.C.	284	Zaghloul, A.I.	347
Lagoudas, D.	241	Zeller, K.	508

# PERFORMANCE PREDICTIONS FOR LINEAR ANTENNAS WITH OFFSET LOADING AND OFFSET EXCITATION

P. E. Mayes, P. W. Klock and S. Barot  
Electromagnetics Laboratory  
University of Illinois at Urbana-Champaign  
Urbana, IL 61801

[p.mayes@insightbb.com](mailto:p.mayes@insightbb.com), [p.klock@mail.ece.uiuc.edu](mailto:p.klock@mail.ece.uiuc.edu), [sbarot@uiuc.edu](mailto:sbarot@uiuc.edu)

**Abstract:** At frequencies below the first resonance the input impedance of a wide-angle conical radiating resonator is primarily an inductive reactance with a small loss. When loaded by inductive reactance around its periphery, the first resonance occurs when the antenna is electrically small. At this resonance, the input reactance changes from inductive to capacitive as frequency increases. This behavior is similar to that of a parallel combination of a lossy inductor and a lossless capacitor. When the same elements are connected in series, the resonance occurs when the reactance changes from capacitive to inductive, the characteristic behavior of a linear dipole. For an unloaded dipole, resonance occurs when the tip-to-tip length is about one-half wavelength. Interior series inductive loading can be used to reduce the size of a dipole at resonance and the current can be made nearly constant over a larger fraction of the dipole length. Also, by moving the feedpoint from the center of the dipole toward an end, the real part of the impedance at resonance can be increased.

Numerical studies using a low-frequency method of moments code (LFMOM) and a finite-elements code (HFSS) are used to demonstrate methods of design that enhance the radiating properties of loaded linear resonators. A report on the progress made in size-reduction, bandwidth enhancement, and efficiency improvement will be given.

## 1. Series Resonators in Parallel

Electrically small antennas are widely believed to be poor performers, primarily for two reasons: (a) the input impedance is difficult to match since the radiation from a small antenna is inversely related to its size in wavelengths, and (b) as the electrical size of a small antenna is reduced, the match bandwidth decreases. The second of these problems has been attacked with some success by increasing the number of resonances within the desired operating band. Early demonstrations of small multi-resonant antennas were done with radiating devices that could be approximately modeled as tanks (parallel resonators) connected in series[1]. Similar results can be obtained from series resonators

connected in parallel. The analysis of these circuits provides guidelines that are useful in the design of small antennas. One advantage of circuit models is that consideration of coupling is optional. This may not be the case for radiating devices since coupling between radiating resonators may be hard to avoid in practice.

Consider the circuit shown in Figure 1 (at the end of the text). The equations of this system are:

$$\begin{aligned} V_1 &= (R_1 + j\omega L_1 + 1/j\omega C_1)I_1 + j\omega M I_2 \\ V_2 &= j\omega M I_1 + (R_2 + j\omega L_2 + 1/j\omega C_2)I_2 \end{aligned} \quad (1.1)$$

which is a special case of the general equations for a two-port network that are usually written in matrix form as:

$$\begin{bmatrix} V_1 \\ V_2 \end{bmatrix} = \begin{bmatrix} Z_{11} & Z_{12} \\ Z_{21} & Z_{22} \end{bmatrix} \begin{bmatrix} I_1 \\ I_2 \end{bmatrix} \quad (1.2)$$

where

$$\begin{aligned} Z_{nn} &= R_n + j(\omega L_n - 1/\omega C_n) \\ Z_{mn} &= j\omega M \end{aligned} \quad (1.3)$$

The currents can be expressed in terms of the voltages by inverting the square matrix of Equation (1.2)

$$\begin{bmatrix} I_1 \\ I_2 \end{bmatrix} = \left( \frac{1}{\Delta} \right) \begin{bmatrix} Z_{22} & -Z_{12} \\ -Z_{21} & Z_{11} \end{bmatrix} \begin{bmatrix} V_1 \\ V_2 \end{bmatrix}$$

When the resonators are paralleled and a unit voltage generator is applied,  $V_1 = V_2 = 1.0$   $I_1 + I_2 = I$

where

$$\begin{aligned} I_1 &= (1/\Delta)(Z_{22} - Z_{12}) \\ I_2 &= (1/\Delta)(Z_{11} - Z_{12}) \\ \Delta &= Z_{11}Z_{22} - Z_{12}^2 \end{aligned}$$

assuming

$$Z_{12} = Z_{21} \text{ (reciprocity).}$$

The result describes the input current of a one-port network,

$$I = (1/\Delta)(Z_{11} + Z_{22} - 2Z_{12}) = \frac{Z_{11} + Z_{22} - 2Z_{12}}{Z_{11}Z_{22} - Z_{12}^2}$$

In the absence of coupling,  $Z_{12} = 0$ , and the input current response to a one-volt source is



$$I = \frac{1}{Z_{11}} + \frac{1}{Z_{22}} = \frac{1}{R_1 + j(\omega L_1 - \frac{1}{\omega C_1})} + \frac{1}{R_2 + j(\omega L_2 - \frac{1}{\omega C_2})}$$

Secondary parameters can be introduced

$$\omega_{0n} = \frac{1}{\sqrt{L_n C_n}} \quad R_{0n} = \sqrt{\frac{L_n}{C_n}}$$

so that

$$L_n = \frac{R_{0n}}{\omega_{0n}} \quad C_n = \frac{1}{\omega_{0n} R_{0n}}$$

$$I = \sum_{n=1}^{n=2} \left( \frac{1}{R_{0n}} \right) \left[ \frac{R_n}{R_{0n}} + j \left[ \frac{\omega}{\omega_{0n}} - \frac{\omega_{0n}}{\omega} \right] \right]^{-1} \quad (1.4)$$

Equation (1.4) is in a form that is easily extended so that an arbitrary number of resonators can be added. When the resonances of the system are related in a log-periodic manner,  $\omega_{0n} = \omega_{01} \tau^{(1-n)}$ . A conventional way to achieve the log-periodic connection among the resonances would be to scale the physical dimensions of each resonator. One result of such scaling would be to achieve the same value of  $R_0$  for all resonators. Furthermore, if the input impedance is normalized to this value, a general expression for the normalized impedance is

$$Z_{nor} = \frac{1}{\sum_{n=1}^N \frac{1}{R_{nnor} + j \left( \frac{\omega \tau^{(1-n)\omega_{01}}}{\omega_{01}} - \frac{\omega_{01}}{\omega \tau^{(1-n)\omega_{01}}} \right)}} \quad (1.5)$$

Several observations about the behavior of the parallel connection of series resonators can be made by inspection of Equation (1.5). When  $R_n$  is not zero, the impedance versus frequency locus will lie inside the unit circle on the reflection coefficient plane (Smith Chart) and variation of  $R_{0n}$  will be effective in the placement of the locus. Radiation loss will always be present in an antenna and the above result can be used advantageously to affect the degree of match to a feeder.

## 2. Lumped-element Networks

The principal advantage of lumped-element networks is the simplicity of analysis. However, it is the theme of this paper that much can be learned from consideration of the results of that analysis. For example, computations of the input impedance versus frequency for a simplified case of Figure 1, in which only one resonator is present and the

coupling is thereby eliminated, leads to the Smith Chart plot of Figure ?. Note that the normalized resistance at resonance can be changed on the chart by varying the value of  $R_{0n} = \sqrt{\frac{L}{C}}$ . Further computations were made by programming *Mathematica* to evaluate a reduced version of Equation (1.5). When two series resonators are connected in parallel, the impedance locus can be made to form a loop. The loop on the left in Figure 2 is an example of an impedance locus that can be achieved with two series resonators in parallel. In this example, the loop is not centered on the center of the chart and so provides a match that varies with frequency. A second loop in Figure 2 is the result of attaching a transformer of appropriate transformation ratio to move the center of the loop closer to the center of the chart, thereby improving the impedance match.

In many cases the improved match can be obtained by changing the parameters of the antenna itself and no external transformer is necessary. Figure 3 shows a case where the impedance loop circles the center of the chart in such a manner that any operating frequency provides approximately the same degree of mismatch. In those cases where the operating specification for the system defines a maximum allowable SWR, often placing the loop so that it passes through the maximum SWR value will produce a degree of mismatch that will be about the same for all other frequencies in the operating band. A single value of  $\tau$ , the ratio of the resonant frequencies of each of the two resonators, will yield the value of input resistance at the parallel resonance that occurs between the two series resonances. This largely determines the size of the loop. Notice that the part of the impedance locus for  $\tau = 0.5$  that is contained within the SWR=2 circle encompasses a bandwidth of around 2:1. The essentials of achieving this result are few: (a) a *normalized* resistance of approximately 0.5 of each resonator at series resonance, and (b) a *normalized* resistance of approximately 2.0 for the total network at the parallel resonance that falls between the two series resonances. The former value is determined from the radiation resistance of the antenna at resonance and the characteristic impedance.

The form of Equation 1.5 suggests that this pattern of behavior will repeat for higher frequencies. The limit on achieving a network having the given degree of impedance match over an arbitrarily wide band seems thus to depend only upon the practical matter of realizability, i.e. how many resonators can be properly connected within the available space.

### 3. Systems of Transmission-line Resonators

To bring physical dimensions into consideration without unduly adding to the complication, transmission-line resonators provide a convenient intermediate point between lumped-element networks and antennas. A small resonator can be fashioned from a section of uniform line that is terminated on one end in an open and on the other end in a short. Such a resonator will be resonant at many values of its length, the smallest one being one-quarter wavelength. This resonance will occur for even shorter lengths when the open is replaced by a capacitive reactance; and the short, by an inductive reactance. Nor is it essential that these reactive elements be placed at the end of the line in order for changes in length at resonance to occur. The realization of various values of normalizing impedance can be achieved in distributed resonators by simply choosing the location of the feedpoint. The input resistance of a radiating resonator can be varied by changing the location of the feed point. Consider, for example, a section of transmission

line that is terminated on one end in an open circuit and on the other in a short circuit. The resistance seen at the input of such a line at resonance can be varied from zero to infinity by moving the feed point along the line from one terminated end to the other.

By connecting in parallel two resonators with resonant frequencies that have the proper ratio, a loop can be produced in the impedance locus. Figure 4 gives the schematic diagram for a system with tx-line resonators that are loaded in the interior to reduce their lengths at resonance. Figure 5 shows the values of input impedance computed by using Microsoft's Excel. In this case, resistive loads provide the loss and the normalized impedance is the ratio of this resistance to the input resistance (at resonance) at the feedpoint. Hence, the normalization can be adjusted by choosing the point of attachment to the resonator. As shown in the figure, the input impedance computed for frequencies between 1 and 2 GHz has a loop that includes the center of the Smith Chart. There is, however, a capacitive shift so that the center of the loop and the center of the chart do not coincide. However, this shift can be compensated by a series inductor at the input of the network. Note that the first resonance occurs at 1 GHz where  $\ell/\lambda = 0.125$ . Hence, the system is electrically small. At the second series resonance,  $\ell/\lambda = 0.25$  and the system remains electrically small. The fourth crossing of the real axis demonstrates the effect of a higher resonance of one of the lines and could be a point within or outside of the operating band.

#### 4. Method of Moment Computations for Linear Blade Dipoles

The application of the above principles to linear dipole antennas has been demonstrated with moment method calculations of the input impedance of dipoles simulated as strips of flat, narrow, thin conducting material. The geometry is shown in Figure 6 which includes lines depicting the edges of planar subsectional divisions of the area of conductor. In the examples shown in Figure 7 the computed input impedance is shown for dipoles of length 14.6 cm and width 0.5 cm that may be fed off-center. The feed location relative to the center of the dipole is given in the first column of the legend. The several curves show the effect of various locations for the source and various values of loading with inductive reactance. The case of center feeding with no load (dots) is given for comparison. As the feed is moved toward the tip, the resistance at resonance increases. This result can be used to increase the input resistance of electrically small antennas. All the loads were located on the lowest patch on the upper half of the dipole, essentially base loading. As the load inductance increases from 0 to 46.5 nH, the resonant frequency and bandwidth decreases.

An example of a design an electrically small antenna using these principles is shown in Figure 9. The input impedance crosses the real axis just below 425 MHz at a point well within the  $\text{SWR} = 2$  circle. The impedance locus remains in the  $\text{SWR} = 2$  circle from about 422 MHz to about 427 MHz, a bandwidth of 5 MHz (about 1.2 percent). Note that this bandwidth, defined on the basis of an  $\text{SWR} = 2$ , is much more restrictive than the usual one that is defined on the basis of half power ( $\text{SWR} = 5.83$ ).

Center loading, as approximated in the results above, will result in a current distribution that is almost triangular. Figure 10 shows the magnitude of the axial current along a dipole with inductive loads placed symmetrically away from the center. Note that the current is very nearly constant between the two inductances. The improvement in power

radiated from this flat-topped current distribution as compared with a triangular one is approximately evaluated as the ratio of the areas under the respective currents.

### **5. Realization of Load Inductors with Ferrite Beads**

At frequencies below 100 MHz the inductances used to lower the resonant frequency (and to shape the current distribution) could possibly be realized with wire-wound coils. However, some investigation of ferrite beads has been carried out to provide design information for use at somewhat higher frequencies. Simulations were done for a monopole of 10.5 cm in height and 1.5875 mm in radius. The monopole is attached to a square ground plane 45.7 cm on each side. Input impedances have been computed using HFSS to simulate the effect of a ferrite bead of 9.525 mm in outside diameter, 4.75 mm in inside diameter, and a height of 6.35 mm. The monopole is excited by a port source at its midpoint (52.5) and base (0.1). Beads of two values of permeability ( $\mu$ ) were used. Since the frequency-dependence of the permeability was neglected, the results are unrealistic for the frequencies given. However, the results are indicative of practical results that might be expected at lower frequencies. As seen in Figure 10, both beads, when located some distance from the end of the monopole, were effective in lowering the resonant frequency. It is also apparent, from Figure 11, that the current distribution on the monopole is altered by the placement of the ferrite bead and this thereby changes the input resistance.

### **6. Conclusions and Plans for the Future**

It has been shown that beneficial results can be obtained for a linear (dipole or monopole) radiator by choice of the locations of feedpoint and load. Such an antenna with either offset feed and/or offset load retains the basic shape for its impedance locus and becomes a candidate for use as an electrically small radiating resonator with series-type behavior. A study of antennas with one or more of these series-type resonators connected in parallel is underway. The influence of coupling between them has already been noted and will become an important part of the investigation.

### **7. Reference**

[1] P. E. Mayes and W. Gee, "Using Multiple Resonant Radiators for Increasing the Impedance Bandwidth of Electrically Small Antennas," *Proc. 24<sup>th</sup> Annual Antenna Applications Symposium*, Allerton Park, Illinois, September 2000.

## 8. Figures

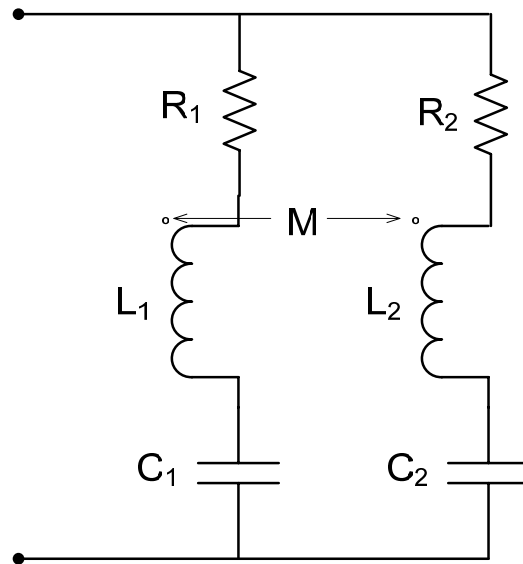


Figure 1. A one-port network comprising two paralleled, lossy series resonators including magnetic coupling.

**Computed Input Impedance for Two Series Resonators in Parallel**  
 **$R_1=R_2=10$ ,  $R_{01}=R_{02}=25$  ohms,  $\tau=0.5$**

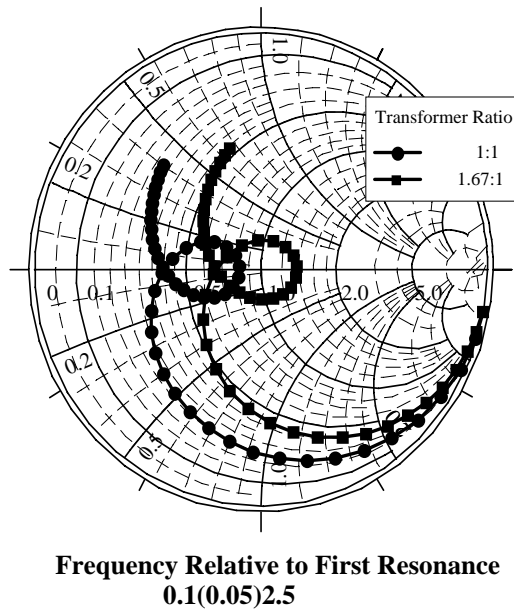
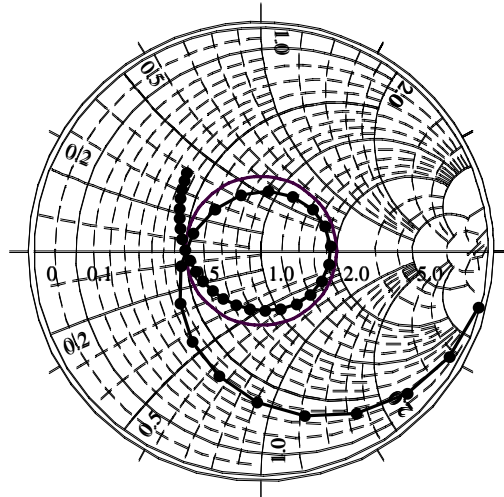


Figure 2. Computed input impedance for a pair of series resonators connected in parallel.

**Computed Input Impedance for Two Series Resonators in Parallel**  
 **$R_1=R_2=12.5$ ,  $R_{01}=R_{02}=25$  ohms,  $\tau=0.3$**



**Frequency Relative to First Resonance**  
**0.1(0.1)4.0**

Figure 3. Computed input impedance for two lumped-element resonators. The value of  $R_n/R_{0n}$  was chosen to place the point of intersection of the impedance loop on the  $SWR=2$  locus. The value of  $\tau$  was chosen so that the point on the opposite side of the loop is also on the  $SWR=2$  curve. The result is that all impedance points in the operating band have  $SWR$  less than 2. By placing the series resonances closer together, the  $SWR$  will be decreased. The center of the impedance loop can be located at various points on the real axis by choosing the characteristic impedances of the resonators.

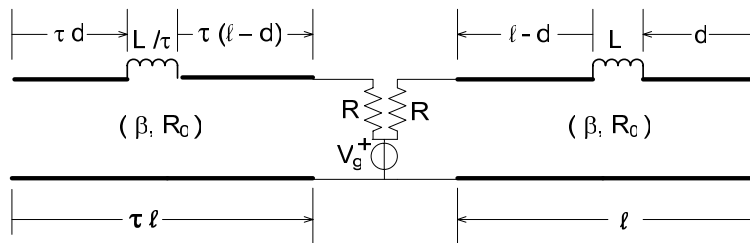


Figure 4. Schematic diagram of two tx-line resonators with offset lumped inductors. The resonators differ in size by the scale factor,  $\tau$ , and are connected in parallel. A lumped inductor is located within each resonator.

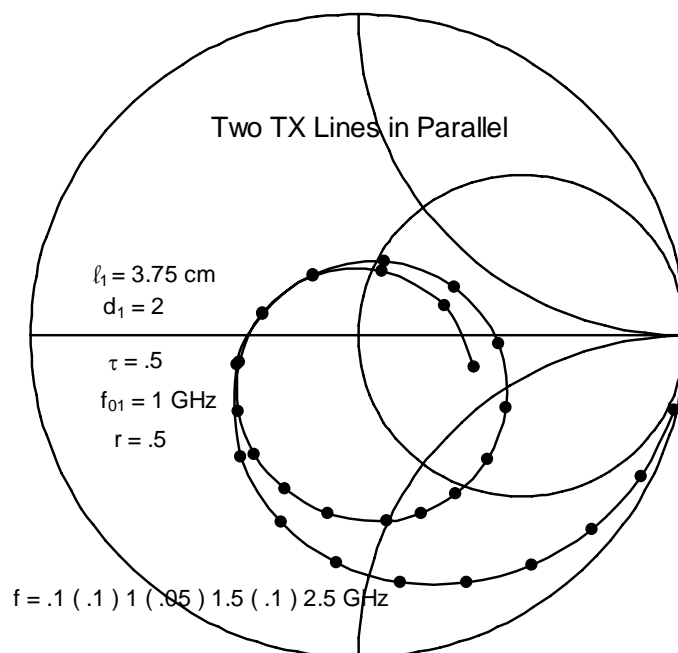


Figure 5. The computed input impedance for two tx-line series resonators in parallel.



Figure 6. Diagram of blade dipole indicating locations and relative sizes of the subsectional patches used in the analysis. As shown here, a load inductance is located on the lower double patches and the source is centered on the upper double patches. However, in the analysis, either or both the source and the load could be moved to any patch.

Calculated Input Impedance of Two Blade Dipoles  
Half-Length=7.3, Half-Width=0.25cm

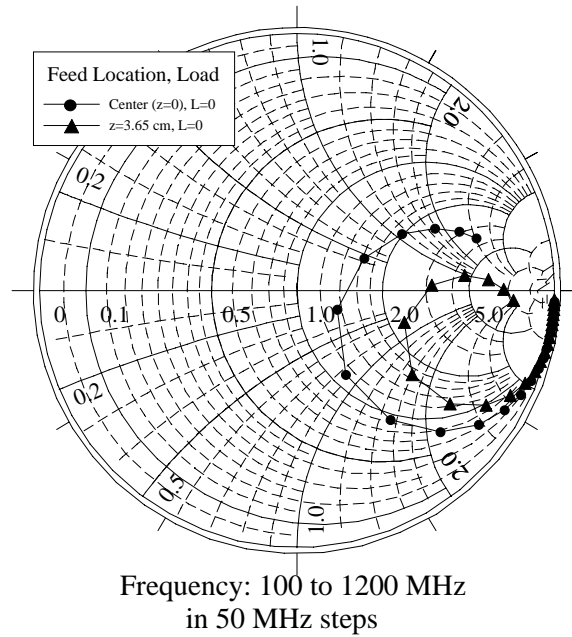


Figure 7. Calculated input impedance of two blade dipoles showing the effect of moving the feedpoint.

Calculated Input Impedance of Three Blade Dipoles  
Half-Length=7.3, Half-Width=0.25cm

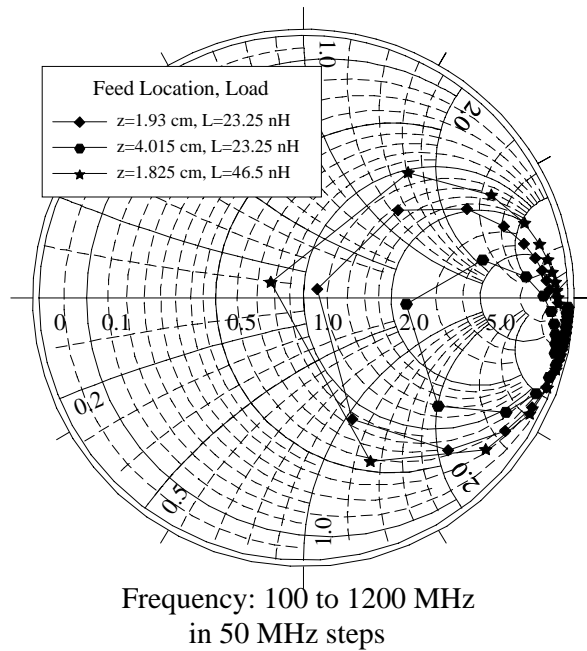


Figure 8. Calculated input impedance of three blade dipoles showing the effect of moving the feedpoint and changing the load inductance.



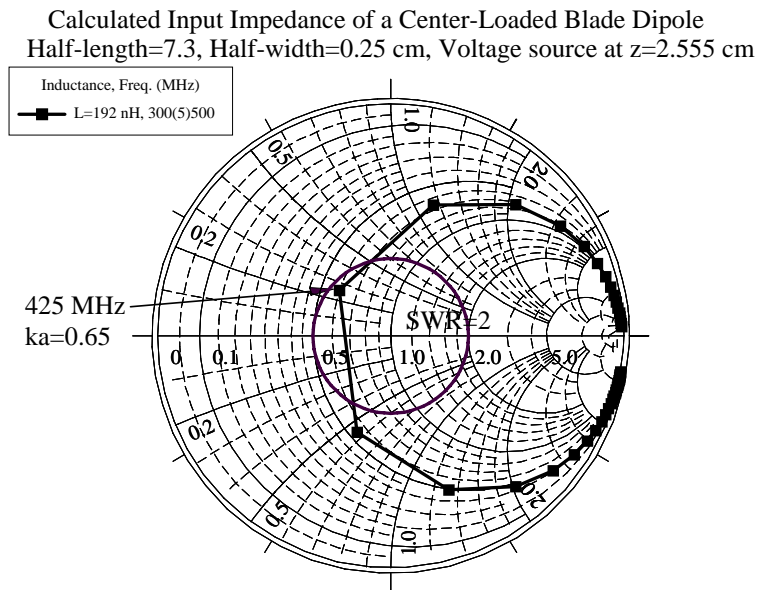


Figure 9. Calculated input impedance of a center-loaded, offset-fed blade dipole.

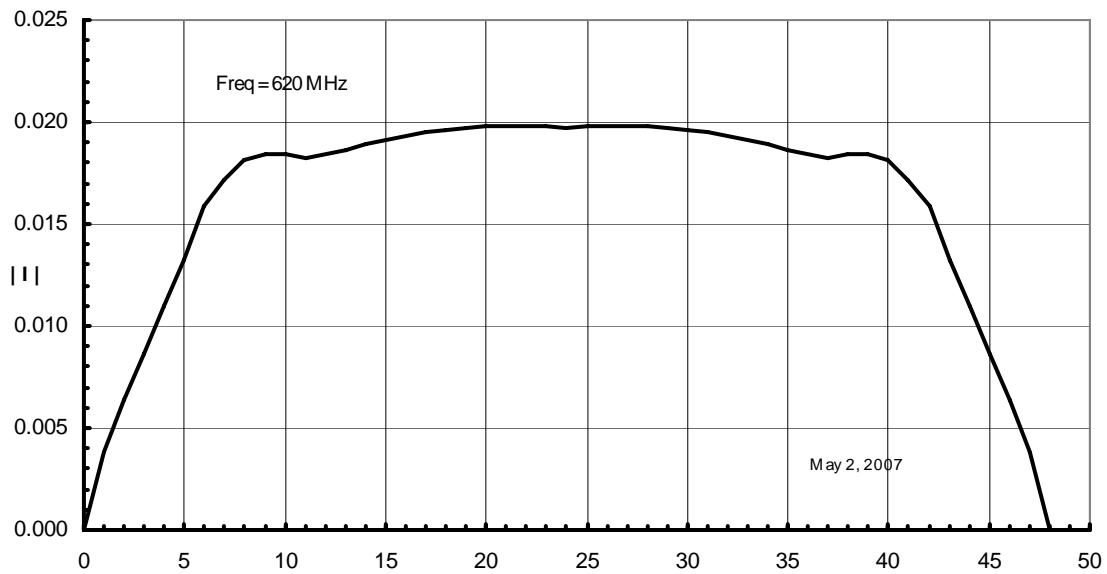


Figure 10. Axial current magnitude versus patch number on linear blade dipole with inductive loads near each end.

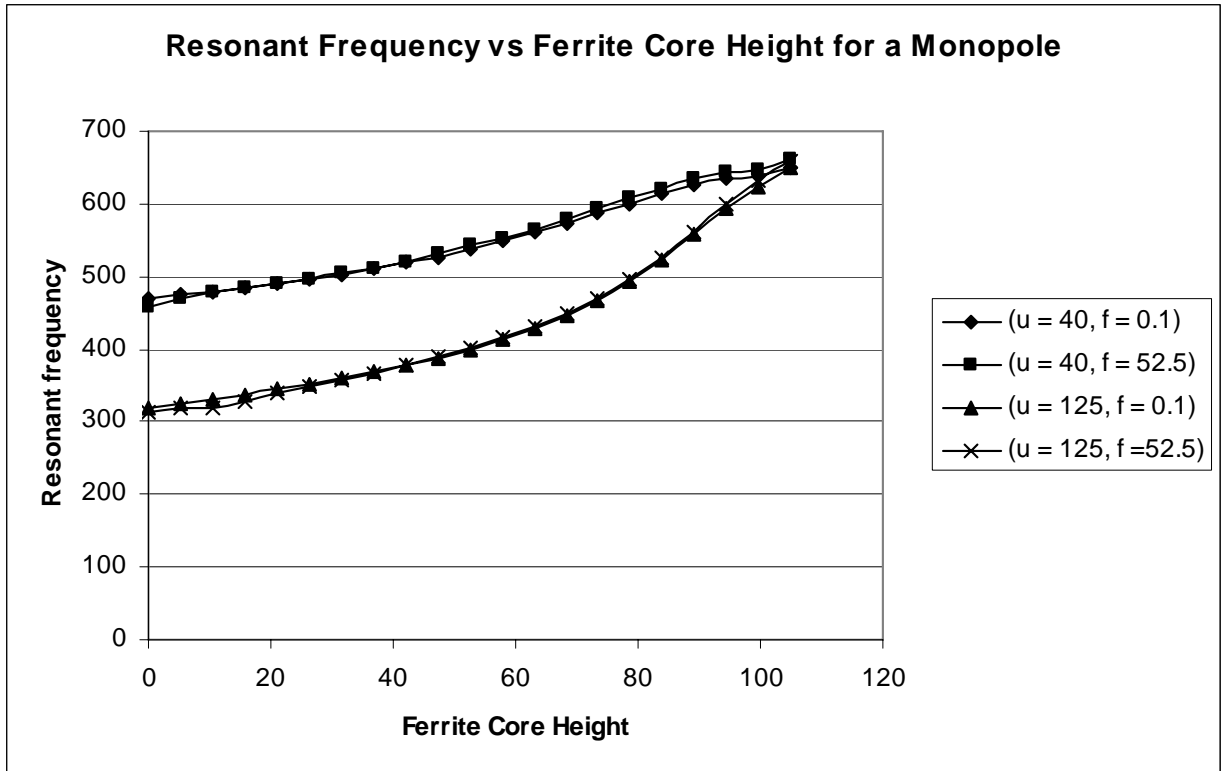


Figure 11. Resonant frequency (MHz) versus height of ferrite bead (cm).

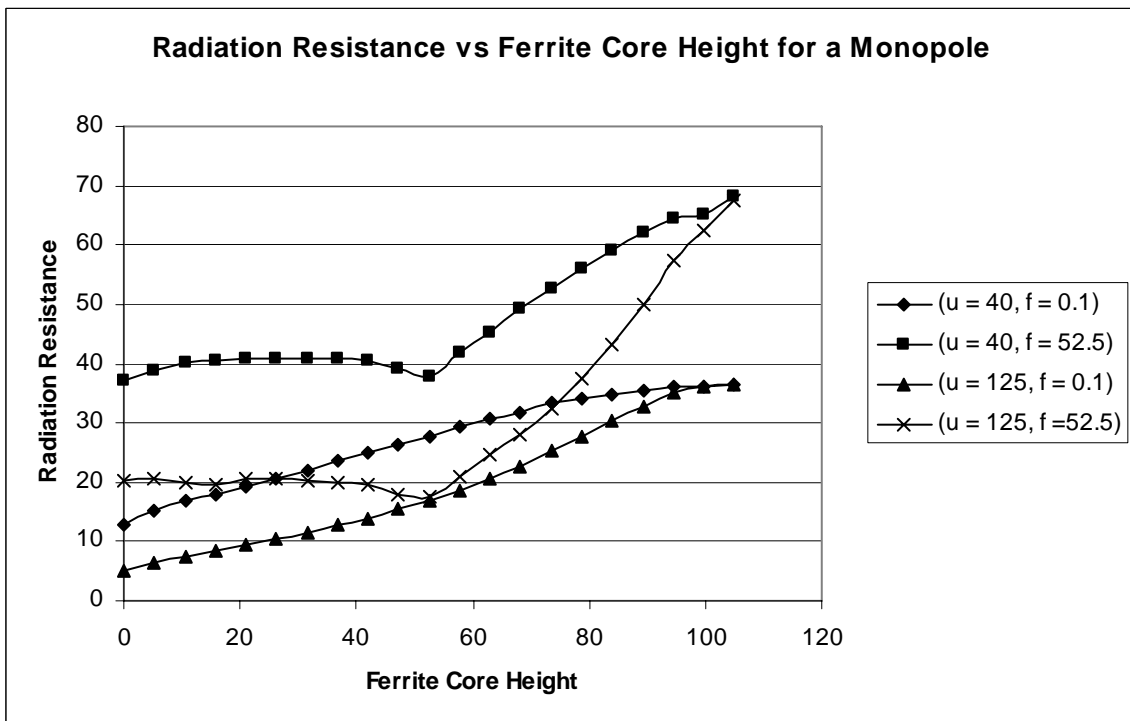


Figure 12. Radiation resistance (ohms) versus height of ferrite bead (cm).

# **Improvements on MF Ground Wave Antennas for the Global Maritime Distress and Safety System (GMDSS)**

Terry R. Vogler<sup>1</sup>, Tyler C. Kramer<sup>2</sup>, and William A. Davis<sup>1</sup>

1. Virginia Tech Antenna Group (VTAG)
2. Virginia Tech Electromagnetic Interactions Lab (EMIL)  
Bradley Dept. of Electrical and Computer Engineering  
Virginia Polytechnic Institute and State University  
Blacksburg, VA 24060

## **Abstract**

**The Global Maritime Distress Safety System requires monitoring of 2182 and 2187.5 kHz for distress calls within 150 nm of shore. A network of monitoring sites is required to cover the large US coastline. The US Coast Guard has selected a 54' monopole antenna for all sites to limit costs. Sites are immediately adjacent to the coast, and ground systems are tailored to the specific location.**

**Comparison of free-space far-field radiation patterns is typical, but this is misguided for ground wave radiation systems. The surface wave component propagates laterally at the air-earth interface and is evanescent vertically. However, the use of MoM and a planar Green's functions to represent the lossy earth lacks the flexibility to design the antenna for one ground type and observe its propagation performance over seawater. Our approach is to develop the antenna ground system over a homogeneous earth, export the currents, and radiate them using full analytical equations. Antenna designs are then compared at a distance of 1 km, per ITU standards. All designs retain the 54' free-standing design and have differing ground systems to emphasize launching the surface wave. Several designs are presented that improve the coverage over seawater without increased installation complexity.**

## **1 Introduction**

This study encompasses two aspects of ground wave-based communications: the propagation mechanism and, separately, the antenna design. Often in the literature, the two subjects are divorced. Our approach fulfills a practical need to be able to improve upon standard antenna installations and compare various design options. These options are the reality of site selection and depend on the availability of land, its current use, and the proximity to the coastline. The Global Maritime Distress and Safety System (GMDSS) has a "Sea Area 2" requirement for the monitoring and response to distress calls at the MF frequencies of 2182 and 2187.5 kHz. The US Coast Guard is currently improving its coverage for these frequencies along all the US coastlines<sup>1</sup>. The US will then declare to the International Maritime Organization when it has fulfilled the

---

<sup>1</sup> An overview of GMDSS can be found <http://www.navcen.uscg.gov/marcomms/gmdss/default.htm>.

requirement for “Sea Area 2” and to what distance seaward that area extends. Currently, the objective distance of 150 nautical miles is being sought. ITU-R M.1467 specifies the procedure for measuring an antenna installation’s field strength at 1 km [1]. It is based on an ideal short monopole, with 1 kW available power and no earth losses. Losses from the ideal monopole are accounted for by measuring the received power with a calibrated short monopole at 1 km. The most notable, and often used, program for predictions is the ITU-R ground wave model, GRWAVE

We observe that this ideal approach lacks the flexibility to compare different design options and sites since these sites may be on different real earths. Separately, the use of planar Green’s Functions in such programs as NEC4d [2][3] and FEKO<sup>®</sup> [4] do not allow for the use of different lossy grounds. Analyzing the problem through a fully numerical solution is impractical, if not entirely unattainable, with today’s 64-bit processors.

Our approach assumes the antenna is installed near the coastline, such that the losses to the ground during propagation before reaching the coastline (i.e., seawater) are minimal. In such, currents on various antennas are solved using standard Method of Moments (MoM) techniques with FEKO<sup>®</sup> for the soil on which such an antenna would be installed. The losses of the ground show a direct effect on the antenna currents and input impedance. Since strongly coupled fields are most important within a half-wavelength of the antenna, as a general rule, an installation within 68m (225 ft) of the coastline will account for the over-land losses well enough for design purposes. This distance is a reasonable limit for many existing Coast Guard properties.

Because this study does not incorporate, currently, the earth’s curvature, refractive atmosphere, or the rough surface scattering from the sea, we evaluate all fields up to the ITU-specified 1 km distance. With these relatively minor additions, a full-featured tool could be developed to determine the range for the minimum field strength for each antenna design.

Section 2 of this report presents the background and development of the propagation solutions. Section 3 presents our antenna designs and parametrically presents how the real ground effects each design. Section 4 discusses future work, and Section 5 has our conclusions.

## **2 Ground Wave Propagation**

Since MF GMDSS communications rely on ground wave propagation, it is necessary to clarify the nature of ground wave propagation. Though the problem of a vertical electric dipole and resulting ground wave were first investigated by Sommerfeld at the turn of the 20<sup>th</sup> century, it is evident from recent papers that the underlying physics and mathematics of the problem are often not entirely understood [5][6]. The ground wave loss factor will be developed and discussed. A means of computing the loss factor will be recommended, and its inherent limitations also discussed.

For this reason, Section 2.2 contains a brief discussion of different solutions to the Sommerfeld problem which have been published in recent years. The reader must understand that the field has been extensively studied by many brilliant minds throughout the years. However, to a certain extent, diverse goals have played a role in shaping the overall understanding, and no “unified” ground wave theory exists. To circumvent this

problem, we discuss the many different approaches, their limitations, and make future recommendations. The most common error encountered in *applied* ground wave literature is a deviation in the definition of “ground wave” from the *theoretical* ground wave literature. Following the *IEEE* standards definition, a true ground wave can be decomposed into three respective components: (1) Direct wave, (2) Ground reflected wave, and (3) Norton surface wave, as shown in Figure 1 [7].

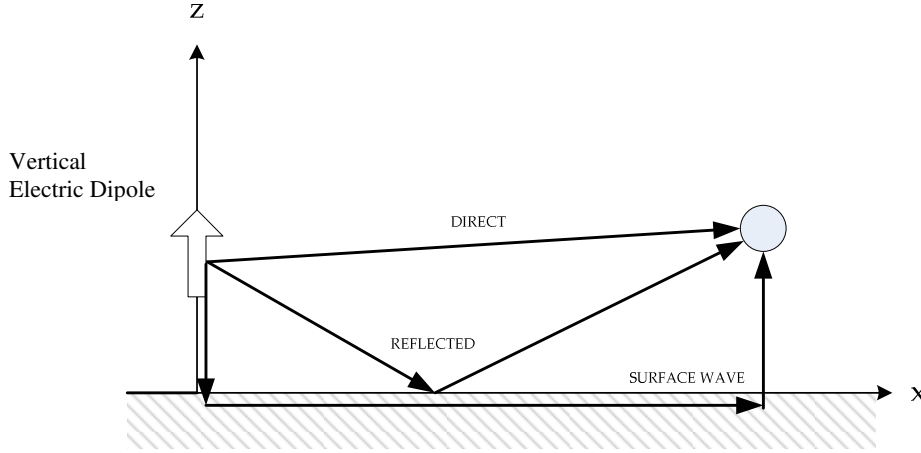


Figure 1. Components of a ground wave.

## 2.1 Ground Wave Propagation & Sommerfeld’s Problem

There has been much controversy surrounding the Sommerfeld problem, as evident in Wait’s review [8]. It is interesting to note that despite being published close to 90 years after Sommerfeld originally proposed the problem, Wait’s paper still contains a conceptual error which was not completely resolved for another 6 years by Collin [6].

The formulation of the Sommerfeld problem can be found in numerous sources, and as such, the reader is referred to them for the derivation. Care must be taken when comparing expressions, as each author approaches the problem from a different perspective. The works of Ishimaru [9], Wait [8], and Banos [10] set up the problem using Hertzian potentials while King [11] and Chew [12] solve directly for the fields. For a basic understanding of the problem and derivation, the work by Ishimaru is recommended, while a more thorough discussion can be found in King’s work.

The Sommerfeld problem attempts to find an analytic solution for the radiated fields of a vertical electric dipole located above (or on) a lossy half-space, as shown in Figure 2. A vertical electric dipole produces only TM fields ( $H_z = 0$ ) and the vertical component of the E-field in the upper half-space can be expressed as [12]

$$E_z = -Idl \frac{\omega\mu_o}{4\pi k_1^2} \int_0^\infty \frac{k_\rho^3}{k_{1z}} \left[ e^{-jk_{1z}|z-d|} + \Gamma_{TM} e^{-jk_{1z}(z+d)} \right] J_0(k_\rho \rho) dk_\rho \quad (1)$$

where

$$k_{nz}^2 = k_n^2 - k_\rho^2$$

$$k_n = \omega \sqrt{\epsilon_n \mu_n}$$

$$\epsilon_n = \epsilon_m - j \frac{\sigma_n}{\omega}$$

$$\Gamma_{TM} = \frac{k_2^2 k_{1z} - k_1^2 k_{2z}}{k_2^2 k_{1z} + k_1^2 k_{2z}}$$

with  $\sigma$  being the conductivity and  $\Gamma_{TM}$  being the TM polarized reflection coefficient for plane waves. Equation (1) is generally referred to as the Sommerfeld Integral. Expressions for all other vector field components can be derived from (1) using the relationships given by Chew [12]. From the above expressions, it is easily seen that the total field in the upper region can be expressed in terms of an infinite number of incident (1<sup>st</sup> term) and reflected (2<sup>nd</sup> term) plane waves. Unfortunately, there exists no analytic solution to (1). Even with today's computers, numerical solutions of (1) are often impractical due to the oscillatory nature of the Bessel function in the integral.

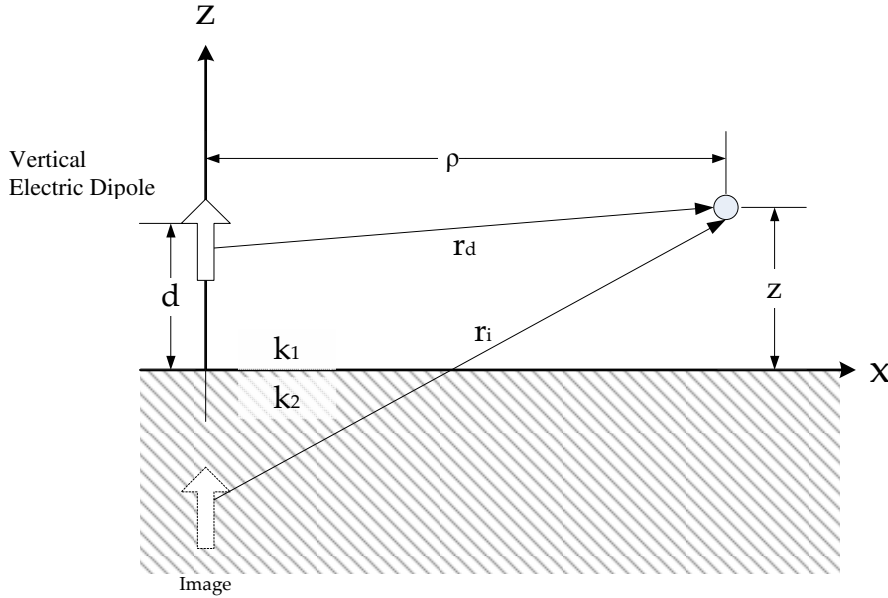


**Figure 2. Coordinate system and geometry for Sommerfeld problem.**

In order to evaluate the Sommerfeld integral, regardless of the approach one uses, there is one universal limitation that must be imposed: *loss must be present within the system*. The purpose of the loss is often not fully explained or understood in the literature. At the start of Sommerfeld's work in the early 1900's, physicists were attempting to understand and explain the propagation of radio waves across the Atlantic Ocean, an effect now attributed to ionospheric refraction and reflection. As a result, the work of Sommerfeld and Norton, among others, focused on the propagation over a lossy

dielectric, with a dielectric constant much larger than air or free-space in order to model the salt water. More recent work by King [11] claims to have removed the condition of a lossy medium and only requires that the magnitude of the earth's wave number be much larger than that of free space. In reality, the loss, no matter how small, is required to guarantee convergence of (1) [10]. This is a minor point since we already assume an infinitesimal amount of loss in a given medium to ensure uniqueness. Furthermore, in many cases we are concerned with the asymptotic behavior of the surface wave. From the early work of Norton, we expect a field that decays as  $1/r^2$  on the dielectric surface. However, to obtain this dependence, an asymptotic series is employed which is only valid if there is finite conductivity [13][6].

More commonly, asymptotic techniques are used to find a suitable solution to Sommerfeld's integral. For "far-field" radiation with the source and observation point above the interface, the saddle point technique of [9] can be applied to (1), resulting in

$$E_z \approx Idl \frac{\omega \mu_o}{4\pi k_1^2} e^{-jk_1 r_d} \left[ -\frac{jk_1^2}{r_d} - \frac{k_1}{r_d^2} + \frac{j}{r_d^3} - \left( \frac{z-d}{r_d} \right)^2 \left( -\frac{jk_1^2}{r_d} - \frac{3k_1}{r_d^2} + \frac{3j}{r_d^3} \right) \right] + \quad (2)$$

$$Idl \frac{\omega \mu_o}{4\pi k_1^2} \Gamma_{TM} e^{-jk_1 r_i} \left[ -\frac{jk_1^2}{r_i} - \frac{k_1}{r_i^2} + \frac{j}{r_i^3} - \left( \frac{z+d}{r_i} \right)^2 \left( -\frac{jk_1^2}{r_i} - \frac{3k_1}{r_i^2} + \frac{3j}{r_i^3} \right) \right]$$

where  $\Gamma_{TM}$  is the TM reflection coefficient defined earlier. The first term is the E-field component that would result from a dipole radiating in free-space at  $z = h$ . The second term is the field that would result from an image source reflected about the xy-plane and multiplied by the reflection coefficient. While very simple to compute, (2) consists of only two spherical waves and predicts no ground wave component. This is evident if we let  $z \rightarrow d \rightarrow 0$ . Then,  $r_d = r_i$  and  $\Gamma_{TM} = -1$ ; and the vertical electric field goes to zero. For ground wave communications, (2) is ineffective in that it fails to predict the correct fields for targets located on or near the earth, such as ships. The failure of (2) rests with the use of the saddle point approximation and its inadequacy as  $z$  and  $d$  approach the surface.

As the dipole or observation point approaches the air-dielectric interface, alternative approaches must be used. This is because as the antenna or field point approach the surface, we approach a grazing incidence problem. The pole located in the denominator of (1) approaches the saddle point used in the derivation of (2) and an alternative technique must be used. The most common approach, which was employed early on by Norton [14] and explained in detail by Ishimaru [9], involves the use of the modified saddle point approach. King [11] developed a slightly different approach to evaluating the Sommerfeld integral. The remainder of this section will focus on the more recent work by King, as it appears to be slightly more general and the explicit expressions are provided for the electric and magnetic fields as opposed to the Hertzian potentials used by other authors. In both cases, an image term is factored out of the reflection term of (1). Though there are many possible deviations, the end result is [10]:

$$E_z = -Idl \frac{\omega\mu_o}{2\pi k_1^2} \int_0^\infty \left[ \frac{e^{-jk_{1z}|z-d|}}{2k_{1z}} + \frac{e^{-jk_{1z}(z+d)}}{2k_{1z}} + k_2^2 e^{-jk_{1z}(z+d)} \left( \frac{1}{N} - \frac{1}{N_o} \right) \right] J_0(k_\rho \rho) k_\rho^3 dk_\rho \quad (3)$$

where

$$N = k_2^2 k_{1z} + k_1^2 k_{2z}; \quad N_o = k_2^2 k_{1z}$$

which clearly shows the direct field, an image field (such as would appear if the dipole was located above a PEC), and a surface-correction term that accounts for the finite conductivity of the dielectric ground. This formulation eliminates the use of the reflection coefficient  $\Gamma_{TM}$ . As the conductivity of the ground tends to infinity, the surface-correction term disappears. On the other hand, if the dielectric constant of the ground approaches the dielectric constant of the air, the third term should completely cancel out the second term. This is indeed the case as  $k_{1z} \rightarrow k_{2z}$  and  $k_1 \rightarrow k_2$ .

The direct and image terms in (3) have closed-form solutions, which are well known. If we rewrite the E-field as a summation of direct, image, and surface correction<sup>2</sup> terms as

$$E_z = E_z^d + E_z^i + E_z^{sc}, \quad (4)$$

then the direct term can be rewritten in closed form as [10]

$$E_z^d = Idl \frac{\omega\mu_o}{4\pi k_1^2} e^{-jk_1 r_d} \left[ -\frac{jk_1^2}{r_d} - \frac{k_1}{r_d^2} + \frac{j}{r_d^3} - \left( \frac{z-d}{r_d} \right)^2 \left( -\frac{jk_1^2}{r_d} - \frac{3k_1}{r_d^2} + \frac{3j}{r_d^3} \right) \right] \quad (5)$$

and the image term is identical with the substitution of  $z+d$  for  $z-d$  and  $r_i$  for  $r_d$ . If (5) is used to calculate the transverse field components, and the cylindrical coordinate system converted to spherical, we would obtain the more familiar expression for an infinitesimal dipole found in the antenna literature. We note that the formulation of the surface correction term of (4) is not an independent surface-wave term. By splitting the E-field into a direct and image term, we are *not* separating the problem into two sky-wave and one surface-wave terms. If  $E^i + E^d$  represented a sky wave then we know that their sum must be zero on the surface for this case. Instead, we see that the two expressions become equal and add together. Therefore,  $E^{sc}$  contains a component of the sky-wave in addition to the surface wave.

With the exception of a finite loss, no other assumptions or approximations have been made up to this point. In order to find an easily computable form for  $E^{sc}$ , all of the aforementioned works, with the sole exception of Collin, assume

$$|k_2^2| \gg |k_1^2|$$

---

<sup>2</sup> The superscript “sc” is used as opposed to King’s superscript “s” to emphasize the point that  $E^{sc}$  is not a classical surface wave.



Because most of the early work centered on propagation over the sea and dealt with low frequencies, this assumption was more than justified in order to obtain an easily computable expression. However, in the contemporary solutions of King, this assumption is still applied. If this assumption is valid, then

$$k_{2z} \approx k_2$$

and

$$E_z^{sc} \approx -Idl \frac{\omega \mu_o k_2}{2\pi} \int_0^\infty \frac{e^{-jk_{1z}(z+d)}}{k_{1z} N} J_0(k_\rho \rho) k_\rho^3 dk_\rho. \quad (6)$$

However, in order to formulate the above expression, one must also assume that the main contribution to the integral comes from when  $k_\rho \sim k_1$ . However, as Collin points out, when  $(z+d)$  and  $\rho$  are small,  $k_\rho$  must be “much larger before the exponential function in  $E^{sc}$  will exhibit a significant decay and the Bessel function will exhibit rapid oscillations” [15]. In the same paper, Collin went on to verify this fact by comparing King’s approximation to a full numerical integration of (6). This, too, is subject to debate, as how small  $(z+d)$  and  $\rho$  are allowed to be is dependent on how much larger  $k_2$  is relative to  $k_1$ . King arbitrarily sets this limit as a factor of 3, however, as pointed out by Collin, this limit is not large enough for points close to the antenna.

For MF GMDSS applications, we are generally not concerned with the field very close to the antenna, and thus King’s expressions should be more than adequate, and are easily computed. By applying the modified saddle-point technique or stationary-phase method to (6), we are left with

$$E_z^{sc} \approx -Idl \frac{\omega \mu_o k_1^2}{2\pi k_2} e^{-jk_{1z} r_i} \left( \frac{\pi}{k_1 r_i} \right)^{1/2} \left( \frac{\rho}{r_i} \right) e^{-P_2} F(P_2) \quad (7)$$

where

$$P_2 = \frac{k_1^3 r_i}{2k_2^2} \left( \frac{k_1 r_i + k_2(z+d)}{k_1 \rho} \right) \quad (8)$$

$$F(\varsigma) = \int_\varsigma^\infty \frac{e^{jt}}{(2\pi t)^{0.5}} dt = \frac{1}{2}(1+j) - [C_2(\varsigma) + jS_2(\varsigma)]$$

and  $C_2 + jS_2$  is an alternative form of the Fresnel integral as defined in equations 7.3.3 and 7.3.4 of Abramowitz and Stegun [13]. The term  $P_2$  is the numerical distance, modified from the Sommerfeld numerical distance to allow for the current source and observation points to both be above the ground. This expression is subject to the conditions that:

1.  $|k_2^2| \gg |k_1^2|$
2. The field point is sufficiently far from the antenna.
3. Loss is present in the system.

Recall, however, that the “sufficient” distance is dependent on how much larger the wave number of the ground is compared to the wave number of the air. For a typical sea, the dielectric constant and conductivity are sufficiently high so that (7) is very accurate, even at distances close to the antenna. If (4) is normalized by the electric field of a dipole in free-space, then the resulting power can be used as a propagation loss factor discussed in the previous section. Recalling that the path gain factor,  $F$ , is the factor by which the propagation differs from that of free space,  $F$  can easily be computed by

$$F = \frac{E|_{Sommerfeld}}{E|_{freespace}}$$

where the  $E_{Sommerfeld}$  is computed from (4), and  $E_{freespace}$  can be found in most antenna literature including King [11]. Generally, the component of the E-field in the above expression is the theta component.

For large numerical distances,  $P_2$ , we know that (4) must reduce to the well known Norton surface wave when  $z = d = 0$ . To achieve this from King’s expressions, we can use the asymptotic series representation of the Fresnel integral in (7). When the first two terms of the asymptotic series are retained and after basic manipulations, (4) reduces to

$$E_z(d = 0, z = 0) \approx -Idl \frac{\omega \mu_o k_2^2}{2\pi k_1^3} \frac{e^{-jk_1 \rho}}{\rho^2},$$

which is the Norton surface wave.

## 2.2 Comments on Sommerfeld Implementations & Propagation

From (4), King’s expression for the field radiated by a vertical electric dipole on or above a lossy ground can be expressed as:

$$E_z = E_z^d + E_z^i + E_z^{sc}$$

where

$$\begin{aligned}
E_z^d &= Idl \frac{\omega \mu_o}{4\pi k_1^2} e^{-jk_1 r_d} \left[ -\frac{jk_1^2}{r_d} - \frac{k_1}{r_d^2} + \frac{j}{r_d^3} - \left( \frac{z-d}{r_d} \right)^2 \left( -\frac{jk_1^2}{r_d} - \frac{3k_1}{r_d^2} + \frac{3j}{r_d^3} \right) \right] \\
E_z^i &= Idl \frac{\omega \mu_o}{4\pi k_1^2} e^{-jk_1 r_i} \left[ -\frac{jk_1^2}{r_i} - \frac{k_1}{r_i^2} + \frac{j}{r_i^3} - \left( \frac{z+d}{r_i} \right)^2 \left( -\frac{jk_1^2}{r_i} - \frac{3k_1}{r_i^2} + \frac{3j}{r_i^3} \right) \right] \\
E_z^{sc} &= -Idl \frac{\omega \mu_o k_1^2}{2\pi k_2} e^{-jk_z r_i} \left( \frac{\pi}{k_1 r_i} \right)^{1/2} \left( \frac{\rho}{r_i} \right) e^{-P_2} F(P_2)
\end{aligned}$$

and

$$\begin{aligned}
P_2 &= \frac{k_1^3 r_i}{2k_2^2} \left( \frac{k_1 r_i + k_2 (z+d)}{k_1 \rho} \right) \\
F(\varsigma) &= \int_{\varsigma}^{\infty} \frac{e^{jt}}{(2\pi)^{0.5}} dt = \frac{1}{2}(1+j) - [C_2(\varsigma) + jS_2(\varsigma)]
\end{aligned}$$

In order to compute the alternative form of the Fresnel integral shown above, we first use the following relationships to the standard Fresnel integral:

$$C_2(z) = C\left(\sqrt{\frac{2z}{\pi}}\right) \quad S_2(z) = S\left(\sqrt{\frac{2z}{\pi}}\right).$$

The Fresnel integral can then be related to the error function by

$$C(\varsigma) + jS(\varsigma) = \frac{1+j}{2} \operatorname{erf}\left(\frac{\sqrt{\pi}}{2}(1-j)\varsigma\right).$$

There are several series representations that can be used to compute the error function in the above expression. We chose the implementation of Zhang and Jin which relies on Abramowitz and Stegun [13] equation (7.1.5) for  $|\zeta| < 5.8$  and the asymptotic series of (7.1.23) for  $|\zeta| > 5.8$  [16]. It is worth noting that although the cutoff values in Zhang and Jin's algorithm appear somewhat arbitrary, modifying these limits resulted in a divergent series or operator overflow. Equation (7.1.29) can also be used, however, this expression relies on hyperbolic functions and so care must also be taken to avoid arithmetic overflow when computing these functions.

By coding the above expressions, it is possible to observe the behavior of the E-field on the surface, as shown in Figure 3. Depending on the distance away from the antenna, the field strength exhibits a fast-decaying  $1/r^3$  near-field dependence, followed by a slower decaying  $1/r$  far-field dependence, and finally at sufficient distances, the well known  $1/r^2$  dependence associated with the Norton surface wave. The dotted line represents the well-known Norton surface wave alone. (A small glitch in the King expression plot appears around  $10^6$  m on the plot, due to a convergence issue in the

asymptotic series of the error function. This issue is purely numerical, and only occurs after the wave is easily identified as a Norton surface wave.)

Figure 4 demonstrates the E-field on a sea surface for various frequencies. Below 10 MHz, one must be very far away for the Norton surface wave to appear. As the frequency increases, the Norton surface wave appears closer to the antenna; however, the amplitude of the surface wave is much lower. The reason that the Norton wave appears closer to the antenna at higher frequencies is due in part to the fact that the distance appears much larger for the smaller wavelength. On the other hand, the reason that the amplitude of the Norton wave is smaller at higher frequencies is due to the smaller wave number of the ground, relative to the air. For example, at 10 MHz over a sea,  $k_{\text{sea}}/k_{\text{air}} \sim 60 - j60$ . However, at 1 GHz, this ratio drops to  $\sim 10 - j4$ . So as the frequency increases, not only does the relative wave number drop, but the imaginary component decreases faster than the real component with increased frequency.

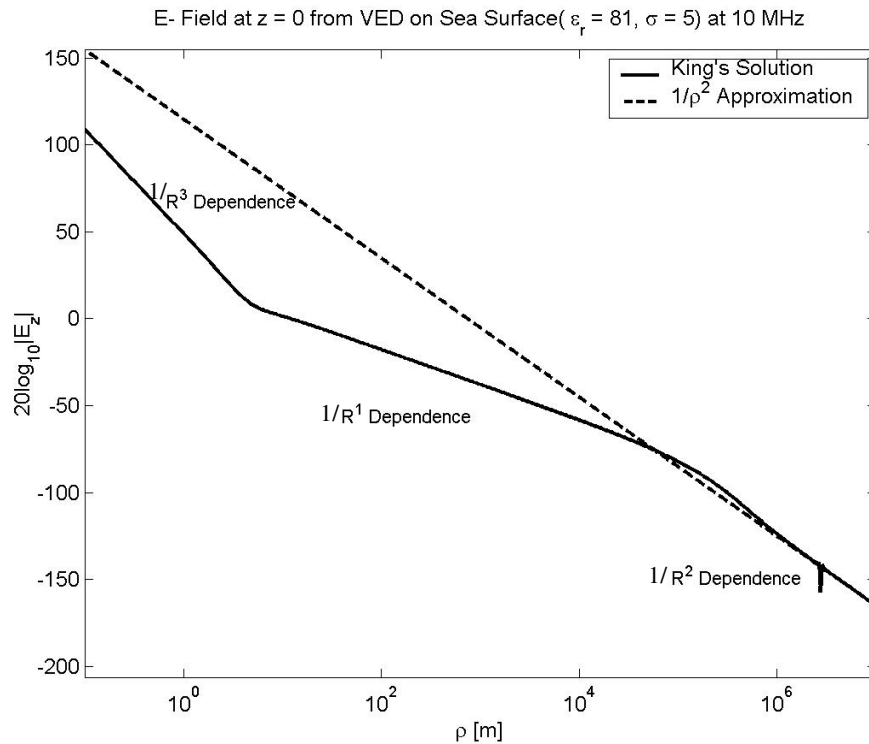


**Figure 3. Example of E-field from vertical electric dipole demonstrating various degrees of field propagation.**

Finally, we consider the definition of “far-field”. In antenna theory, the far-field region is generally thought of as the region away from the antenna in which the angular field distribution is independent of distance. For example, the well known “cosine-squared” pattern of a unit dipole in free space is the same at any two radial distances; assuming the distances are much larger than a wavelength and the largest dimension of the antenna. However, for dipole systems close to a real ground, the ground is essentially

part of the antenna, and a conventional far field has little meaning. This is illustrated in Figure 5 which shows the far-field patterns of a vertical electric dipole on a sea surface at 2.2 MHz for various radial distances. While all radial distances were chosen to be much larger than a free space wavelength, there are drastic variations in the pattern near the ground due to the surface wave component. We found that above 1 GHz the pattern to be independent of distance.

Although we compare field strengths in our antenna design in Section 3 only at  $z = 0$ , for the MF frequency, we see little vertical variation of the field within the practical height limits of ships. The height variation is observed in Figure 6 for frequencies 2.2 MHz, 10 MHz, and 100 MHz.

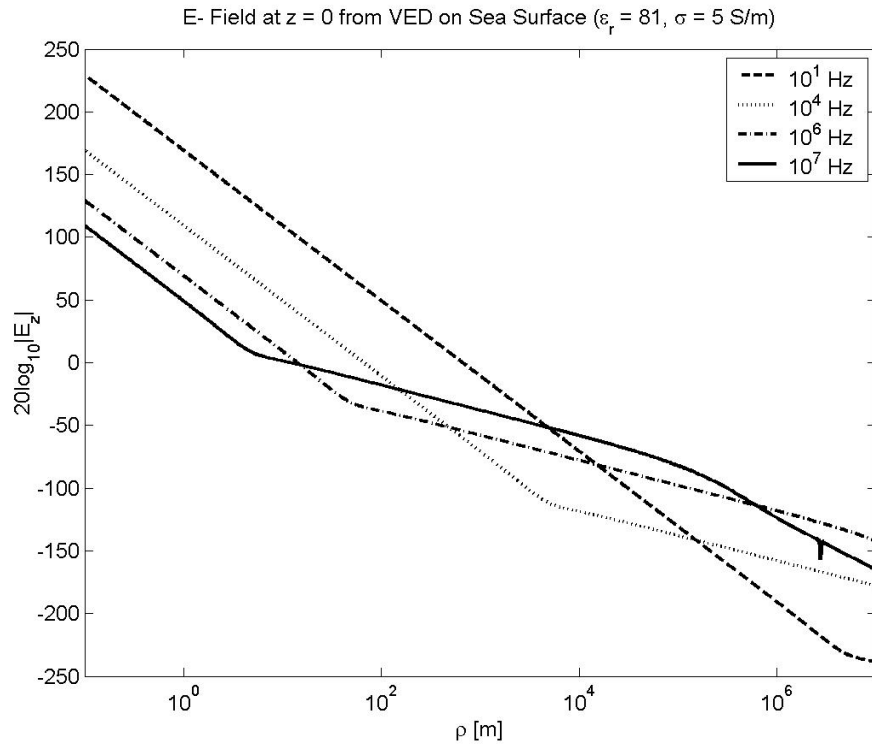


**Figure 4. Electric field on sea surface from a vertical electric dipole.**

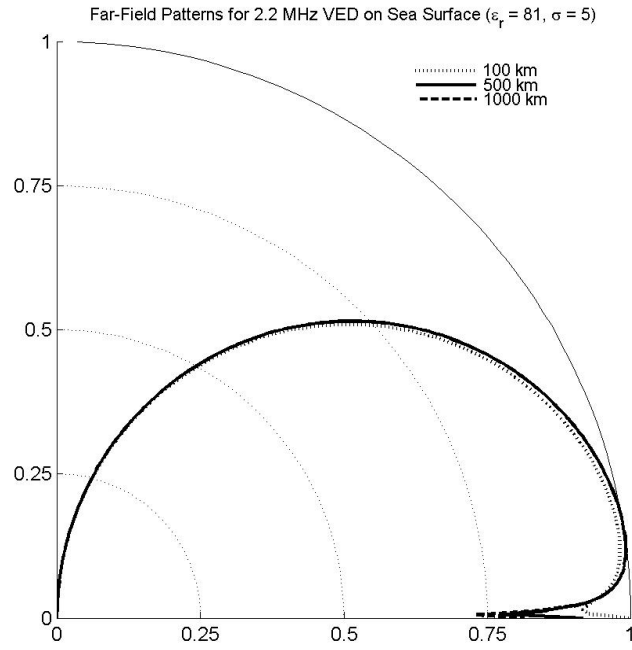


**Figure 5. Normalized vertical electric dipole far-field patterns on sea surface for various radial distances at 100 MHz.**

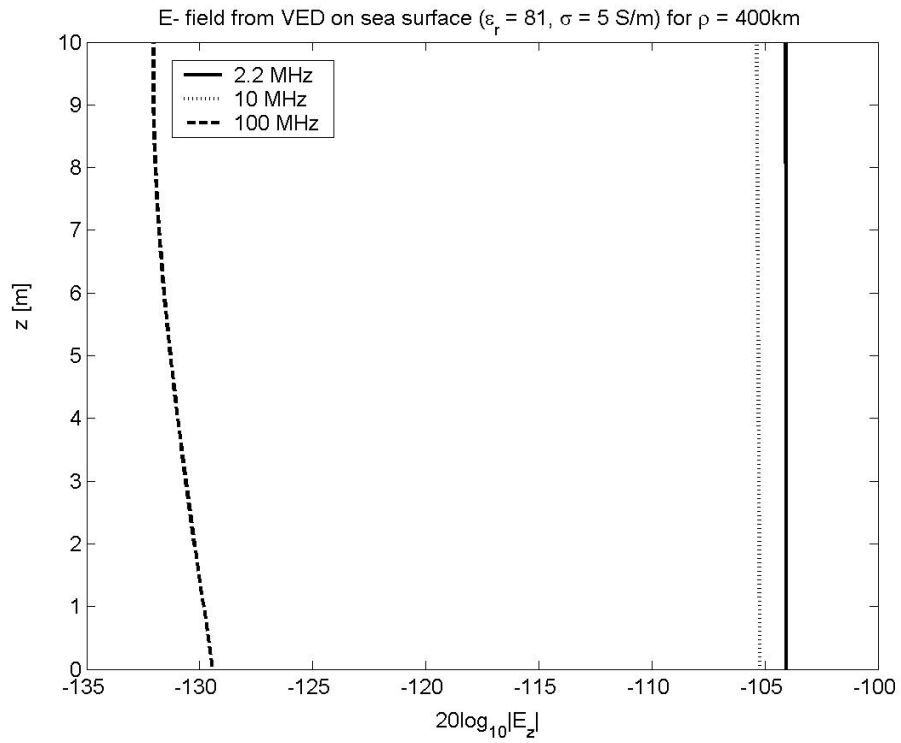


**Figure 6. Field strength as a function of height for vertical electric dipole on sea surface for three frequencies.**

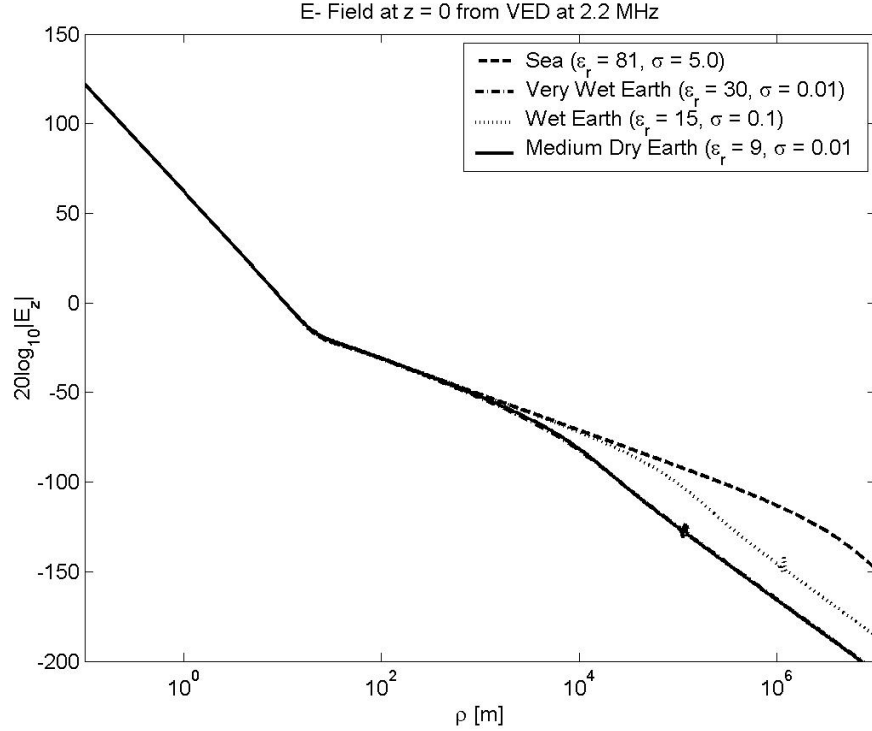


**Figure 7. Electric field of a vertical electric dipole on various ground types at 2.2 MHz (Medium Dry Earth line and Very Wet Earth line overlap).**

The effects of conductivity should be taken into account when predicting ground wave propagation. Figure 7 demonstrates the effects of ground type on the overall propagation at the surface. For MF frequencies, we see that conductivity plays a large role in maintaining the strength of the surface wave. Within the  $\lambda/2$  distance of 68 m, and may be extended out to 500 m, only a 0.2 dB divergence was found between the wet earth and seawater. This is a tenant assumption made in Section 3. At frequencies in the GHz range, the real component of the dielectric constant determines the behavior of the surface wave. This is related to the scaling of the imaginary component of the wave number mentioned earlier.

### 2.3 Comments on GRWAVE

Since the ITU recommended program GRWAVE is openly available and considered the de facto standard for ground wave propagation predictions, we should discuss the methodology GRWAVE uses to compute the propagation loss. Unfortunately, the underlying algorithms in the GRWAVE code are undocumented. To the best of our knowledge, the current version of GRWAVE is still based on of a paper by S. Rotheram [17]. Based on Rotheram's paper, GRWAVE accounts for all components of the ground wave, plus an additional term representing the ionospheric propagation path (i.e. sky wave), all over a spherical earth<sup>3</sup>. To do so, three general methods are used based on the

<sup>3</sup> In other words, GRWAVE does not compute the ground wave propagation factor as defined by IEEE standards referenced earlier, but rather a ground wave plus an ionosphere wave.

system parameters such as antenna height, observation height, and distance from the dipole.

For long distances, generally over the horizon of a spherical earth, a residue series summation is used for a dipole over a lossy earth. Above the dipole is an exponentially varying atmosphere. Most of the expressions are based on several of J.R. Wait's papers, which are summarized in [8]. While most of Wait's work focuses on a linearly varying atmosphere, Rotheram expanded upon it to account for a more realistic exponential atmosphere. However, the added accuracy is somewhat unnecessary, as Rotheram concedes in his paper that above 1 MHz, the exponential atmosphere provides no additional accuracy over the linear atmosphere. Furthermore, if a linear atmosphere can be assumed, the "4/3 equivalent radius" approximation can be used with negligible loss of accuracy. The equivalent radius approximation assumes that the effects of the linear atmosphere can be accounted for by using a homogeneous atmosphere above an earth with a radius 4/3 larger than the original earth.

For short distances, the "extended Sommerfeld" solution of Wait is used. In this case, "extended" refers to the fact that the effect of the earth's curvature is accounted for unlike in Sommerfeld's original problem. At short distances, ionospheric propagation should have little to no effect, and it appears that Rotheram does not include it at these short distances. For intermediate distances where the antenna and receiver (observation point) are located at distances above the ground, geometrical optics is used. At this time, we are not concerned with this situation as it does not lend itself to surface waves.

Despite the lack of documentation for GRWAVE, it appears that for many applications, it offers a suitable alternative to new code development. We find the main shortcoming of GRWAVE to be the lack of control it provides to the engineer to consider alternative antenna designs to the short ideal monopole and to account for antenna losses into the earth.

### **3 Ground Wave Antenna Development**

In Section 2 we presented the propagation mechanisms for ground wave communications and developed our approach for calculating the fields at and above the surface of a real earth. Now, we turn our attention to the development the antenna for the MF GMDSS system. The field results presented in this Section are the combination of finding the antenna currents as installed on a real earth and then computing the ground wave fields using the equations from Section 3. Again, this assumes that the antenna is installed near the coastline and that there are no significant propagation losses between the antenna and the seawater. This 2-part approach to the antenna design meets a practical need to compare various ground wave antenna installation designs that are possible in a moderately sized geographic area. As an example, we needed a method to compare a pier installation to an over-land installation, where both sets of fields propagate over seawater. In both FEKO<sup>®</sup>[4] and NEC4d[2], the real ground cannot transition, and comparing the ground wave fields from one antenna installed and radiating over a dry earth and from another designed and radiating over seawater is meaningless.

This study does not incorporate, currently, the earth's curvature, refractive atmosphere, or the rough surface scattering from the sea. We evaluate all fields up to the ITU-specified 1 km distance, but with these relatively minor additions, a full-featured



tool could be developed to determine the range for the minimum field strength for each antenna design.

The antenna designs considered in this study began with a 54-ft (16.46 m) freestanding monopole, but at the end we consider a 54-ft dipole as well. The monopole is typically installed on at 1.5 m high concrete pillar and attached to a ground radial network of 60 60-foot long radials that are buried slightly below grade. The US Coast Guard selected this antenna in part because of the reduced material costs and much lower installation costs than taller freestanding or guyed towers. This monopole is slightly less than  $\lambda/8$  in length, and we know that its current distribution as a thin-wire short antenna will be nearly triangular. Typical installations use an L-network with series and shunt inductors to achieve a narrowband conjugate match, which is tuned on site.

In beginning our designs we chose to ignore the mismatch and in simulation have 1 kW power delivered to the antenna. Part of this assumption was that the realized efficiencies from most possible antennas, including matching, would be around 60% +/- 10% and not a driving factor. This assumption may not in the end hold true.

These simulations were completed using the MoM engine and planar Green's functions within FEKO<sup>®</sup> with a voltage source. All simulations were completed at 2194 kHz, a test frequency that was made available for this project since some related work compared predictions to measured data. The effects of surrounding structures were not considered.

### **3.1 Baseline Antenna Design**

We defined the 54-ft freestanding monopole installed on at 1.5-m high concrete pillar and attached to a ground radial network of 60 60-foot long radials as our baseline design. This antenna does a sufficient job in ensuring a large current magnitude at the antenna feed; however, it requires a substantial amount of land space for most Coast Guard locations or the costs of leasing coastal land. Thus, one motivation in this work was to reduce the area needed for the ground radial network while achieving the same coverage performance.

The first investigation of the baseline antenna is to modify the height of the base on which it is mounted. The 1.5-m base is convenient in reality because it allows for the mounting of the L-network on its side and provides some protection against flooding. A typical installation photo is shown in Figure 8. The simulation model is shown in Figure 9 (real ground is not shown). The base is accounted for by moving the feed location to above the ground and shifting the antenna upward.

Three base heights were simulated and compared: 0, 1.5 m, and 2.44 m (8 ft). We limited our base to 8 ft because it is only incrementally more difficult than creating a 1.5 m pillar. While it is clearly understood that the ground radials perform the function of creating a counterpoise to the monopole, the presence of the real ground is certainly observable. For all investigations, four grounds were considered as shown in Table 1. The last is hypothetical since a seawater installation of ground radials is not realizable.



**Figure 8. Typical baseline installation**

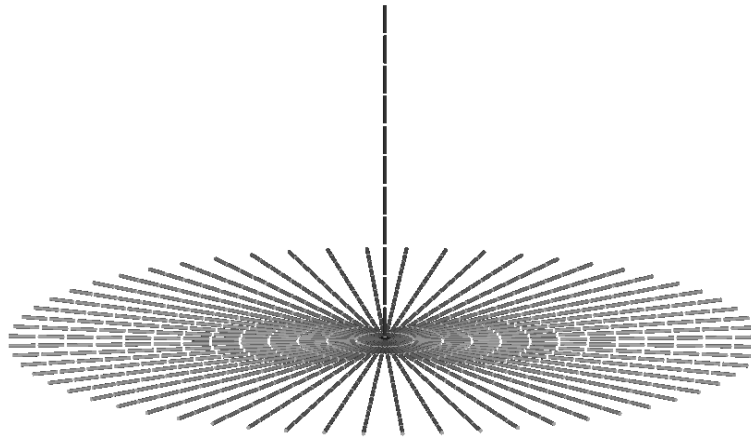


**Figure 9. Model of baseline simulation**

**Table 1 – Real Ground Parameters Considered**

Soil Label	Description	$\epsilon_r$	$\sigma$
S1	Medium Dry Earth	9	0.01
S2	Wet Earth	15	0.1
S3	Very Wet Earth	30	0.01
S4	Seawater	81	5

The first observation from the currents shown in Figure 10 for 2.194 MHz is that the conductivity is the driving factor in the development of the currents on the antenna. This matches the observations put forth in Section 2.2. We received similar current results and thus field results from antenna on soils S2 and S4 because both are considered good conductors by  $(\sigma/\omega\epsilon)^2 \gg 1$ . We chose in some figures only to show results for soils S1 and S4 because they represent the two extremes. Still, the currents between the four soil types under the baseline antenna are not greatly different. The presence of the large ground radial system in the baseline design is sufficient to mitigate most lossy effects of the real ground.

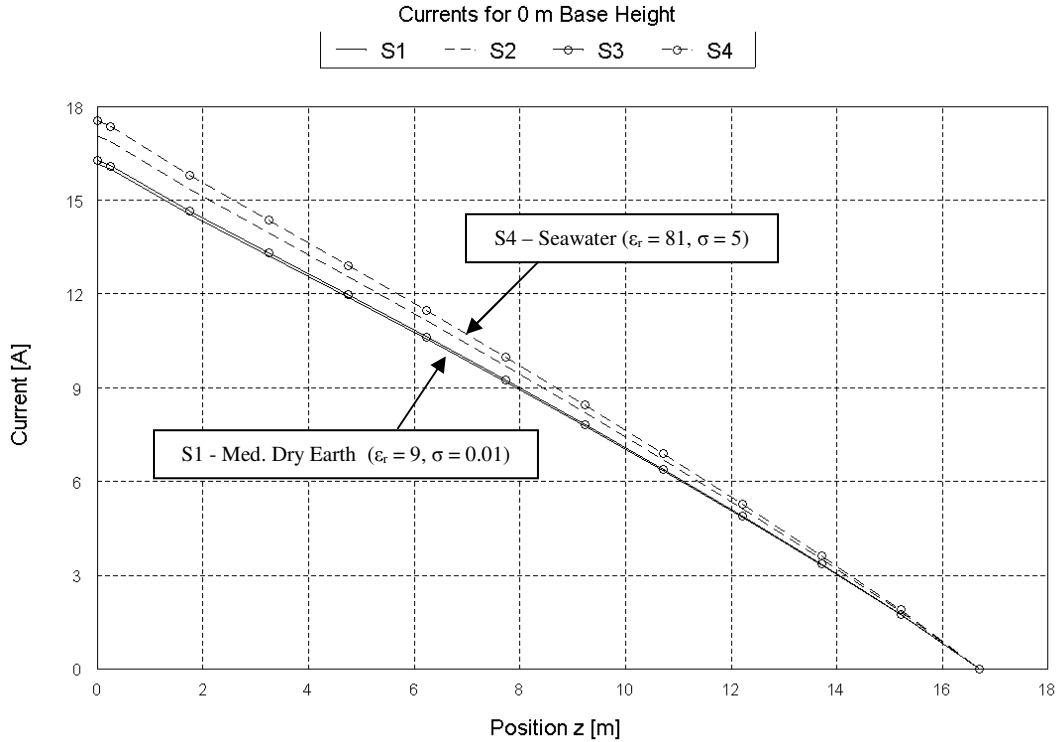


**Figure 10. Currents for baseline antenna with base height = 0 on different real grounds**

With this basic understanding of the difference in the currents for different soils, the currents over soil S2 are observed for different base heights in Figure 11. The changes in the pillar height show an effective lengthening of the antenna (its  $J_z$  components) and offsetting of the feed from the center of a theoretical monopole and PEC image. Raising the antenna on a base serves to make the lower half appear as an inverted top-hat and the current distribution takes on a uniform shape. While the peak current is reduced, there is an improvement in the average current, and as shown in Figure 12, a slight improvement in the fields. This lengthening is evident by observing the input impedance on the antenna shown in Table 2. Improved resistance and a smaller negative reactance are observed with increased length.

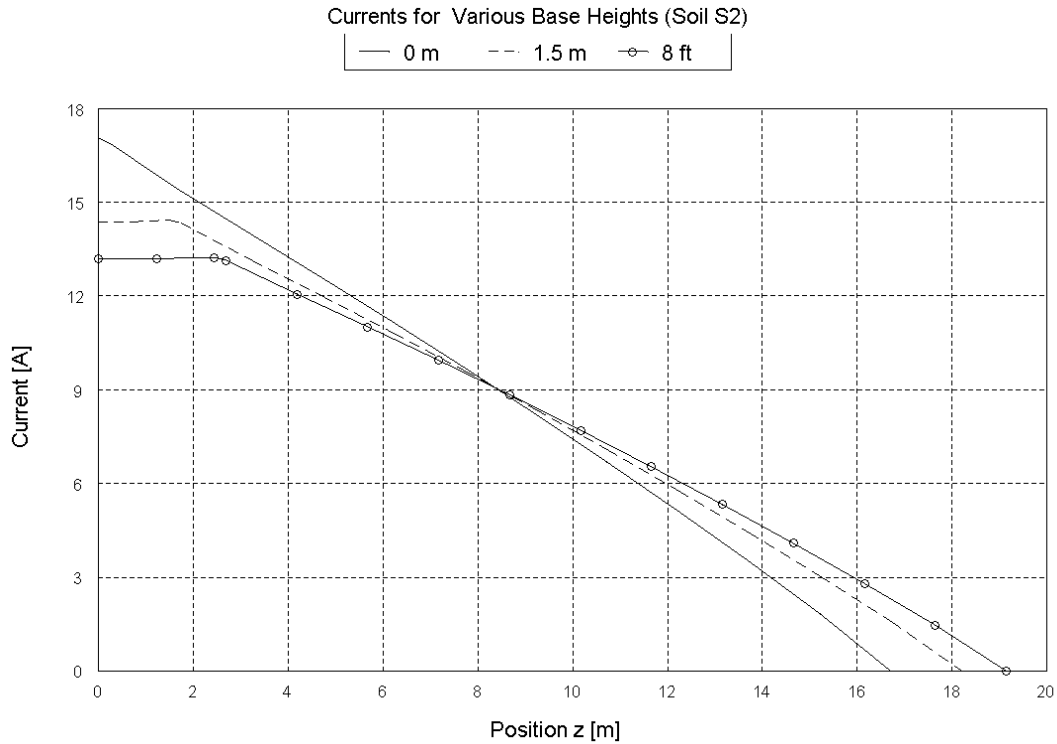


**Figure 11. Currents for different base heights on Soil S2**

**Table 2 – Impedances for Baseline Designs**

	S1	S2	S3	S4
<b>0 m</b>	7.7 - j 441.6	6.9 - j 441.4	7.6 - j 441.7	6.6 - j 441.8
<b>1.5 m</b>	10.7 - j 419.4	9.7 - j 419.1	10.6 - j 419.6	9.1 - j 419.6
<b>8 ft</b>	12.7 - j 401.8	11.5 - j 401.4	12.5 - j 402.0	10.9 - j 401.9

Applying the formulas from Section 2, we predict the field strength at a height  $z = 0$  for distances up to 1 km as propagating over seawater ( $\epsilon_r = 81$ ,  $\sigma = 5$ ) using the ground wave solution presented in Section 2.2. These results are shown in Figure 12 for the four soil types and 0 and 8-ft base heights (to illustrate a range) where the antenna would be installed. The first observation is that the different base heights have a minor role in improving the ground wave field strength; differences in field strength are less than 0.1 dB. The most dominating factor remains the conductivity of the real ground over which the baseline antenna is installed. Note how the fields from antennas on soils S1 and S3 are nearly identical. At 1 km, the overall field strength differs a maximum of 0.77 dB.

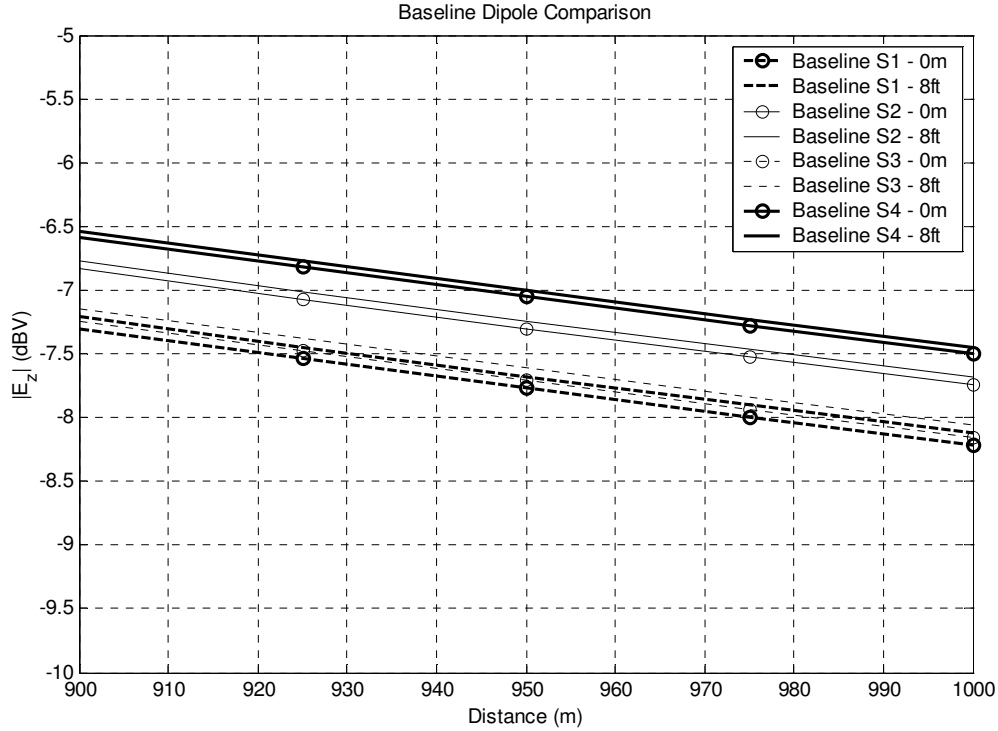


Figure 12.  $|E_z|$  at  $z = 0$  over seawater for baseline antennas installed on various real grounds

### 3.2 Buried Dipole

In this section, we investigate the burial of a single vertical ground rod in lieu of a ground radial network. This design can be considered the limit of reducing the ground radial network and is in concept tempting, but its value here is in inferring the effects of the real ground on the antenna currents. In these results, the ground rod was sunk an impractical 54 ft vertically into the ground.

One early observation was an issue with convergence of the solution. Due to the increased dielectric constants of real ground, higher segmentation requirements should be needed. Results for soils 1 and 4, which have the largest differences in both permittivity and conductivity, are compared in Figure 13 and Figure 14 with increasing segmentation. Soil S1 converges within a  $\lambda_0/100$  segmentation, although probably much sooner, but soil S4 requires at least a  $\lambda_0/500$  segmentation. As a general rule, segmentation of  $\lambda_0/10$  is appropriate for the air dielectric. We observe here that the sampling should occur at least at a rate of 1 per skin depth and possibly higher, where the skin depths of these two soils are 3.585 m and 0.152 m, respectively. Normalizing the skin depth to the wavelength yields segmentations of  $\delta/\lambda_0 = 38$  for Soil S1 and  $\delta/\lambda_0 = 900$  for soil S4.

We originally hypothesized that the establishments of large currents within the ground portion of the antenna would lead to the best ground wave field strength. This remains a true statement, but the losses to the antenna currents from the real ground reduce the above-ground currents significantly. This understanding points to the need to insulate the buried section of the antenna from the real ground. Analytical solutions for buried antennas were presented by Wait [18]. We have not fully analyzed these designs

and compared them to others presented herein. Numerical solutions would not be easily achieved. Such an investigation requires significant computing resources since we will need to represent the ground as a large dielectric volume and do several studies to ensure the convergence of the solutions.

The current magnitudes of each installation are also very telling of the ground loss mechanisms. Not only does seawater (Soil S4) show significantly higher currents than for medium dry earth (Soil S1), but the losses within the soil are quickly evident. The current distribution is significantly reduced for a Soil-S1 antenna and slightly reduced for a Soil-S4 antenna from their respective baseline antenna currents. While the seawater behaves like a good ground at 2.2 MHz, these results argue for designs that electrically remove the antenna from the lossy ground as much as possible.

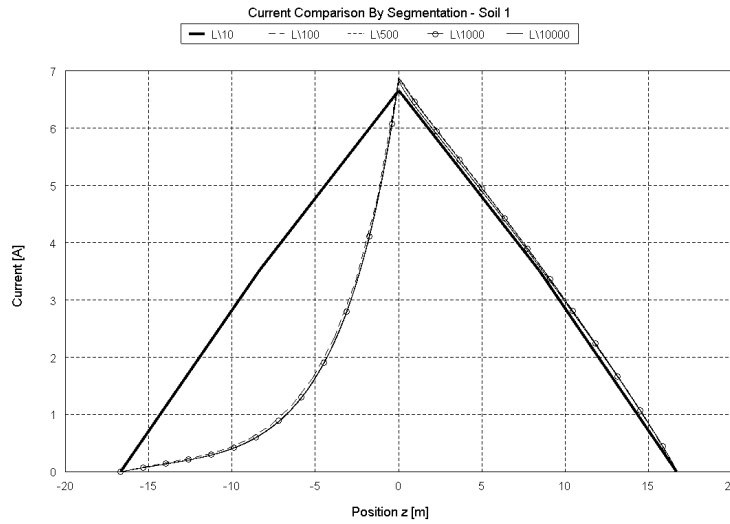


**Figure 13. Currents for buried dipole in medium dry earth (Soil S1) for increasing  $\lambda_0$  segmentation**

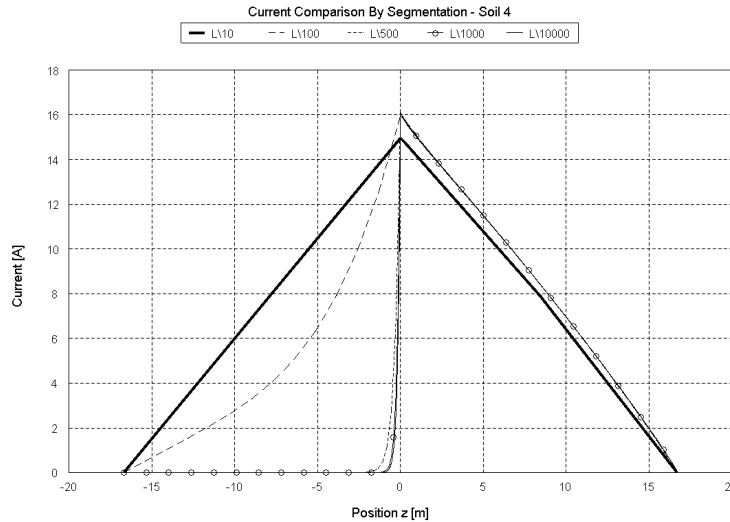


**Figure 14. Currents for buried dipole in seawater (Soil S4) for increasing  $\lambda_0$  segmentation**

### 3.3 Elevated Radials

Christman put forth in several papers the idea of elevated radials [19]. We adopt his design here as an attractive solution with a much smaller ground radial system. When considering such an installation, we limited the base height to 8 ft and to horizontal ground radials, whatever their count and length, to a height of 8 ft as well. We envision such a design for both its ease in installation (ground radials tensioned to insulated mounting poles) and maintenance issues, such as grass mowing under the radials. Our comparisons are made to the 1.5-m baseline height because of its current standard use.

There are many options possible with this mounting, but a definite reduction in the number and length of ground radials is needed to make it more appealing than a baseline installation. For the four soil types, improved field strengths are achieved with 4 60-foot elevated radials. These results are in line with those presented by Christman [19]. We believe this is an attractive design for the Coast Guard, and thus we present several options over each soil type in Figures 15-18.

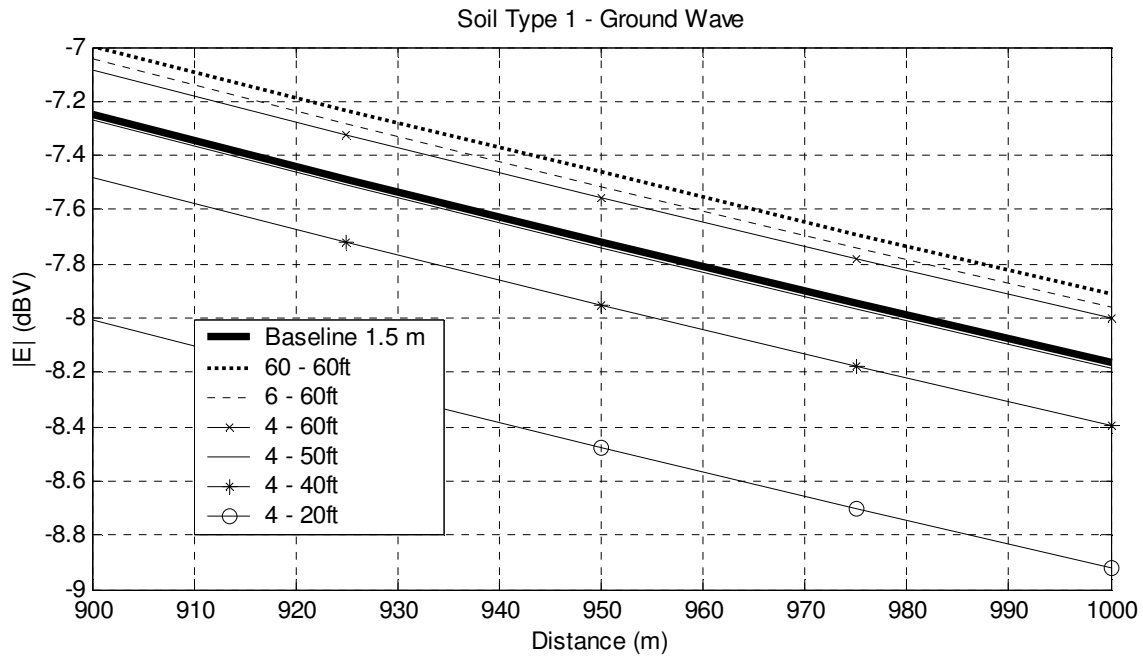


Figure 15.  $|E_z|$  at  $z = 0$  over seawater for various elevated radial designs installed on Soil 1

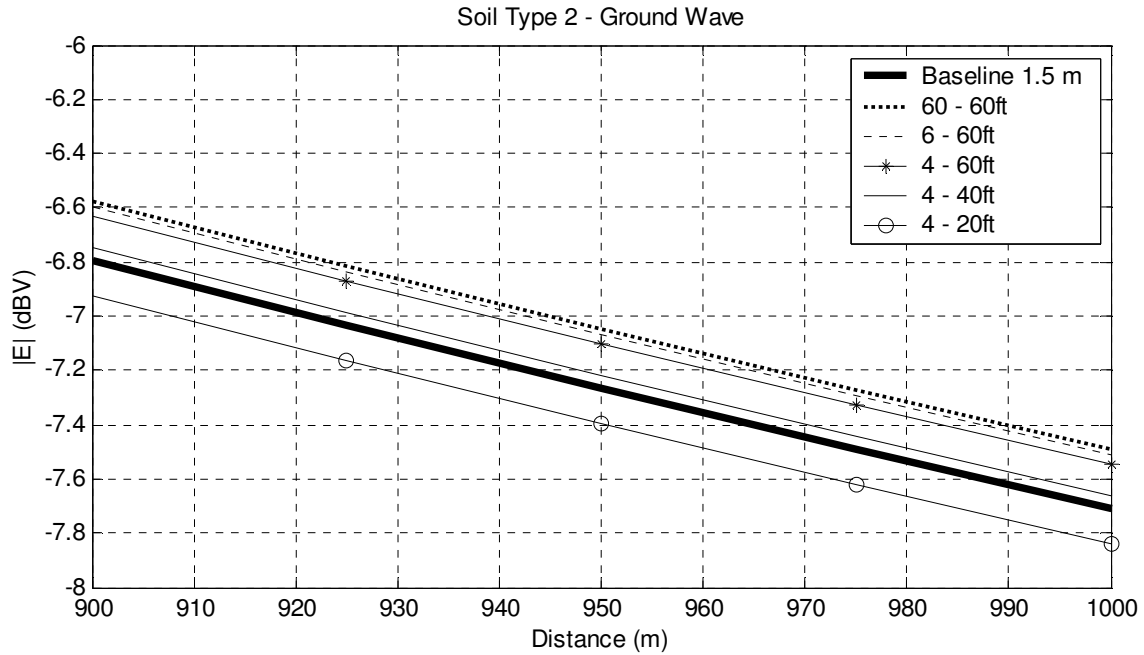


Figure 16.  $|E_z|$  at  $z = 0$  over seawater for various elevated radial designs installed on Soil 2

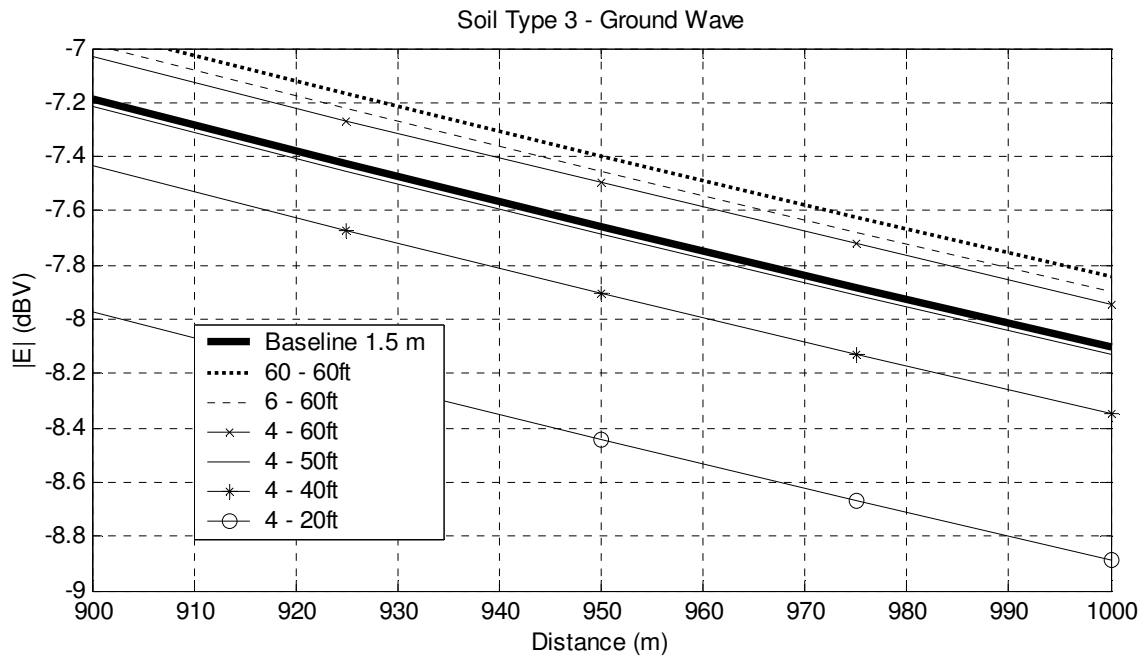


Figure 17.  $|E_z|$  at  $z = 0$  over seawater for various elevated radial designs installed on Soil 3



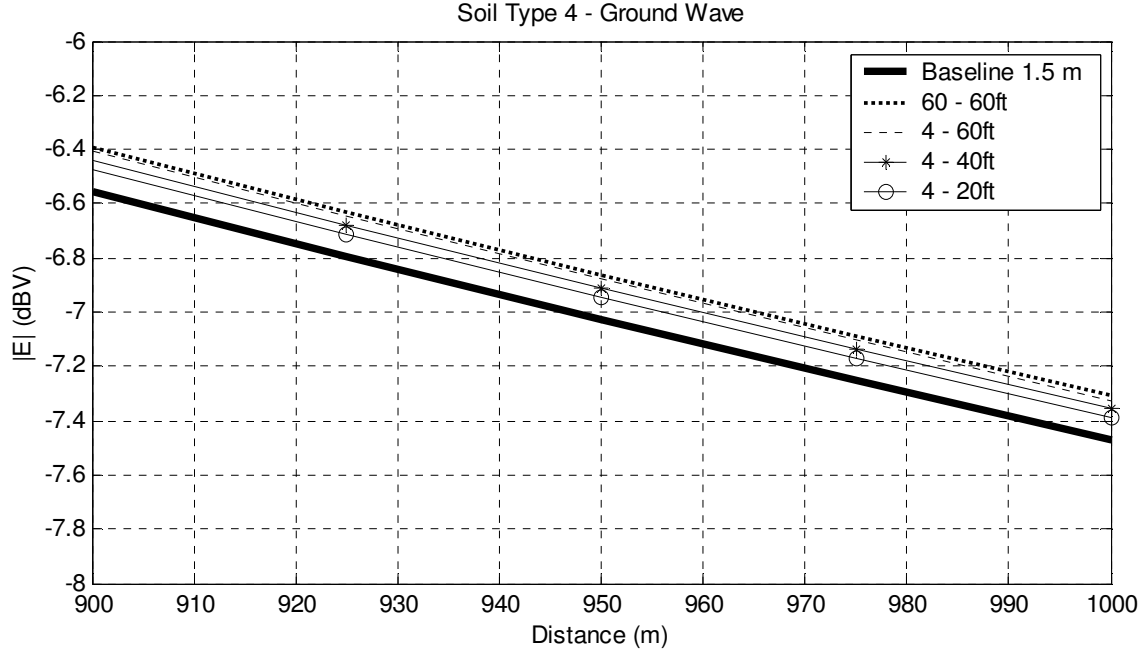


Figure 18.  $|E_z|$  at  $z = 0$  over seawater for various elevated radial designs installed on Soil 4

### 3.4 Vertical Dipole over Ground

We next investigate the idea of raising the feed point within the 54-foot monopole. This design, like the buried dipole, eliminates the large ground radial system entirely. This departs somewhat from the Coast Guard's approach and would require a different antenna to be manufactured. However, we believe that this antenna could be satisfactory made to be structurally freestanding and include a matching network at the feed. We look at both a grounded antenna and an ungrounded antenna. The ungrounded antenna is effectively a dipole, and we observe impedance changes in line with a shorter antenna.

There are a number of variations possible, but we limit the presentation of our results to an antenna mounted on a 1.5-m base with a center feed. The current distributions in Figure 19 show the triangular distribution expected from short dipoles installed over soils S1 and S4. The variation between the different ground types is minimal, indicating that improvements from a *disconnected* ground radial system will offer minimal improvement, which we observed.

The fields produced by these designs are compared in Figure 20 to the fields from the Baseline designs on 1.5-m bases. It is clear that the connected dipole antenna suffers more loss, and when the conductivity of the soil is low, the losses increase. The dipole is not as good a design on Soil 1, where the baseline design remains dominant. The drawback of the short dipole design is first and foremost the input impedance. The input impedances for all six antennas are shown in Table 3. Although better field strength can be achieved using the dipole design when there is 1 kW of delivered power, the increased negative reactance is substantial enough that losses in the L-network will likely eliminate these benefits.

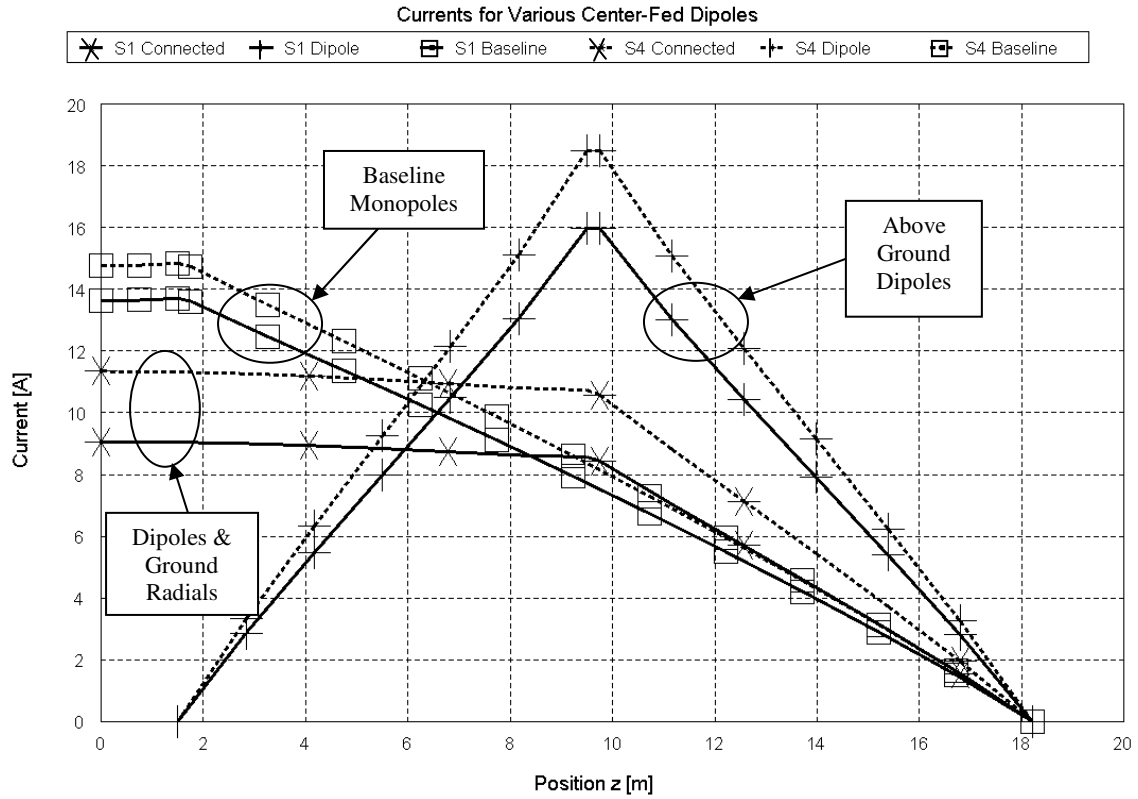


**Figure 19. Current distributions for various dipoles and baseline antennas on soils S1 and S4**

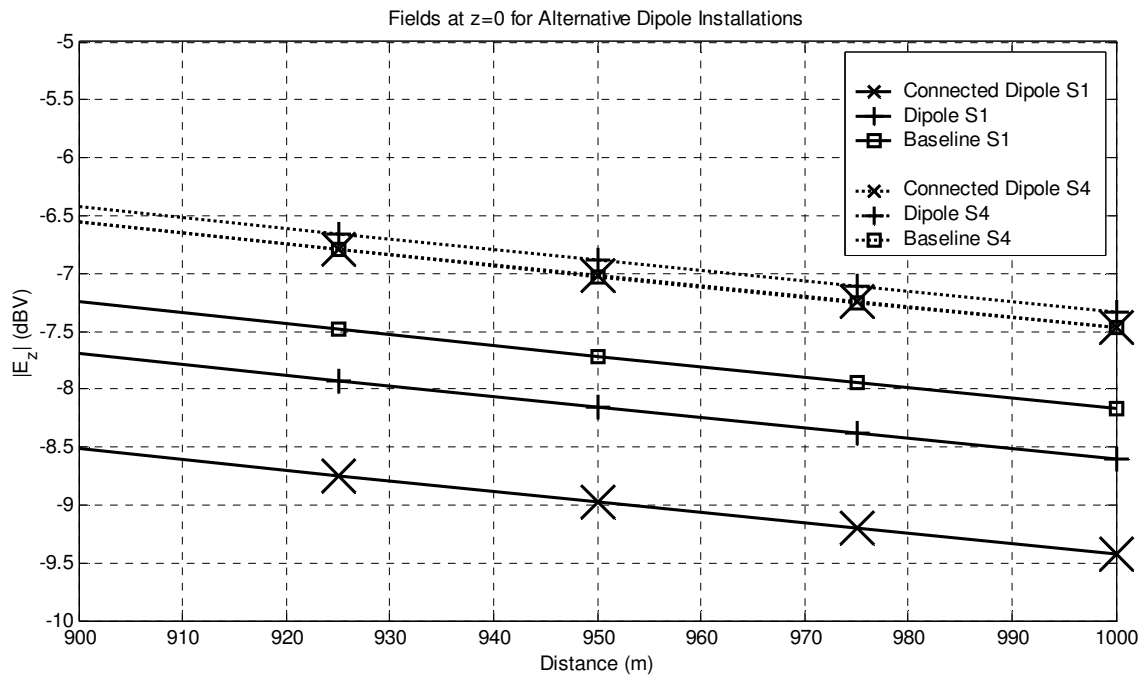


**Figure 20.  $|E_z|$  at  $z = 0$  over seawater for dipole and baseline designs over medium dry earth (Soil S1) and seawater (Soil S4)**

**Table 3 – Impedances for dipole and baseline designs**

	<b>S1</b>	<b>S4</b>
<b>Connected Dipole</b>	27.7 – j 794.2	17.6 – j 796.6
<b>Dipole</b>	7.8 – j 1929.1	5.8 – j 1929.3
<b>Baseline 1.5m</b>	10.7 – j 419.4	9.1 – j 419.6

### **3.5 Pier Installation**

Our last design concept arrives from a very common installation option seen with this project. The installation of the antenna on a pier eliminates the need for a large land area, reduces the possibility of near-field structures, and capitalizes on the good conductivity of seawater. Typically, the design of these installations is to mount the antenna on a 1.5-m base and run a ground rod down about 10 ft into the water. Such an installation is shown in Figure 21.

With the pier installation, based on the presented work, we ask whether the grounding of the feed into the water is beneficial. We also consider the height of the antenna above the water since this changes with tides and between different piers. Two sea levels were approximated from Figure 21: 8 feet and 16 feet below the base. In the monopole pier installations, a ground rod is typically extended down to the water and about 10 ft below. This is an effective lengthening of the antenna until the water is reached, where it acts like a resistive load. In the 2-radial designs, ground radials are extended 30 ft along the pier, which are within the physical limits of a typical pier. However, if a wider or longer pier were available, the inclusion of more ground radials would improve the reactance. We also consider the performance of the dipoles presented in Section 3.4. The currents for these designs are presented in Figure 22.



**Figure 21. Typical pier installation**

Avoiding a ground results in a 0.4 dB improvement in the field strength at 1 km, as shown in Figure 23. While not a large improvement, the argument to avoid sinking a ground rod into the sea is made; and the higher that the antenna can be installed over the water, the better the performance will be. The 2-radial design may also benefit from reduced maintenance cost since there are no elements directly contacting the corrosive seawater. The major detriment of this 2-radial design is the rise in the reactance, which may result in more losses in a matching network. The reactances are not as negative as with the dipole designs.

**Table 4 – Impedances for Pier and Baseline Designs**

	Low Water	High Water
<b>Grounded</b>	21.3 – j 310.3	15.3 – j364.1
<b>2-Radial</b>	8.1 – j 821.8	8.4 – j 804.2
<b>Dipole</b>	5.5 – j 1947.9	5.7 – j 1943.0

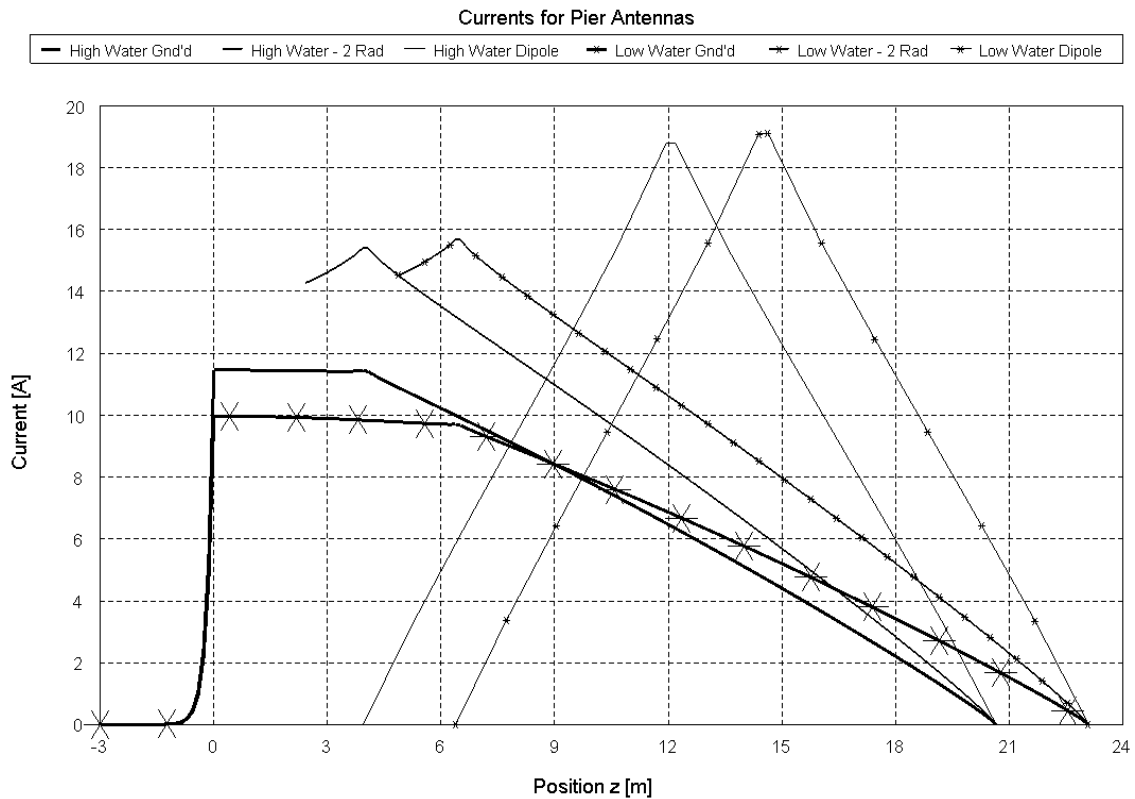


**Figure 22. Current distributions for pier installations**

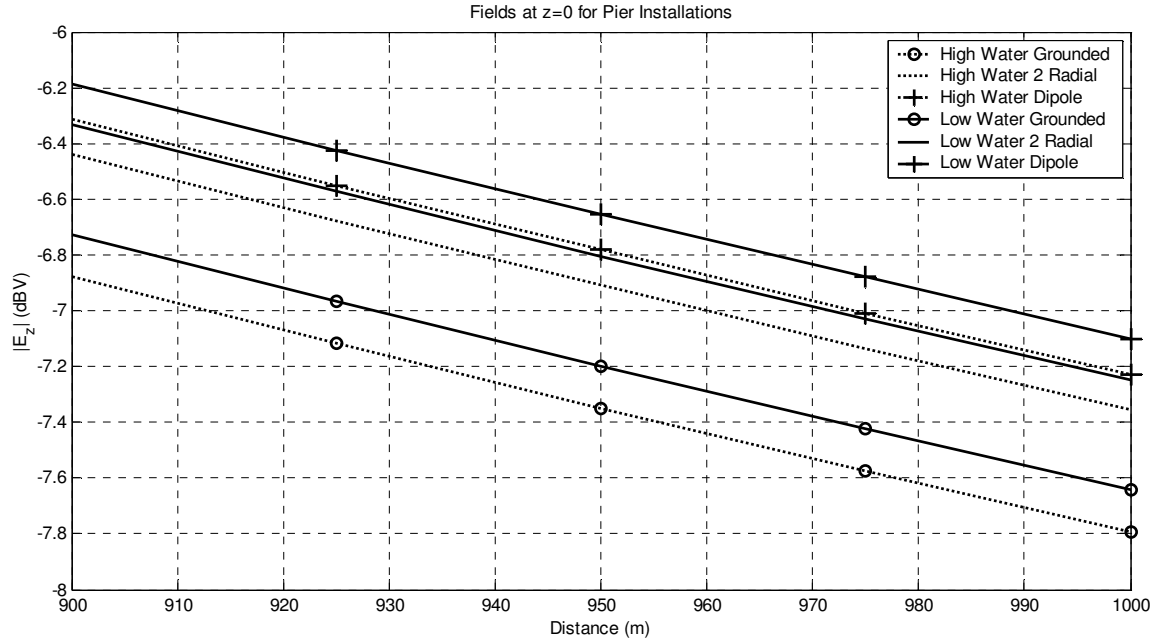


Figure 23.  $|E_z|$  at  $z = 0$  over seawater for various pier designs

## 4 Recommendations and Future Work

### 4.1 Ground Wave Propagation

We intend to adapt our ground wave propagation solution for a spherical earth using the methodology of Wait, if possible. Wait's solution for propagation over a large earth has the added advantage in that it consists of a Sommerfeld flat earth term, plus several "correction factors" for a spherical earth [8]. Next, numerical integration schemes should be investigated. While Sommerfeld's integral will inherently be burdensome to compute numerically due to the oscillations of the Bessel function, it may be necessary to perform a numerical computation in order to determine the range of validity of the asymptotic solutions presented above. Due to the slow convergence of the Sommerfeld integral, this may not be feasible for all ground types. Alternatively, the analytic solutions could be compared to recent parabolic wave equation techniques. Finally, the effects of surface roughness on surface wave propagation should be investigated. A recent paper by Ishimaru explores the effects of random surface height on the Sommerfeld problem. It is recommended that this paper be studied and its methods implemented and compared to the flat-surface model of King and others [20]. As the surface roughness increases, the attenuation of the surface wave will inevitably increase, making roughness an important factor in coverage availability and verification testing.

### 4.2 Antenna Designs

Due to the physical limitations of GMDSS installations and the cost and logistics requirement for self-supporting antennas, there are limited additional variations to these

designs. Three main installation details remain: baluns, matching networks (and their losses), and detailed site analysis. Baluns are a critical piece of the installation, and they are not clearly addressed in current installations. For pier installations, where the cable is not buried in a lossy medium, baluns are especially needed. Matching network designs, mainly for the dipole design, and the incorporation of their losses into a design model are critical to the full analysis and comparison of competing designs. This task is not especially difficult but it is required in order to make informed design selections. Lastly, an analysis and optimization of standard site details should be completed. In this, the location and effect of the near-field environment can be clearly captured. These would include details such as: wooden fences surrounding the antenna, piers optimized for GMDSS installations and that avoid negative conducting objects, such as metal railings, and lastly, details of the feed region.

## 5 Conclusions

We have presented a 2-part method to design and compare MF antenna installations designs for the Global Maritime Distress and Safety System (GMDSS). The first step is to determine the current distribution of the antenna for a given real ground; the second step is to propagate this current distribution over a homogenous seawater boundary layer. Considerations have included the loss and impedance effects on the antenna from different real grounds/seawater and the physical placement of the antenna over ground.

Our research into the rich history of ground wave propagation has yielded an efficient prediction code that allows this comparison at close distances and provides substantial insight into the ground wave radiation mechanisms. We also investigated and found several design improvements to standard installations. Using the ground wave propagation code, we compare the fields from different antennas after propagating 1 km over seawater. We evaluated improvements provided by raised radials and optional designs for pier installations that reduce the size ground radial system and associated loss.

## 6 References

- [1] ITU-R M.1467, "Prediction of A2 and NAVTEX Ranges and Protection of A2 Global Maritime Distress and Safety System Distress Watch Channel", International Telecommunication Union, Geneva, Switzerland, 2000.
- [2] *Numerical Electromagnetic Code - NEC-4, Method of Moments, Part I: User's Manual (NEC-4.1)*, Lawrence Livermore Laboratory, 1992.
- [3] *Numerical Electromagnetic Code (NEC-2) Part I: NEC Program Description – Theory*, Lawrence Livermore Laboratory, 1981.
- [4] *FEKO User's Manual, Suite 5.2*: EM Software & Systems Inc., August 2006.
- [5] Wait, J.R.; "Ancient and Modern History of EM Ground-Wave Propagation," *IEEE Antennas and Propagation Magazine*, vol. 40, no. 5, 7-24, 1998.
- [6] Collin, R.E., "Hertzian dipole radiating over a lossy earth or sea: some early and late 20th-century controversies," *IEEE Antennas and Propagation Magazine*, vol. 46, no. 2, pp. 64-79, April 2004

- [7] *IEEE Standard Definitions of Terms for Radio Wave Propagation*, IEEE Std 21-1997.
- [8] Wait, J.R. (1996). Electromagnetic Waves in Stratified Media. New York, IEEE Press (originally published in 1962).
- [9] Ishimaru, A., Electromagnetic Wave Propagation, Radiation and Scattering, New Jersey, Prentice Hall, 1991.
- [10] Banos, A., Dipole Radiation in the Presence of a Conducting Half-Space, New York, Pergamon Press, 1966.
- [11] King, R.W.P., M. Owens, and T.T. Wu, Lateral Electromagnetic Waves: Theory and Applications to Communications, Geophysical Exploration, and Remote Sensing. New York, Springer, 1992.
- [12] Chew, W.C., Waves and Fields in Inhomogeneous Media. New York, IEEE Press, 1995.
- [13] Abramowitz, M.; Stegun, I. E., Eds.; *Handbook of Mathematical Functions with Formulas, Graphs, and Mathematical Tables*, 10th printing, U.S. Department of Commerce, National Bureau of Standards, Washington, DC, 1972.
- [14] Norton, K.A. (1936 & 1937), "The Propagation of radio waves over the surface of the earth: Parts I & II," *Proceedings of the IRE*, (24 & 25): 1367-1387, 1203-1236.
- [15] Collin, R.E., "Some observations about the near zone electric field of a Hertzian dipole above a lossy earth," *IEEE Trans. Antennas and Propagation*, vol. 52, no. 11, 3133-3137, 2004.
- [16] Zhang, S. and J. Jin, Computation of Special Functions. New York, Wiley-Interscience, 1996.
- [17] Rotheram, S., "Ground-wave propagation Parts I & II: Theory for short distances & Theory for medium and long distances and reference propagation curves," *IEE Proceedings Part F*, vol. 128, no. 5, 275-295, 1981.
- [18] Wait, J.; Fuller, J.; "On Radio Propagation Through Earth," *IEEE Trans. Antennas and Propagation*, 19(6), Nov 1971, 796- 798.
- [19] Christman, A., Radcliff, R.; "Elevated vertical monopole antennas: effects of changes in radiator height and radial length," *IEEE Trans. Broadcasting*, 36(4), Dec 1990: 262-269.
- [20] Ishimaru, A.; "Sommerfeld and Zenneck Wave Propagation for a Finitely Conducting One-Dimensional Rough Surface," *IEEE Trans. Antennas and Propagation*, vol. 48, no. 9, 1475-1484, 2000.

# **A Compact, Wide Bandwidth UHF / L-band Communications System Antenna for Ground-Based Applications**

Thomas Goodwin  
Tyco Electronics M/A-COM  
1011 Pawtucket Boulevard  
Lowell, MA 01853

**This paper describes the design and development of a dual-band communications antenna incorporating several unique features. The antenna operates over UHF and L Bands, providing ground-based transmit/receive capability for next generation radios. Filters are integrated into the antenna to provide the required channel isolation. The antenna is compact – less than 12” in height, and includes a spring mechanism to enable it to survive accidental mechanical impacts. It also incorporates a quick-disconnect feature using blind-mate RF connectors, allowing the antenna to be removed from its mount base for ease of transportation. It can be disconnected and re-installed without tools in under 1 minute. The paper describes the electrical and mechanical development of this new communications antenna. Test results, including effects of the proposed installation, are also described.**

## **1. Introduction**

A requirement for a unique ground-based Communications Antenna (CA) to support next-generation dual-channel radios operating in the UHF and L bands has been identified. While the electrical requirements for this antenna are fairly standard (albeit demanding), the mechanical and installation provisions present a significant challenge. This paper describes the antenna design developed by M/A-COM to address these challenges.

The specific application the CA is designed for consists of a ground-fixed, transportable platform. The CA provides the radiating interface for simultaneous transmit/receive capability at both UHF and L-bands for the platform’s radio. The location on the platform was specified to be at the edge of the top surface (ref. Figure 1) which influences the pattern coverage, as well as the impedance match, particularly for the UHF frequencies. Since the application is designed to be transportable by ground vehicle and rotary wing aircraft, the antenna is required to be removable without any tools. Additionally, it is anticipated that the platform may be moved with the antenna in place on the top surface; therefore, a requirement to be able to survive an impact with, for example, a tree branch, was also specified. The real estate available to install the antenna on the platform was also restricted to an approximately three inch diameter circle.



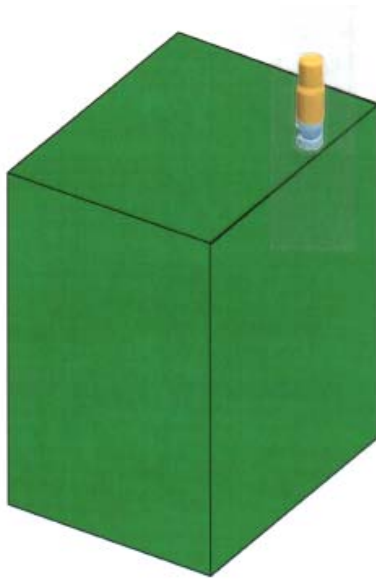


**Figure 1** CA Platform (approximately to scale)

M/A-COM's antenna designed for this application is shown in Figure 2. The CA consists of an Antenna assembly and a separate Mount assembly. The Mount assembly is permanently installed on the top of the platform. It should be noted that while the CA is designed for a specific platform, it is easily adaptable and well-suited for use on practically any ground-fixed or ground mobile application requiring simultaneous UHF and L band communications capability.

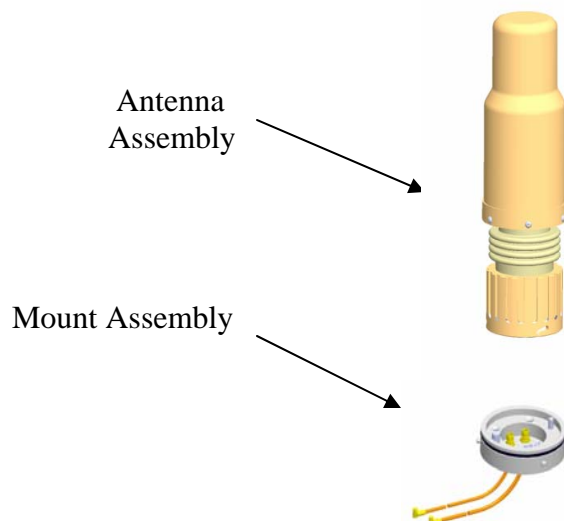


**Figure 2** Communications Antenna Assembly

Before describing the antenna development in detail, presented here are the key performance goals driving the design. Table I defines the key electrical performance parameters, and Table II defines the key mechanical characteristics.

**Table I. Key Electrical Characteristics**

<b>Parameter</b>	<b>Performance Goal</b>
Frequency Range	UHF and L-band, 100 MHz bandwidth both bands
VSWR	3.0:1 max UHF / 2.0:1 max L-band
Isolation	45 dB min between Operating Bands
Pattern Coverage	Omnidirectional in azimuth; horizon to +45° in Elevation
Power Handling	50W CW Both Bands

**Table II. Key Mechanical Characteristics**

<b>Parameter</b>	<b>Performance Goal</b>
Installation	Base Permanently Mounted / Antenna Detachable/Replaceable Without Tools
Size	Base 3.0” max Diameter x 1.0” max Height / Antenna 3.55” max Diameter x 14” max Height
Weight	Base 0.55 lb max / Antenna 3.28 lb max
Flexure	Antenna Capable of Flexing 90° when Installed on Base
Mechanical Impact	Antenna Capable of Withstanding Multiple 15 mph Impacts when Installed on Base

In addition to the performance goals defined in the Tables above, the CA must also withstand typical environmental conditions of exposure to temperature extremes, thermal cycling, vibration, humidity, salt fog, rain, blowing snow, etc. The development of M/A-COM’s Communication Antenna designed to meet these demanding requirements is detailed in the next sections.

## 2. Antenna Development

At the initial stages of the development, the real estate available for antenna installation was loosely defined as an approximately 8" x 4" footprint with no initial height restriction. Since M/A-COM already produces a family of broadband blade antennas for airborne applications, this seemed like a logical solution. A straightforward development path was identified to modify an existing blade design which provided UHF and L-band coverage, albeit at slightly different frequency ranges. There was no requirement for isolation (initially planned to provide external filtering), quick-disconnect capability, nor a requirement for flexure or mechanical impact. However, shortly into the development cycle, these new requirements were imposed, as well as the dimensional restrictions listed in Table II. This necessitated starting over with an entirely new antenna design incorporating these new features. In order to meet the mechanical impact requirement, the antenna assembly must incorporate some type of spring mechanism. Integrated filtering/diplexing was also required.

The first stage in development was to select an appropriate radiating element, or elements. The first tradeoff was between a single, broadband element or a dual radiating element configuration. A broadband element such as a blade or a bicone could be adequate to cover the required frequency range. This would allow running a single RF cable up through the spring mechanism. However, this would also allow less freedom in optimizing performance, especially pattern coverage, at the two distinct operating frequency ranges. Also, the size restrictions – diameter and height – would make the design of a single broadband element more challenging. Dual elements, on the other hand, would allow more freedom in selecting element types for each frequency band, providing more opportunity for optimizing performance at each band. Additionally, this approach would allow the use of individual filter assemblies rather than a more complex diplexer arrangement. The only disadvantage to the dual element approach seemed to be the requirement to run two separate cables through the spring arrangement, or to provide a splitter at the top of the spring assembly. The advantages of the dual element approach clearly outweighed this minor disadvantage, and this approach was selected for further development.

In order to establish the baseline antenna design, M/A-COM used Ansoft's HFSS to evaluate a number of different combinations of antenna elements. Several of these combinations are shown in Figures 3A through 3D. Elements evaluated included thick monopoles, bicones, helixes, blades, and slots. The main driver in selecting antenna elements was achieving the required bandwidth within the size constraints – approximately 25% at UHF. Achievable pattern coverage was also a primary consideration – only elements providing omnidirectional coverage could be considered. At this time, antennas were evaluated while positioned at the center of a symmetric ground plane; the effects of the actual installation would be evaluated later. A brief description of the antenna candidates that were studied in some detail follows.

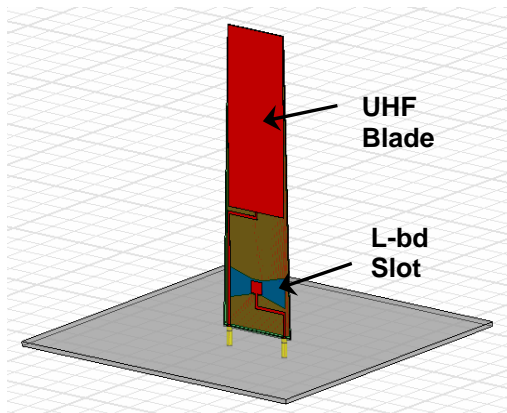


**Fig. 3A Blade / Slot**

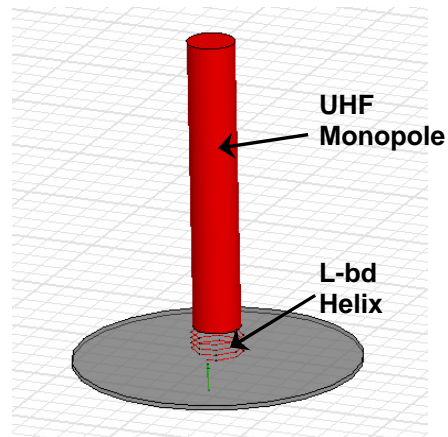


**Fig. 3B Monopole / Helix**

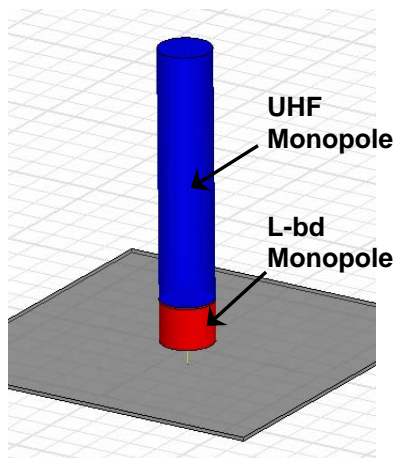


**Fig. 3C Monopole / Monopole**

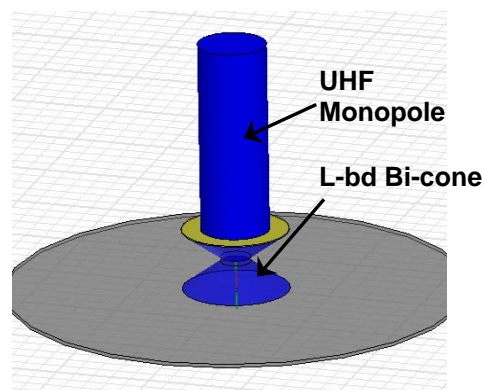


**Fig. 3D Monopole / Bicone**

The antenna shown in Figure 3A – a blade element over a slot – is based on an existing M/A-COM design. The UHF blade element had to be made considerably smaller than the existing design in order to fit within the size constraints, and this significantly reduced the achievable bandwidth. In addition, due to the asymmetric shape of the antenna (i.e. rectangular versus circular profile), it was determined that meeting the mechanical requirements would be very difficult. Fabricating and testing a physical prototype validated these concerns, and this approach was abandoned.

Another configuration studied was a monopole stacked over a normal mode helix as shown in Figure 3B. This configuration has a favorable form factor for the specified mechanical requirements. However, the normal mode helix, sized to fit within the specified constraints, exhibited narrow bandwidth. This approach was not pursued further, and no physical prototypes were fabricated.

A third configuration was the stacked monopole configuration shown in Figure 3C. This approach appeared to have several advantages. It would be the simplest to fabricate and it has a favorable form factor for the specified mechanical requirements. However, the presence of the UHF monopole stacked over the L-band monopole significantly (and adversely) affected the L-band performance. After an extensive modeling effort, several configurations of physical prototypes were fabricated and tested. The prototype testing confirmed the L-band sensitivity issue. While it appeared that this approach may ultimately prove feasible, it was abandoned in favor of the selected monopole / bicone design.

The antenna design downselected at the conclusion of the modeling / prototyping effort is shown in Figure 3D. This configuration is a thick UHF monopole stacked over an L-band bicone. Modeling demonstrated that bandwidth and pattern coverage were achievable, and that there was more independence between the individual element performance than in the stacked monopole case. In addition, the form factor is favorable, and it allows for simple fabrication. Several physical prototypes were fabricated and tested to verify performance. One of these is shown in Figure 4; measured patterns are shown in Figures 5A and 5B. Based on modeling results as well as prototype measurements, this approach clearly was the most likely to achieve the electrical as well as mechanical specifications.



**Figure 4 Stacked Monopole / Bicone Prototype on Spring Simulator**

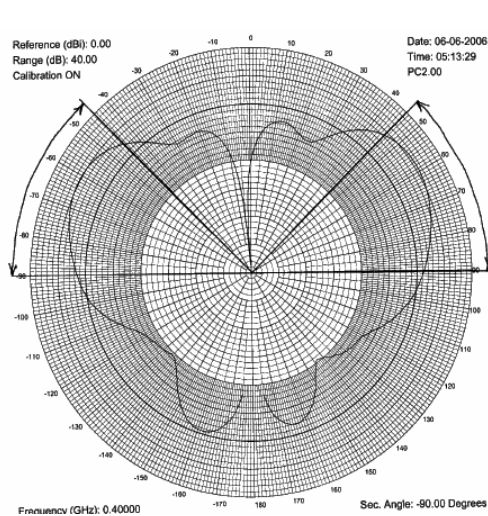


**Fig. 5A UHF Pattern**

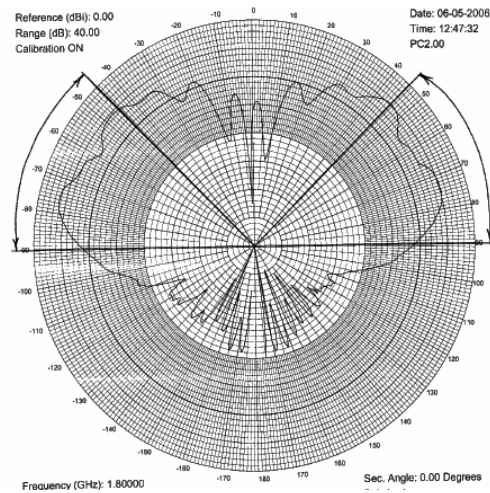


**Fig. 5B L-band Pattern**

Once the basic antenna element configuration was defined, the next step in development was to integrate the required spring mechanism, quick-disconnect features and isolation filters, and optimize performance in the actual installation.

The design of the isolation filters was straightforward; however, in order to meet the height requirement, it was desired to keep the volume required for the filters as small as possible. As the antenna is a dual element design with individual feed lines for each element, two discrete filters could be implemented rather than a diplexer. With the wide frequency separation between operating bands, a high-pass / low-pass filter combination works well for this application. M/A-COM used Ansoft's ADS to perform the filter design. Discrete filter elements were used to minimize the size of the filters. The overall size of each filter board is approximately 1" x 1.3"; they are enclosed in a housing which also serves as the base of the antenna (see Figure 6). The filters achieve approximately 40 dB (UHF low-pass) and 50 dB (L-band high-pass) rejection respectively; this, along with the inherent antenna element isolation, enables meeting the overall isolation requirement.

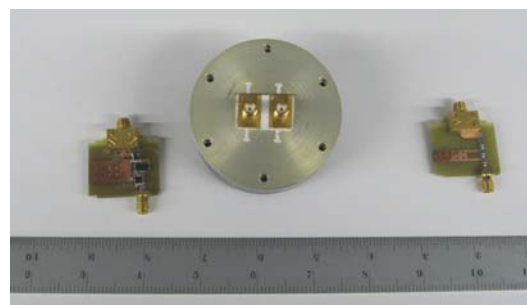


**Figure 6 Isolation Filters and Housing**

A mechanical design effort was undertaken concurrently with the electrical design effort. Once the flexure / mechanical impact requirement was included in the specification, the need for some type of spring mechanism was identified. Initially, M/A-COM contacted several commercial spring vendors, but we were unable to identify a suitable off-the-shelf device. M/A-COM had previously produced a GRC-206 antenna that incorporated a spring mechanism; however, this mechanism did not allow for passing RF cables through it. Therefore, we implemented a custom spring design adapted to the CA.

The constraints on the spring mechanism were that it must allow full 90° flexure, and that it must return the antenna to vertical after repeated 15 mph impacts. In addition, it must keep the antenna in a vertical (within  $\pm 10^\circ$ ) position under conditions of up to 55 mph vehicle speed combined with wind speeds up to 40 mph. The spring must be as compact as possible to enable the overall assembly to meet the 14" max height requirement. It must also be flexible enough so that the 15 mph impacts do not cause permanent damage to the antenna itself. Finding a balance between these somewhat contradictory requirements was a major challenge. Obtaining accurate results from a structural analysis of a spring mechanism proved difficult due to approximations necessary to create a useable model. Therefore, M/A-COM embarked on a structured testing program to downselect a suitable spring mechanism. More than a dozen spring types were evaluated for flexure, stiffness, and retention (memory) characteristics before the working version was chosen. The selected spring mechanism is on the order of 3" long by 1.625" diameter. M/A-COM also developed a customized means of securing the top and bottom of the spring while allowing RF cabling to pass through the center.

The other unique mechanical feature on the CA is the provision for quick disconnect / re-assembly without the use of tools. The quick-disconnect mechanism must provide sufficient structural integrity to withstand the 15 mph impact shock as well as other vibration and shock loads, and it also must provide for a seamless RF connection between the antenna and the mount base. BMA type blind-mate connectors were identified as the optimum RF interconnect for this application. The BMA connectors allow for axial misalignment while still providing good RF performance. The alignment between the antenna and mount is established by two dowel pins; the dowel pins engage before the BMA connectors, providing a measure of protection and ensuring that the connectors are properly aligned prior to contact. The pins are also two different sizes to prevent any potential mis-mating.

Several means were considered to provide a tool-free mating. A threaded coupling was examined. However, in order to protect the antenna assembly from environmental conditions of rain, snow, etc., the spring must be enclosed within a sealed rubber boot. This arrangement does not allow the coupling mechanism to rotate more than about  $\pm 30^\circ$ , so that any kind of threaded mechanism was ruled out. Instead, a "bayonet locking ring" was implemented. This arrangement is loosely based on a BNC connector locking mechanism. A customized coupling ring, with a ridged exterior to allow for easy gripping, was designed to provide a lockable mating with only an approximately  $\pm 15^\circ$

turn. A wave spring provides the retention force to keep the locking ring in place during mechanical impact and other vibration and shock events. A cutaway 3D model of the final antenna is shown in Figure 7; this view shows the antenna attached to the mount assembly.

This completed the basic design of the Communication System Antenna. The remaining design tasks were to optimize the RF performance, in particular the pattern coverage in conjunction with the intended installation, and to ensure that the antenna had sufficient mechanical robustness to withstand its intended environment, particularly the 15 mph mechanical impact.

The size of the filter housing, the minimum spring length required, and the quick-disconnect features dictate the height of the radiating elements above the surface of the platform the antenna is mounted on. Additionally, as noted above, the location of the antenna on its platform is less than ideal. Specifically, the antenna is located on the edge of the top of the platform, and at approximately 2/3 of the platform width rather than centered (reference Fig. 1). This location has the effect of skewing the radiation patterns due to the presence of a ground plane on only one side of the antenna. M/A-COM performed measurements with antenna prototypes installed at the center of a symmetric round ground plane, as well as with the antenna installed in its actual location on a platform mockup, to evaluate this pattern skewing and to investigate any potential mitigation.

The UHF element is a monopole; it was not feasible to introduce an asymmetry into the antenna to modify its radiation pattern characteristics to mitigate the effects of the installation. The monopole element is fed directly by a coaxial line. The impedance match at the element is optimized by adjusting the capacitance at the input through varying the height of the monopole element above the bicone element, as well as the use of a metal disk at the coaxial input.

The L-band radiating element is a bicone. A bicone in free space has a symmetric radiation pattern. In the CA, the bicone pattern is affected both by the asymmetry of the installation as well as the height of the bicone in relation to the ground plane (i.e. the top surface of the platform). The height of the element is fixed by the required size of the required antenna mechanical features. Through a combination of electromagnetic modeling and physical prototyping, M/A-COM devised a means to partially mitigate the pattern asymmetry introduced by the installation. Instead of running the UHF feed line through the center of the bicone, the feed line is located at a distance from the centerline. This has the effect of introducing an asymmetry to the radiation pattern. By judiciously orienting the location of the feed cable with respect to the edge of the platform, the two asymmetries can be made to oppose each other and partially mitigate the effect of the installation.



In order to provide structural integrity, the antenna has a protective radome over the radiating elements. The radome is fabricated from a high-strength resin. The area under the radome not occupied by the antenna elements is filled with a low-density structural foam. Mated parts in the antenna assembly are connected with both mechanical fasteners and an adhesive bond wherever feasible. The entire assembly is sealed watertight. The final antenna assembly is shown in Figure 7.

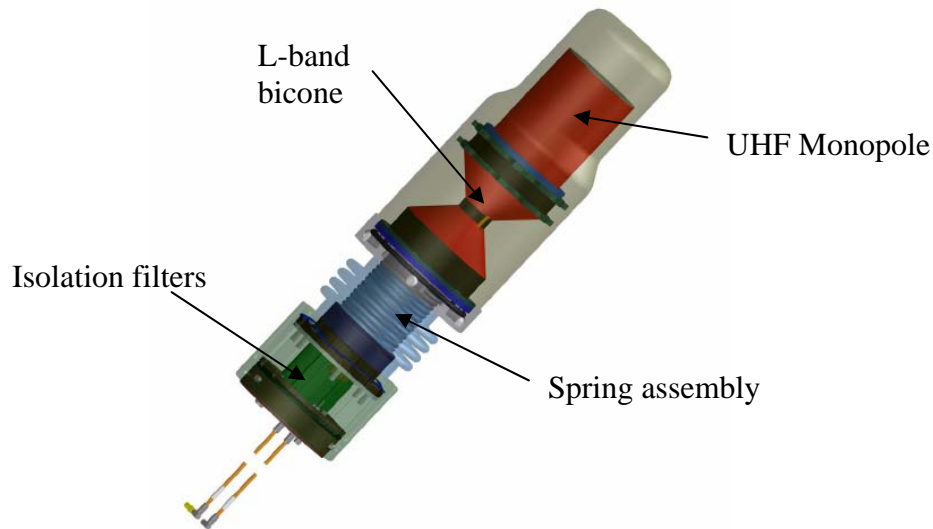


**Figure 7      Antenna Assembly 3D Model**

### **3.      Antenna Performance**

A number of prototype / engineering development units have been fabricated to date. This section summarizes the performance achieved by the development model antennas, and provides a comparison to the desired performance goals.

The antenna's VSWR performance at UHF and L-bands is shown in Figures 8A and 8B respectively. Isolation, both UHF-to-L-band and L-band-to-UHF, is shown in Figures 9A and 9B. Typical pattern performance is shown in Figures 10 and 11; shown here are principal plane cuts (10A and 11A) and conic cuts (10B and 11B) for both UHF and L-bands. In addition, the calculated percent coverage is shown in Figures 12A and 12B for UHF and L-bands respectively. In addition to the RF performance measurements, mechanical inspections and tests were performed. In particular, units were subjected to multiple (total 25) simulated 15 mph impacts with a wooden beam and survivability was demonstrated. Tables III and IV summarize actual performance versus design goals for the key electrical and mechanical parameters.

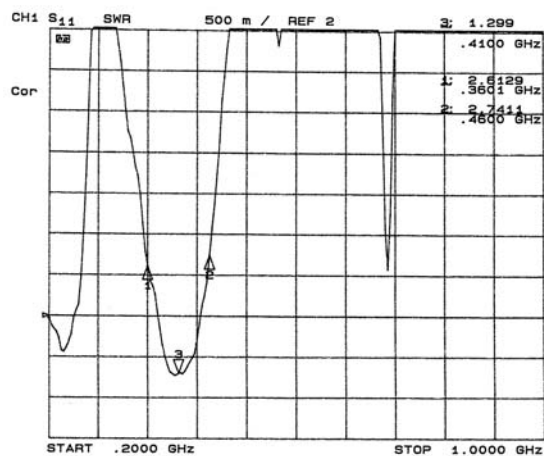


Fig. 8A UHF VSWR

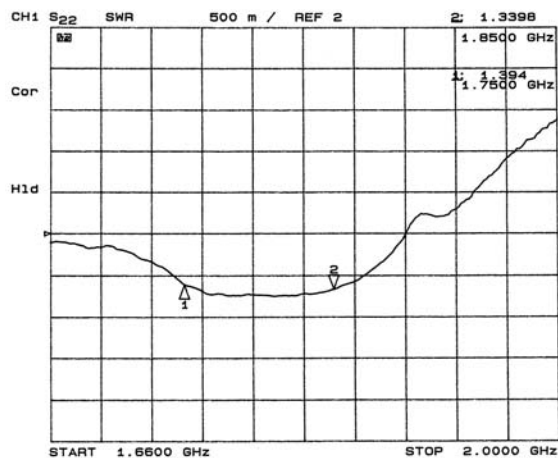


Fig. 8B L-bd VSWR

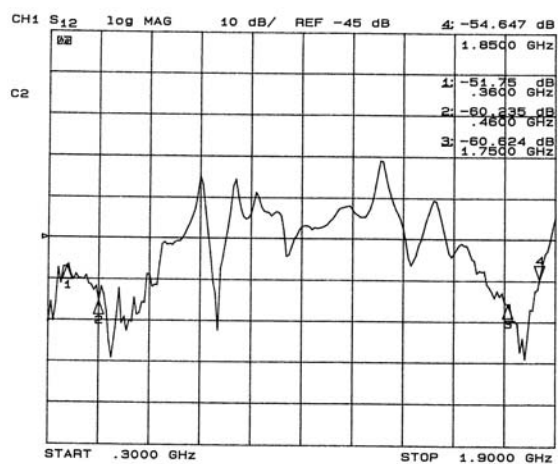
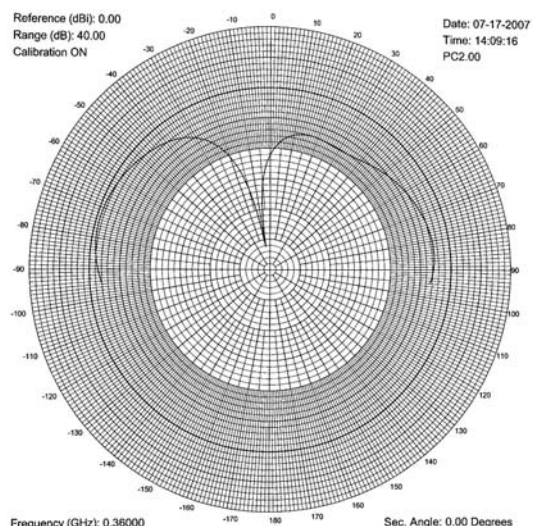
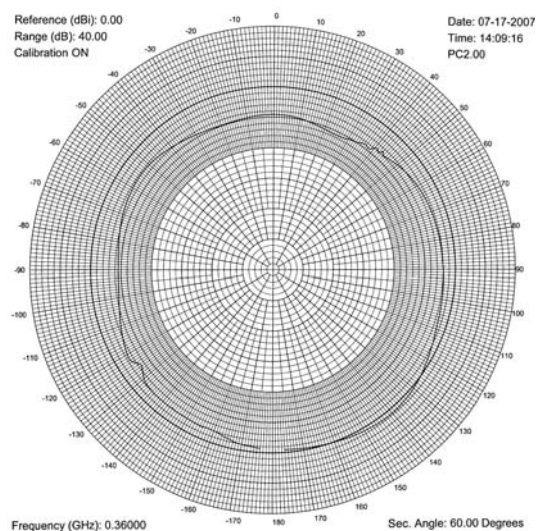


Figure 9 Isolation



**Fig. 10A UHF Principal Plane**



**Fig. 10B UHF Conic**

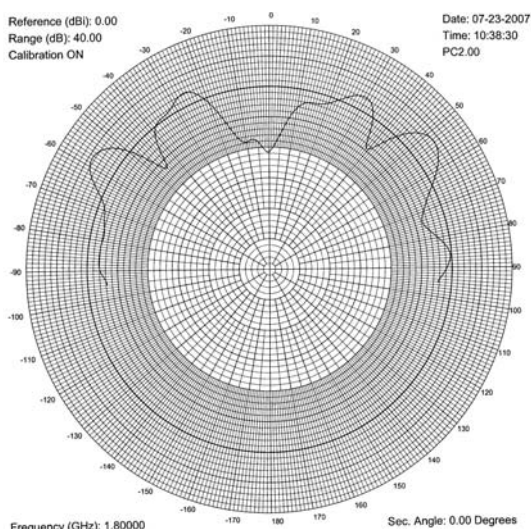


**Fig. 11A L-bd Principal Plane**

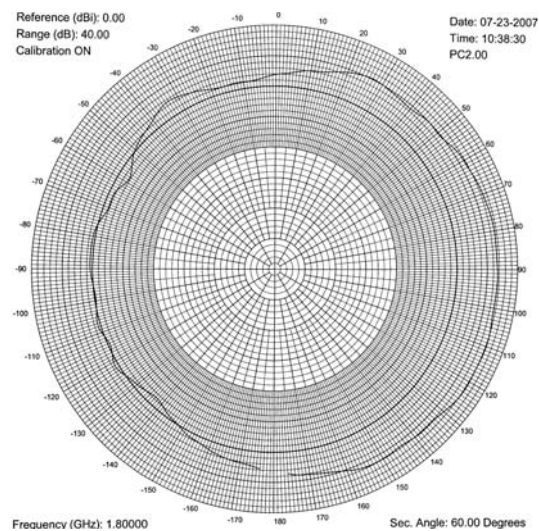


**Fig. 11B L-bd Conic**

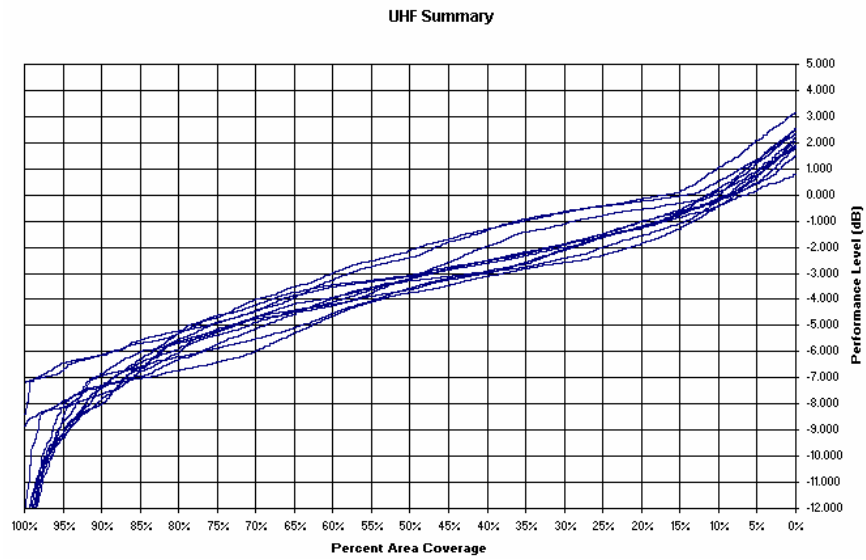


**Figure 12A UHF Pattern Coverage**

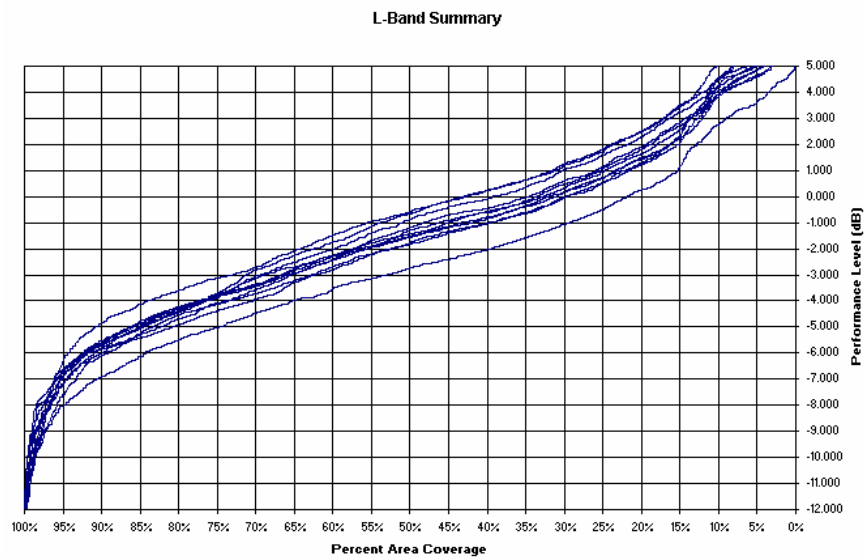


**Fig. 12B L-bd Pattern Coverage**

**Table III. Key Electrical Performance Parameters**

<b>Parameter</b>	<b>Performance Goal</b>	<b>Measured Performance</b>
Frequency Range	UHF and L-band, 100 MHz bandwidth both bands	UHF and L-band, min. 100 MHz bandwidth both bands
VSWR	3.0:1 max UHF / 2.0:1 max L-band	2.8:1 max UHF / 1.8:1 max L-band
Isolation	45 dB min between Operating Bands	50 dB min
Pattern Coverage	Omnidirectional in azimuth; horizon to +45° in Elevation	Omnidirectional in azimuth; horizon to +45° in Elevation  See Figs. 12 for typical percent coverage
Power Handling	50W CW Both Bands	TBD

**Table IV. Key Mechanical Characteristics**

<b>Parameter</b>	<b>Performance Goal</b>	<b>Measured Performance</b>
Installation	Base Permanently Mounted / Antenna Detachable/Replaceable Without Tools	Antenna Detachable/Replaceable without tools in < 1 minute
Size	Base 3.0" max Diameter x 1.0" max Height / Antenna 3.5" max Diameter x 14" max Height	Base 2.98" Dia x 0.98" Height / Antenna 3.54" Dia x 12" Height
Weight	Base 0.55 lb max / Antenna 3.28 lb max	Base 0.5 lb / Antenna 3.15 lb
Flexure	Antenna Capable of Flexing 90° when Installed on Base	Flexure > 90°
Mechanical Impact	Antenna Capable of Withstanding Multiple 15 mph Impacts when Installed on Base	Demonstrated to withstand Qty. 25 x 15 MPH Impacts

In addition to the mechanical impact testing, HALT testing, consisting of thermal soak, thermal cycling, vibration, and vibration at temperature extremes, was also successfully performed. As of this writing, M/A-COM is in the process of fabricating pre-production units and preparing for a full Qualification program.

#### **4. Conclusion**

M/A-COM has designed and developed a unique ground-based communication system antenna. The antenna provides transmit / receive capabilities at both UHF and L-bands. In addition, it incorporates features that allow for quick-disconnect capability, as well as flexure and the ability to withstand accidental mechanical impact. This antenna is anticipated to go into full scale production in the near future.

# Effects of Modulation Ratio on the Performance of 4 Arm MAW Spirals

William N. Kefauver<sup>1</sup>, Thomas P. Cencich<sup>2</sup>, Dejan S. Filipovic<sup>1</sup>

<sup>1</sup>Department of Electrical and Computer Engineering  
University of Colorado at Boulder, CO 80309-0425

<sup>2</sup>Lockheed Martin Space Systems Company, Denver, CO

**Abstract:** The performances of 4-arm MAW spirals including a classical self-complementary structure, and various modifications aimed to improve its characteristics are studied. The differences between two of the most common growths, equiangular and Archimedean are contrasted. The non-self-complementary designs, bi-layer arm and higher arm count configurations are investigated as possible means for improving the MAW spiral performance. Impedance, gain, polarization purity, and other parameters are researched. Conclusions are supported by the extensive method of moments simulations using a commercial package FEKO.

## 1. Introduction

Applications of an antenna which can detect the entire polarization matrix over most directions are extremely useful for number of applications including remote sensing, multi-functional communications, radar, radar warning receivers and other electronic warfare needs, just to mention a few. Ideally, one would like to receive two orthogonal polarizations through a sensor that uses the same aperture for both polarizations. The most commonly used flush-mounted antenna for omni-polarized, ultra wideband frequency and broad beam coverage applications, is the sinuous antenna invented by R. DuHamel in 1987 [1]. This antenna can also operate in two-orthogonal linearly polarized regimes, where the main polarization axis wobbles around the axis bounded by the sinuous tips. An alternative for the dual-circularly polarized applications is a modulated arm width (MAW) spiral developed by P. Ingerson around 1970 [2]. The MAW spiral can also operate in a linearly polarized mode; however, the main polarization axis rotates with frequency thus precluding its use in this mode of operation. The basic design has no real bandwidth constraint, but the quality of performance is affected by some structural parameters and has limited polarization purity, beam azimuthal symmetry and efficiency [3]. The MAW spiral complements the sinuous in that the individual arm polarization is circular whereas the sinuous individual arms are linearly polarized. Shown in Figures 1 and 2 are the layouts of 4-arm self-complementary MAW spirals with equiangular and Archimedean growth rates.

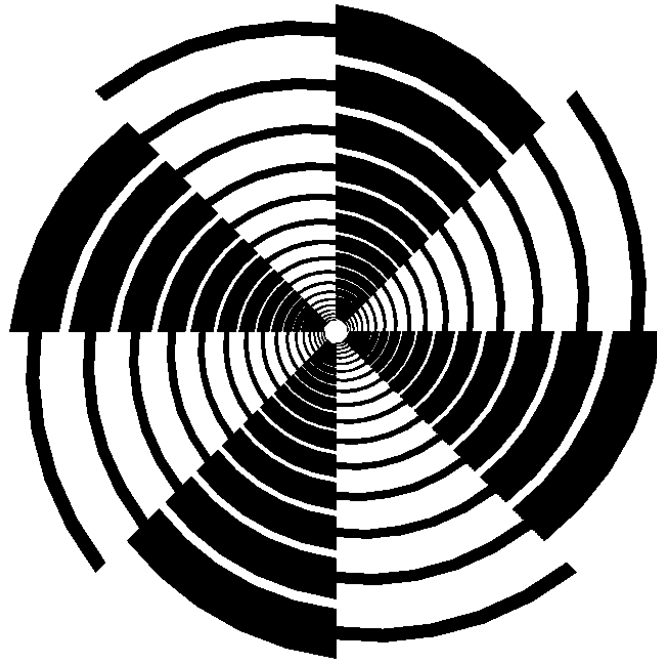


**Figure 1.** A layout of an equiangular self-complementary 4-arm MAW spiral with modulation ratio of 4.

A MAW spiral etched on the same side of the substrate has been extensively investigated, and many ideas have been patented. For instance various implementations including six and eight arms [4], tuning chokes and tapered modulation [5, 6], modulation of the arms at a high angular rate to increase electrical size [7], and other less closely aligned work. For understanding the MAW spiral, some basic understanding of its parent antenna, a spiral, needs to be first revisited. The nature of a spiral is that as the wave travels along its arms the phasing between these arms prevents radiation until the resonant circumference in wavelengths is achieved. If the spiral is too small the traveling wave will reflect off the far end of the spiral and try to radiate traveling the other direction resulting in the opposite polarization for the physical wrap of the spiral. If the spiral is much larger than the nominal resonance, higher order modes will radiate. For example if a four arm spiral is more than five wavelengths in circumference it will radiate both modes, mode 1 ( $M_1$ ) and mode 5 ( $M_5$ ). The ratio of power coupled into these two modes is driven by whether the design radiates efficiently through the primary ( $M_1$ ) region. If so, then minimal radiation occurs for  $M_5$ . If a simple spiral is large enough to radiate  $M_5$ , it also radiates  $M_3$  (a difference mode) which is not desired when radiating  $M_{-1}$  (the opposite polarized mode). Unfortunately a simple spiral has no way to distinguish between the two modes so how does one make  $M_3$  an inefficient radiator when it has lower impedance to  $M_{-1}$ ? These problems are the limitations to a broadband dual polarization operation of a conventional spiral, i.e., it will radiate in a forward mode before reflecting leaving no power to couple into the desired mode. If fed from the outside the simple spiral will also radiate  $M_{-1}$  efficiently, resulting in better bandwidth – 4:1 instead of 2:1 for feeding both



modes inside, but this method will result in having a more complex antenna with two separate beamformers.

In this paper, we study the performance of the 4-arm MAW spirals including the classical self-complementary structure, and various modifications aimed to improve its characteristics. Specifically, the non-self-complementary designs, bi-layer arm and higher arm count configurations are investigated. Impedance, gain, polarization purity, and other parameters are contrasted. Earlier published research has dealt with the self-complementary MAW spiral design with a coplanar technology. The self-complementary design will be compared to a lower impedance design able to support a more efficient modulation. A bi-layer arm tracing with half of the arms patterned on either side of the dielectric will be evaluated. This allows greater flexibility in choosing a modulation ratio, which is one of the most important parameters for the MAW spiral. The modulation ratio, defined as the ratio of the low impedance arm width to the high impedance arm width, is typically taken to be about 8 to 1 with the conventional etching tolerances. This, along with the lower growth rates needed for best performance, impose practical limitations. Higher arm counts are also evaluated for mode purity relative to the best case four arm geometries. Conclusions are supported by the extensive method of moments simulations using a commercial package FEKO.

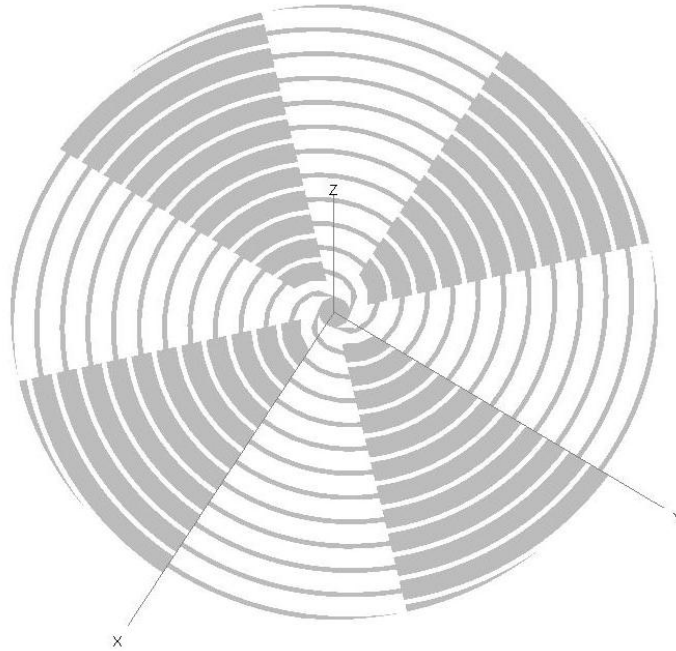


**Figure 2.** A layout of an Archimedean self-complementary 4-arm MAW spiral with modulation ratio of 4.

## 2. Theory of Operation of MAW Spirals

If one examines the basic spiral geometry regardless of growth method (Archimedean, equiangular or some hybrid of the two) the capability to radiate orthogonal polarizations

requires the direction of propagation on the spiral to be in the opposite direction for the second polarization. If the spiral is right handed, it will radiate left handed when it is fed from the outside. A four arm spiral will also radiate the opposite polarization when fed  $M_3$  if the spiral is small enough to allow reflection at the outside (the ultimate impedance discontinuity). For two arms the problem is degenerate because the phasing is the same for both right and left ( $0$  and  $180^\circ$ ), unless non-traditional feeding techniques are utilized [4]. For three arms and more, the two modes can be created by straightforward phasing techniques and the bandwidth will increase with the number of arms.

The reverse mode will always have higher ohmic loss in practical implementation since it has to reflect off the outside end of the arm to return to the radiation region to re-radiate resulting in a significantly longer path length. The MAW spiral, shown in Figures 1 and 2, avoids the bandwidth constraints of the basic spiral antenna. Specifically, the MAW spiral is modified such that impedance modulation is introduced in its arms. This modulation causes the currents to reflect when they encounter a region where the length of the modulated impedance section is one quarter of a wavelength. The reflections from the beginning and end of the modulation interfere constructively to give a high reflection level. This region of the MAW is referred to as a band stop in the literature. The ratio of the arm width between the bandstop and nominal armwidth is commonly referred to as the modulation ratio. For a self-complementary MAW, the antenna gap between arms must average out to 1:1 or 50% of the area, the other portion being metal. In other words, thin sections of metal (nominal) will have the same width as the thin gaps on the adjacent sections. The structure ceases to be self-complementary when the gap and the nominal armwidth are not equal. The nominal impedance of the structure will shift up or down uniformly across the band as long as the structure is still maintaining a constant ratio even if it is not self-complementary. Based on the number of arms in the spiral, the normal circumference to place a band stop will be  $c=N\lambda/2$ , where  $N$  is the number of arms. Thus, the band stop is at  $c=2\lambda$  for four arms,  $c=3\lambda$  for six arms and  $c=4\lambda$  for eight arms. By setting the band stop at this circumference the geometry is also angularly symmetric since the diameter is equal to twice the arm count in quarter wavelengths. Although the polarization of an individual arm is circular, the linear polarization can be achieved by combining the left and right ports through a  $90^\circ$  hybrid resulting in two orthogonal linear polarizations. The polarization axis of the resulting linear modes for the hybrid will rotate with the frequency, thus significantly constraining the applicability of this antenna. Rotating linear polarization would require a lookup table to keep straight the polarization with frequency. Sinuous antennas already have a mild version of the rotation polarization condition, typically limited to  $20^\circ$ .

In trying to create pure orthogonal polarizations two items are in opposition. First, the normal mode must radiate efficiently before the bandstop to avoid the higher-order mode contamination or off-broadside axial ratio deterioration due to the reflection from the arm ends and re-radiation in the cross-polarized mode. In the case of a four arm spiral, the first higher order mode is  $M_5$ , while the mode reflected is  $M_{-3}$ .  $M_5$  will increase pattern undulations (WOW) while  $M_{-3}$  will degrade axial ratio and possibly the impedance

match, since the radiation region is too small to radiate efficiently. Not surprisingly, cross-pol is more difficult to control than WOW since the MAW cannot terminate the outside to reduce reflections. If the bandstop is not effective the pattern will have degraded WOW due to higher mode radiation which may also be cross-polarized if it reflects from further along the arm producing both  $M_5$  and  $M_3$  (for reverse operation the modes flip and the radiation mode  $M_1$  occurs after the undesired  $M_3$ , whereas contribution from  $M_5$  should very small). With the MAW, this result typically occurs for low modulation ratios. Additionally, if the power is not reflected the efficiency of the reverse mode will be degraded. For this paper we will evaluate methods to improve WOW and polarization. Optimization of the impedance match will not be investigated, but the impedance will be evaluated on a comparative basis without implementation of a feeding geometry.

The relationship between the two impedance sections can be chosen so that the antenna will still be on average self complementary and allow one to use the Deschamps relationship for self-complementary structures [5] of

$$Z_m^{fs,comp} = \frac{\eta_0/4}{\sin\left(\frac{m \cdot \pi}{N}\right)} \quad (2.1)$$

which for a mode 1 four arm spiral results in an expected impedance of  $133.3\Omega$  to ground since  $\eta_0 = 377\Omega$  (free space impedance). In 2.1,  $m$  is the desired mode of excitation (operation), and  $N$  is the number of arms. The problem in making etches with extremely high modulation ratios is the close tolerance on the gap between the wide sections and also the potential for undercutting the trace width on the narrow sections. Given that for the same etching technology, the modulation ratio can be doubled by using both sides of the dielectric. The Booker relationship based on Babinet's principle gives us assurance that if the sections are mirror images of each other that the ratio can be calculated trivially once one is known. In the self complementary case, (two arms) the result is half free space impedance, or  $188.5\Omega$ . This results in the impedance to ground of  $94.2\Omega$  when looking at the potential to ground instead of the other arm. The reflection off a bandstop section then can be easily determined from knowing the impedance of a simple non-complimentary spiral. However, if the non-complimentary spiral is taken to the limit of a thin single wire the impedance is still only approximately  $254\Omega$  (less if dielectrically loaded). This was calculated from a computer simulation for a four arm spiral, therefore using Booker's relationship, the practical result for a band stop of the planar spiral cannot be less than  $70\Omega$ . For the case of extremely high modulation ratios a mismatch of about 0.56 is the maximum, which means at the resonant diameter the reflection barely approaches unity. If the two impedances of the two sided MAW can be assumed double (a result consistent with computer simulation) then the reflection efficiency does not improve drastically over the 8:1 modulation, but the slightly increased reflection reduces WOW and axial ratio in the reverse mode.

### 3. Archimedean vs. Equiangular MAW Spirals

The Archimedean spiral has been used since the earliest days of spiral antenna engineering and though not truly frequency independent it performs very similarly to a frequency independent equiangular spiral. The most common implementations of the MAW spiral are those with the equiangular growth rates [3, 10]. The potential differences with Archimedean MAW spirals or the dependence of antenna performance on the type of the growth have not been thoroughly researched in the open literature. The unmodulated Archimedean and equiangular spiral forms in planar form are drawn in Figure 3 (a, b).

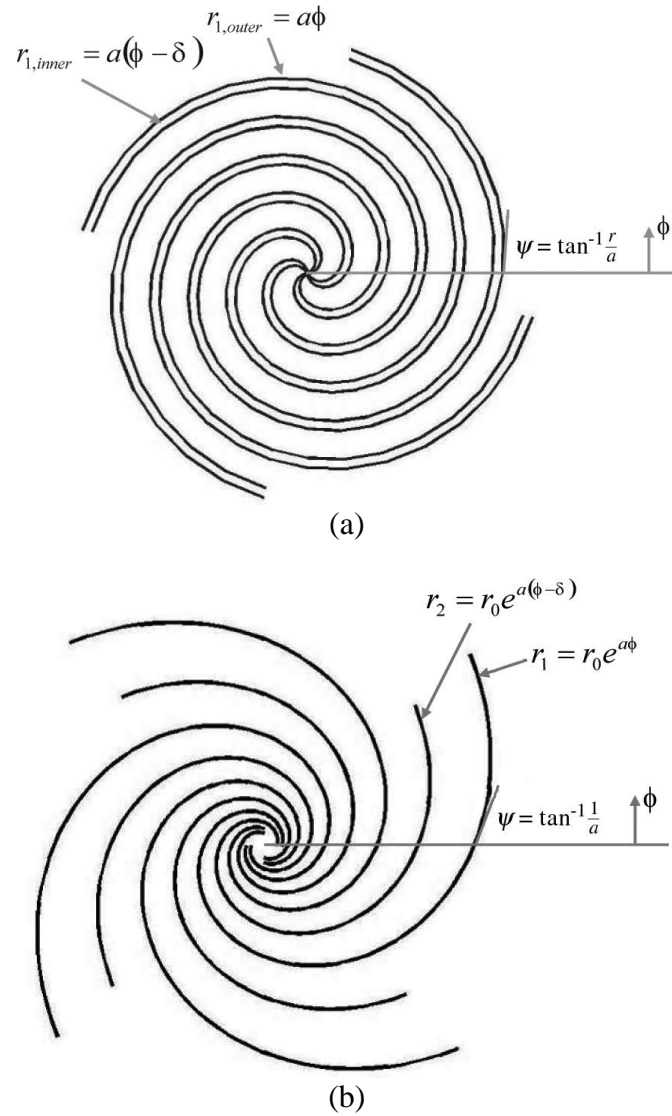


**FIGURE 3.** Four-arm Archimedean (a) and equiangular (b) spirals. Shown also are the equations used to generate the outline of their arms.

The Archimedean spiral has a constant arm width and constant separation between arms through the entire aperture. The defining equation for this antenna is

$$r = r_0 + a\phi \quad (3.1)$$

where  $r_0$  is the starting radius,  $a$  is the growth rate, and  $\phi$  is the progressive growth angle. The equiangular spiral has progressively increased arm width and separation between the arms as they open toward the outside. This shape can be entirely described by angles and is the basis for the frequency independent principles. The defining equation for an equiangular spiral is

$$r = r_0 e^{a\phi} \quad (3.2)$$

where  $r_0$  is the starting radius,  $a$  is the growth rate, and  $\phi$  is the progressive growth angle. Another term frequently used to describe tightness of the equiangular spirals is the so-called expansion factor (EXP), defined as

$$EXP = e^{2\pi a} \quad (3.3)$$

For an expansion factor approaching 1, the spiral arm width and separation between the arms, will remain the same for each turn converging to the Archimedean case. Shown in Figure 3 are also the equations for the angles subtended between the radius vector and the tangent on the spiral line at the same point. With the equiangular structure this angle is constant, while it changes with the Archimedean spiral. When the MAW spiral is phased to operate in the reversed mode, establishing a good band-stop is very important. Relevant parameters to evaluate the band-stop include reverse gain, cross-polarization and WOW. Tables 1-3 compare the forward and reverse performance parameters for several 4-arm equiangular and Archimedean MAW spirals as a function of the modulation ratio. Results listed here for the Archimedean were averaged from  $2f_0$  to  $5f_0$  with a logarithmic density, where  $f_0$  denotes the cut-of frequency determined by the location of  $M_1$  radiating region. Frequencies below  $2f_0$  were eliminated from the data set because the MAW spiral cannot radiate other modes below this frequency. Archimedean MAW spirals are computed in FEKO, while the reference data from [3] were obtained using GNEC.

Shown in Table 1 is the comparison between the averaged broadside gains. As seen, in the forward mode of operation both designs yield similar performance with the gain virtually unaffected by the modulation ratio. The nominal gain is around 5.5 dBic. As expected, the modulation ratio becomes very important for the reverse mode. As the modulation ratio increases, the gain results converge to those of the forward mode. Interestingly, the Archimedean MAW spiral shows better performance, i.e., the faster convergence of the reverse gains. For modulation ratios above 4, there is virtually no difference in averaged gains in forward and reverse modes for the Archimedean spiral.

<i>Modulation</i>	<i>Eq. Forward</i>	<i>Eq. Reverse</i>	<i>Ar. Forward</i>	<i>Ar. Reverse</i>
1.1	5.6	-2.9	5.6	-6.1
2	5.5	-1.0	5.4	2.4
4	5.6	2.1	4.9	4.3
8	6.0	4.6	5.4	5.6

**Table 1.** Average Gains (dBic) of Self-Complementary Equiangular [3] and Archimedean MAW Spirals with Different Modulation Ratios

Shown in Table 2 is the comparison between the averaged cross-polarization levels at elevation angle of  $30^\circ$ . As seen, the performance of the MAW spirals is similarly affected in both designs, which results in good performance for the modulation ratio of 8 in both designs. As the modulation ratio increases, the cross-polarization level in the forward mode deteriorates, while it improves for the reverse mode. This is not surprising as the modulation ratio will directly control the quality of the band-stop region and also add to the reflections in the forward mode that can contribute to the radiation of the cross-polarized mode.

<i>Modulation</i>	<i>Eq. Forward</i>	<i>Eq. Reverse</i>	<i>Ar. Forward</i>	<i>Ar. Reverse</i>
1.1	-35	-2.9	-35.9	--
2	-34	-9.0	-35.3	-6.3
4	-33	-12.5	-30.8	-12.8
8	-32	-16.5	-27.0	-18.0

**Table 2.** Average Cross-polarization (dB) for Self-Complementary Equiangular [3] and Archimedean MAW Spirals with Different Modulation Ratios

Shown in Table 3 is the comparison between the averaged levels of pattern undulations at elevation angle of  $30^\circ$ , computed in terms of the WOW. As seen, the modulation ratio does not affect the forward WOW for either of the two designs. Also, for the forward mode, the equiangular and Archimedean MAW spiral, both have the same WOW. However, the WOW is very low and consistent with the Archimedean MAW spiral, even for the small modulation ratios at high frequencies, as opposed to the observably higher values for the equiangular. This result is surprising since the equiangular spiral has a finer center structure.

<i>Modulation</i>	<i>Eq. Forward</i>	<i>Eq. Reverse</i>	<i>Ar. Forward</i>	<i>Ar. Reverse</i>
1.1	0.3	7.5	--	--
2	0.3	1.0	0.3	0.3
4	0.3	1.2	0.2	0.3
8	0.3	1.0	0.3	0.2

**Table 3.** Average WoW (dB) at  $\theta=30^\circ$  for Equiangular [3] and Archimedean Spirals with Complementary Geometry with Different Modulation Ratios

The geometries chosen in the above study had the same number of turns (as shown in Figures 1 and 2), however, due to the different growth rates the arm-length is over twice as long for the Archimedean. The results presented in Tables 1-3 can be summarized as follows: the major difference is most striking in the reverse gain, which in the Archimedean case, shows significant improvement for all modulation ratios except for the degenerate 1:1 case. The cross-polarization is similar. WOW of the Archimedean is slightly better, probably due to the better radiation efficiency over most of the operating band. It is possible that the equiangular would achieve similar results to the Archimedean MAW spiral if designed with a lower expansion factor. However, the study presented in this section is based on the same number of turns on the MAW spiral element.

#### 4. Non-Self-Complementary MAW Spirals

Although the classical spiral work has emphasized the self complementary approach to the design of frequency independent structures, we also know that the impedance of the spiral can be varied by changing the metal to non-metal (slot) ratio. Specifically, increasing the width of the metalized sections will lower the antenna impedance and often is used to match to the impedance of the conventional coax lines [3].

In this section, we investigate the impact of MAW spiral non-complementarities on its performance. The growth type is Archimedean and impedance, gain and cross-polarization are of interest. For this case, the non-self-complementary structures are created in the following way. First, the ratio of the widths of the metal to the slot in the low-impedance section of the MAW spiral is set to 8:1. Then, the width of the metal sections in the high impedance regions is increased to achieve the overall modulation ratios of 2:1 and 4:1. The initial 8:1 self complementary structure was chosen since it has the best dual-polarized performance; however it also has a significant mismatch problem.

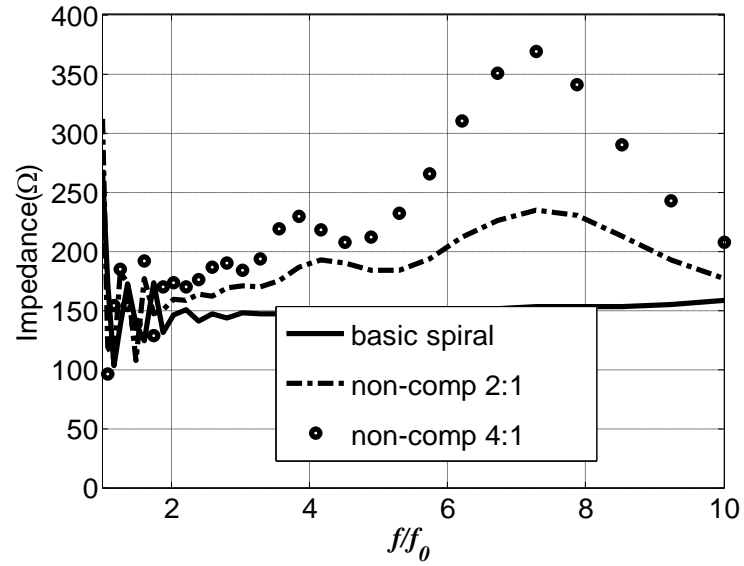
The averaged broadside gain comparison is shown in Table 4. As seen, the forward gain is improved by about 0.5dB for the two studied modulation ratios. At the same time, the reverse gain has seen improvement of 2.1dB and 1.2dB for modulation ratios of 2 and 4, respectively.

<i>Modulation</i>	<i>Com. For.</i>	<i>Com. Rev.</i>	<i>Non-Com. For.</i>	<i>Non-Com. Rev.</i>
2	5.35	2.35	5.71	4.44
4	4.88	4.30	5.32	5.55

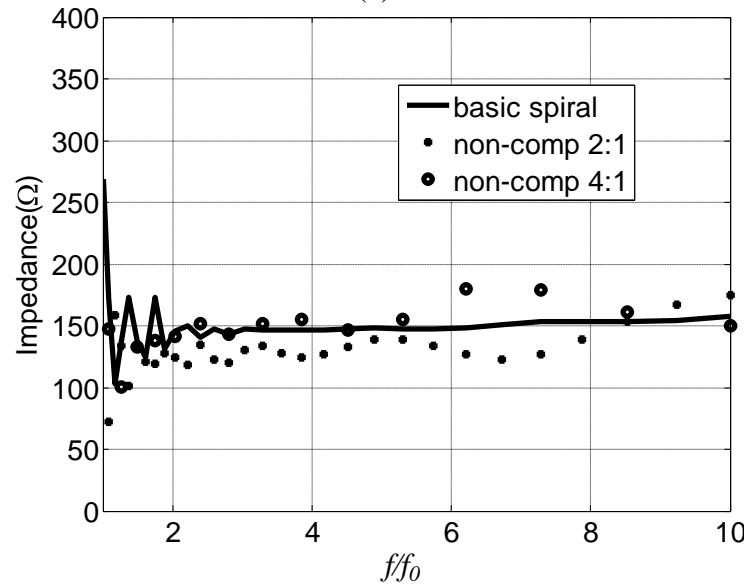
**Table 4.** Comparison of Average Broadside Gains (dBic) Between the Self- and Non-self-complementary Archimedean MAW Spirals

Shown in Figure 4 is a significant improvement in the expected impedance ripple and its overall stability with non-self-complementary MAW spirals. As seen, by increasing the ratio of metal to slot widths in the low-impedance region only, while maintaining the same modulation ratio, the impedance variations became almost insignificant when

compared with the self-complementary 4-arm spiral antenna. Shown in the figure is only the forward mode of operation.



(a)



(b)

**Figure 4.** Input Resistances of Archimedean Self-Complementary (a), and Non-Self-Complementary (b) MAW Spirals with the Band Stop Metal to Slot Width Ratio of 8:1.

The averaged cross-polarization at  $30^\circ$  for the two modes of operation and self- and non-self-complementary Archimedean MAW spirals are shown in Table 5. As seen, both designs have very good cross-polarizations in the forward mode. In the reverse mode, the cross-polarization levels with the non-self-complementary MAW spiral are improved by about 1.3dB and 0.6dB when the modulation ratios are 2 and 4, respectively.



<i>Modulation</i>	<i>Com. For.</i>	<i>Com. Rev.</i>	<i>Non-Com. For.</i>	<i>Non-Com. Rev.</i>
2	35.3	-6.3	-30.4	-7.6
4	-30.8	-12.8	-29.4	-13.4

**Table 5.** Comparison of Average Cross-polarization (dB) Between Self- and Non-self-complementary Archimedean MAW Spirals. Elevation Angle is  $\theta=30^\circ$

In summary, with the non-self-complementary MAW spirals, the gain, polarization and impedance improve indicating that band stop is more significant to overall performance than the modulation ratio itself. Based on the conclusions from this section, the logical step in continuing our studies is to find the way of improving the band stop. This leads to consideration of placing two opposite out of phase excited sets of two arms on either side of the dielectric and thus achieving further reduction in the impedance of the low-impedance section.

### 5. Bi(Dual)-Layer MAW Spiral

The most important design parameters for a dual side (or bi-layer) MAW are the separation between the arm sets due to the dielectric thickness, and the overlap, i.e. the new modulation ratio that now allows for overlap between the low-impedance sections. The initial evaluation showed some improvements over the 8:1 baseline, single layer MAW spiral. The growth rate, feed region size / geometry, and overall diameter are kept the same for two structures and their effects will not be considered at present time. The impedance for various spacings between the 12:1 modulated bi-layer MAW spiral is shown in Figure 5. As expected, the impedance is affected by this parameter, however, it also converges to the nominal value after certain separation is achieved.

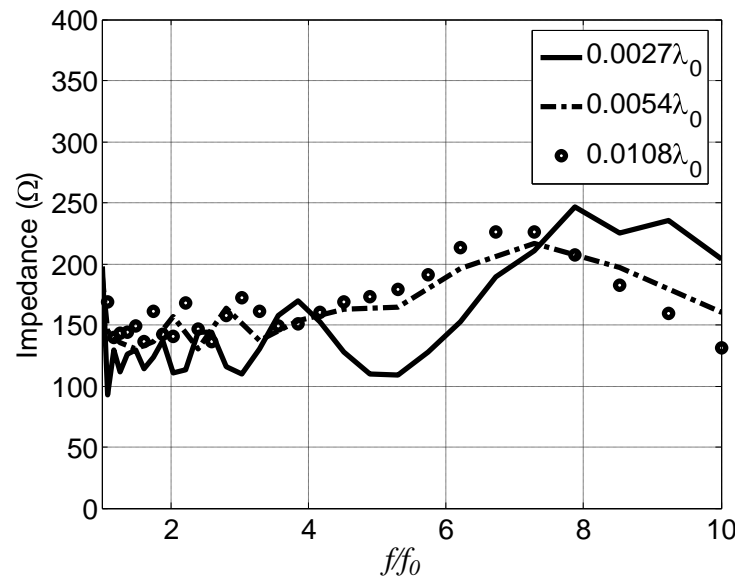
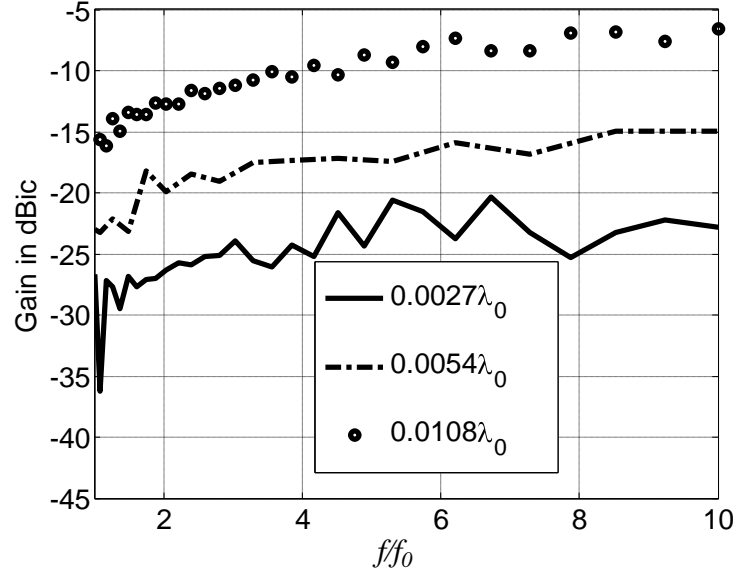
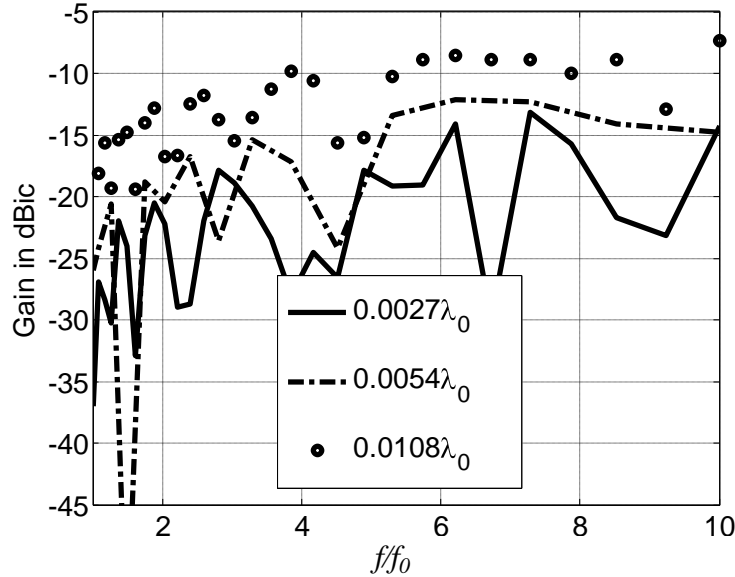


**Figure 5.** Impedance for Different Spacings Between the Layers

Shown in Figure 6 are the effects of the spacing between the two sets of MAW spiral arms to the cross-polarization at broadside ( $\theta=0^\circ$ ) and at  $\theta=30^\circ$  for the reverse mode and modulation ratio of 12:1. As seen, the increased spacing significantly deteriorates the circular polarization quality. It is important to note that the numerical convergence is also affected by this parameter, and typically the problem arises when the layer thickness is smaller than  $0.002\lambda_0$ . The dielectric was not introduced into the model due to computational time. The dielectric will load fabricated antenna relative to free space predictions since significant coupling is occurring through the dielectric.



(a)



(b)

**Figure 6.** Pattern Cross-Polarization (X-Pol) for Antenna with 50% Arm Overlap and 12:1 Modulation Ratio at: Broadside (a),  $\theta=30^\circ$  (b)

The improvements associated with the ability to increase the modulation ratio by etching on both sides of the substrate are best illustrated in Figure 7. As seen, the 12:1 dual-layer MAW spiral has improved reverse mode cross-polarized gains over most of the frequencies. The forward mode remains good at all times; however, the performance of an un-modulated spiral remains about 10 dB better.

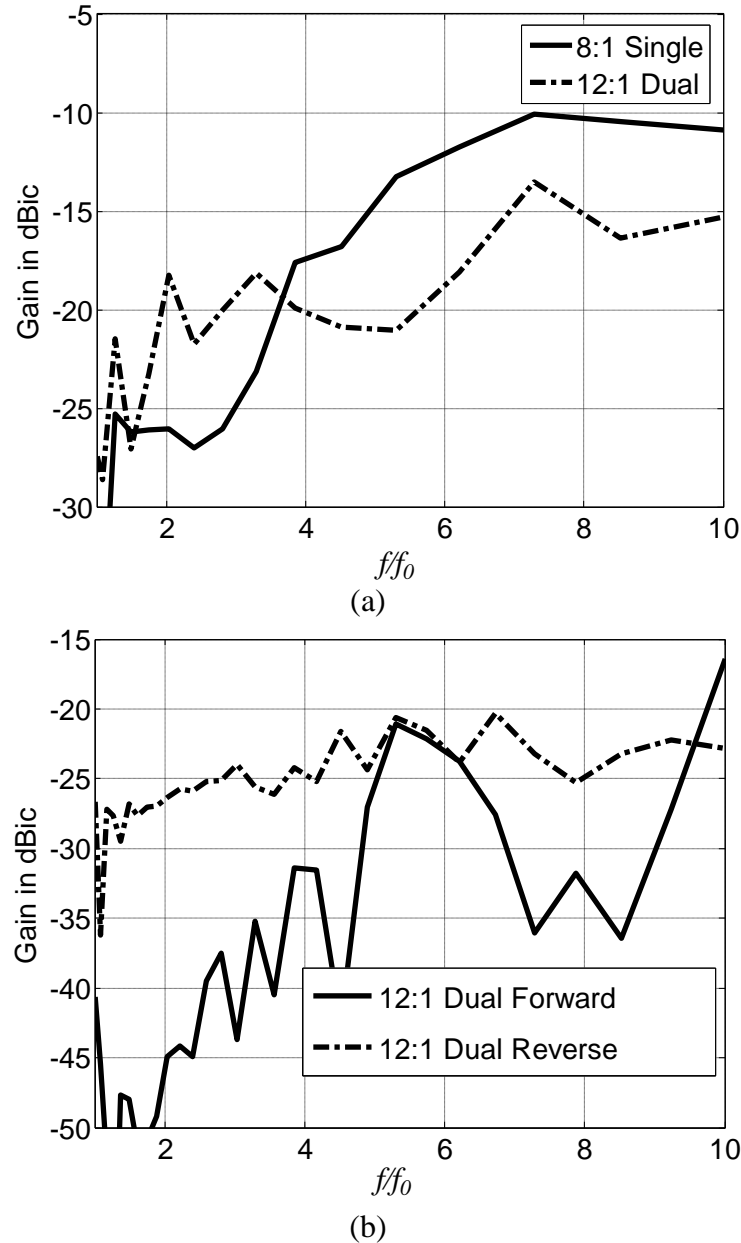


**Figure 7.** Cross-polarized Gain for the Reverse Mode of Operation for 8:1 and 12:1 Modulation Ratios with a Single and Dual Layer MAW Spirals (a), and Forward and Reverse Cross-Polarized Gains for the Dual Layer MAW Spiral.

Shown in Figure 8 is a pattern comparison between the two antennas phased for operation in the reversed mode. As seen, the dual-layer design has better pattern purity for elevation angles above about  $20^\circ$ . The maximal cross-polarization gain for the dual layer MAW spiral is about -13dBic at  $27^\circ$  and -8.5dBic at  $40^\circ$  for a single layer MAW spiral. Overall, up to about 5 dB improvement in cross-polarization is obtained with the dual-side MAW spiral. The most important phenomenon arising from the non-planar structure is the broadside cross-polarization. The planar antenna element never has a problem with broadside cross-polarization due to symmetry, but the non-planar antenna has a significant broadside cross polarization term arising from the gap between the two surfaces even though the non-planar can sometimes reduce off broadside cross-pol.

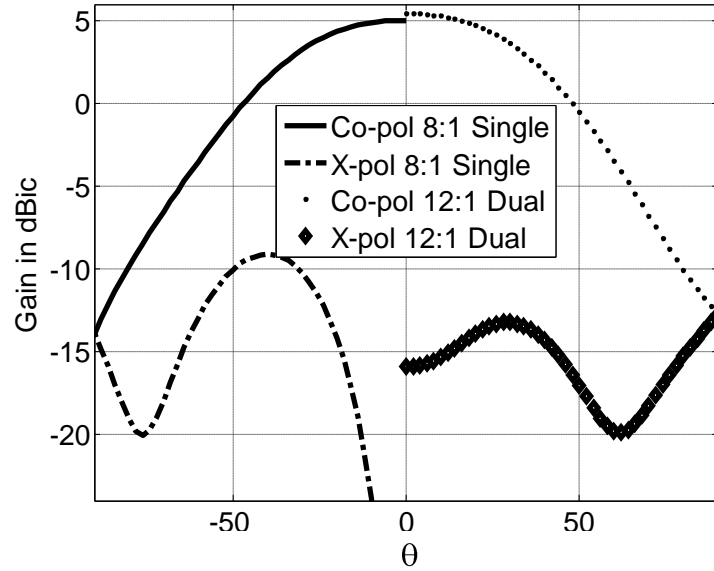


**Figure 8.** Pattern Comparison of Planar versus Dual (Bi)-Layer Archimedean MAW with 0.064" Spacing and 50% Overlap at  $f=6f_0$ .

The results shown in this section clearly demonstrate that the dual-layer design can be a valuable option for improving the performance of the MAW spiral. It is important to note that the numerical computations with method of moments have sometimes experienced convergence issues, particularly when the thickness of the separation layer was small. This, along with a more detailed optimization study involving the amount of overlap, dielectric constant and the thickness of the separation layer, additional verifications with other tools or measurements are needed.

Finally, the dual-layer MAW spiral configuration can be designed and fabricated with a somewhat simpler beamformer network. Specifically, to beamform modes  $M_1$  and  $M_{-1}$  with a single layer MAW spiral, one needs to incorporate either a Butler matrix network or a combination of a  $90^\circ$  hybrid and broadband baluns. Instead, a simple dual-coaxial line feed structure with a single  $90^\circ$  hybrid can be utilized for beamforming the dual-layer MAW spiral.

## 6. Arm Count: 8-Arm MAW Spiral

The bandwidth of dual polarized spiral antennas can be increased by adding more arms even without modulation[3]. A theoretical uncontaminated bandwidth for a center fed N-arm dual polarized spiral is  $(N+1):2$ . To investigate the same effects on the dual-polarized performance with the MAW spiral, we compare the characteristics of a 4-arm Archimedean MAW spiral, shown in Figure 2, with that of an 8-arm Archimedean MAW spiral, shown in Figure 9.

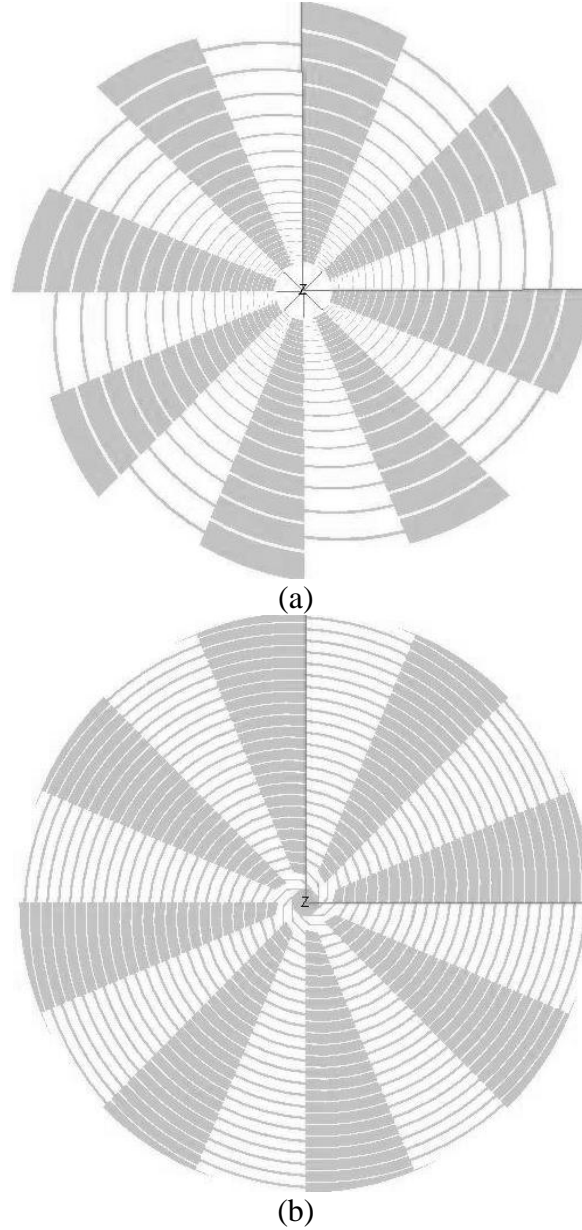
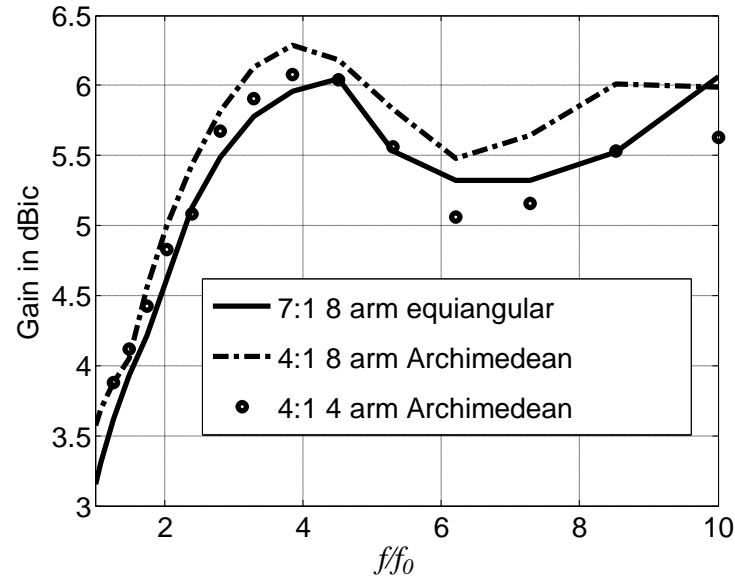
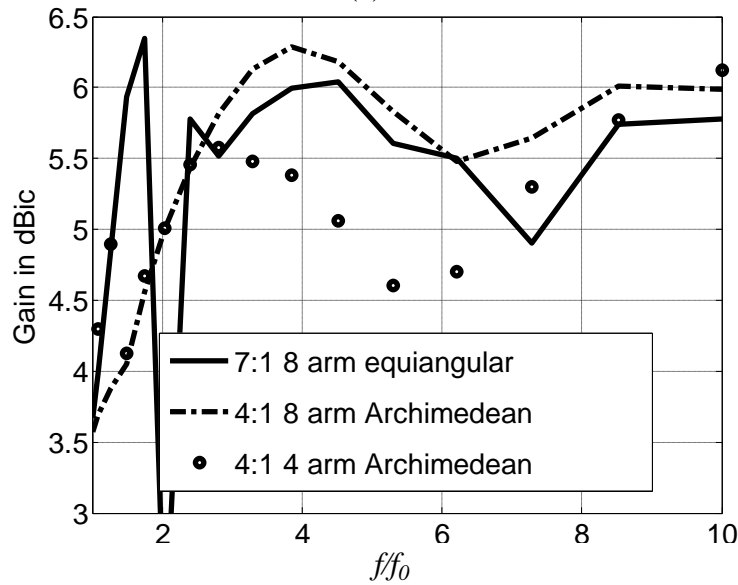


**Figure 9.** Self-Complementary 8-Arm Equiangular with modulation ratio 7:1 (a), and Archimedean with modulation ratio 4:1 (b) MAW Spirals.

Shown in Figure 10 is the comparison between the broadside gains in forward and reverse modes for the MAW spirals from Figures 2 and 9. As seen, the Archimedean eight arm has higher gain than the four arm, but would probably lose a similar amount with a matching network for the much higher impedance approaching  $400\ \Omega$  (see Figure 12). The anomaly at  $ff_0=2$  in the equiangular reverse mode is a computational convergence problem.



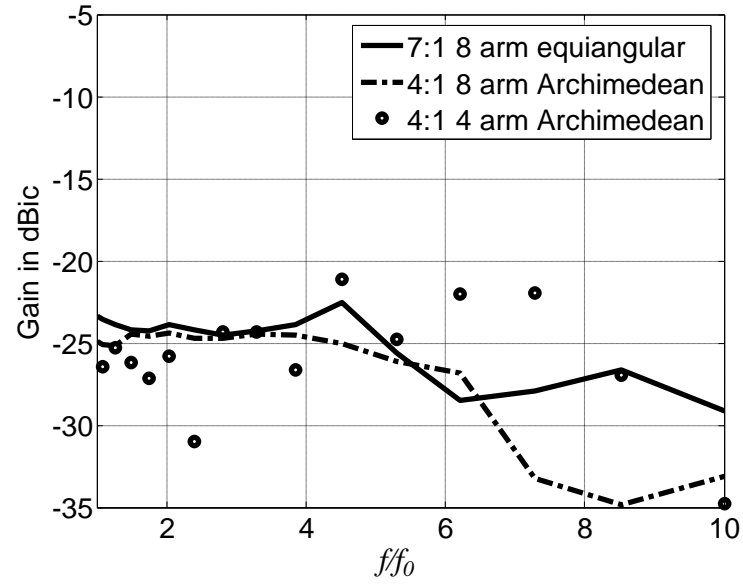
(a)



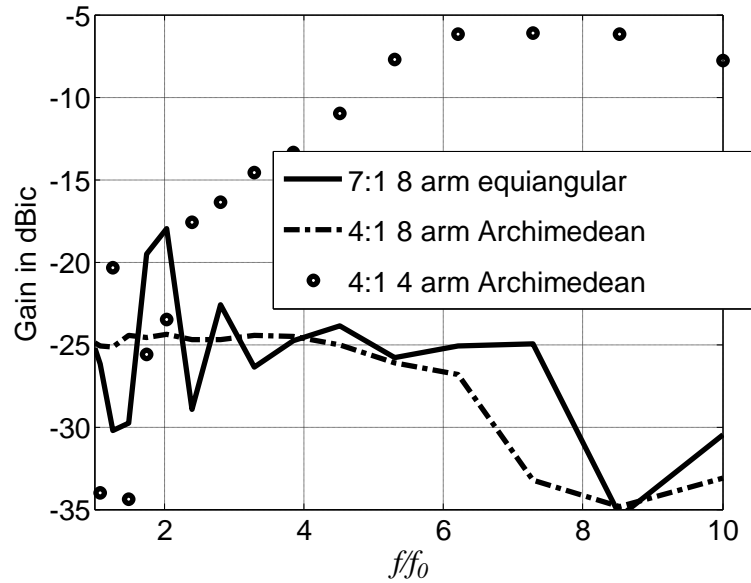
(b)

**Figure 10.** Broadside Gains for 4- and 8-Arm MAW Spirals in Forward (a) and Reverse (b) Modes of Operation.

Shown in Figure 11 is the comparison between the cross-polarization gains at  $\theta=30^\circ$  for the MAW spirals from Figures 2 and 9. WoW remains low for all antennas. The improvement in cross-polarization is due to the additional modal rejection capability of the 8-arm MAW spiral. More than a 10:1 bandwidth can be obtained with 8-arms. The best cross-polarization performance of the reverse mode for a 4-arm antenna is about 10 dB worse than that of an 8-arm MAW irrespective of the growth.



(a)



(b)

**Figure 11.** Cross-polarization at  $\theta=30^\circ$  for 4- and 8-Arm MAW Spirals in Forward (a) and Reverse (b) Modes of Operation.

Finally, to evaluate the effects of the growth type (Archimedean vs. equiangular) on the performance of 8-arm MAW spiral, the comparison between two structures, which the layout is given in Figure 9, is shown in Figure 12. Results were slightly better for the Archimedean for all parameters.

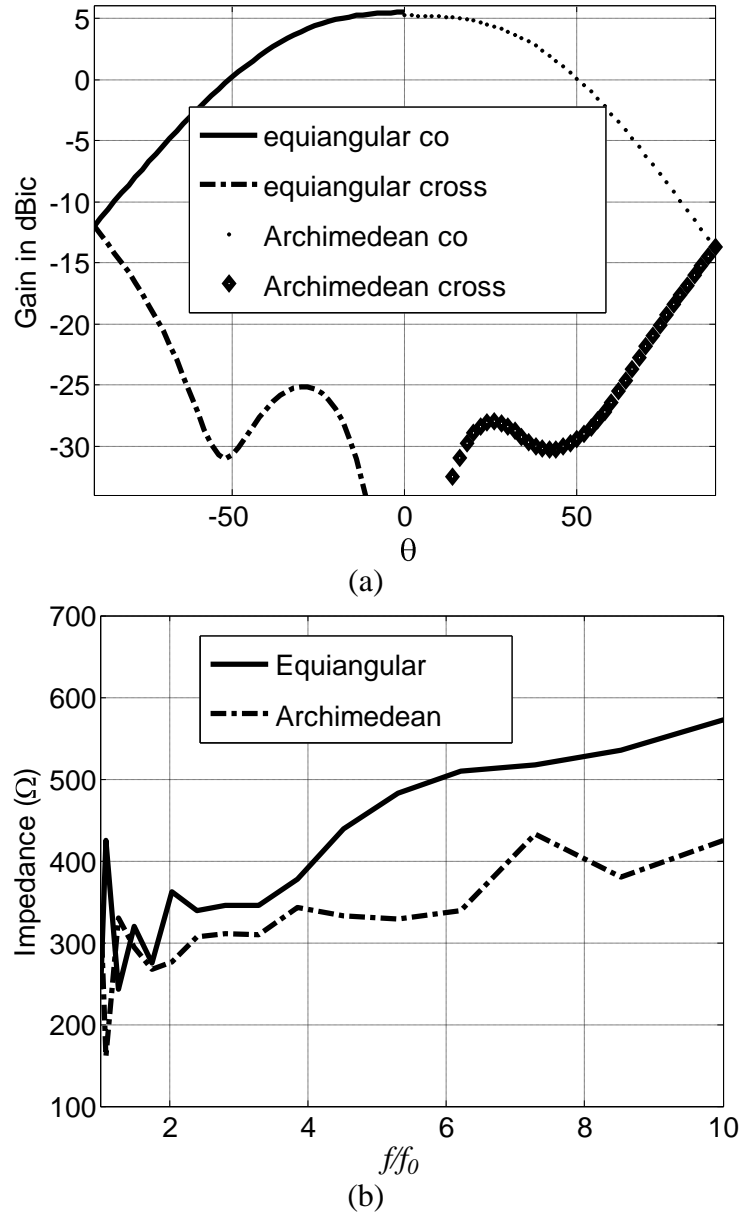


**Figure 12.** Comparison of Equiangular and Archimedean 8-Arm MAW spirals: radiation pattern at  $f=6f_0$  (a) and impedance sweep (b).

It is important to note that the greater number of arms, although significantly improving the far-field properties of the MAW spiral, also increases the complexity of the beamforming network. Assuming that additional modes are needed (example monopulse



direction finding), an 8-arm MAW will enable the simultaneous excitation of modes 1, 2, 3, -1, -2, and -3. Certainly the overlapping mode bandwidth will be reduced with the addition of these higher order modes. Additionally, the impedance matching will also represent a significant loss to the mode not optimized.

## 7. Conclusions

The performance of 4-arm MAW spirals and several approaches for performance enhancement are studied and demonstrated in this paper. It is shown that the Archimedean MAW spiral exhibits improved far-field purity and more consistent patterns and impedances than the most commonly used equiangular MAW spiral. Deviation from the self-complementary principles by progressively increasing the width of the metal low-impedance sections (than at the same rate reducing the width of the high-impedance sections) also enhances the far-field characteristics. It is also shown that printing the MAW spiral arms on both sides of the substrate can further improve the antenna performance. Importance of various parameters, including the separation layer thickness and modulation ratio is demonstrated and directions for the future research are denoted. Finally, an increased arm count has shown to contribute to the most important and the best improvements in the far-field purity at the cost of more complex beamformer implementations and additional loss.

## References

- [1] DuHamel, R. H.; "Dual Polarized Sinuous Antennas," U. S. Patent 4,658,262, Apr. 14, 1987
- [2] Ingerson, P. G.; "Modulated Arm Width Spiral Antenna," U. S. Patent 3,681,772, Aug. 1, 1972
- [3] Filipovic, D. S., Cencich, T.; "Frequency Independent Antennas," Antenna Engineering Handbook, Fourth Edition, Chapter 13, McGraw Hill, 2007
- [4] Walter, C.; "Multi-mode Dual Circularly Polarized Spiral Antenna," U. S. Patent 5,451,973, Sept. 19, 1995
- [5] Andrews, G.; "Broadband Center Fed Spiral Antenna," U. S. Patent 4,243,993, Jan. 6, 1981
- [6] Andrews, G.; "Broadband Spiral Antenna with Tapered Armwidth Modulation," U. S. Patent 4,605,934, Aug. 12, 1986
- [7] Newham, P.; "Broadband Antennas," U. S. Patent 6,191,756, Feb. 20, 2001
- [8] Stutzke, N. A., Filipovic, D. S., "Broadband Two-Arm Dual Mode Dual-Polarized Spiral Antenna," IEEE Ant. Propagat. Soc. Internat. Sympos., 2005
- [9] Deschamps, G.; "Impedance Properties of Complementary Multiterminal Planar Structures," IRE Trans. Ant. Propagat., vol. AP-7, pp. 371-378, Dec. 1959
- [10] Ingerson, P. G., Ingerson, P. M., and Senior, D. C.; "Comparison of Sinuous and MAW Spiral Antennas for Wideband, Dual Polarized Multi-Arm Applications," Proc. 1991 Ant. Applicat. Sympos., 1991

# Dual-Substrate Capacitive Loading Technique in Linearly and Circularly Polarized Shorted Annular Ring Antennas

W. Mark Dorsey<sup>1, 2</sup>, John Valenzi<sup>1</sup>, Amir I. Zaghloul<sup>2</sup>

<sup>1</sup>US Naval Research Laboratory, Washington, DC, USA

[dorsey@radar.nrl.navy.mil](mailto:dorsey@radar.nrl.navy.mil)

[valenzi@radar.nrl.navy.mil](mailto:valenzi@radar.nrl.navy.mil)

<sup>2</sup>Virginia Polytechnic Institute and State University, Virginia, USA

[amirz@vt.edu](mailto:amirz@vt.edu)

**ABSTRACT:** Size reduction of the antennas in personal wireless communications has become an important task for the antenna engineer due to the increasing popularity of compact handsets. The shorted annular ring antenna (SAR) is often used because its two critical radii can be manipulated to satisfy the dominant mode resonance condition of a circular patch and also keep from exciting a surface wave mode. However, in applications placing size and weight restrictions on the antenna, a reduction in the overall size of the device is desirable.

In this paper, a new technique to reduce the size of a SAR antenna is presented. This technique uses a dual-substrate capacitive loading structure that is analogous to a parallel plate capacitor. One of the substrates is beneath the radiator, and another potentially high dielectric substrate is present only beneath the capacitive loading patch. The capacitive patch is connected to the radiating SAR antenna through a capacitive loading ring which is a cylindrical structure located at the outer radius and perpendicular to the radiating and capacitive patches. For this study, SAR antennas operating near 3GHz with and without the loading technique were designed, simulated, built, and tested.

## 1. INTRODUCTION

Many RF applications place a size and weight restriction on the antenna. For instance, a payload that is to be deployed on a satellite has a restricted overall weight. Thus, a lighter antenna leaves more weight available for pertinent electronics on the payload. Another example stems from the ever-advancing technology in the field of cellular communications. With the increased popularity of compact cellular handsets and personal SATCOM devices, the ability to reduce the antennas size has become a necessity. Additional restraints on the antenna size have resulted from the need for antenna diversity, which requires the placement of multiple antennas within a single handset.

The shorted annular ring antenna (SAR), shown in Figure 1, is often used because its two critical radii can be manipulated to satisfy the dominant mode resonance condition of a standard circular patch and also keep from exciting a surface wave mode in the substrate [1]. These two conditions are met as long as the inner radius and outer radius are chosen to satisfy a transcendental equation. However, in applications placing size and weight restrictions on the antenna, a reduction in the overall size of the device is desirable. The radii of the SAR antenna must satisfy the transcendental equation in (1). Using the Bessel function identity of (2), the transcendental equation can be simplified to the form shown in (3) that does not involve taking the derivatives of any Bessel functions.

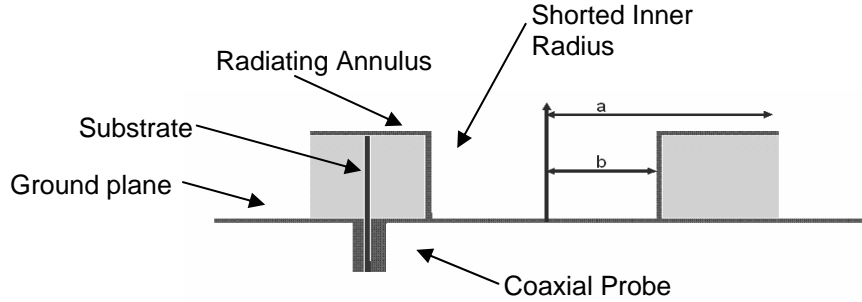


**Figure 1: Cross-section of a probe fed SAR antenna**

$$J_1'(ka)Y_1(kb) - J_1(kb)Y_1'(ka) = 0 \quad (1)$$

$$\frac{d}{dx} Z_p(\alpha x) = \alpha Z_{p-1}(\alpha x) - \frac{p}{x} Z_p(\alpha x) \quad (2)$$

$$\left[ kJ_0(ka) - \frac{1}{a} J_1(ka) \right] Y_1(kb) - J_1(kb) \left[ kY_0(ka) - \frac{1}{a} Y_1(ka) \right] = 0 \quad (3)$$

, where  $a$  is the outer radius and  $b$  is the inner radius

This document discusses a novel edge loading technique that introduces a capacitive loading into a shorted annular ring antenna resulting in significant size reduction. If the inner radius in (1) and (3) is selected to result in a compact outer radius, an even smaller radius can be obtained once the edge loading technique is added to the design. For comparison, we modeled a SAR antenna in CST Microwave Studio [2], built the element, and tested it in the compact range at the Naval Research Laboratory. In addition, a shorted annular ring using the proposed capacitive loading technique was modeled using CST Microwave studio, built, and tested.

The bandwidth of the capacitively loaded SAR antenna can be enhanced utilizing a technique where a parasitic element – shorted at the same radius as the driven element – is placed above the driven element. The addition of this element increases the volume of the antenna element without significantly increasing the surface area of the antenna's footprint. Additionally, this element can be used for applications requiring circular polarization. The circular symmetry of this element makes it ideal for applications requiring circular (or dual-linear) polarization. A sequential phase quadrature feeding of

the element has been seen to produce circular polarization with excellent axial ratio across the operational bandwidth.

## 2. SIZE REDUCTION TECHNIQUES

A limited size reduction can be obtained by reducing the inner radius in (1) and (3) and solving for the outer radius. In some instances a higher frequency antenna is placed within the inner radius of the shorted annular ring antenna to provide dual-band operation [3, 4], thus limiting the minimum value for the inner radius. Additional size reduction can be achieved by increasing the dielectric constant of the substrate. Figure 2 shows a plot of the transcendental equation in (3) as a function of the outer radius ( $a$ ) for various dielectric constants for a SAR antenna designed to operate to 250 MHz. The null in each curve represents the solution to the transcendental equation of (1) and (3). By increasing the dielectric constant of the substrate by a factor of  $\xi^2$ , the outer radius of the SAR can be reduced by a factor of  $\xi$ . In this plot, the resonant frequency is 250MHz, and the inner radius is held fixed at 3.2”.

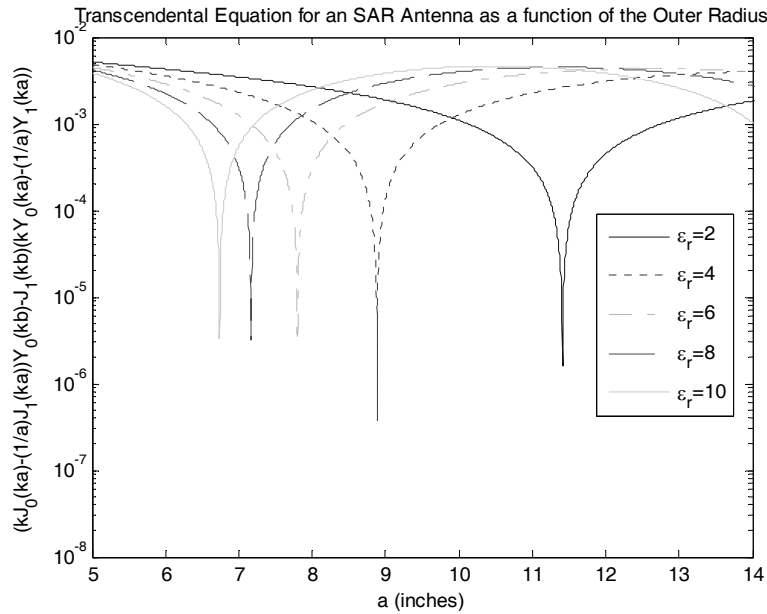


**Figure 2: Solution to the SAR transcendental equation for various substrate dielectric constants:  
 $f_0=250\text{MHz}$ ,  $b=3.2''$**

In recent years, different capacitive loading schemes have been used to manipulate the resonant frequency of an antenna, and thus reduce its size. Ciaia et al showed that the size of a planar inverted-F antenna (PIFA) can be decreased by adding a capacitive loading post at the edge of the device [5]. The size of the device decreases as the capacitance of the loading structure increases. A figure of the element described in that reference is shown in Figure 3, and the capacitive loading structure shown in that figure helped motivate the idea for the concept proposed in this document. A similar technique is used in [6] to reduce the size of a cellular handset antenna and is shown in Figure 4.

This antenna places a capacitive loading at the edge of each section of the Y-shaped patch. This structure creates a capacitance between the load and the ground plane.

However, this size reduction is not obtained without a drawback. It has been shown that the quality factor of the structure increases with load capacitance [7] causing the bandwidth of the antenna to decrease with the size of the loaded antenna. The techniques described in [5,6,7] make use of capacitive conductor in a plane perpendicular to the radiating conductor. The gap between the capacitive conductor and the ground plane determines the capacitance of the load structure. One drawback of these methods is that a single substrate is present beneath the radiator and the capacitive loading structure. A higher dielectric constant material leads to an increased capacitance, resulting in greater size reduction. However, this results in a high dielectric constant beneath the radiating substrate. The use of high-dielectric constant beneath the radiating structure of a patch antenna has the drawbacks of narrow bandwidth, low efficiency, and poor radiation pattern that result from the excitation of surface waves [8].

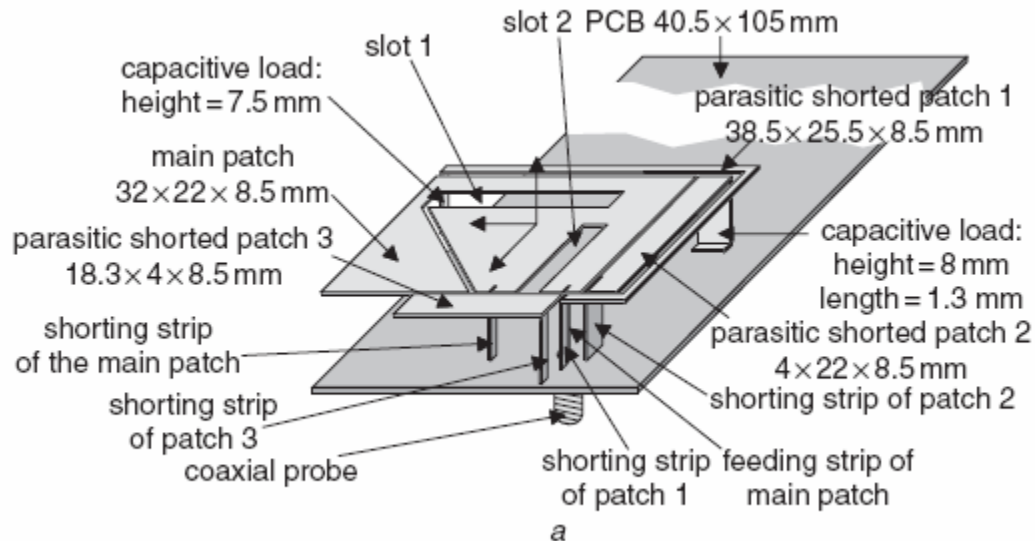


Figure 3: Capactively Loaded PIFA Antenna from [5]

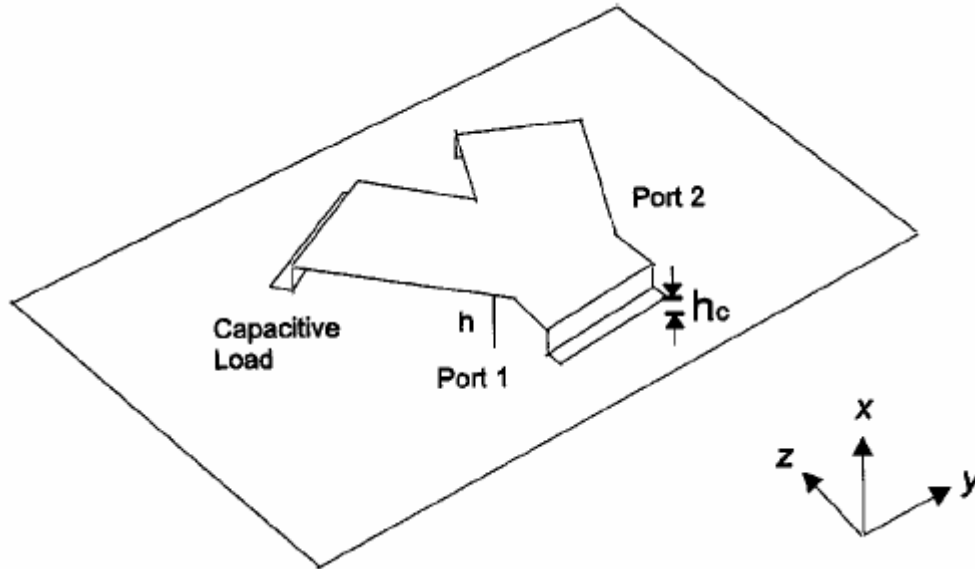


Figure 4: Capacitively Loaded Y-Patch Antenna from [6]

### 3. DUAL-SUBSTRATE CAPACITIVE LOADING TECHNIQUE

Our aim is to design a capacitive loading techniques and reduce the drawbacks that are present in the previous concepts. A novel capacitive loading technique that reduces the size of a shorted annular ring antenna is illustrated in Figure 5. This structure has several key features that control the capacitive loading. In this antenna, there are two separate substrates. The larger substrate is called the *radiator substrate*, and this material can consist of an RF substrate with a low dielectric constant and low loss tangent. The smaller substrate, contained beneath the capacitive patch, can be a high dielectric constant material and is referred to as the *capacitive substrate*. The capacitive patch is connected to the radiating SAR antenna through a capacitive loading ring which is a cylindrical structure located at the outer radius and perpendicular to the radiating and capacitive patches.

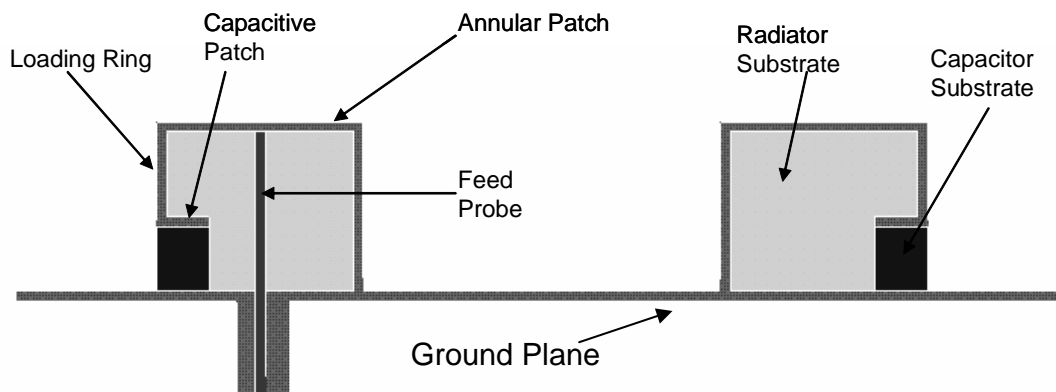


Figure 5: Cross-section of a probe fed edge-loaded SAR antenna with a capacitive patch for increased loading effect

The distance between the bottom of the loading ring and the ground plane is one key parameter in controlling the capacitance of the load. However, the inner radius of the capacitive patch and the dielectric constant of the capacitor substrate also impact the loading. For a parallel plate capacitor, the capacitance is determined by (4) [9], where  $S$  is the width of the plate,  $d$  is the separation between the plate, and  $\epsilon$  is the dielectric constant of the substrate. The capacitance of this loading technique behaves in a similar manner to a parallel plate capacitor; it can be increased by increasing the dielectric constant beneath the patch, decreasing the inner radius of the capacitive patch (i.e. increasing the radial width of the patch), and/or decreasing the distance between the ground plane and the capacitive patch. This provides the antenna engineer more design variables to use to control the size and performance of the antenna.

$$C = \epsilon \frac{S}{d} \quad (4)$$

#### 4. SIMULATED AND MEASURED RESULTS: TRADITIONAL SAR ANTENNA

Two SAR antennas were constructed to verify the proposed loading technique. First, a SAR operating at 3GHz – with no capacitive loading – was designed using CST Microwave Studio [2]. Then, the element was built and tested to verify the accuracy of the simulation software. The model used in the simulations is shown in Figure 6, and a photograph of the constructed element is shown in Figure 7. This element used a substrate from Polyflon Company called CuFlon. CuFlon is a polytetrafluoroethylene (PTFE) material plated with Copper. It has a dielectric constant of 2.1 and comes in various thicknesses. For this element, a 0.062” thick substrate was used. The dimensions of the element are presented in Table 1. The antenna had an outer radius of 0.87”; it was shorted at an inner radius of 0.25” using half-inch copper refrigeration pipe. The pipe was located in the hollowed out center and soldered to the radiating annulus as well as the ground plane.

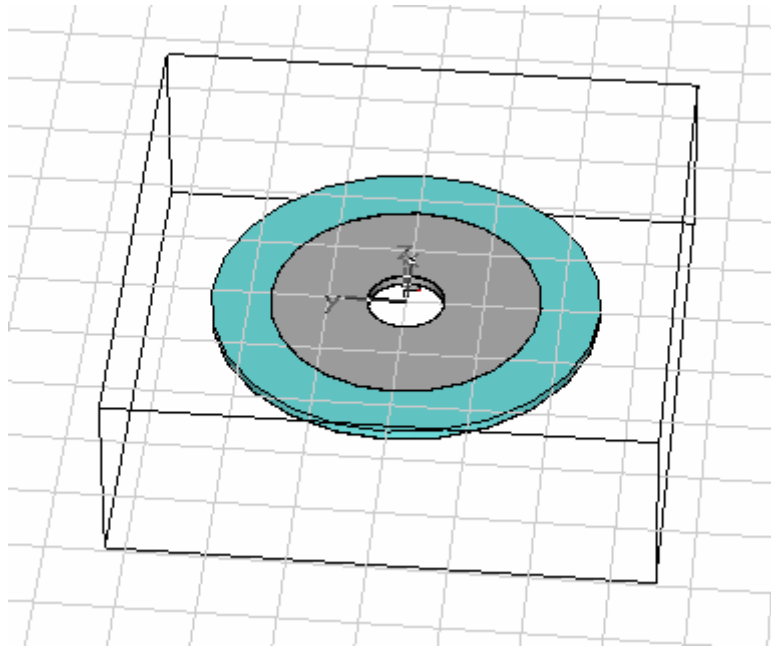


**Figure 6: CST Microwave Studio Model of 3GHz SAR Element**

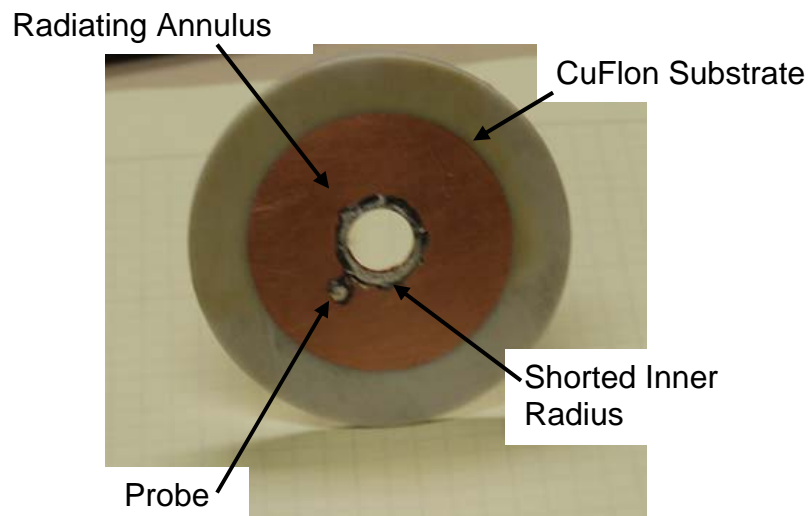


**Figure 7: Photograph of 3GHz SAR Element**

<i><b>Parameter</b></i>	<i><b>Value</b></i>
Radiator Outer Radius (a)	0.87"
Radiator Inner Radius (b)	0.25"
Feed Location	0.40"
Substrate Outer Radius	1.25"
Substrate Thickness	0.062"

**Table 1: Dimensions of Unloaded 3GHz SAR Antenna**



The measurements compared very favorably to the simulated results. The return loss of the simulations is compared to the measured results in Figure 8. This figure shows a 1.7% error between the measured and simulated resonant frequency. The E-plane and H-plane patterns are compared in Figures 9 and 10 respectively. The measured patterns were performed in the compact range at the Naval Research Laboratory, and the measured results show an excellent agreement with the simulated patterns from CST Microwave Studio.

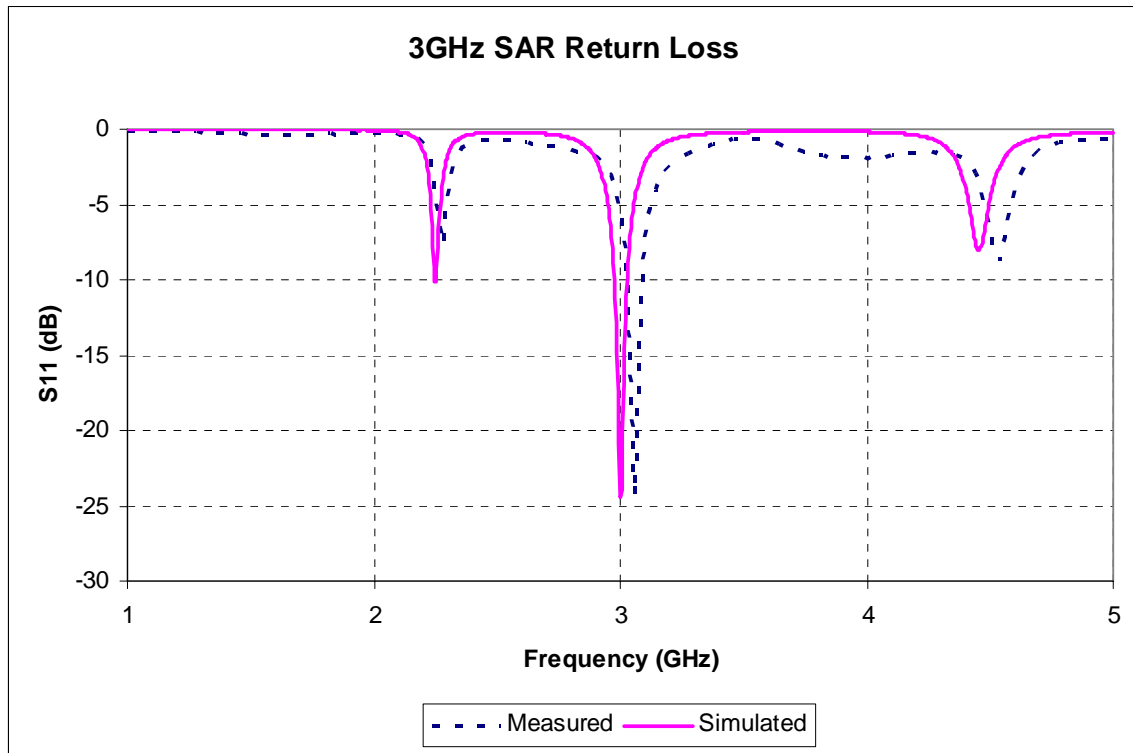


**Figure 8: Measured and Simulated Return Loss of 3GHz SAR Element**

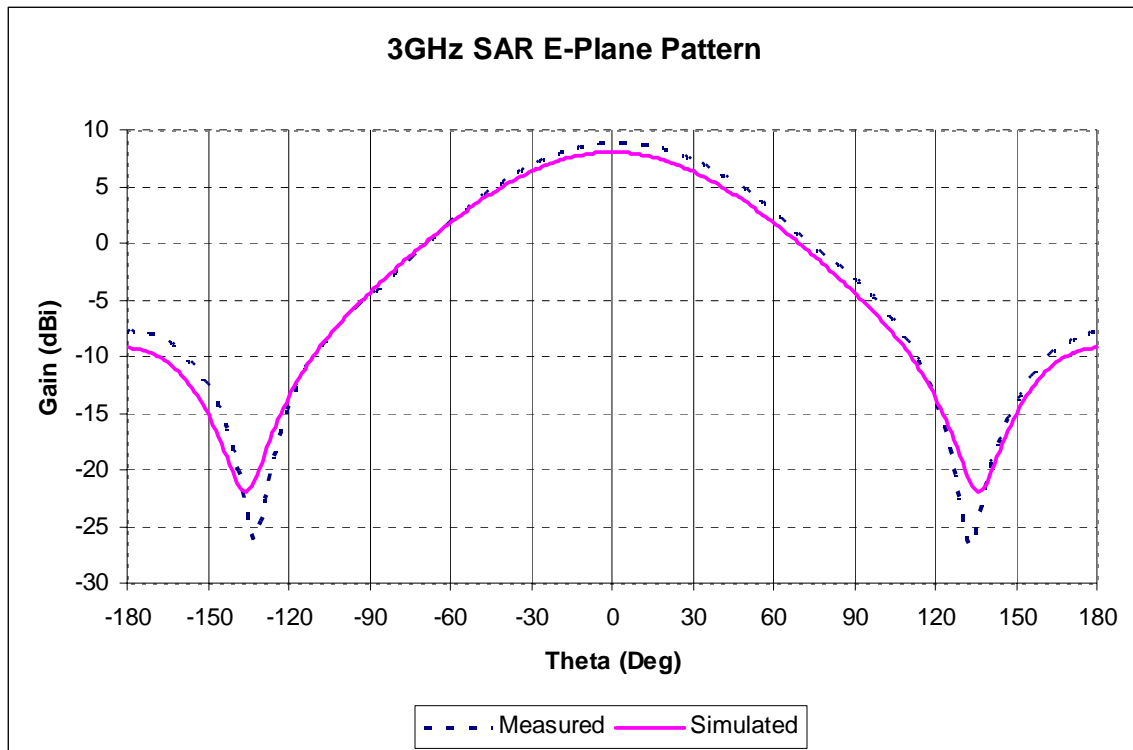


**Figure 9: Measured and Simulated E-Plane Pattern of 3GHz SAR Element**

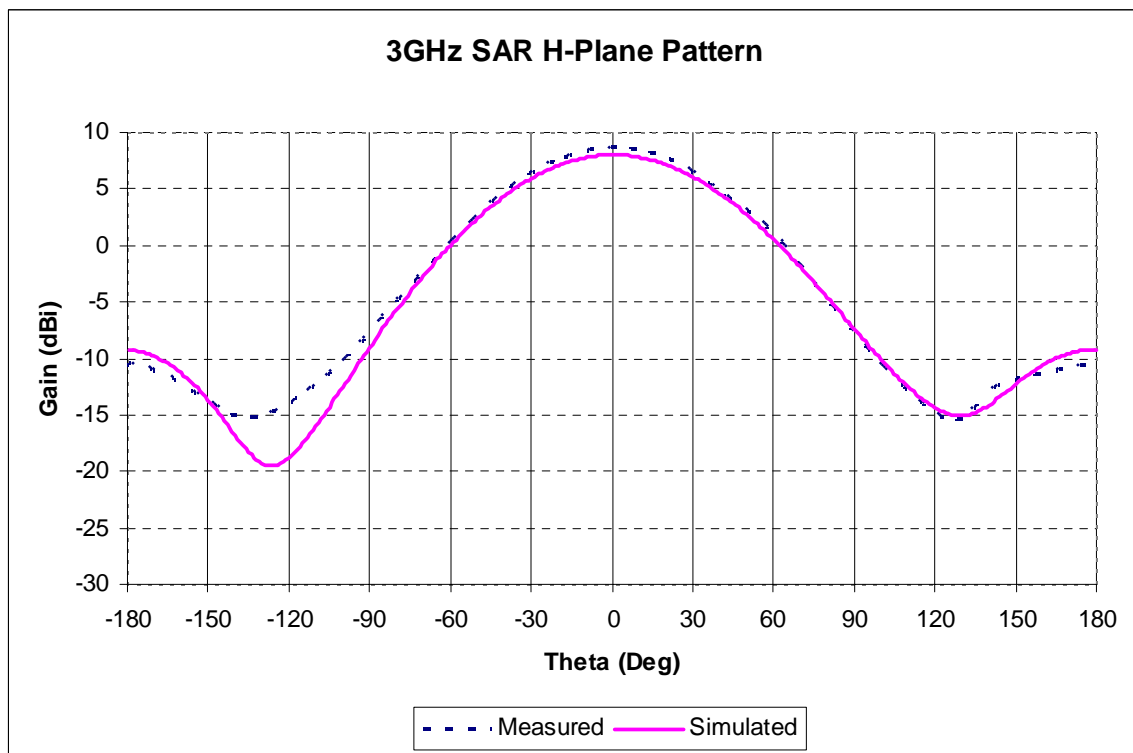


**Figure 10: Measured and Simulated H-Plane Pattern of 3GHz SAR Element**

## 5. SIMULATED AND MEASURED RESULTS: CAPACITIVELY LOADED SAR

Next, an element utilizing the proposed capacitive loading technique was simulated using CST Microwave Studio. Prior to performing the simulations, a fabrication process was decided upon to facilitate the construction of this element. That process consisted of three pieces for this element as shown in Figure 11. *Piece 1* used the low dielectric constant substrate. The radiating annular patch and capacitive loading patch were printed on the top and bottom of the piece, and they were connected by plated through holes around the outer edge of the patches. *Piece 2* is ring of the low dielectric constant material that will sit beneath *Piece 1*. Finally, *Piece 3* is a ring of the high dielectric material that will sit beneath the capacitive patch to serve as the capacitive substrate. *Piece 2* and *Piece 3* are then placed below *Piece 1*, a ground plane is placed on the bottom, and a conducting pipe is placed in the hollowed-out center. The conducting pipe is then soldered to the radiating annular ring and the ground plane to short the ring. Finally, a feed probe was placed 0.326" from the center of the element. The ground of the coaxial probe was shorted to the ground plane of the antenna, and the center conductor was shorted to the radiating annular ring. A photograph of these pieces is shown in Figure 12.

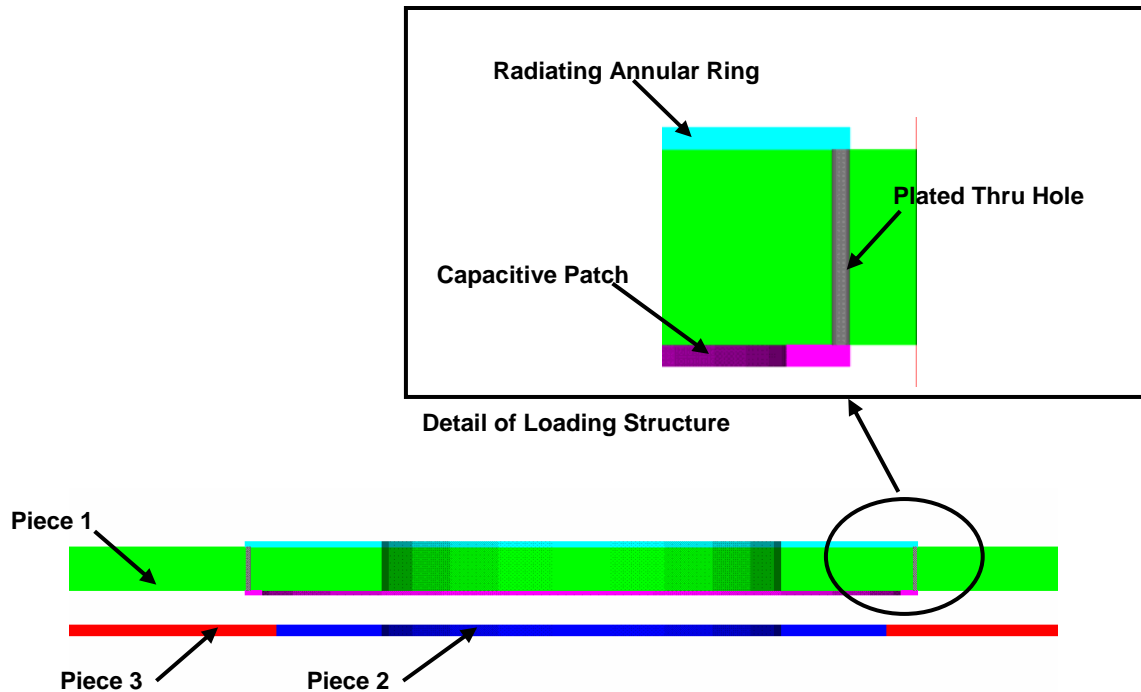
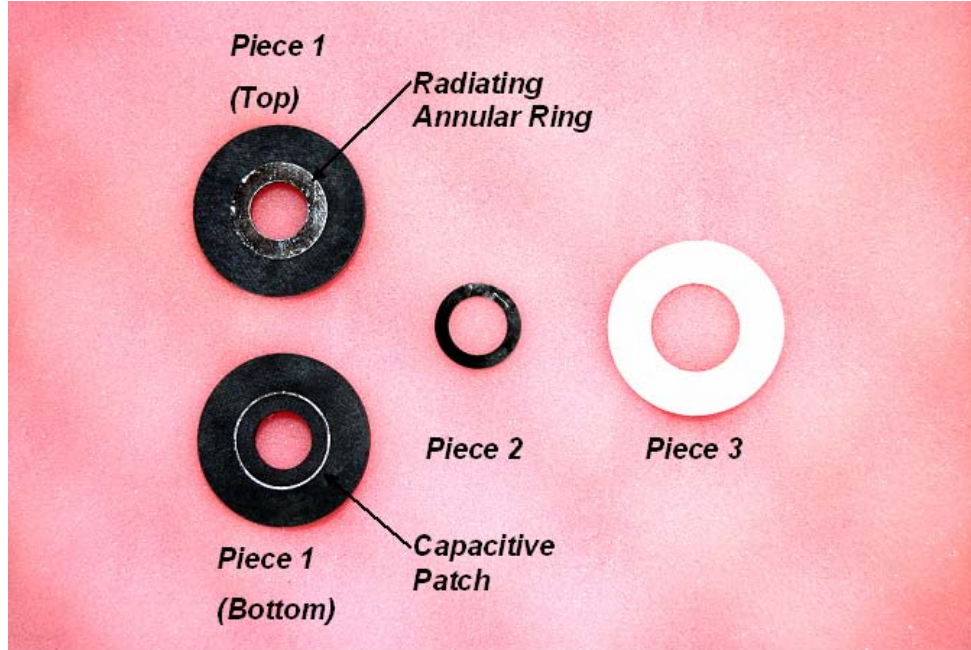


Figure 11: Diagram of Assembly Process for Capactively Loaded SAR Element



**Figure 12: Photograph of Capacitively Loaded SAR Pieces**

For this design, *Piece 1* and *Piece 3* were not truncated close to the edge of the patch to allow room for tuning the element and to simplify construction; working with skinny annular pieces of the high dielectric ceramic substrate is difficult in a laboratory environment due to the fragility of the material.

The two low dielectric constant pieces (*Piece 1* and *Piece 2*) were constructed on Rogers RT5880 ( $\epsilon_r=2.2$ ). *Piece 1* had a thickness of 0.062", and *Piece 2* had a thickness of 0.015". The high dielectric piece (*Piece 3*) was used as the capacitive substrate, and this piece was constructed out of 0.015" thick Rogers TMM10 ( $\epsilon_r=10$ ). The dimensions of all three pieces are shown in Table 2. This table shows an outer radius for the radiating element of 0.419". This radius is just over 48% of the outer radius for the radiator in the unloaded element. These two elements had the same inner radius and were constructed on substrates with very similar dielectric constants. Thus, the capacitive loading technique results in a size reduction of almost 52%.

	<b>Piece 1</b>	<b>Piece 2</b>	<b>Piece 3</b>	<b>Radiating Annular Ring</b>	<b>Capacitive Patch</b>
$r_{in}$	0.25"	0.25"	0.375"	0.25"	0.399"
$r_{out}$	0.75"	0.375"	0.75"	0.419"	0.419"

**Table 2: Dimensions of Capacitively Loaded 3GHz SAR Antenna**

Once the element pieces were constructed and assembled, the element performance was tested and compared to simulations. The simulations of this element showed a resonant frequency of 3 GHz. Figure 13 shows the initial return loss measurements showed a resonant frequency of 3.38 GHz representing a 12.6% deviation from the simulated results.

There are many variables in this design, and thus there are many sources for errors. One source of these errors is the uncertainty in the dielectric constant of the capacitive substrate. Rogers TMM10 has a nominal dielectric constant of 9.2, but the data sheet for this microwave substrate defines the dielectric constant to be  $9.2 \pm 0.23$ , which represents a possible 2.5% deviation.

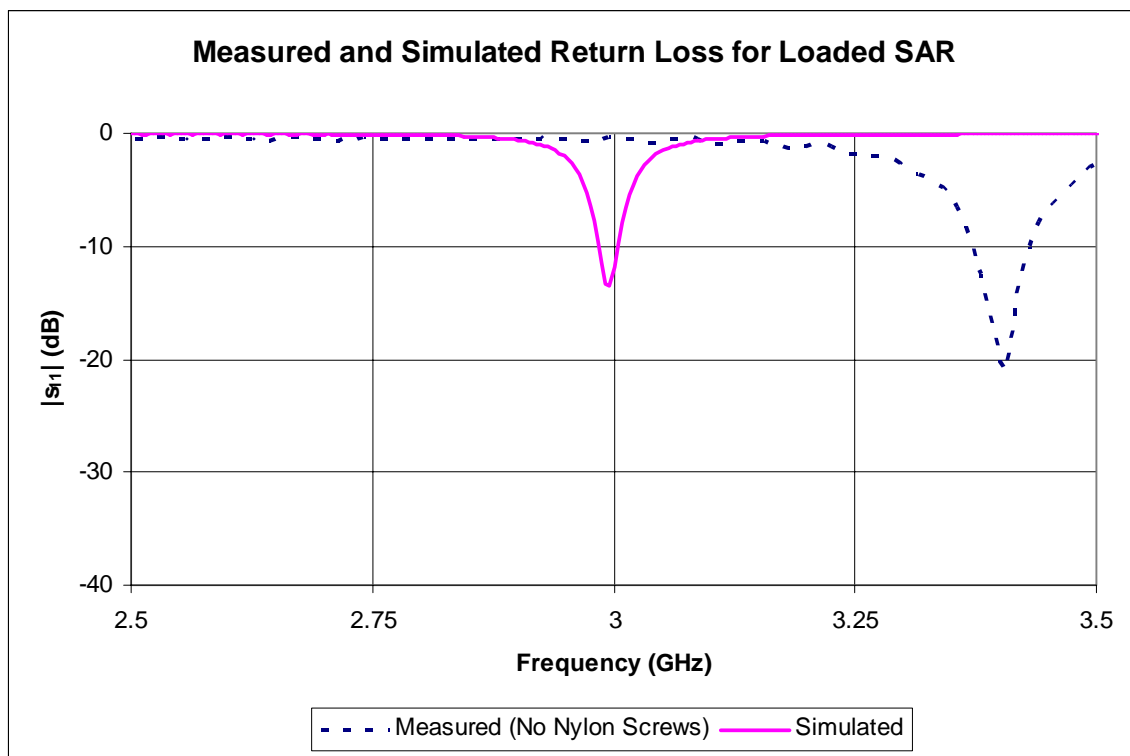


**Figure 13: Measured and Simulated Return Loss of Capacitively Loaded 3GHz SAR Element**

During the construction and measurement process, it was noticed that there were some small gaps between the pieces. These gaps were present between the bottom two pieces and the ground plane as well as between the top and bottom pieces. This was due to the small difference in thickness for *Piece 2* and *Piece 3* as well as some warping of the pieces. Two errors occur because these elements are not tightly bonded together. First, an increase in the distance between *Piece 1* and the ground plane increases the distance between the capacitive patch and the ground. Second, the addition of an air gap between the pieces and the ground plane adds air gaps into the capacitive substrate region which will decrease the effective dielectric constant of this region. Both of these problems will decrease the capacitance of the loading structure and increase the resonant frequency of

the antenna. Additional gaps can occur between *Piece 2* and *Piece 3*, which would result in a similar source of error in the effective dielectric constant. These sources of errors would contribute toward the discrepancy between the measured and simulated results of Figure 13.

In an attempt to alleviate this problem, nylon screws were inserted into the antenna as shown in Figure 14. These screws went through *Piece 1*, *Piece 3*, and the ground plane and were tightened down to hold the pieces together tightly. Initial measurements with the screws showed a higher resonant frequency than before (3.9GHz). The dielectric constant of the nylon screw is assumed to be in the range of 3.2-5, and this screw went through the high dielectric material. The presence of a low dielectric cylinder in the high dielectric substrate would lower the effective dielectric constant of the material, and subsequently result in a decreased capacitance. Thus, an increased resonant frequency of the antenna makes sense.

Since the effects of the nylon screws were not known, simulations were performed with the screws in place to see the impact. The model used in these simulations is shown in Figure 15. The results confirmed the fact that the presence of the screw increased the resonant frequency of the antenna. In the simulations, the resonant frequency increased from 3GHz to 3.22GHz when the screws were added.



**Figure 14: Photograph of Loaded SAR Antenna with Nylon Screws**

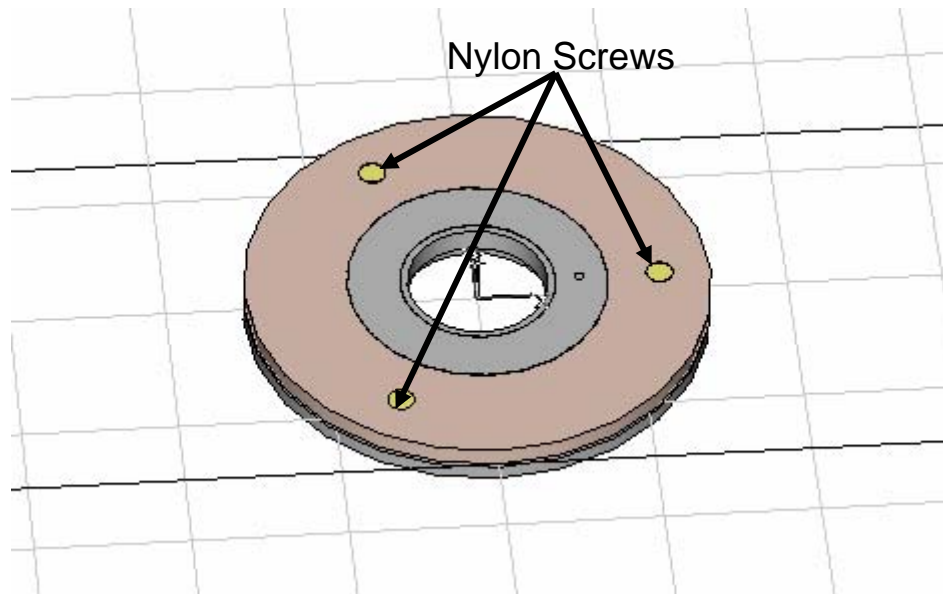


**Figure 15: CST Microwave Studio Model of Loaded SAR with Nylon Screws**

While the resonant frequency of the measured antenna increased in a similar fashion to the simulations, there was still a significant error of approximately 21% between the two results. An experiment was performed in which the screws were tightened several times. After each tightening, the return loss was measured and recorded. The results of three such measurements are shown in Figure 16. In this plot, each successive measurement corresponds to a tighter screw placement. From this plot it becomes evident that as the pieces are drawn closer together, the resonant frequency of the element decreases. The measured and simulated results are compared in Figure 17, and a 10% discrepancy is still present between the measurements and the simulations. This discrepancy could be due to a non-uniform tightening of the screws or gaps between *Piece 2* and *Piece 3* that could not be resolved in this manner. Moreover, the measured return loss indicates a loss in the range of 1-2 dB across the frequency band which will be discussed later in the section on antenna pattern measurements.

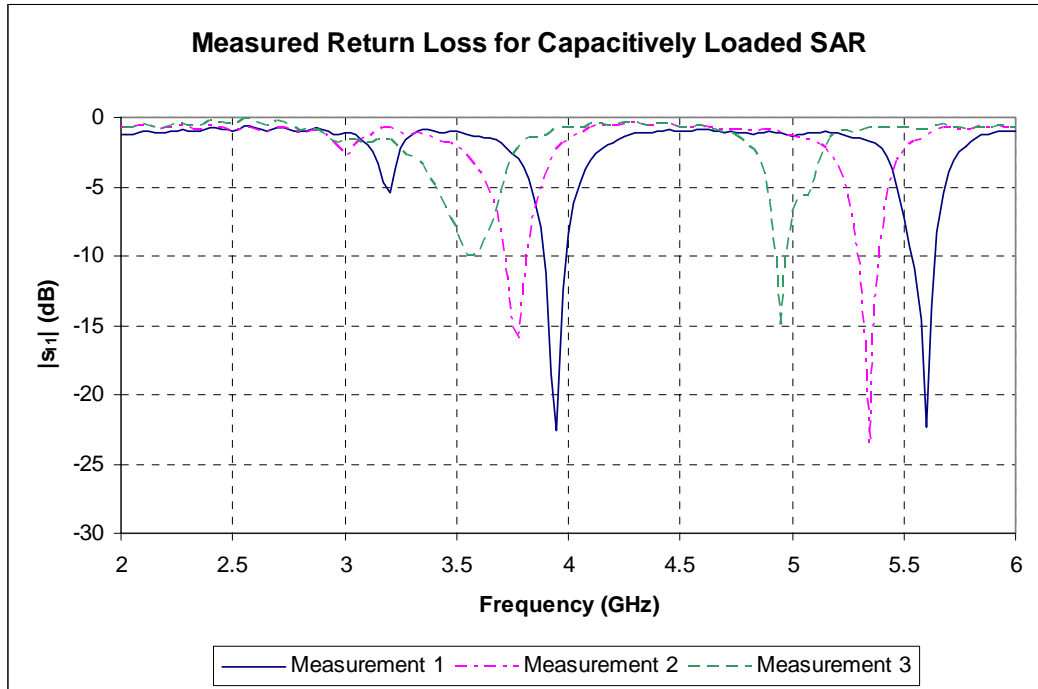


**Figure 16: Measured results of loaded SAR during the installation of the screws**

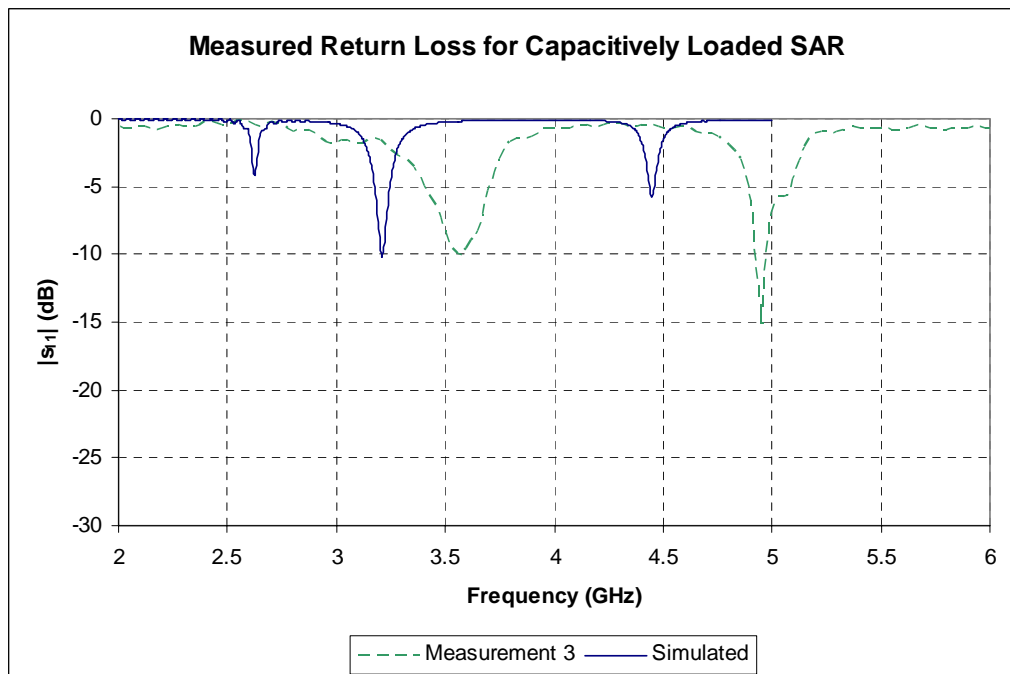


**Figure 17: Comparison of Measured and Simulated Results for Loaded SAR with Nylon Screws**



In Figure 18, the simulated and measured H-Plane radiation patterns at resonance are compared. For these plots, the gain is normalized to 0dB to compare the pattern shape. The measured antenna showed a lower gain than the simulated radiation patterns. There is a loss mechanism in the constructed antenna that was also seen in the return loss measurements shown in Figure 17. Additionally, since the resonance of the antenna is so narrow in frequency, a measurement just off of the resonant frequency would have a poor match that would degrade the gain. However, the comparison of Figure 18 shows a good agreement between the shapes of the simulated and measured H-Plane radiation patterns. A small ripple is present in the measured pattern for wide values of the theta due to an interaction between the backlobe of the antenna and the mixer and cables that were used in the measurement procedure.

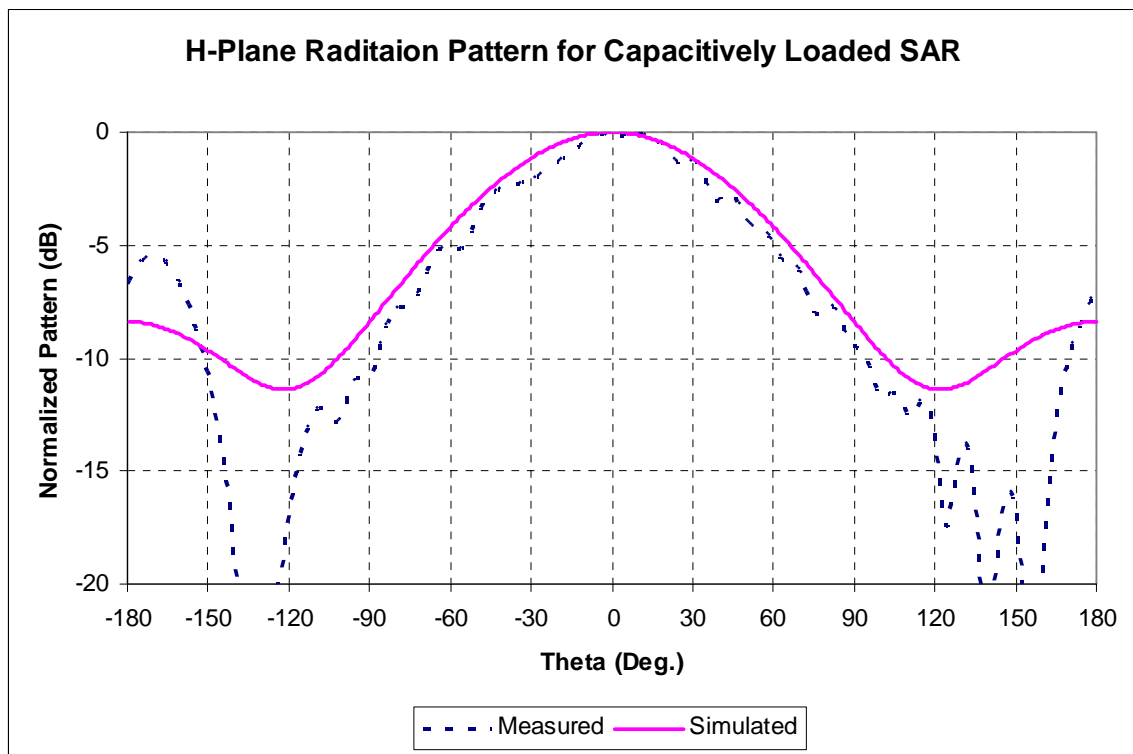


**Figure 18: Comparison of Measured and Simulated H-Plane Pattern for Loaded SAR**

The element that was constructed used a capacitive patch with a 0.020" radial width. Additional size reduction can be achieved with an increase in the width of this patch. Figure 19 shows the results of a parametric study where the width of this patch is increased. For this study, all variables were kept the same, but the radial width ( $dr$ ) of the patch was varied. From this figure, it can be seen that increasing  $dr$  resulted in a lower resonant frequency of the structure. To shift the resonance back to the desired frequency of 3 GHz, the outer radius of the structure has to be reduced. From these curves, it can be seen that increasing  $dr$  is a way to increase the capacitance and decrease the size of the antenna.

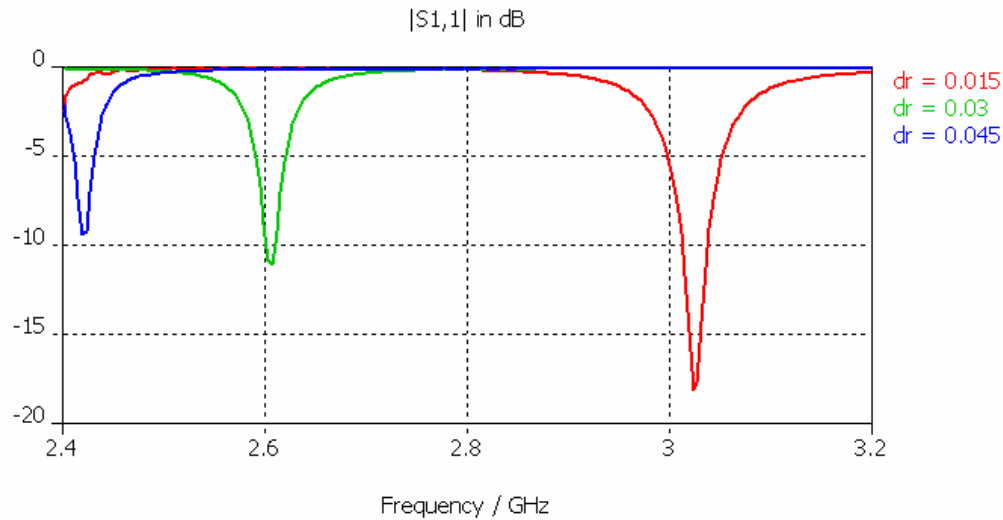


**Figure 19: Simulated results of parametric study exploring impact of capacitive ring radial thickness ( $dr$ )**

## 6. CONCLUSION

A multi-substrate capacitive loading technique has been proposed that provides the antenna engineer with a wide range of variables that can be used to reduce the size of a shorted annular ring (SAR) antenna. A high dielectric constant material can be used beneath a capacitive loading patch, while the remaining substrate can be a low dielectric constant material. This minimizes some of the problems – such as low efficiency, excitation of surface waves, cost, and uncertainty in dielectric constant – that are inherent in designs using high dielectric material beneath the entire radiating structure.

A traditional SAR antenna and a capacitively loaded SAR antenna were simulated using CST Microwave Studio. These elements were then built and tested. The measure results for the capacitively loaded SAR antenna had a 12.6% discrepancy when compared to the simulated results because the elements were not tightly bonded together. When the element was modified to eliminate the gaps between the pieces and the ground plane, the measured and simulated results had a closer agreement. Throughout the experimental procedure, it was seen that the bonding between the pieces is critical in establishing a good performance in the antenna.

Through simulations, this loading procedure has been seen to achieve a size reduction of greater than 50% compared to the unloaded element. Additional work is planned to assemble an element with the gaps minimized to hopefully bring measurements and simulations in closer agreement. But, at the time of this report, this study had not been completed. Although the simulations and measurements performed in this study involved a linearly polarized element, the circular symmetry in this element would allow for the

addition of an orthogonal feed (or three more feeds spaced by  $90^\circ$ ) to allow for dual-linear or circular polarization.

- [1] S. Jiang, D.R. Jackson, S.A. Long, J.T. Williams, and V.B. Davis: “Characteristics of the Shorted Annular-Ring Patch Antenna”, IEEE AP- International Symposium, Vol. 2, 11-16 July 1999, pp.814 – 817.
- [2] CST Microwave Studio, v. 2006.0.0.
- [3] H. Kan, R. Waterhouse, and D. Pavlickovski: “Compact Dual Concentric Printed Antennas”, IEE Proc. – Microw. Antennas Propag., Vol. 151, No. 1, Feb. 2004 pp. 37-42.
- [4] C.B. Ravipati and A.I. Zaghloul, “A Hybrid Antenna Element for Dual-Band Applications”, IEEE AP-S International Symposium, Vol. 4, June 2004, pp. 3412-3415.
- [5] P. Ciaisi, R. Staraj, G. Kossiavis, and C. Luxey, “Compact internal multiband antenna for mobile phone and WLAN standards”, Antennas and Wireless Propagation Letters, Vol. 2, Issue 1, 2003, pg. 143-146.
- [6] Samuel C. K. Ko and Ross D. Murch, “Compact Integrated Diversity Antenna for Wireless Communications”, IEEE Transactions on Antennas and Propagation, Vol. 49, No. 6, June 2001, pg. 954-960.
- [7] Corbett R. Rowell and Ross D. Murch, “A Capacitively Loaded PIFA for Compact PCS Handsets”, IEEE Transactions on Antennas and Propagation, Volume 45, Issue 5, May 1997, pg. 837-842.
- [8] Fan Yang, Chul-Sik Kee, and Yahya Rahmat-Samii, “Step-Like Structure and EBG Structure to Improve the Performance of Patch Antennas on High Dielectric Substrate”, IEEE AP-S International Symposium, Volume 2, 8-13 July 2001, pp. 482-485.
- [9] David K. Cheng, Field and Wave Electromagnetics: Second Edition, Addison-Wesley Publishing Company: New York, 1992, Page(s):121-123.

# A connector design for coplanar waveguide

Youn M. Lee  
Electronics Engineer  
U.S. Army Research Laboratory  
2800 Powder Mill Road  
Adelphi, MD 20783  
[ylee@arl.army.mil](mailto:ylee@arl.army.mil)

Theodore K. Anthony  
Electronics Engineer  
U.S. Army Research Laboratory  
2800 Powder Mill Road  
Adelphi, MD 20783  
[tanthony@arl.army.mil](mailto:tanthony@arl.army.mil)

**Abstract:** A Coplanar Wave Guide (CPW) connector for a wafer was designed by modifying an existing a commercially available connector designed as an end-launcher. The modification was specifically aimed at the CPW operating in K-band, but the new design can be used at other frequency bands. The focus of the design was to match input impedance for a very wide range of frequency, which was carried out by using a Finite Element Code, HFSS (High Frequency Structure Simulation).

## 1. Introduction

As the size of an antenna and an associated electronic system become smaller, a wafer level antenna and a CPW will become attractive to more antenna designers due to fabrication challenges imposed by very tight tolerances. The CPW, which was proposed by Wen [1] in 1969, can be used at extremely high frequency. It is particularly attractive in a microwave-integrated circuit (MIC) and a monolithic microwave-integrated circuit (MMIC) design since they can be easily integrated with active devices without the need for via holes [2]. An antenna can be directly connected to circuits via the CPW, thereby eliminating a need for a connector and a coaxial cable. However, one usually needs a connector for the CPW to check the performance of the antenna before integrating it to the system. Nonetheless, existing and commercially available connectors are not well suited for the CPW on a wafer. According to several published papers, researchers have used a probing station to inject a signal [3, 4]. However, the probing station has to be placed very close to the antenna, creating unwanted coupling or interference. By using the newly designed connector, one can readily measure a radiation pattern in an anechoic chamber without much interference. It was discovered that J. Chramiec, Technical University of Gdansk, and J.K. Piotrowski, Warsaw University of Technology, have characterized coaxial to microstrip transitions, and developed equivalent circuits of two SMA-microstrip connectors. Based on that work, they, along with B. Janiczak, J. Komisarczuk, W. Gwarek, developed CAD (Computer Aided Design) models of connectors and transitions used in a hybrid microwave integrated circuits, feeding CPW [5, 6].

## 2. Characterization and Modeling

The jack receptacle – edge mount (end launcher) designed for 0.062” thick circuit board was modeled using the three dimensional Finite Element Code, HFSS. The purpose was to modify the connector suitable for CPW on a wafer, 8 mm by 8 mm, with an antenna fabricated on the bottom of it. To analyze the end launch connector before the modification, 17 mm by 17 mm wafer was used to analyze the performance of the end launcher. Figure 1a shows the connector placed on either end of the CPW with two ground contact tabs. Each tab is 4.5 mm long, 2.25 mm wide and 1.02 mm high. The gap between them is 1.7 mm wide, and the center conductor is placed at the center of the gap with Teflon dielectric material around it. The outer diameter of the Teflon dielectric material is 1.264 mm, and the dielectric constant is 2.08. The center conductor is 0.38 mm in diameter and 0.76 mm long. As shown in figure 1b, the connector has an extrusion on the bottom, originally designed to hold a circuit board. The end view of the connector is shown in figure 1c along with a wafer board, which is 17 mm wide, 17 mm long and 0.5 mm thick. It is made of silicon and the dielectric constant is 11.9. The wafer board has SiO<sub>2</sub> film, 2000 Å thick, coated on the front side and the backside surface of the wafer. The CPW is made of gold, the centerline is 0.56 mm wide, and its gap between the ground plane and the centerline is 0.28 mm. The gold is 7300 Å thick. Modeling the connector and the wafer board was fairly straight forward, but the SiO<sub>2</sub> film was too thin compared to the wavelength of interest around 20 GHz, and therefore, it was not included. However, its effects may not be significant since its dielectric constant is fairly low ( $\epsilon_r = 4$ ) and its thickness is only  $1.3 \times 10^{-5}$  relative to the wavelength at 20 GHz. One of the difficult items to model using the computer simulation is a soldering joint. A few different types of joints were tried as a part of this work. Since the ground contact tabs of the end launcher provide good contact surfaces, solder joints were not used at these surfaces. The center conductor was modeled as a cylindrical rod with the flat end as the first simulation model. This design provides a fine line of contact surface with the CPW. As expected, the simulated model, the end launchers and the CPW, did not appear to be working properly, clearly shown by the return loss (S11), shown in figure 2a, and the transmission loss (S21), shown in figure 2b. Thus, the computed results showed that the model generates an appreciable amount of radiation rather than acting as a transmission line and connectors. Therefore, it was first suspected that it is caused by inadequate contact between the center conductor of the end launcher and the CPW centerline.

To pinpoint the source of the radiation, the wafer, extrusions on the bottom of the end launchers, ground contact tabs, and a portion of the center conductors, short pins that provide contact surface between the CPW and the end launchers, were removed. Therefore, the model has two short coaxial sections butted against each other, as shown in figure 3a. Computed S11 and S21 shown in figure 3b and 3c, prove that the short sections of the coaxial sections are working properly. Figure 3d shows the radiation pattern of the short section coaxial model. Also shown in the figure 3d, total radiated electric field times the distance,  $r$ , is 0.23 volt, radiation efficiency is 0.08, and maximum radiated power is 0.5 milliwatt. Input was one volt into the 50-ohm line.

Next, removed elements of the end launcher and the wafer were restored, and a solder joint was added as follows: an image of the circular end section of the center conductor was rotated ninety degrees, creating a right angle solder joint as shown in figure 4a. The S11 in figure 4b surprisingly shows that the additional contact surface does not solve the problem, or the additional contact surface is still inadequate. Computed radiation pattern, displayed in figure 4c, shows that the radiated total electric field times a distance  $r$  ( $rE_t$ ) is about ten times higher than that of the two short coaxial sections (see figure 3d). Another attempt was made to increase the contact surface of the center conductor by uniting rectangular gold material to the bottom portion of the center conductor as shown in figure 5a. In addition, to minimize the scattering by the end launch connector, the radius of the coaxial section and outer edges of the ground contact tabs were reduced to bare minimum, 4.44 mm, without weakening the coaxial wall too much (see figure 5b). Further, lengths of the ground tabs were reduced to 2.5 mm from their original lengths of 4.55 mm, and it was tapered down. Figure 4c indicates most of the energy was radiated toward the bottom of the wafer/connector when the solder joint was only a circular right angle. Consequently, the extrusion on the bottom of the end launcher was removed to remove the scattering from the extrusion. Computed S21 shown in figure 5d points out some energy was radiated, though very low in intensity. Computed S11 shows (see figure 5c) some improvement around 19 GHz, but the return loss was approximately reduced from -20 dB to -17.5 dB around 21 GHz. However, radiation patterns, figure 5e, confirm that most of the energy was transmitted through the CPW. Notice that the quantity  $rE_t$  is approximately 0.037 volt, smaller than those of the short coaxial sections butted against each other.

Finally, the additional rectangular contact material was removed, and the resulting computations were shown in figures 6a (S11), 6b (S21), and 6c (Smith Chart). The range of the frequency was reduced for detailed view around 20 GHz, showing the return loss of -38 dB at 20.7 GHz. Insertion losses at this frequency, (see figure 6b) was -0.32 dB.

### 3. Fabrication and Measurements

To verify the simulated results, three pieces of the CPW line were fabricated on a wafer, 8 mm by 8 mm, and the modified end launchers were attached using silver-loaded epoxy. Initially, efforts were made to attach the end launcher using solder, but failed. As it turned out, the silver loaded epoxy is not strong enough to withstand the force exerted by a flexible coaxial cable attached to a network analyzer. The first one broke at the bonded surface, and therefore, it was repaired with additional silver loaded epoxy, and epoxy was added on the bottom edge of the end launcher/wafer. This time wafer was broken around the ground contact tabs during the measurement setup. Second wafer was shattered during the setup.

On third wafer, a little more epoxy was applied to the bottom edge of the wafer/end-launcher contact surface to ensure good bonding, leaking to the center pin area on the other side. Using a knife with a fine blade, the epoxy covering the center pin, the ground contact tabs, and the wafer was removed as much as possible. An ohmmeter was used to measure resistance from end to end to get a feel of silver epoxy at DC. Results of the

ohmmeter measurements are shown in table 1. Direct current (DC) resistance from the center conductor to the center conductor was 0.74 ohm, and the outer conductor of the first end launcher to the outer conductor of the other end launcher was 0.02 ohm after probe resistance, 0.2 ohm, was taken out. These values indicate DC resistance of the silver epoxy applied at the interface between the end launchers and the CPW. The end launchers/wafer was connected to a Wiltron network analyzer model 37269A. However, the wafer broke again, but four data points at markers were written down as shown in table 2. Comparison with simulated data at 19 GHz and 20 GHz shows differences of 0.04 dB and 0.95 dB. These values are very good despite the epoxy accident.

The modified end launcher was connected to CPW with an antenna on the opposite side. Figure 7a shows a return loss as a function of frequency from 18 GHz to 22 GHz, and Figures 7b and 7c show pictures of the modified end launcher/antenna, next to a dime. Figure 7d shows dimensions of the CPW and the antenna. Length of the CPW is 4.7 mm.

#### 4. Conclusion

A commercially available edge mount connector was successfully modified for wafer level CPW applications. Computed radiation pattern was crucial in pin pointing the problem area. In addition, creating a contact surface as a solder joint plays an important role.

A silicon wafer is very brittle, requires careful handling, and is difficult to bond using adhesives or epoxy. However, super glue provides strong bond to the silicon wafer, and therefore, the superglue maybe used to bond the ground tabs to the CPW, and then apply silver-loaded epoxy to provide electrical connection.

#### 4. References

- [1] Wen, C.P., "Coplanar Waveguide: A Surface Strip Transmission Line Suitable for Non-Reciprocal Gyro magnetic Devices Applications," IEEE Trans., Vol. MTT-17, 1969, pp. 1087-1090.
- [2] Coplanar waveguide fed quasi-Yagi antenna, Sor, J.; Yongxi Qian; Itoh, T.; [Electronics Letters](#) Volume 36, ssue 1, 6 Jan. 2000 Page(s):1 - 2 Digital Object Identifier 10.1049/el:20000132
- [3] E.A. Soliman, S. Brebels, P. Delmotte, G.A.E. Vandenbosch and E. Beyne, " Bow-tie slot antenna fed by CPW", Electron. Lett., 1999, Vol. 35, (7), pp. 514-515.
- [4] Rainee Simons, N., and Richard Q. Lee, "ON-Wafer Characterization of Millimeter-Wave Antennas for Wireless Applications, IEEE transactions on Microwave Theory and Techniques, vol. 47, No. 1, 1999, pp. 92-96.



[5] J. Chramiec, and J.K. Piotrowski, "Novel Approach to the Characterization of Coaxial-to-Microstrip Transitions", Proc. 27<sup>th</sup> Europ. Microwave Conf., 1997 Vol. 2, pp. 697-702.

[6] J. Chramiec, B. Janiczak, J. Komisarczuk, J.K. Piotrowski, W. Gwarek, "CAD Models of Connectors and Transitions used in Hybrid Microwave Integrated Circuits", European Microwave Conference, 1998, 28th, Volume: 1, On page(s): 457-462.

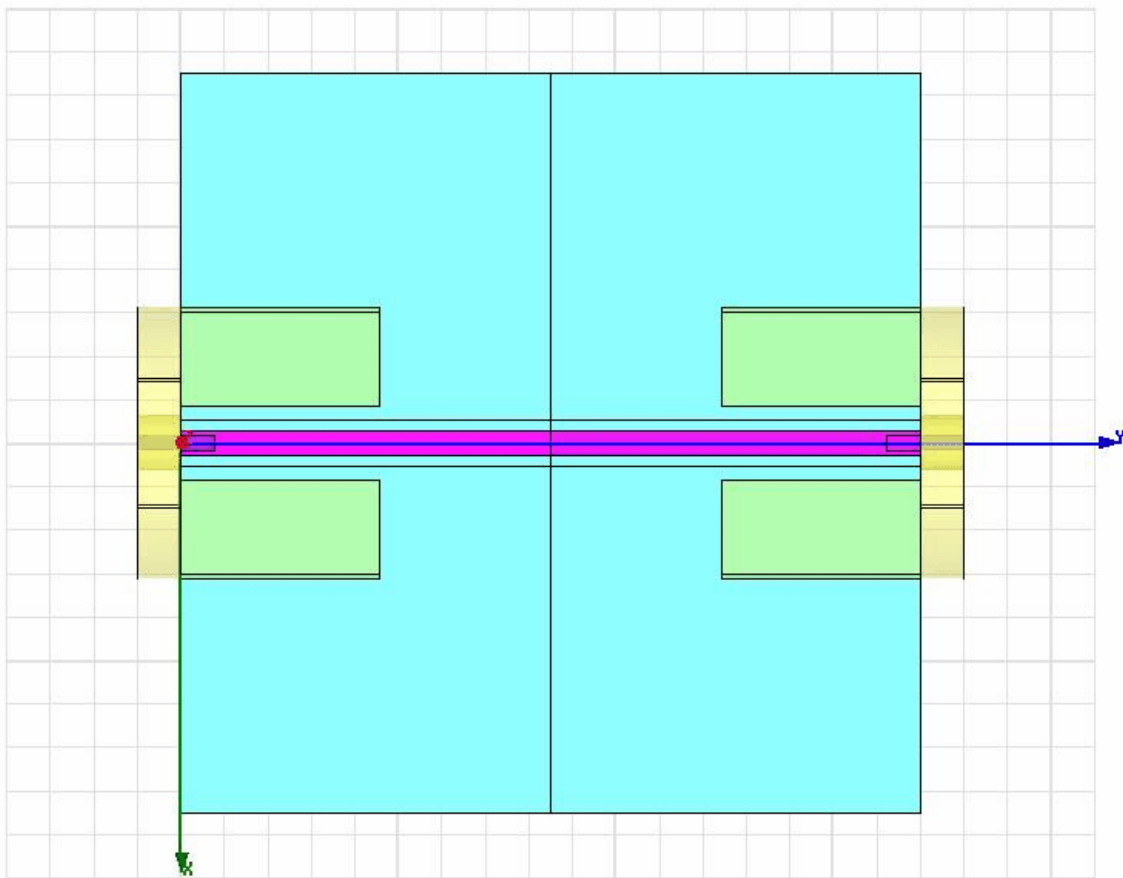


Figure 1a. Plan view of the connector placed on either end of the CPW with two ground contact tabs. Each tab is 4.5 mm long, 2.25 mm wide and 1.02 mm high. The gap between them is 1.7 mm wide, and the center conductor is placed at the center of the gap with Teflon dielectric material around it. The center conductor is 0.38 mm in diameter and 0.76 mm long. The wafer board is 17mm wide, 17 mm long and 0.5 mm thick. It is

made of silicon and the dielectric constant is 11.9. The silicon wafer board has  $\text{SiO}_2$  film coated on the front and backside of the surface and 2000 Å thick. The CPW is made of gold, the centerline is 0.56 mm wide, and its gap between the ground plane and the centerline is 0.28 mm. The gold is 7300 Å thick.

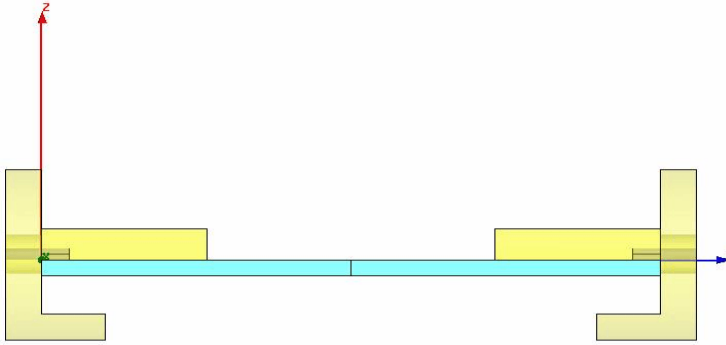


Figure 1b. Side view of the setup. The end launcher has an extrusion on the bottom, originally designed to hold a circuit board.

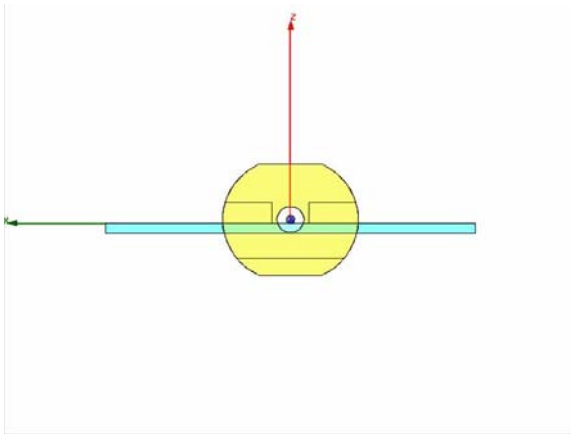


Figure 1c. End view of the setup. The outer diameter of the Teflon dielectric material is 1.264 mm, and the dielectric constant is 2.08.

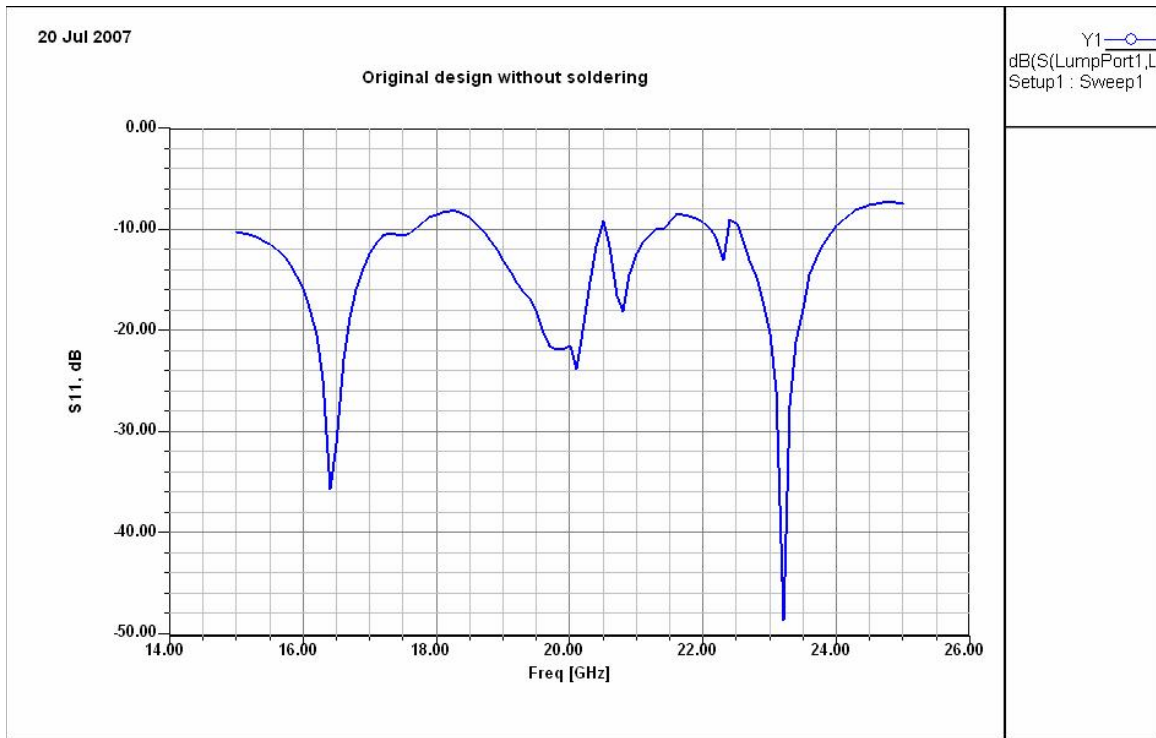


Figure 2a. Computed return loss (S11) of the setup as a function of frequency, shown in figure 1.

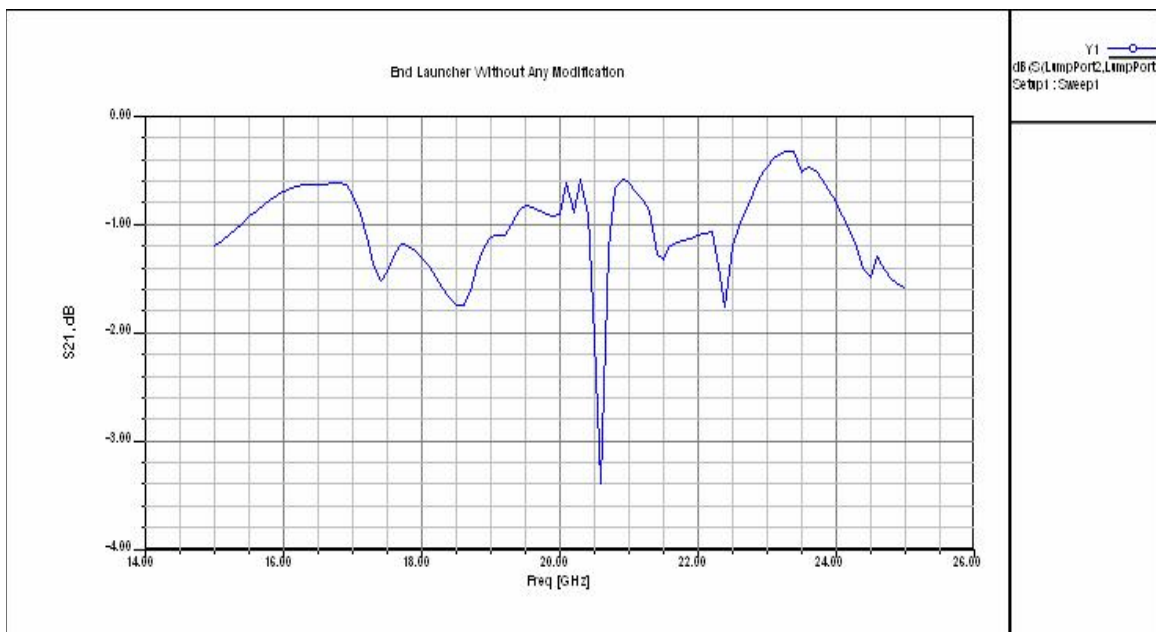


Figure 2b. Computed transmission loss (S21) as a function of frequency.

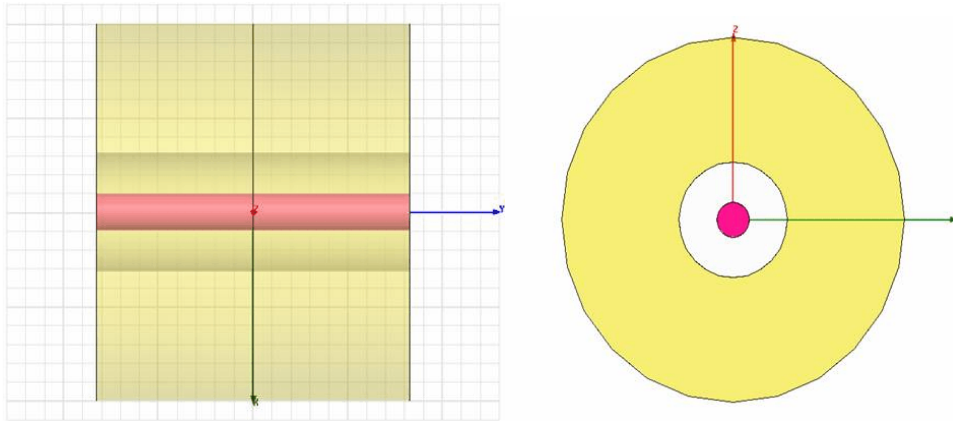


Figure 3a. A side and an end view of two short coaxial sections butted against each other for a baseline simulation.

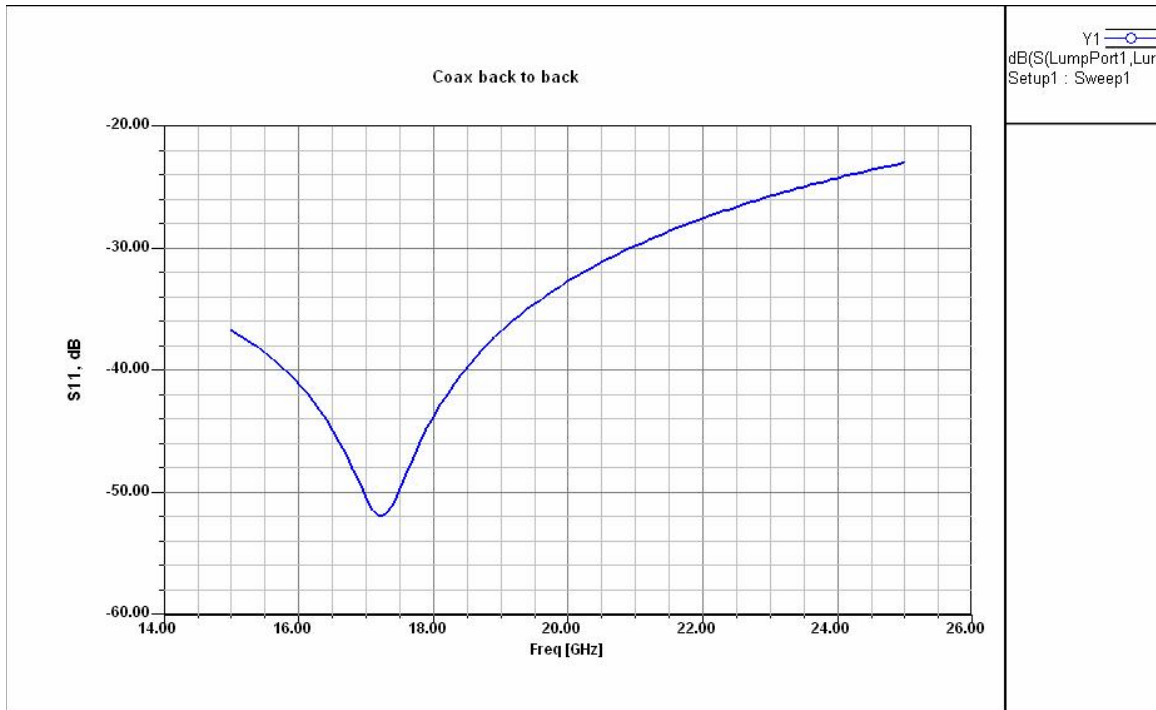


Figure 3b. Computed S11 for the setup shown in figure 3a as a function of frequency.

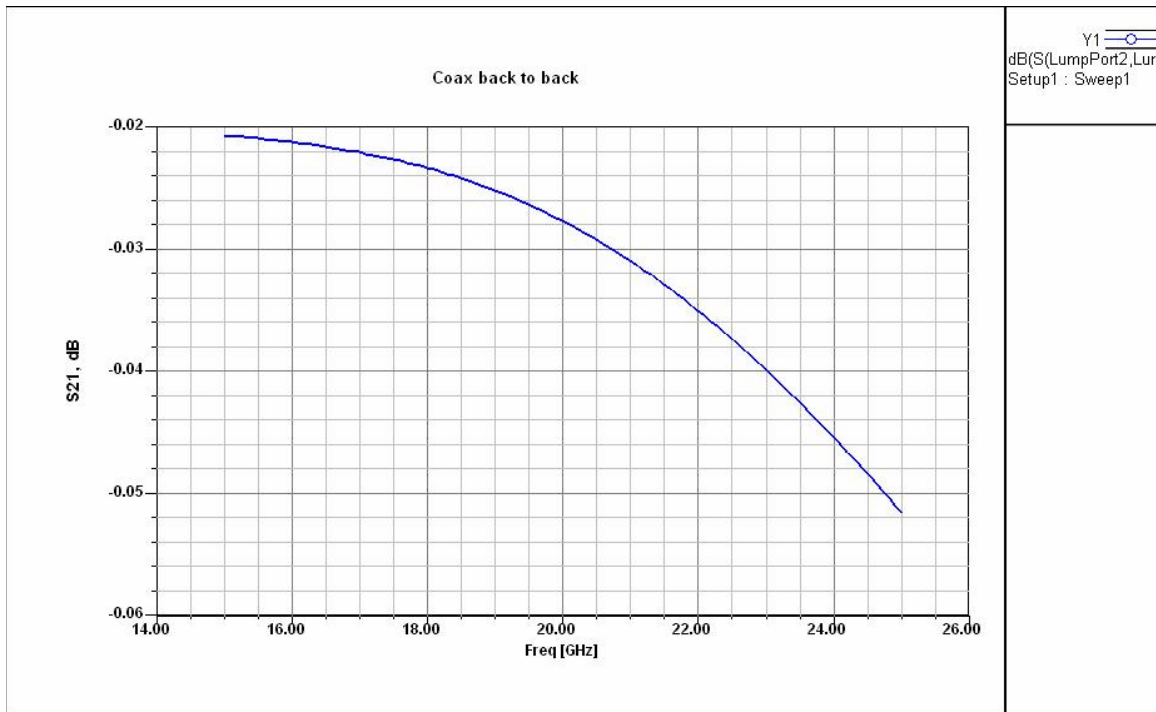


Figure 3c. Computed S21 for the setup shown in figure 3a as a function of frequency.

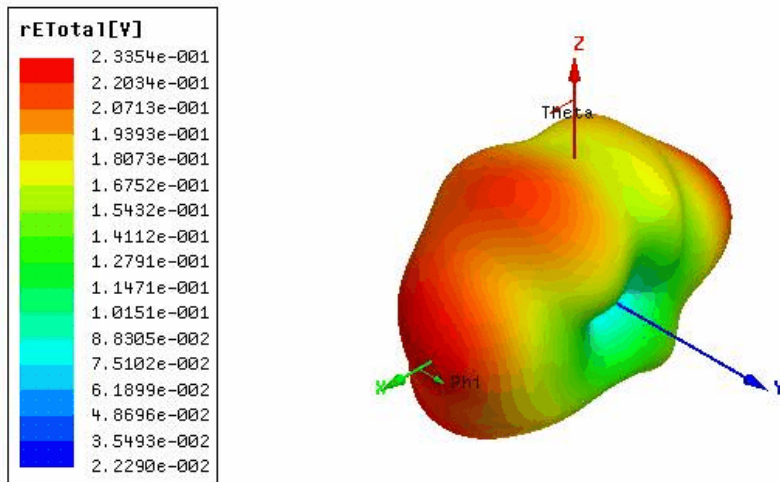


Figure 3d. Radiation pattern of the setup shown in figure 3a. Total electric field times the distance  $r$ ,  $rE_t$ , is 0.23 V, and radiation efficiency is 0.08, and maximum radiated power is 0.5 mW. Input voltage is one volt.

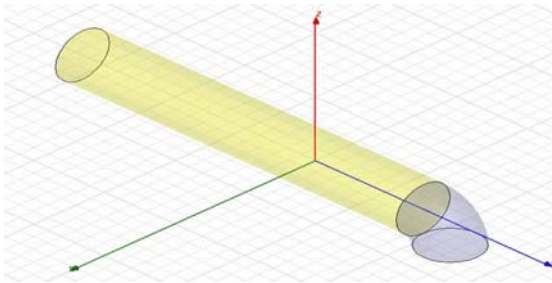


Figure 4a. An image of the circular end section of the center conductor was rotated ninety degrees, creating right angle gold cylinder as a solder joint.

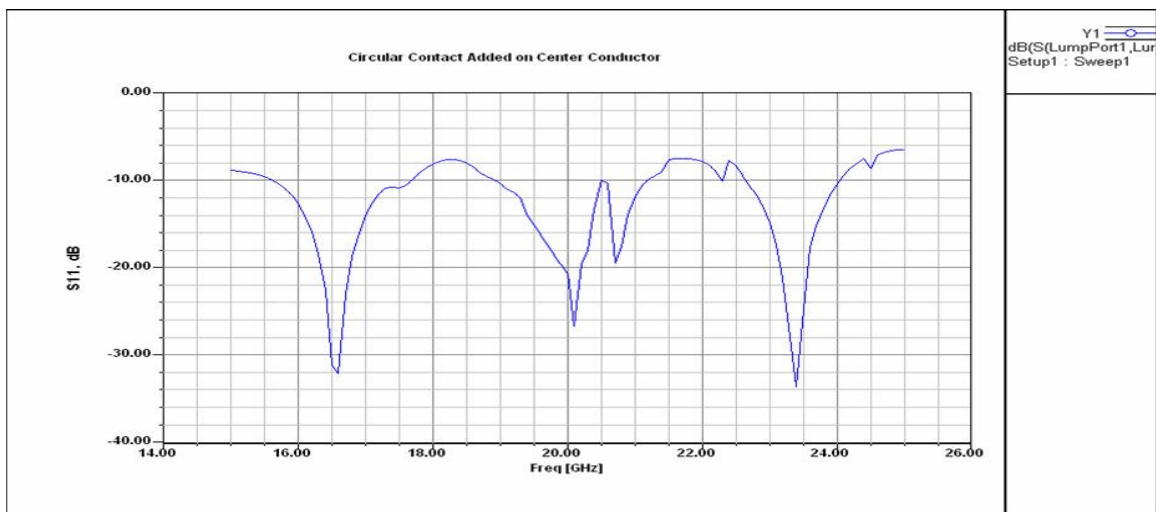


Figure 4b. Computed S11 after adding right angle as solder joint, which did not affect the S11 response very much.

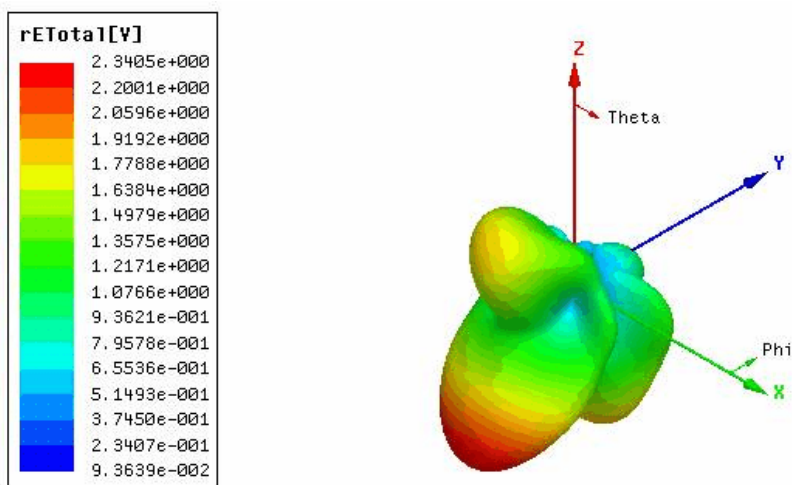


Figure 4c. Radiation pattern of the previous setup plus a right angle solder joint as shown in figure 4a. Computed  $rE_t$  is about ten time higher than that of the two short coaxial sections (see figure 3a).

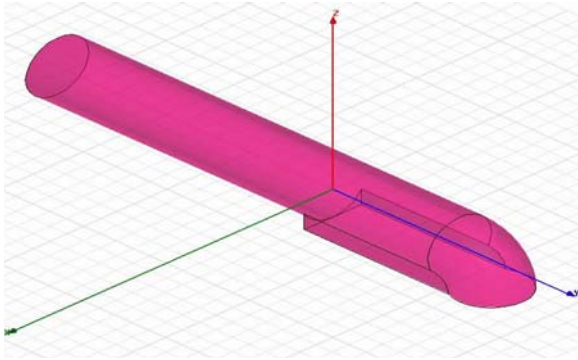


Figure 5a. To increase contact surface of the center conductor a rectangular gold material was united to the bottom portion of the center conductor.

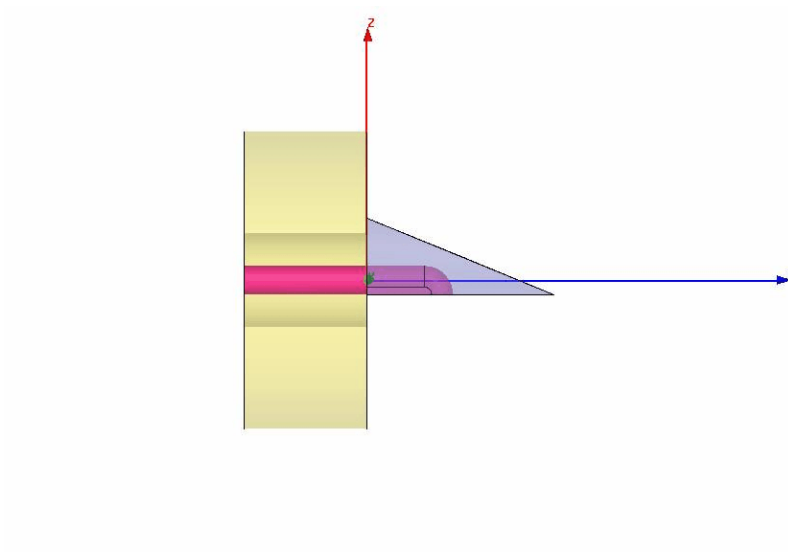


Figure 5b. Lengths of the ground tabs were reduced to 2.5 mm, and they were tapered down.

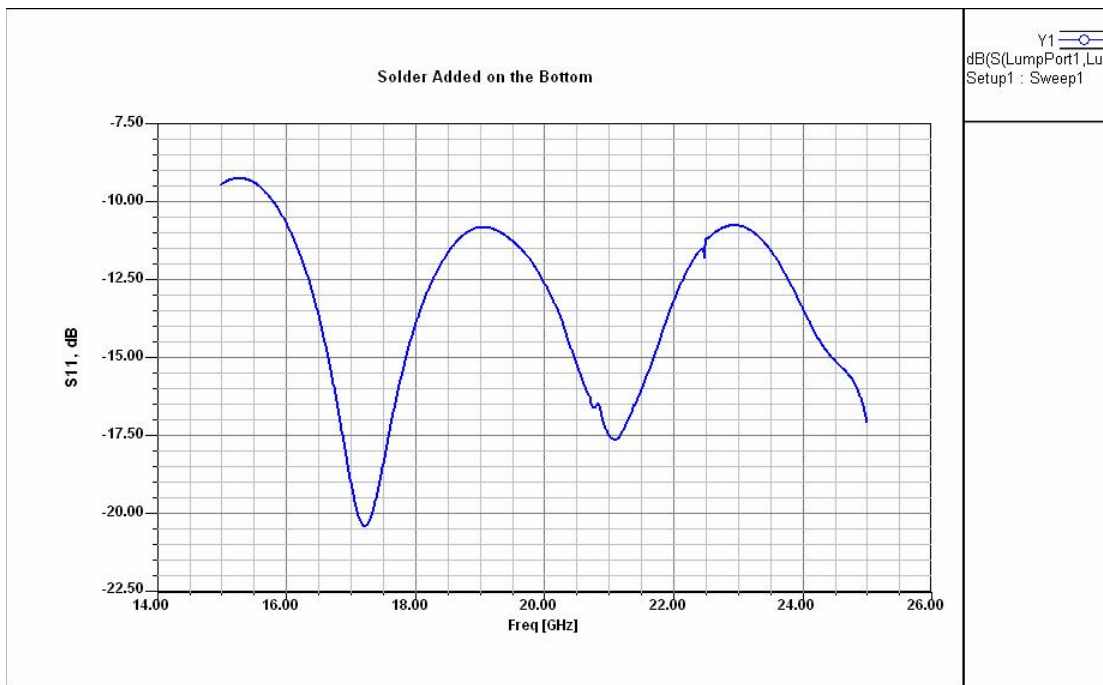


Figure 5c. Computed result  $S_{11}$  exhibits some improvement around 19 GHz, but the return loss was approximately reduced from -20 dB to -17.5 dB around 21 GHz.

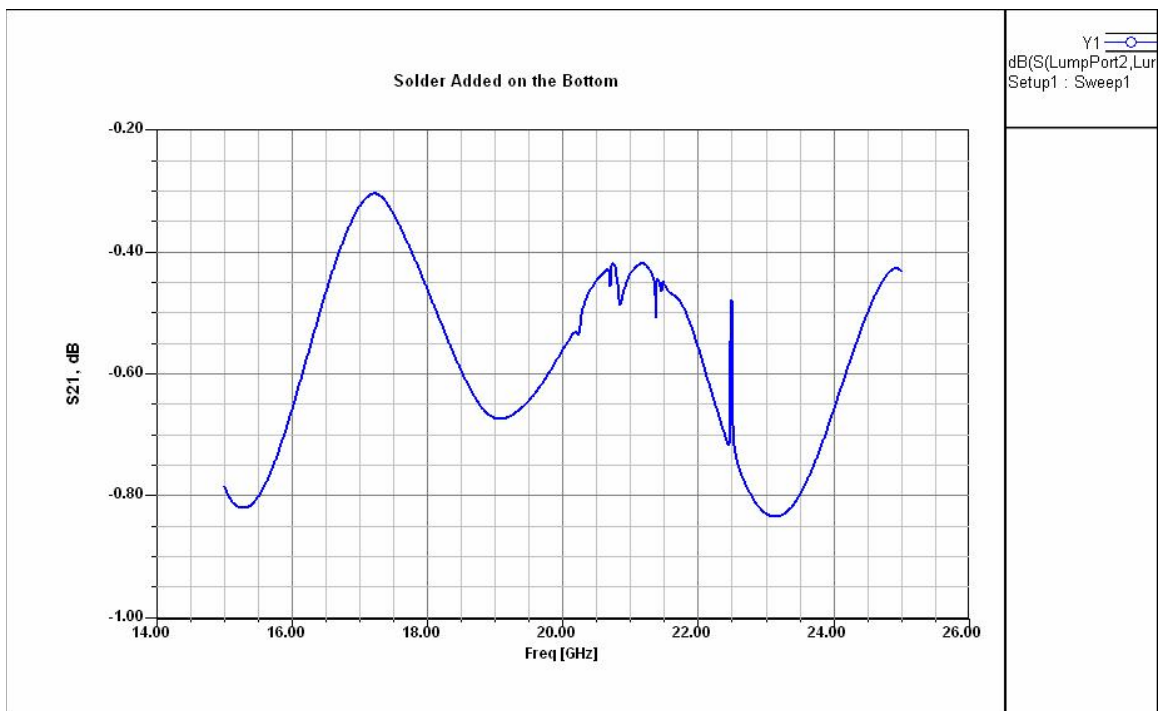




Figure 5d. Computed S21 tells us that some energy is being radiated at the added contact surface area of the center conductor.

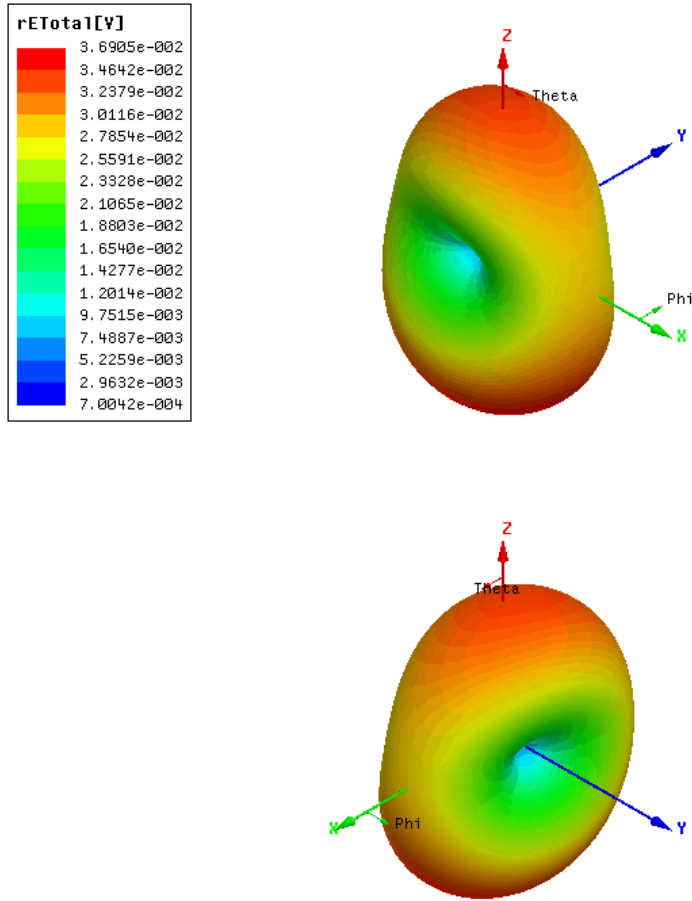


Figure 5e. Radiation patterns of the setup when additional contact surface was added to the center conductor. Notice that the quantity  $rE_t$  is approximately 0.037 Volt, smaller than that of the short coaxial sections butted against each other.

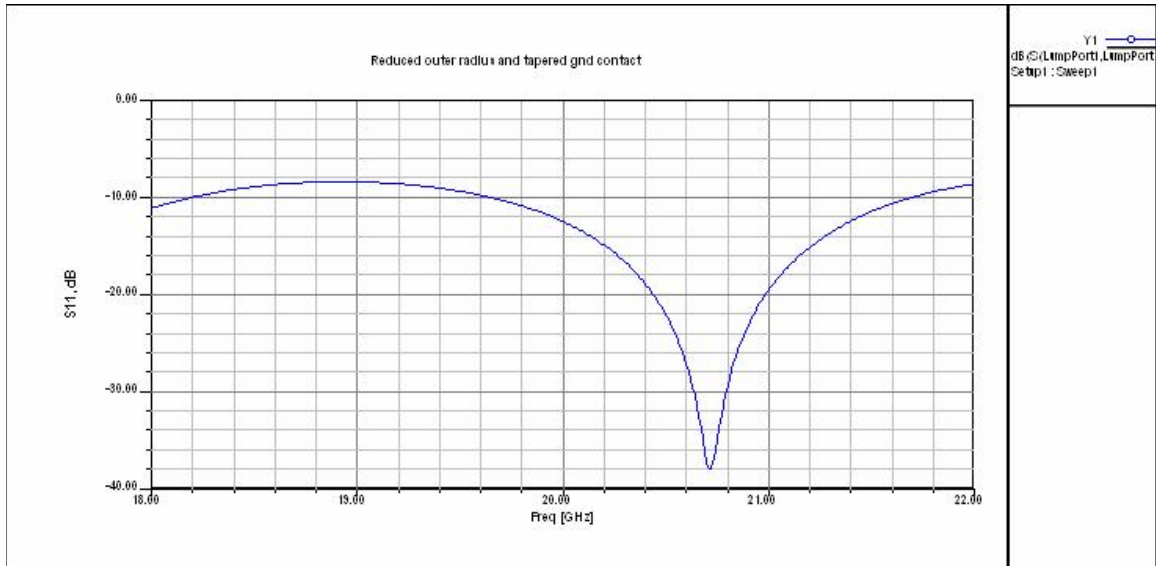
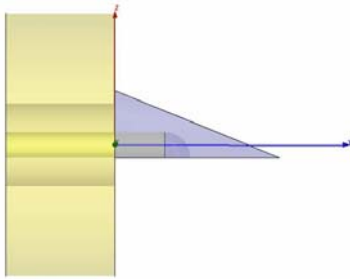


Figure 6a. Computed response S11 of the CPW with end launch connectors. Center conductor had circular right angle contact and additional contact surface shown in figure 5 was removed.

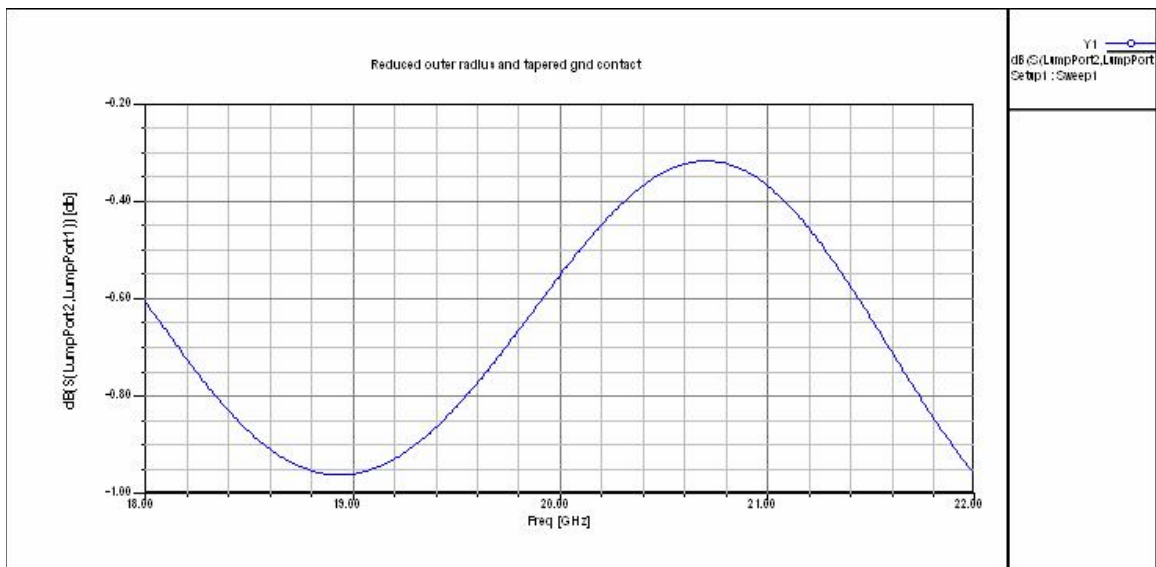


Figure 6b. Computed S21 of the CPW with end launchers. Center conductor had circular right angle contact and additional contact surface shown in figure 5 was removed.

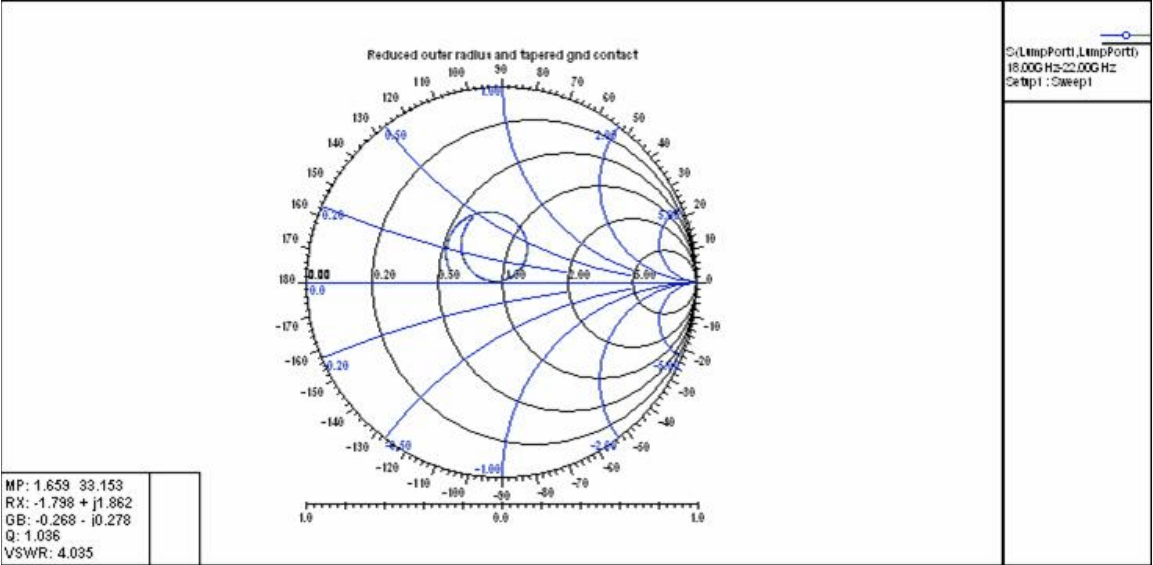


Figure 6c. Smith chart, showing impedance curve of the final setup.

Table 1. DC resistance from end to end. Measured using an ohmmeter.

Setup for measurement	Measured	Actual Value
Direct contact from probe to probe	0.20 Ohm	0.20 Ohm
Center conductor to center conductor	0.94 Ohm	0.74 Ohm
End launcher outer conductor (OD) to end launcher OD	0.22 Ohm	0.02 Ohm

Table 2. Measured Transmission loss (S21) of the end launchers and a CPW, 8 mm long, on a wafer combined.

19 GHz	20 GHz	25 GHz	27.4 GHz
-1.0 dB	-1.5 dB	-0.5 dB	-3.4 dB

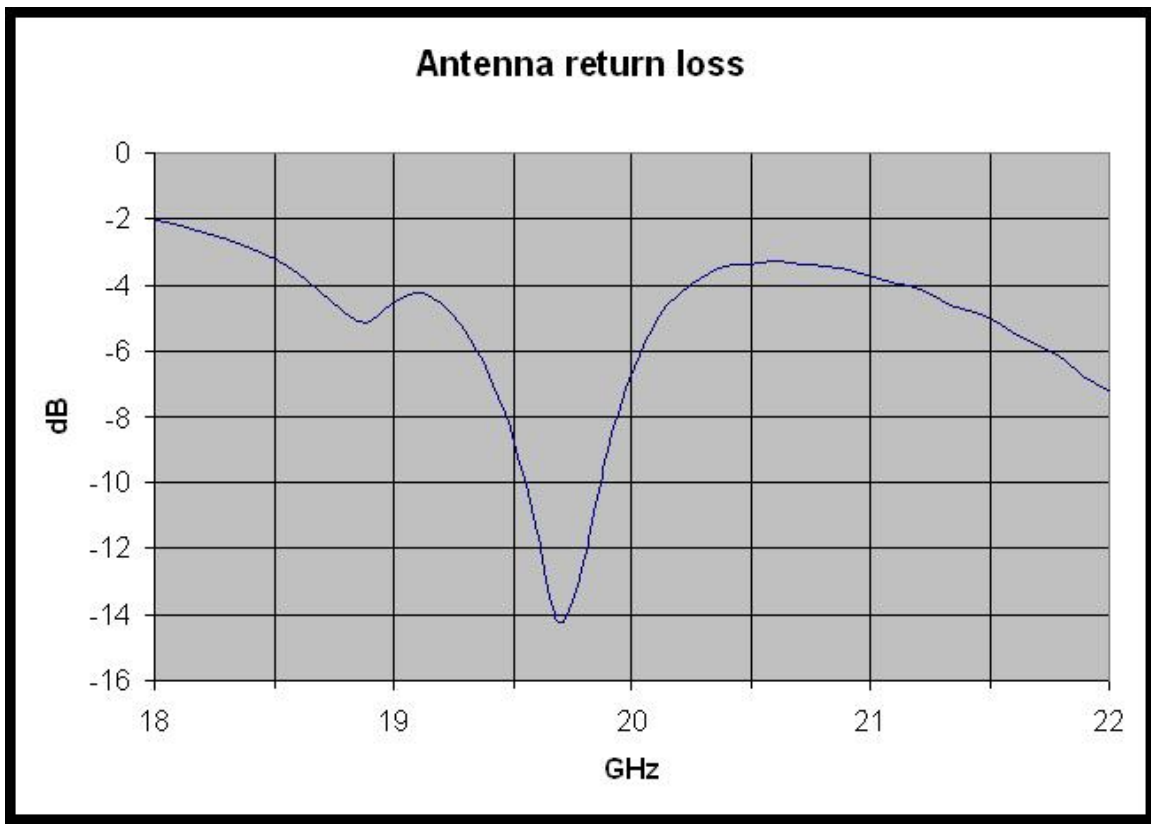
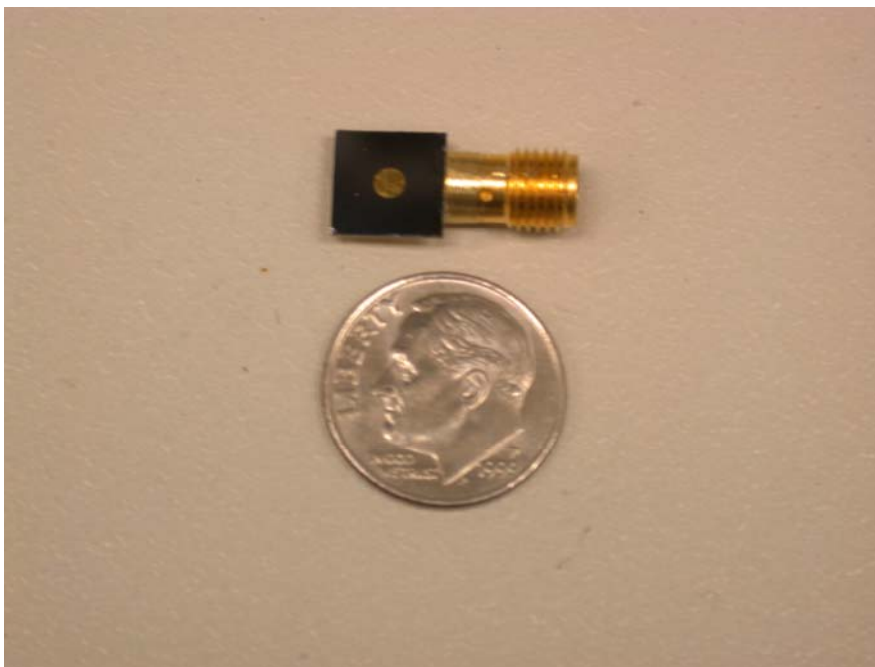
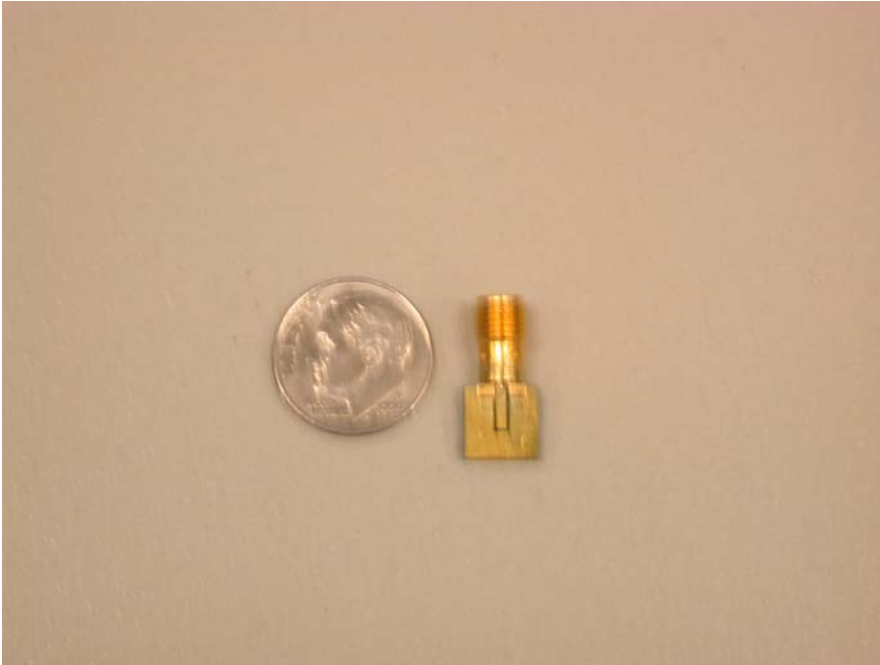


Figure 7a. A return loss of the wafer level antenna with CPW as a function of frequency from 18 GHz to 22 GHz.



Figures 7b. Picture of the modified end launcher with antenna next to a dime. CPW on the opposite is shown in figure 7c.



Figures 7c. Picture of the modified end launcher mounted on a silicon wafer, shown CPW side next to a dime. Antenna on the opposite side is shown in figure 7b.

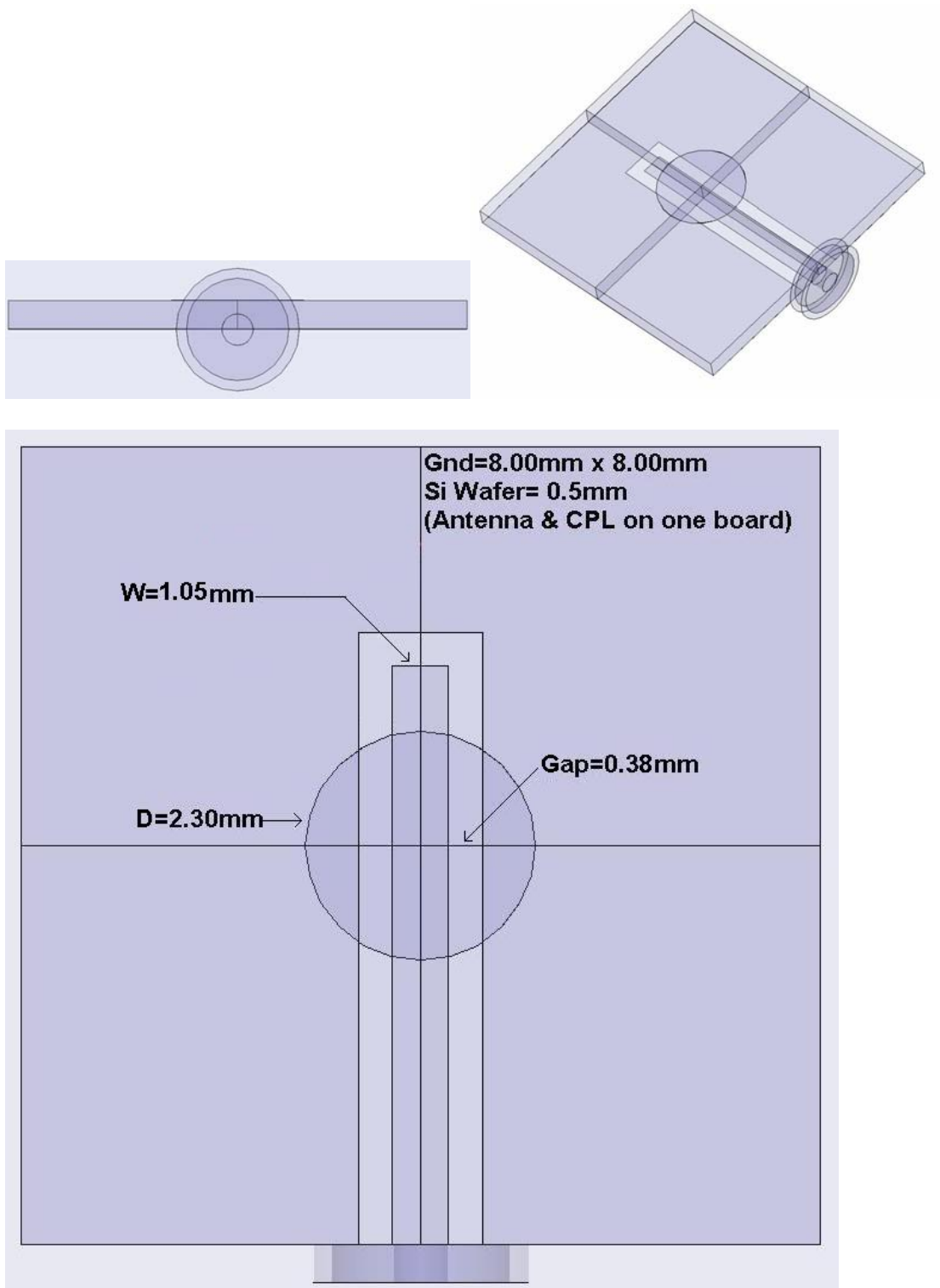


Figure 7d. Wafer level antenna and CPW with three different views. Length of the CPW is 4.7 mm. Notice that this drawing is not to scale.

# A NEW RADIO DIRECTION FINDER FOR WILDLIFE RESEARCH

Todd A. Borrowman, Steven J. Franke and George W. Swenson, Jr.  
Department of Electrical and Computer Engineering  
University of Illinois at Urbana-Champaign

## Abstract

A new direction-finding system has been developed, consisting of  $N$  identical VHF receivers, each with its own dipole antenna, closely situated so that the mutual interactions of the dipoles produce identical complex receiving patterns for each receiving channel, successively spaced in azimuth angle. A single incoming r-f pulse a few milliseconds in length thus produces  $N$  samples of the common, known, reception pattern. By optimally fitting the pattern to the data with respect to azimuth an estimate of the direction of arrival is determined. Use of multiple receivers, coherent detection of complex analytic signals, modern estimation algorithms and modern software-defined receiver technology permits a manifold improvement in speed and convenience over currently available wildlife radio tracking methods.

## 1 INTRODUCTION

Direction finding systems have been a great help to the environmental sciences by enabling the tracking of wildlife through radio transmitters. Originally the bearings were found with hand-held antennas—either a highly directional antenna, or one with a narrow null in the pattern. As the tracking of animals has gained importance, automated systems for direction finding and animal tracking have been developed. These systems allow more information on the animal's location to be recorded continuously and quickly. However, these direction finders are an automation of the hand-held techniques and do not take full advantage of the hardware and computational power now available.

A currently deployed automated direction finding system [1] calculates bearings by a special adaptation of the classical Watson-Watt direction finder. This system uses several directional antennas arrayed in a circle. The receiver for this system is switched sequentially between successive antennas and a bearing is calculated once all the antennas have been read. The ratio of the largest signal to second largest signal gives the bearing with respect to the boresight direction of the antenna with the strongest signal. This assumes that the two antennas receiving the strongest signals are adjacent to each other. The signals received by the other antennas are ignored.

Also in that current system the receiver must tune separately for each different transmitter frequency, reducing the number of bearings for each transmitter since the time spent receiving must be shared between all transmitters. This need to retune also requires more complicated hardware in the receiver. The last filtering stage must have a small enough bandwidth to eliminate the other transmitters at frequencies near the desired transmitter and the oscillators must be precise enough to place the desired transmitter's signal in that small bandwidth. Another drawback of this receiver is that it records only the amplitude information from the antenna, ignoring more data that could

be utilized for direction finding.

The multichannel coherent radio receiver and direction finder uses a different approach. The antenna is less complicated, using simple dipoles instead of Yagi-Uda or other directional antennas. This less directional design allows every antenna to receive each pulse and use all the information collected in the bearing calculation. The mutual impedance of the dipoles is used in the design to increase the azimuthal differentiation.

The use of a software defined receiver increases the speed and flexibility of the system. The receiver is able to record a large band of frequencies at once and then to perform the bearing calculation on each signal received in that band. Each antenna is connected to an independent quadrature receiver so the signals are received simultaneously on every antenna. This increases the speed of the direction finder by receiving multiple transmitted signals on every antenna at once. Both in-phase and quadrature signals are used in the bearing calculation, increasing the information collected per signal, thus increasing the accuracy of the estimated bearing [2].

The new direction finding system has been tested incrementally through to the final completed system. The antenna was modeled using computer software to visualize the mutual impedance contribution to the antenna patterns and the difference from idealized models. These calculated patterns were then used in direction finding simulations to test the viability of the designed antenna and direction finding algorithms. The antenna models were also verified independently by field tests which measured the antenna patterns. Finally the entire system was tested in the field using actual animal transmitters and GPS coordinates as test data.

## 2 DIRECTION FINDING SYSTEM OVERVIEW

The direction finding system is comprised of four parts: antenna, RF front-end, software-defined receiver, and detection and direction finding algorithm. Each component is independent and separate, to be replaced as needed in case of a change in frequency, modulation, or polarization. Also, this made for quicker, parallel development as each element was built and tested independently before integration into the completed direction finder.

### 2.1 Antenna

The software Nec-Win Pro [3] was used to estimate the antenna patterns. The software implements NEC (Numerical Electromagnetics Code), which uses the method-of-moments to determine the electric field produced by the antenna. The Nec-Win Pro software was chosen because it calculates and reports the electric field magnitude, phase, and polarization. Figures 1, 2, 3, and 4 show the modeled characteristics of the chosen array configurations.

The schematic layout of the chosen antenna array for vertical polarization is shown in figure 5. The aluminum dipoles are 85.7 cm long and each dipole is attached to the ends of adjustable PVC arms set in a cross pattern. The arms can telescope between 58 and 68 cm and can turn 360° to receive various polarizations (Fig. 6). For the field experiments the arms were set to 63.8 cm ( $.35\lambda$  at 164.5 MHz).

Each dipole is center-fed with 75- $\Omega$  RG6 coaxial cable connecting each dipole to an independent receiver. Ferrite chokes are applied to these lines to suppress antenna currents on the outer conductors of the transmission lines.

The measured vertically polarized antenna pattern has a smoother transition from the main lobe to the two side lobes as compared to the NEC simulation (Fig. 1). Also the antenna has a larger front-to-back ratio than was simulated. Both of these variations from simulation make the antenna a better direction finder by raising the gain between lobes and having an increased directional asymmetry. The phase pattern was almost identical between the NEC simulation and the measured values (Fig. 2).



For the horizontally polarized antenna pattern (Fig. 3), the measured values had a slightly broader main lobe accompanying a smaller back lobe. The phase measurements (Fig. 4) show a more elongated pattern but still have the expected shape.

## 2.2 RF Front-End

The antenna lines are fed to the two-stage RF front-end. It has four independent channels, each consisting of a preamp and two down-converting and filtering stages. The preamp is a low noise preamp with 10-11 dB of gain. The signal is then mixed with the output from an external oscillator. This oscillator is tuned to  $f_{Transmitter} - 70$  MHz so that the output of the mixer is at a frequency of 70 MHz. The oscillator is passively split to each channel so as to maintain the correct phase relation between channels. An internal computer-controlled oscillator will replace this external oscillator in a future version.

The 70-MHz output of the mixer is filtered to eliminate duplicate images due to the mixing, with a surface acoustic wave (SAW) filter with center frequency 70 MHz and 500-kHz bandwidth. At this point the signal enters an amplifier with 22 dB of gain to recover losses incurred in the mixing and filtering. The second stage uses a fixed oscillator at 80.7 MHz to mix the signal down to 10.7 MHz. The signal is filtered using a ceramic filter with center frequency 10.7 MHz and bandwidth of 200 kHz. Finally the signal is sent to another amplifier with 22 dB of gain to recover losses.

## 2.3 Receiver

The receiver itself consists of computer controlled operations. The output of the RF front-end is fed to a Universal Software Radio Peripheral (USRP) [4]. The input to the USRP is amplified using a programmable gain amplifier (PGA) with gain 0-20 dB. The signal is then sampled with an analog-to-digital converter (ADC) giving 12-bit samples at 64 Msamples/s. This digital signal is down-converted to 256 ksamples/s using an Altera Cyclone field-programmable gate-array (FPGA). At this point the four complex channels (in-phase and quadrature data) at 256 ksamples/s are interlaced and streamed to a universal serial bus (USB 2.0) port.

A software-defined radio is implemented on the computer using the GNURadio project [5]. The program reads the data from the USB port and deinterlaces the channels into separate signals. These signals are then filtered and decimated to produce 8-ksamples/s complex signals. The center frequency of the filter is tuned by the user, within the 256-kHz band; however, the 8 ksamples/s is hardcoded into the receiver software. This bandwidth will be increased to allow simultaneous reception of multiple targets, but is currently limited to speed up development and processing.

The signals are sent through an adjustable FIR filter for audio output. Also, they are Fourier transformed to display the spectrum. These audio and visual cues help the user tune the receiver. Finally, signals are written to a binary file for later processing.

## 2.4 Detection and Direction Finding Algorithms

The current detection and estimation analysis is implemented in Matlab for ease of development. The complex signals are read from the binary file saved by the GNURadio program. The amplitude of these raw signals is calculated and then filtered using a matched filter whose length is the same as the pulse width (in the field experiments the pulse transmitters had a pulse width of 20 ms). These filtered signals are then subjected to a threshold test to minimize false positives. If the filtered signals are larger than the threshold, these signals are a pulse. This pulse is extracted from the data.

The fast Fourier transform (FFT) is performed on the detected pulse. The complex amplitudes of the pulse are calculated, for each channel, from the FFT by Parseval's Theorem. This data is

then fitted to the receiving pattern of the system. By using a least mean square error estimator, an azimuth bearing estimate is produced for each detected pulse.

### 3 MONTE CARLO TESTS

To test the usability of this antenna configuration for direction finding, a Monte Carlo test was performed using the NEC simulations as the given antenna pattern. The pattern is sampled at one degree intervals. At each sample, 100 test signals ( $\mathbf{V}_i$ ) are generated for each signal-to-noise ratio (SNR) to be tested.

$$SNR = 10 \log_{10} \left( \frac{\max(\text{diag}(\mathbf{G}(\theta)\mathbf{G}(\theta)^H))}{\sigma^2} \right) \quad (1)$$

The test signals are produced by adding Gaussian noise ( $\mathbf{N}_i = \mathcal{N}(0, \sigma^2 I) + j\mathcal{N}(0, \sigma^2 I)$ ) to the antenna pattern,  $\mathbf{G}(\theta)$ .

$$\mathbf{V}_i = \mathbf{G}(\theta) + \mathbf{N}_i \quad (2)$$

These test signals are then used as the input to the estimator algorithm to be tested to produce the estimated bearing ( $\hat{\theta}_i(V_i)$ ).

The error of the estimated bearing ( $\delta\theta_i$ ) is calculated,

$$\delta\theta_i = \hat{\theta}_i - \theta \quad (3)$$

as is the estimator bias ( $\bar{\delta\theta}$ ),

$$\bar{\delta\theta} = \frac{1}{100} \sum_{j=1}^{100} \delta\theta_j \quad (4)$$

and standard deviation of the error ( $std(\delta\theta)$ ),

$$std(\delta\theta) = \frac{1}{99} \sum_{j=1}^{100} (\delta\theta_j - \bar{\delta\theta})^2. \quad (5)$$

The bias shows the accuracy of the estimator, while the standard deviation is a measurement of precision. For optimization, one will find an antenna configuration which has the lowest maximum standard deviation in terms of frequency and azimuth.

In these tests the antenna model performed well (Fig. 7). The standard deviation is relatively smooth with the larger features consistent at all the noise levels. At 40-dB SNR, all estimation errors are within 1° of the target azimuth. As the SNR decreases the standard deviation of errors increases proportionally, as is expected with Gaussian noise.

### 4 GPS EXPERIMENT

A pulse transmitter was placed in a vehicle and driven around the Monticello Rd. Field Site. The transmitter was accompanied by a GPS receiver which recorded its location. The received signals were recorded by the GNURadio receiver. The computer was configured to receive a GPS time signal to synchronize the computer and the GPS receiver that will be with the transmitter. The GNURadio receiver was set up with LO1 at 94.266 MHz, LO2 at 80.7 MHz and the NCO at -10.704 MHz. This placed the animal transmitter at around 500 Hz in the baseband spectrum.

The truck, with the animal transmitter and GPS receiver, initially was at the end of the driveway on Rising Rd. (County Road 700E) for 2 min to line up the actual bearings and the estimated bearings (Fig. 8). The transmitting truck turned left and began traveling south on Rising Rd. At

the corner of Rising Rd. and C.R. 900N the truck turned left to travel east on C.R. 900N. At the corner of C.R. 900N and Staley Rd. (C.R. 800E) the truck turned left to travel north on Staley Rd. At this point the transmitter lost the line of sight to the receiving antenna. This shows up as a lack of estimates for these bearings. At Monticello Rd. (C.R. 1000N) the truck turned left to travel west. Approximately halfway down this road the transmitter regained line of sight. At Rising Rd. the truck turned left and began traveling south. At the driveway of the field station the truck turned left and drove up the driveway east until coming to a stop at the field station building.

The bearings from the antenna to the transmitter were calculated (Fig. 9) using the GPS coordinates recorded in the truck. Then the bearings were estimated by using the LMSE estimator in Matlab. Each pulse detected was used independently to estimate a bearing. SNR was calculated (Fig. 10) using the pulse energy divided by the noise power per hertz. From signal  $S(t)$  the pulse energy is calculated by

$$Inst.Power = \frac{1}{R} S^*(t)S(t) \quad (6)$$

$$Energy = \frac{1}{R} \int_0^T S^*(t)S(t) dt = \frac{1}{rR} \sum_{k=0}^{rT} S^*(k)S(k), \quad (7)$$

where  $R$  is the resistance,  $r$  is the sampling rate and  $T$  is the length of the pulse in time. The noise power per hertz is calculated from a noise signal  $n(t)$

$$n(t) \longrightarrow_{DFDT} N(f)$$

$$Power/Hz = \frac{r}{RBL} \sum_{f=0}^{\frac{LB}{r}} N^*(f)N(f), \quad (8)$$

where  $L$  is the total length of the dfdt in samples and  $B$  is the bandwidth of the noise. SNR then becomes

$$SNR = 10 \log_{10} \left( \frac{B \sum_{k=0}^{rT} S^*(k)S(k)}{r^2 L \sum_{f=0}^{\frac{LB}{r}} N^*(f)N(f)} \right). \quad (9)$$

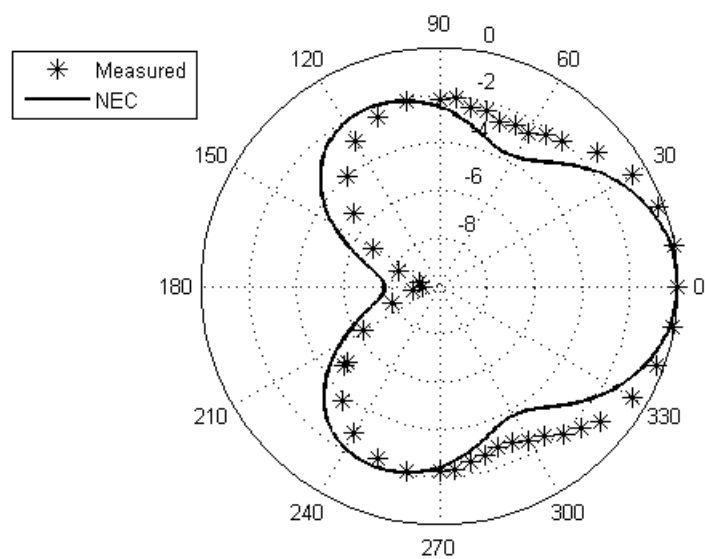


Figure 1: Comparison of NEC simulation and measured four-element vertical dipole array magnitude pattern at a frequency of 164.5 MHz. The radial axis is in dB.

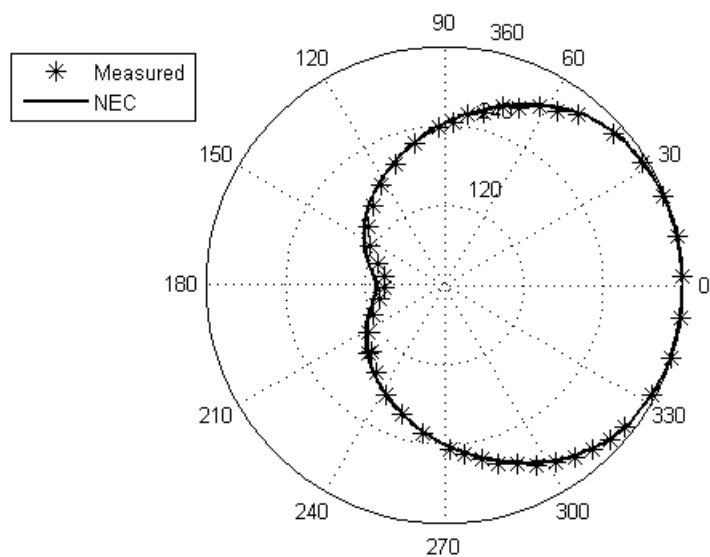


Figure 2: Comparison of NEC simulation and measured four-element vertical dipole array phase pattern at a frequency of 164.5 MHz. The radial axis is in degrees.

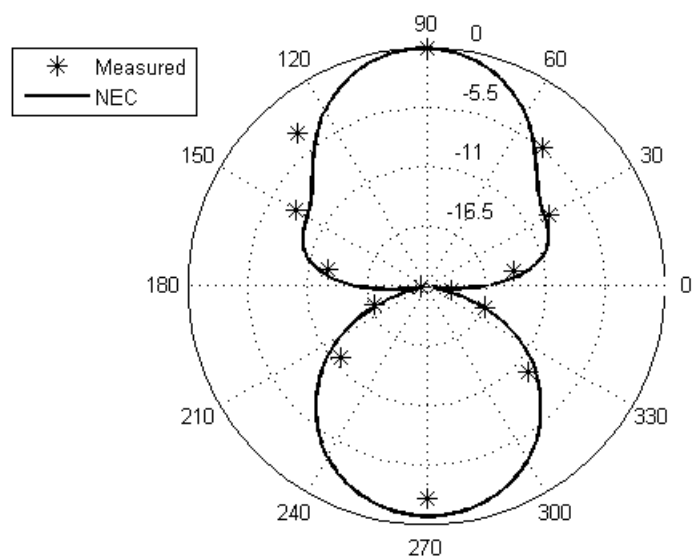


Figure 3: Comparison of NEC simulation and measured four-element horizontal dipole array magnitude pattern at a frequency of 164.5 MHz. The radial axis is in dB.

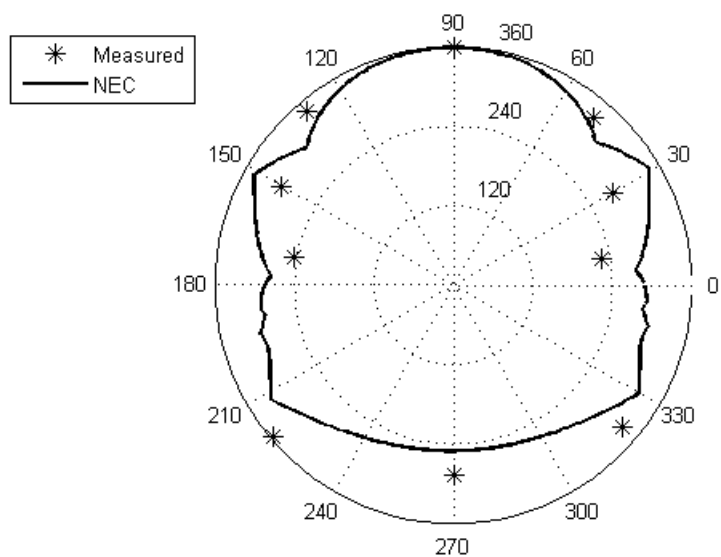


Figure 4: Comparison of NEC simulation and measured four-element horizontal dipole array phase pattern at a frequency of 164.5 MHz. The radial axis is in degrees.

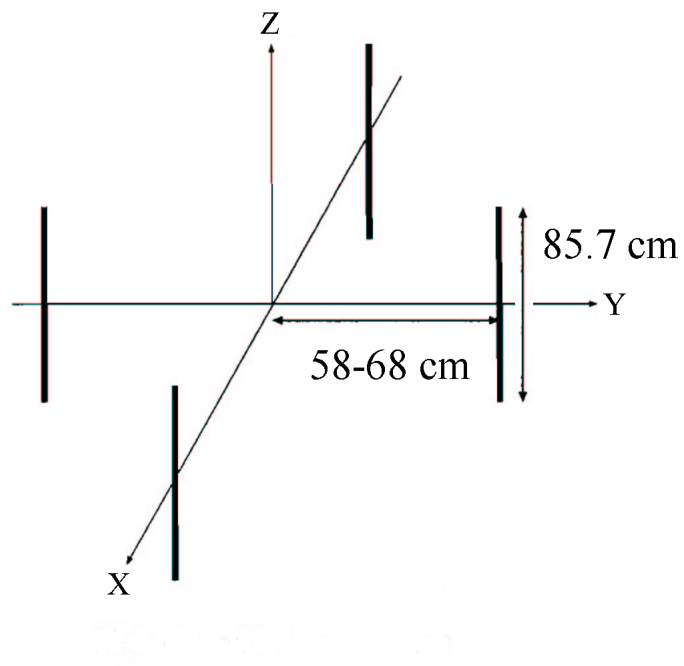


Figure 5: Layout of four-element dipole array.

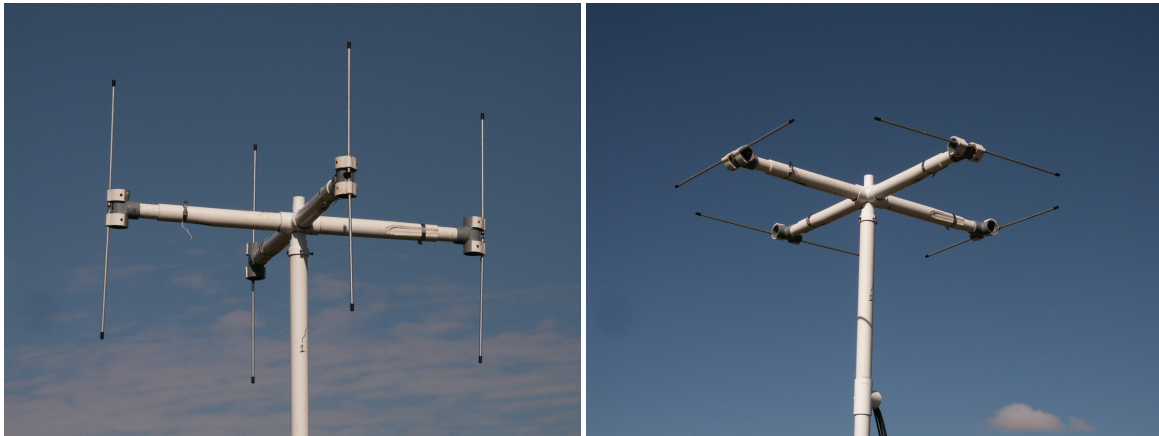


Figure 6: Antenna in the vertical (left) and horizontal (right) configurations.

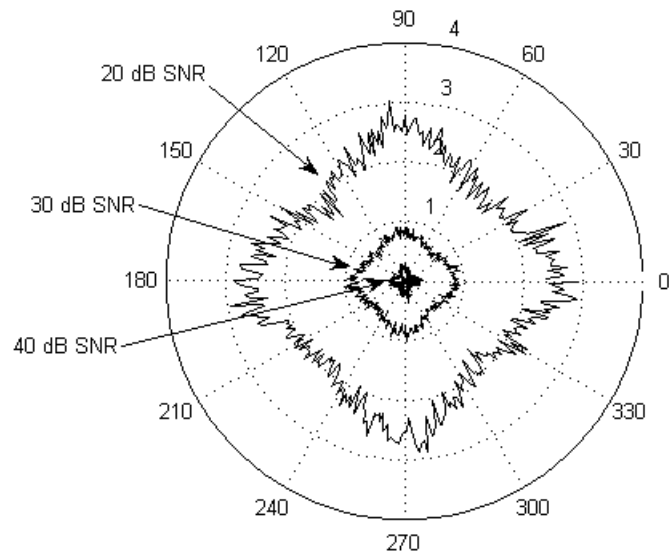


Figure 7: Direction finding simulation results using LMSE estimation. The radial scale is the standard deviation of error in degrees.

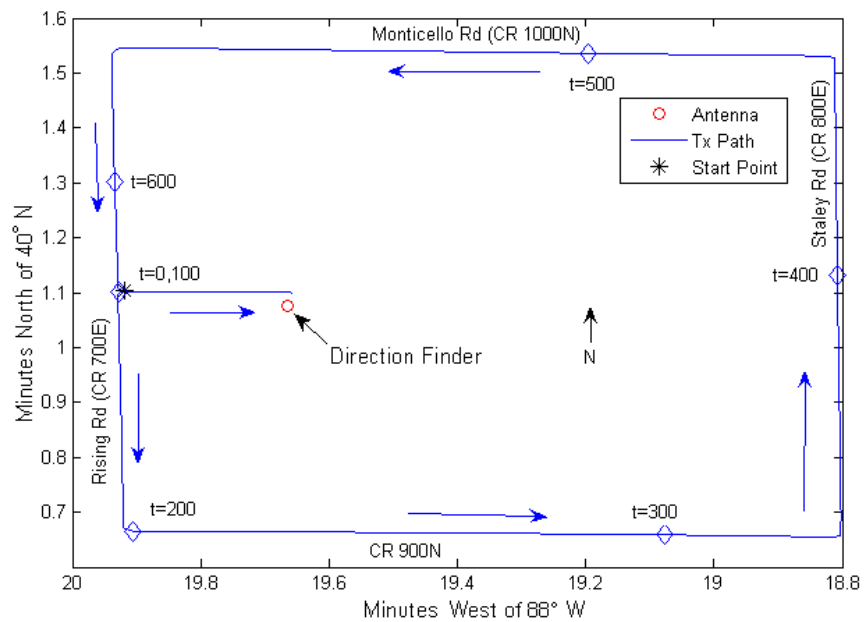


Figure 8: The direction finder location and the path the transmitter traversed for the GPS experiment.

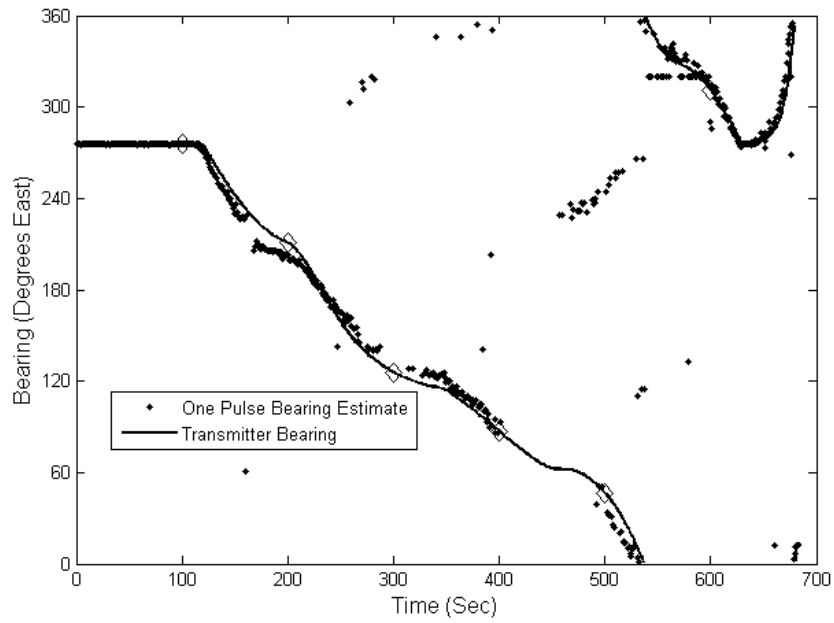


Figure 9: Transmitter bearings calculated from GPS locations and estimates. Each dot represents one pulse on which the estimate was based. The diamonds denote the bearings of the diamonds in Figure 8.

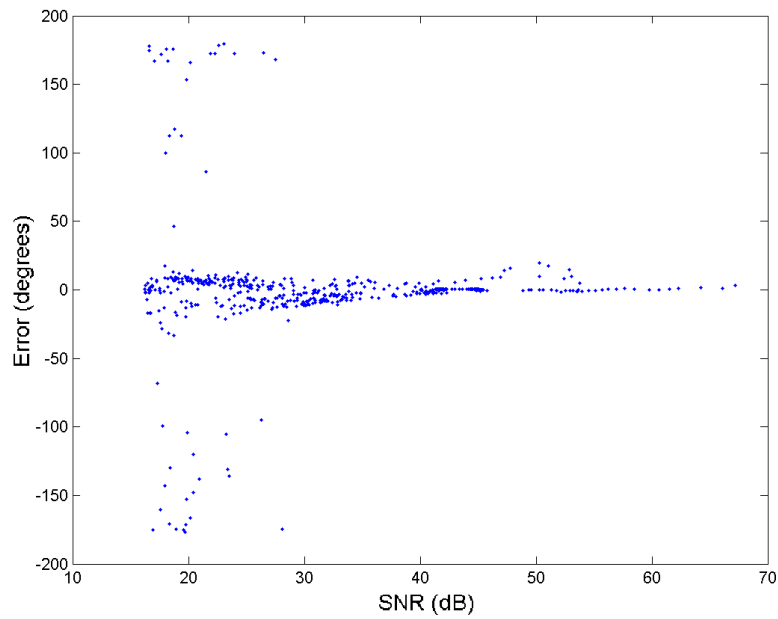


Figure 10: Error of estimate dependence on SNR. Each dot represents one pulse on which the estimate was based.



## Acknowledgement

This work was supported financially by CESU Agreement No.W9132T-06-2-0011 between the U.S. Army Engineer Research and Development Center, Construction Engineering Research Laboratory and the Department of Electrical and Computer Engineering, University of Illinois at Urbana-Champaign.

## References

- [1] W.W. Cochran, G.W. Swenson Jr., L.L. Pater, "Radio direction finding for wildlife research," in *Proceedings of the 2001 Antenna Applications Symposium, Allerton Park*, 2001, pp. 295-307.
- [2] G.W. Swenson Jr., L.L. Pater and M.J. White, "A direction finding system for transient signals," Construction Engineering Research Laboratory, U.S. Army Corps of Engineers ERDC/CERL SR-07-3, March 2007.
- [3] Nittany Scientific Inc., "NEC-Win Pro," 2003,  
<http://www.nittany-scientific.com/nwp/index.htm>.
- [4] Ettus Research LLC, "Ettus research," <http://www.ettus.com/index.html>.
- [5] GNURadio FSF Project, "The GNU software radio," March 2007,  
<http://www.gnu.org/software/gnuradio/index.html>.

# **CHALLENGES AND SOLUTIONS FOR THE EFFICIENCY MEASUREMENT OF AN ELECTRICALLY SMALL ANTENNA FOR ANIMAL TRACKING**

J.M. Martin, G.W. Swenson Jr., and J. T. Bernhard

Department of Electrical and Computer Engineering  
University of Illinois at Urbana-Champaign  
Urbana, IL 61801

**Abstract:** Tracking migratory birds involves outfitting them with transmitters and antennas so that their whereabouts can be detected by tracing a specific signal assigned to them. Common practice in wildlife studies dictates that the mass of the transmitter plus the antenna placed on an animal should not exceed 3-5% of the animal's body weight. When the bird is large, such as a goose, this weight limit poses no severe restrictions on the transmitter antenna. However, when the animal of interest is a small songbird (~ 26 g in weight, 15 cm in length), both the transmitter and antenna face severe size limitations that are further compounded by an operating frequency of 150 MHz. These size and frequency limitations translate into an antenna that is electrically small and that has a non-ideal counterpoise, which makes measuring the efficiency extremely difficult. This paper describes the experimental methods developed for use with the Wheeler cap technique to arrive at repeatable and representative measurements of efficiency with and without a bird model present. Important considerations for efficiency measurements of electrically small antennas and antennas in close proximity to biological bodies will be presented and discussed.

## **I. Introduction**

Currently an effort, known as ICARUS [1], is investigating the ability to track songbird migration globally from space. There are currently several tracking-specific transmitters that are capable of producing a signal detectable by a satellite; however, these transmitters are only appropriate for relatively large animals. Common practice in wildlife tracking dictates that the mass of the transmitter plus the antenna should not exceed 3-5% of the animal's body weight. For larger animals such as an albatross, this weight limit poses no problem. Indeed, several researchers, e.g., [2], have investigated tracking system performance as a function of antenna size, topology, and orientation on larger

birds, such as geese, at 400 MHz. However, smaller animals, such as a songbird, pose a unique challenge for satellite tracking because many songbirds are both small (~15 cm in length) and light (averaging 26 g). While several lightweight transmitters have been developed that are appropriate for these birds [3], the relationship between antenna size and tracking feasibility for this kind of system has not been studied.

If a songbird is to be tracked from space, the power radiated by the bird's transmitter is a critical parameter that can make the difference between tracking success and failure. Therefore, being able to accurately measure the efficiency of the antenna used is crucial to the link budget calculation. While antenna efficiency measurements are generally straightforward, there are several factors that complicate the efficiency measurement of an antenna used in tracking a songbird.

First, the only practical choice for an antenna that is to be attached to a songbird is a simple monopole because it is both lightweight and minimally interferes with the behavior of the bird. Size and weight restrictions dictate that this monopole must be small. Furthermore, the operating frequency for this system is 150 MHz, which corresponds to a free space wavelength of 2 m. Since the bird is only 15 inches from beak to tail, outfitting it with an antenna more than 25 cm would be unreasonable. Therefore, only monopoles one-eighth of a wavelength long or less should be considered—and of course there is great motivation to make the antenna as short and light as possible such that it minimally hinders the bird.

Second, the transmitter itself is extremely small, on the order of 1 cm<sup>3</sup> or less [3]. Therefore, without the bird present, the monopole has a very small counterpoise at best – with the transmitter mounted to the bird (usually with glue), the radiating system becomes more complex. In fact, the lack of a large or well-defined ground plane in this case means that both the body of the transmitter as well as the bird may serve as counterpoises for the monopole.

Due to these conditions, measurement techniques must be examined and amended to ensure an accurate and repeatable measurement. This paper discusses the obstacles and solutions encountered while tackling this problem.

## **II. Antenna Efficiency and the Wheeler Cap Method**

Antenna efficiency is the ratio of the power radiated by an antenna to the power delivered to the antenna. It can be expressed as a function of the antenna resistances,

$$e = \frac{R_R}{R_R + R_D}, \quad (1)$$

where  $R_R$  is the radiation resistance of the antenna,  $R_D$  is the ohmic resistance of the antenna, and the sum of these two resistances is equal to the total resistance of the antenna.

Some popular methods for measuring efficiency include the directivity/gain method, the radiometric method, and the random field method [4]. However, these methods are either not appropriate for small, low gain antennas such as this one at 150 MHz or they require special equipment, a large anechoic chamber, or a large mode-stirred reverberation chamber in order to provide accurate measurements. Therefore, the Wheeler cap method [5, 6] was chosen for evaluation of antenna efficiency in the present study. This choice, however, presented a number of challenges, since fields inside the Wheeler cap can terminate on feed cables and result in erroneous and unstable measurements.

The Wheeler cap method is a straightforward approach to measuring the resistances necessary to calculate efficiency [5, 6]. A Wheeler cap is a large conducting box or sphere that encloses an antenna over a ground plane. Effectively, this cap shorts the radiation resistance of the antenna, so that when an impedance measurement is taken with the antenna inside the Wheeler cap, the resistive component of the impedance is equal to the ohmic resistance,  $R_D$  [5]. Therefore, only two measurements are necessary to determine the efficiency of an antenna:

1. A free space measurement, which yields  $R_{FS} = R_R + R_D$ .
2. A Wheeler cap measurement, which yields  $R_{WC} = R_D$ .

The original Wheeler cap was a perfectly conducting spherical shell with a radius equal to one radianlength, which is equal to  $\lambda/2\pi$  [5]. Wheeler initially chose this shape and size because the radiansphere represents the transition point between the reactive near-field region and the radiating near-field (Fresnel) region. Theoretically, by placing a large conductive hemisphere at this boundary, the fields radiated by the antenna will be shorted out before the radiation fields predominate. In 1975, Newman and Bohley showed that the shape and size of the Wheeler cap are not critical, meaning that it does not matter in which region the fields are shorted [6]. This conclusion made Wheeler caps much easier to construct because they could simply be a cube or box of any size. However, in practice the shortest distance between the surface of the Wheeler cap and the antenna should be at least  $\lambda/6$ . This restriction generally creates a cap that avoids resonances within the Wheeler cap at the desired frequency.

(Theoretically, a cap can be any size as long as it is not resonant within the frequency range of interest [7].)

For this work, the Wheeler cap has inner dimensions of  $69 \times 69 \times 90$  cm, which corresponds to a lowest-order resonant frequency of 273 MHz. In order for the antenna to be mounted within the cap, a small piece was cut out from the bottom of the structure. Both this mounting piece and the hole it left behind were lined with copper tape, so that when they were in place for a measurement, good electrical contact was ensured.

### **III. Measurement System Components and Procedures**

#### ***A. Cable Choke Design***

When measuring any antenna that is not over a well-defined ground plane, care must be taken to eliminate currents that occur on the measurement cable as a result of two separate mechanisms: (1) the mismatch between the measurement cable and the antenna and (2) the reradiation of the antenna's radiated field by the measurement cable. These currents are often reduced substantially by implementing a ferrite choke or a quarter-wavelength choke. For this work, the large impedance mismatch between the 50-ohm cable and the antenna precluded the use of a ferrite choke. Moreover, a basic quarter wavelength choke at 150 MHz would be unreasonably large (50 cm).

In order to decrease the overall length of the choke, we implemented a quarter-wavelength choke design based on Icheln and Vainikainen's dual-band balun [8]. This balun was originally designed to test a phone that operates at bands around 900 MHz and 1800 MHz. It is constructed of two concentric conducting cylinders. At the end closest to the phone, the smaller cylinder is open to the device under test, but the larger is not. At the end furthest from the phone the whole device is shorted to the test cable. Also, there is a small gap between the inner cylinder and the shorting plate. This narrow gap creates a capacitance that acts as a low pass filter. At the higher frequency (1800 MHz) the stacked cavity is blocked and the main cavity is the active quarter-wavelength balun. The lower frequency has access to the stacked cavity, though, so its currents travel the length of the balun twice to make up the active balun.

This elegant design can easily be adapted to build a choke for the presented problem. Using standard L-type copper pipes, a 25-cm-long choke was constructed with the dimensions shown in Fig. 1. Luckily, because our choke need only operate at one frequency, the capacitance of the narrow gap does not need to function as a low pass filter. Therefore, the gap between the inner pipe

and the shorting plate does not need to be narrow at all. This simplifies the fabrication process immensely. Because of the folded design of the choke, its electrical length appears as a quarter-wavelength while its physical length is one-eighth of a wavelength.

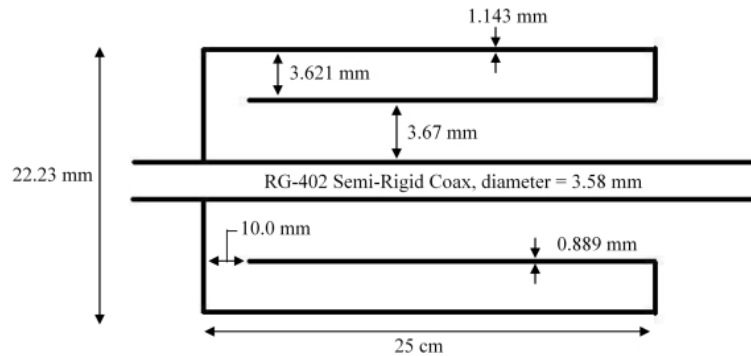


**Figure 1. Dimensions of the folded choke used to eliminate currents on the measurement cable.**

In order to ensure that the choke worked properly, a test was devised to examine the electrical length of the choke at 150 MHz. First, the RG-402 coax running through the choke is outfitted with male SMA connectors on either end. Then, an electric delay is dialed into the network analyzer to effectively eliminate the length of coax running through the choke. After this step, a short standard is placed on the end of the choke. If the choke is electrically equivalent to one-fourth of a wavelength, the measurement when the short standard is on the choke should look like an open. Conversely, if an open standard is placed on the end of the choke, the impedance measured should be that of a short. It was found that with and without the bird model, the choke operated ideally around 142 MHz. Without a much more precise fabrication procedure, it wasn't expected that we could produce a choke any closer to the operational frequency.

### ***B. Bird Model***

When choosing how to include the bird in the experimental set up, live or dead birds were an option, but we instead adopted an alternate approach that would preserve the repeatability of the procedure and avoid all animal handling issues. A natural sponge was carved into the shape of a small songbird in the dimensions mentioned above. The average mass of this class of songbird is 26 grams, so to complete the bird model, it was saturated with biological saline (a 0.9% NaCl solution) to a mass of 26 grams. The sponge easily absorbed the solution without being excessively wet and was easy to handle. Even though this model does not

mimic the relative permittivity of the various tissues within a bird, it is representative of the average conductivity taken over the whole bird and it will contribute to any resistive system losses measured with the Wheeler cap method.

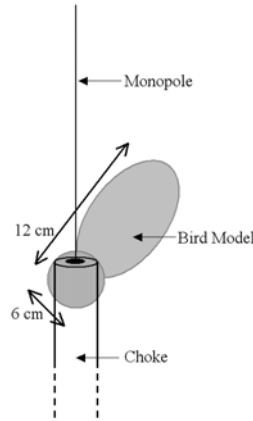


**Figure 2. Bird model constructed from natural sponge in testing configuration with antenna and choke.**

To prepare the bird model for measurement, it was first rinsed in tap water and wrung out until it was approximately 14g. This mass corresponded closely to the amount of water that could be removed from the bird easily after it had been saturated (the mass of the sponge when dry was 3.8 g). Following this, the bird was saturated with biological saline (0.9% NaCl) until it weighed 26 g, the average mass of a typical songbird of interest. This method was followed for each measurement set that included the bird model in an attempt to minimize variations in salinity.

### ***C. Impedance Measurement Procedure***

The impedance measurements called for modifications to the choke that was described in section A. After several attempts to obtain measurements, we decided that we did not want to have to utilize a SMA connector to attach the antenna to the choke structure. With the SMA connector in place, it was easy to have several different sized monopoles available for testing. However, there was evidence that the junction at the SMA just outside the choke was affecting the behavior of the choke. As an alternative, the inner coax cable was removed and replaced with a longer strip of coax. This single piece became both the inner coax running through the choke and the antenna extending out from the choke, as in Fig. 3. The antenna was fashioned by stripping the outer conductor and dielectric material from the RG-402 coax. It became clear through more measurements that the choke had to be electrically isolated from the bird model. To accomplish this, the end of the choke was wrapped with electrical tape to isolate the bird from the

choke. Also, the opening of the choke was covered with a thin sheet of plastic in order to prevent any moisture from entering the choke from the bird model.

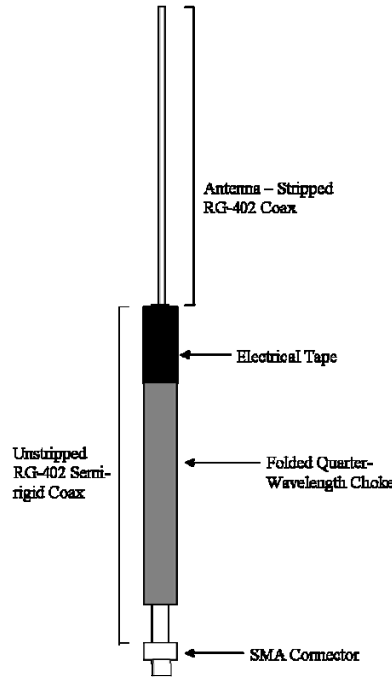


**Figure 3. Modified quarter-wavelength choke for impedance measurements**

Initially the monopole was constructed to be 25 cm in length (one-eighth of a wavelength). Once all measurements for this length were taken, the antenna was cut to a shorter length and the measurements were repeated. This process continued until the antenna was 10 cm long. In order to analyze the effects of the bird model on the monopole, we took measurements of the monopole by itself and the monopole with the bird model. The measurements of the monopole antenna in free space were taken first. These readings were taken in an anechoic chamber away from any conducting bodies with the choke resting on a piece of foam to keep it upright. The portion of the measurement cable that was in the anechoic chamber was covered with absorber to prevent it from reradiating the field of the monopole under test. Five separate measurements of the input impedance were taken for each antenna length. Each of these five measurements was completed with the antenna at a different location in the anechoic chamber. This was done to confirm that the input impedance was not dependent on the position of the antenna in the chamber.



Second, the free space measurements of the antenna with the bird model were taken. Again, five separate measurements were taken at different locations within the anechoic chamber. The bird model was placed on the choke/antenna structure to mimic the mounting configuration in the field and the measurements were immediately taken.

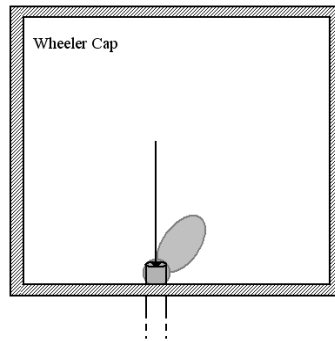
Third, the Wheeler cap measurements of the monopole were taken. To insert the antenna into the cap, the piece that had been cut from the cap to allow insertion of the antenna was affixed to the choke. This cut-out of the Wheeler cap is referred to as the Wheeler cap mounting piece. For this measurement, the mounting piece was flush with the end of the choke so that none of the choke resided in the Wheeler cap. The mounting piece was then reinserted into the Wheeler cap, placing the antenna within the cap. Next, five separate measurements were taken. For each set of measurements, the antenna was removed and reinserted into the Wheeler cap at least 2-3 times to ensure that slight changes in the position of the mounting piece did not significantly alter the measurements.

Finally, the Wheeler cap measurements of the monopole with the bird model were taken. First the bird model was rinsed and saturated with biological saline as in the free space measurement discussed previously. Then the choke, antenna, bird model, and choke-piece were assembled. The face of the Wheeler cap mounting piece that completes the inner lining of the cap was partially covered with electrical tape to isolate the bird model from the conductive surface. For this part of the procedure, a small portion of the choke extended into the Wheeler cap simply because the bird was pulled over the choke so that it would not be covering the monopole. Figure 4 shows the antenna configuration when it is placed within the Wheeler cap. Once again, five separate impedance measurements were taken for each setup and the antenna was removed and reinserted into the Wheeler cap 2-3 times during those measurements. For a more detailed discussion of the procedure, please refer to [9].

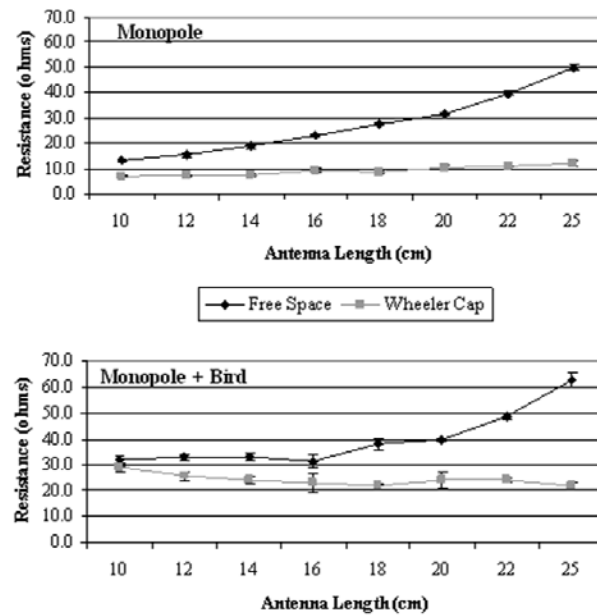
#### **IV. Results**

Fig. 5 displays the average resistances measured following the procedure above for both the test setup with just the monopole and the test setup with both the bird and the monopole. (The standard deviations are also included in this graph, though for many data points the standard deviations were low enough that they are not easily visible.) In both cases, as the length of the antenna increases, the difference between the free space antenna impedance (the sum of the radiation and ohmic resistance) and the Wheeler cap antenna impedance (the ohmic resistance) also increases. This means that the radiation resistance is increasing

with increasing length, which agrees with the theoretical model of an ideal monopole.



**Figure 4. Antenna configuration within Wheeler cap. A small part of the choke is contained within the cap, but the majority of it resides outside of the cap.**



**Figure 5. Measured resistances for an electrically short monopole (above) and the same monopole with the bird model.**

Note that the impedances of the monopole seem to be converging towards a resistance of about 10 ohms as the antenna length decreases. The impedances of the monopole and bird model, however, are increasing to a much higher resistance. Obviously, as an antennas length decreases towards zero, it's expected

that all resistances associated with the antenna would also approach zero. This is clearly not the case of the monopole with the bird model. This effect is due to the resistance that is inherent to the bird model (and a real bird), which becomes part of the system once the antenna and transmitter are attached to it.

Approximate radiation patterns taken of the monopole with the bird model indicate that the bird model will absorb and perhaps reradiate a small amount of power. In most cases, this effective power loss is small compared to the radiation of the antenna and thus not usually detectable. However, when the antenna length is very short (around 10 cm), the effective losses presented by the bird model are apparent in a radiation pattern measurement. Since the bird model is essentially dissipating energy, we can consider it an equivalent resistance in the circuit diagram of the system. This resistance attributed to the bird will always be present in any measurement, and this is why the resistances of the monopole with the bird model do not approach zero with decreasing antenna length. In fact, the resistances approach the effective resistance of the bird model, which with this particular model could be estimated at 30 ohms.

According to the resistances measured, the efficiency of the monopole alone at 25 centimeters is about 65% while at 10 cm the efficiency is 45%. With the bird model added, the efficiencies for the 25 cm and 10 cm antenna are 50% and 5% respectively. Because the efficiency of the monopole alone is greater than 40% at 10 cm, it appears that the major physical factor in determining the efficiency of an animal-monopole system is not antenna length. Recalling the discussion regarding the inherent resistance of the bird model and examining Figs. 4 and 5, one sees that when the free space resistance (or total resistance) is large compared to the animal's effective resistance, the efficiency of the radiating system will be similar to that of the monopole by itself, with the animal essentially acting as a part of a lossy, non-ideal counterpoise resulting from any direct or capacitive coupling between the transmitter, the antenna, and the bird's body. This is a slightly different from the case of antennas near but not connected to biological bodies (e.g., [10]) where the load presented by an organism is a near-field radiative phenomenon. However, as the total radiating system resistance approaches the effective animal resistance, efficiency will drop off rapidly since most of the input power will be dissipated in the bird. From this observation, we can conclude that for each new tracking system that requires an electrically small antenna, a similar study should be conducted to determine the effective resistance of the subject animal. Then the appropriate antenna length can be determined according to the desired efficiency and, therefore, the desired detection range of the tracking system.

## V. Acknowledgments

The authors thank several colleagues for useful discussions on this topic, especially Profs. Steven Franke and Paul Klock of the University of Illinois Electrical and Computer Engineering Department, and Prof. Martin Wikelski of the Department of Ecology and Evolutionary Biology at Princeton University.

## VI. References

- [1] Wikelski M, Kays RW, Kasdin J, Thorup K, Smith JA, Cochran WW, Swenson GW Jr., "Going wild – what a global small-animal tracking system could do for experimental biologists," *J Exp Bio*, vol. 210, pp. 181-186, 2007.
- [2] K. Tsunekawa and N. Kanmuri, "An experimental study of antennas for a small radio attached on an animal" *Trans. IEICE B-II*, vol. J75-B-II, no.12, pp. 993-995, Dec. 1992 (In Japanese).
- [3] B. Naef-Daenzer, D. Früh, M. Stalder, P. Wetli, and E. Weise, "Miniaturization (0.2 g) and evaluation of attachment techniques of telemetry transmitters," *The Journal of Experimental Biology*, vol. 208, pp. 4063-4068, October 2005.
- [4] J. D. Kraus and R. J. Marhefka, *Antennas for All Applications*, 3<sup>rd</sup> Edition. McGraw- Hill: New York. 2002.
- [5] H.A. Wheeler, "The radiansphere around a small antenna," *Proc. of the IRE*, pp. 1325-1331, Aug. 1959.
- [6] E.H. Newman, P. Bohley, and C.H. Walter, "Two methods for measurement of antenna efficiency," *IEEE Trans on Antennas and Propagation*, vol. 23, no. 4, pp. 457-461, July 1975.
- [7] P.W. Klock (private communication), 2004.
- [8] C. Icheln, J. Krogerus, and P. Vainikainen, "Use of balun chokes in small-antenna radiation measurements," *IEEE Transactions on Instrumentation and Measurement*, vol. 53, no. 2, pp. 498-506, April 2004.
- [9] J. Martin, "Efficiency of an electrically small monopole for animal tracking," M.S. thesis, University of Illinois at Urbana-Champaign, Urbana, IL, USA, 2005.
- [10] O. P. Gandhi, G. Lazzi, and C. Furse, "Electromagnetic absorption in the human head and neck for mobile telephones at 835 and 1900 MHz," *IEEE Trans. on Microwave Theory and Techniques*, vol. 44, no. 10, pp. 1884-1897, October 1996.

# **TRANSFORMATIONAL ELEMENT LEVEL ARRAYS (TELA) TESTBED**

Thomas Dalrymple, Jonathan Buck, Peter Buxa, John McCann, Robert Neidhard, Gary Scalzi, Caleb Shreffler, Dan Spendley, Paul Watson  
Air Force Research Laboratory  
2241 Avionics Circle, Bldg 620  
Wright Patterson AFB, Ohio 45433

**Abstract:** The Air Force is in need of sensor technologies to support surveillance operations in complex Radio Frequency (RF) environments. Requirements dictate the need to find weak and strong scatterers simultaneously over broad bandwidth, while resolving emitter signal characteristics such as angle of arrival and time of arrival for signal identification and tracking.

Previous work at AFRL has resulted in many technologies that support these needs. Many components and subsystems exist today that were only theoretical a few years ago, such as phased array antennas that support 10:1 bandwidth, broadband MMIC components, and miniaturized digital receivers.

An effort is underway at AFRL to develop systems combining these elements, resulting in wideband phased arrays encompassing multiple receiver channels and capable of forming multiple beams through digital beamforming. The key elements of this effort revolve around three key areas: RF modeling, system integration, and system testing. The TELA Testbed allows for the integration of these technologies as a system that can be tested and verified through modeling.

The ultimate goal is a broadband aperture simultaneously supporting EW, communications, and multiple radar modes. This approach will lead to reduced size, cost, weight, and power consumption while serving multiple simultaneous users with minimal impact on an airframe.

## **1. Introduction**

As the Air Force looks ahead to future threats and hardware needs, there is a constant push for more functionality and bandwidth from the various sensors used for radar, electronic warfare (EW), and communications. In the past, a state of the art radar or EW receiver would consist of a passive aperture with a fairly large analog backend receiver. These systems typically had a relatively small bandwidth. While many such systems are still in use today, phased array technology has been growing in use over the last 10 to 15 years. Active phased arrays containing low noise amplifiers and phase shifters have greatly increased the system performance available to the warfighter. These arrays

feature lower noise figures, multiple beams, and graceful degradation of performance as various elements fail over time. The receiver/exciter systems have evolved as well, increasing in bandwidth, incorporating multiple channels, and including some digital signal processing.

Now is the time to consider the future generation of these systems. Over the last decade many basic technologies have improved dramatically. Phased array antennas, formerly limited to 2:1 bandwidth, are now capable of greater than 10:1 bandwidth. Several groups, including Harris Corp., Raytheon, and Georgia Tech Research Institute, have produced and demonstrated arrays with these capabilities<sup>1-2</sup>. Broadband monolithic microwave integrated circuits (MMICs) also have greatly increased in capability. Some groups have reported up to 1 nanosecond of on-chip time delay for a true time delay MMIC design<sup>3</sup>. This MMIC is capable of covering a 10:1 frequency range, allowing element level broadband beamsteering up to  $\pm 60^\circ$  for a one square foot phased array at X-Band. This type of technology also has great potential for reducing the complexity and the cost of integrating the hardware of the analog front end of a sensor.

Receiver technology has also continued to evolve over the last few years. Broadband block downconverters and tuners can cover from DC to 20 GHz with an output bandwidth of 500 MHz or higher. Also, engineers at AFRL have recently focused on developing “Receiver on a Chip” technology using silicon germanium and fully depleted silicon on insulator processes<sup>4</sup>. Plans in the near future will see the combination of broadband tuning capability combined with analog to digital converters (ADCs) on a single die. Even commercially available ADCs continue to push to higher levels of performance. Currently, off the shelf ADCs are capable of sampling 10 bits at greater than a two gigahertz sample rate.

Combining all of these elements – broadband phased arrays, broadband MMICs, and broadband digitizing receivers – is the emphasis of the Transformational Element Level Arrays (TELA) Testbed. Miniaturized receivers allow for multiple digital channels behind these broadband arrays. Applying digital beamforming to these digital channels can allow the system to create simultaneous beams to detect multiple signals without sacrificing performance. AFRL has been working on digital beamforming for many years, and has recently demonstrated a real-time beamforming system at X-Band<sup>5</sup>. These techniques will be applied to system demonstrations in the testbed.

As a home for broadband sensor technologies, the TELA Testbed will allow for a place to bring together all the components mentioned above for testing. The areas of focus – System Integration, RF System Modeling, and RF System Testing – will be described below. The initial work will focus on a 4-channel system also described below.

## 2. RF String Description

The initial demonstration of the TELA testbed is composed of several of the elements described above, including a wideband phased array antenna, low noise amplifier, a wideband block downconverter, and a multichannel high speed digitizer. A block diagram of a single RF channel (referred to as an RF String) is shown in Figure 1. The full receiver includes 4 channels digitized simultaneously. The band of interest for initial experiments is from 2 to 10 GHz.

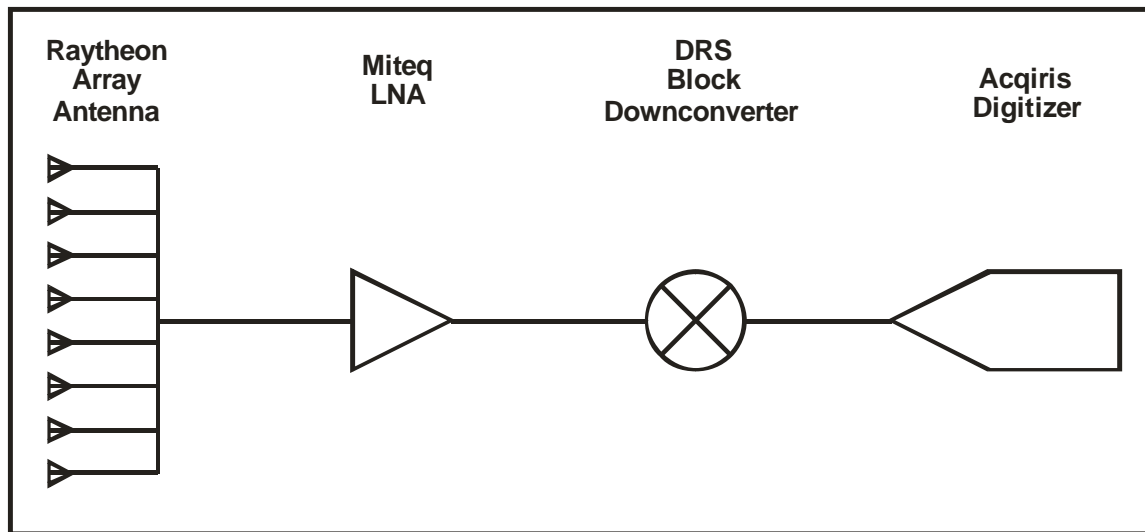


**Figure 1:** RF String Block Diagram

The Raytheon phased array was developed and delivered to AFRL under the DARPA RECAP program and covers 1.8 to 18 GHz. It is a 64-element array and has been configured in columns using passive power combiners. The array grid spacing is set to 0.325" in order to avoid grating lobes at the high end of the frequency range. This does not make for very attractive antenna patterns in the 2 to 10 GHz range, so the columns were set up to alternate between channel feeds and terminations, creating an effective element spacing of 0.650".

Each antenna column is fed through a Miteq LNA to set the noise floor for the system. The LNA provides 33 dB of gain and a 2 dB noise figure covering 2 to 10 GHz. The LNA is followed by a DRS SI-9250 block downconverter. The 9250 comes in a compact PCI format and covers 500 MHz to 18 GHz. The input RF is converted to a 1.6 GHz intermediate frequency (IF) with an 880 MHz bandwidth.

The final stage of the RF String is the four channel high speed digitizer, an Acqiris DC282. This digitizer comes in a compact PCI format, making it easy to integrate with the block downconverters for compactness and control of the system. Using an external

clock for our testing, the digitizer provides 10 bits of data at 2.133 GigaSamples/second. Data is captured simultaneously for the four channels and processed offline.

### 3. System Integration

System integration for the TELA testbed consists of integrating the Raytheon antenna, Miteq LNAs, DRS downconverters, and Acqiris digitizer in a 4-channel configuration. Control and testing of the whole receiver chain was accomplished by means of an onboard computer which was able to address the 4 block downconverters, 4-channel digitizer, and an external clock signal generator.

Figure 2 below shows how the individual components are integrated to form the RF strings. The Raytheon array is configured so that columns 2, 4, 6 and 8 are fed to the amplifiers. This doubles the element spacing and allows for improved antenna patterns in the 2-10 GHz range. The output of these four columns is then passed to the Miteq LNAs, which amplify the signal by ~33 dB. The amplified signal then passes through the SI-9250's and is downconverted to an Intermediate Frequency of 1.6 GHz with a  $\pm 440$  MHz bandwidth. The IF signal is then digitized by the Acqiris DC282 at 2.133 GS/s with 10 bits of resolution in the 2nd Nyquist zone of the onboard Atmel ADCs. This digitized data is stored to a hard disk on the single board computer and displayed with the data acquisition software. The external 2.133 GHz clock is provided by an Anritsu signal generator.

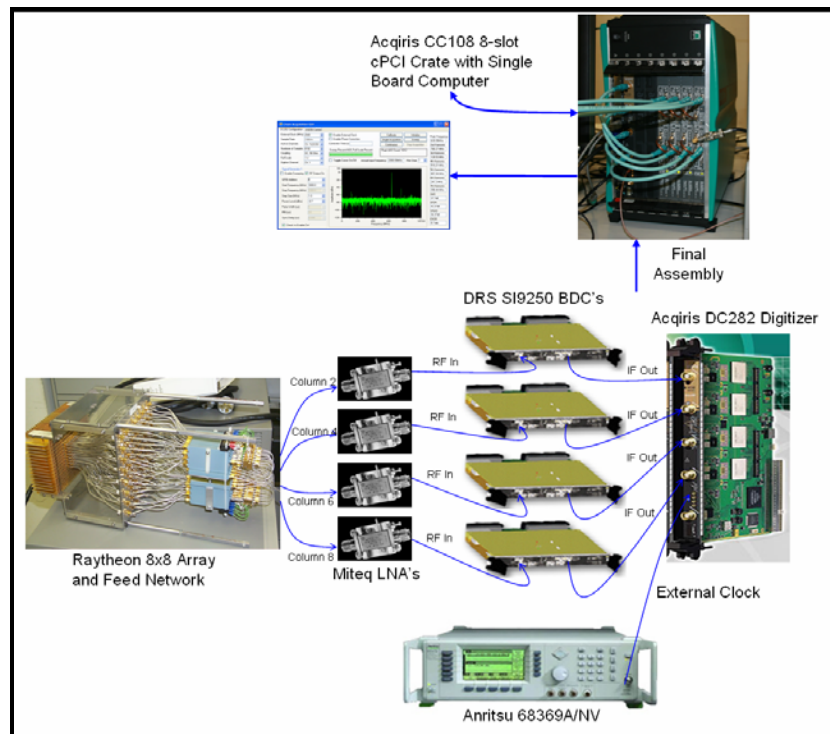


**Figure 2:** RF String Block Diagram



The devices that are software controlled include 4 DRS SI-9250 Block Downconverters, the Acqiris DC282 digitizer, and the external signal generator. These devices utilize the Compact PCI form factor and are installed in an 8-slot cPCI crate which also includes a Concurrent Technologies onboard computer.

The Acqiris DC282 is a 4-channel 10-bit digitizer with up to a 2.2 GS/s sample rate per channel when using an external clock source (2 GS/s max for internal clock). The full scale input voltages are user selectable and include 50 mV, 100 mV, 200 mV, 500 mV, 1 V, 2 V, and 5 V. Each channel can acquire up to 256 megasamples of continuous data, which translates to 120 ms of data using an external 2.133 GHz clock. The 4 channels can also be combined to achieve a sample rate of more than 8 GS/s. For all RF String testing the full scale voltage was kept constant at 500 mV which is the default setting for the onboard Atmel ADCs.

### **3.1 Software Integration**

To interface with the SI-9250s, a driver was created using Jungo WinDriver™. This tool generated library functions that could be called from a C++ application. These library functions and the Application Programming Interface (API) provided by Acqiris were used to create the control software. The GUI was created with Visual C++ 2005 and utilizes tools from National Instruments Measurement Studio.

Figure 3 shows a screenshot of the main GUI window which is used to control the digitizer. The application programming interface (API) provided by Acqiris allows the user to control every aspect of the digitizer. The GUI allows the user to control the sample rate and external clock, active channels, channel combinations, number of samples, coupling, and full scale input voltage. The software has 3 data acquisition modes; Single, Continuous, and Sweep. Single mode simply acquires the requested number of samples, computes the FFT and writes the digitized data to a file. Continuous mode repeatedly collects the requested number of samples and computes the FFT and does not write the data to a file. Sweep mode utilizes a GPIB-attached signal generator and sweeps across a user defined range of frequencies. As the signal is swept, data is collected, the FFT is computed, and the data is stored to a file. For all 3 modes, the signal harmonics as well as Spur Free Dynamic Range, Signal to Noise Ratio, Signal to Noise And Distortion, and Effective Number of Bits of the digitizer are computed and displayed. The full scale percentage is also monitored so that the user can see if they are overpowering the digitizer. The frequency spectrum is generated using the National Instruments Measurement Studio Signal Processing library and a scatter plot.

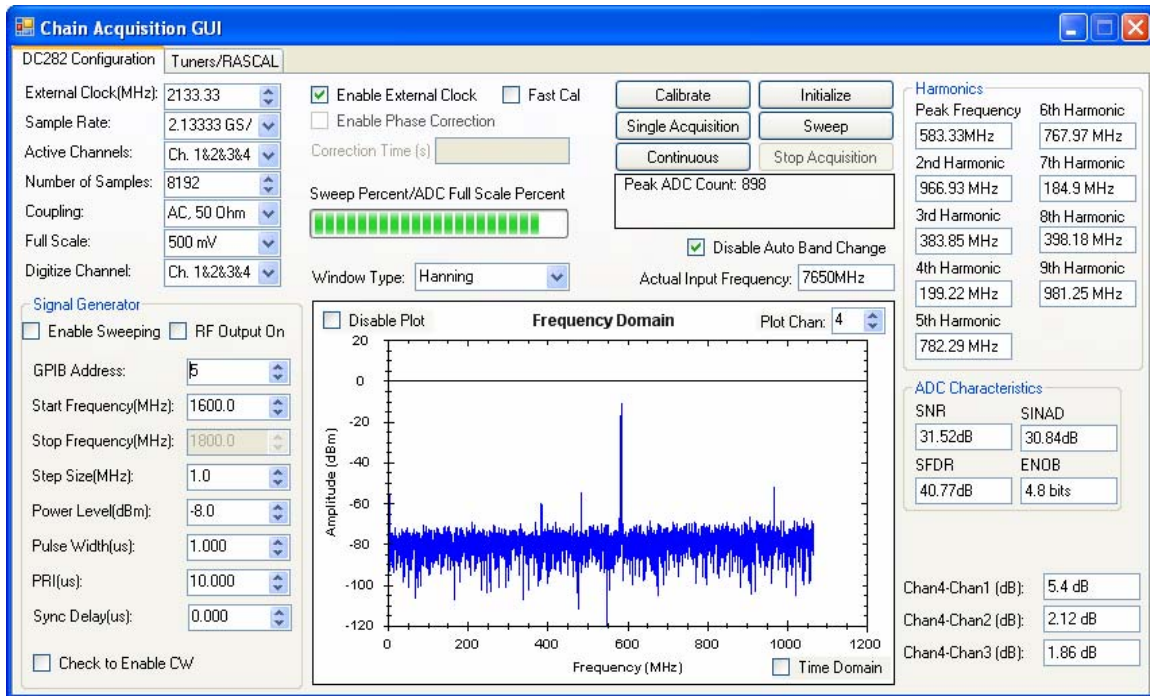


**Figure 3: Acqiris Control GUI**

Figure 4 shows the GUI which is used to control the DRS Block Downconverters. When executed, the software searches the PCI bus using generated library functions for any devices that are installed in slots 5-8 of the Acqiris MAQbox cPCI chassis. If there is a device installed in a slot, the checkbox for that slot is enabled so that the user can select it and send commands. To change the band of the selected tuner(s), the user simply selects one of the bands from the drop down list and the appropriate commands are sent to the device.

The software also has the ability to automatically change the band of the downconverters. This is done by comparing the calculated actual input frequency to the edges of a band. If a signal crosses the edge of a frequency band, the program will automatically switch the tuner band to the next one higher or lower depending on which edge the signal crossed.

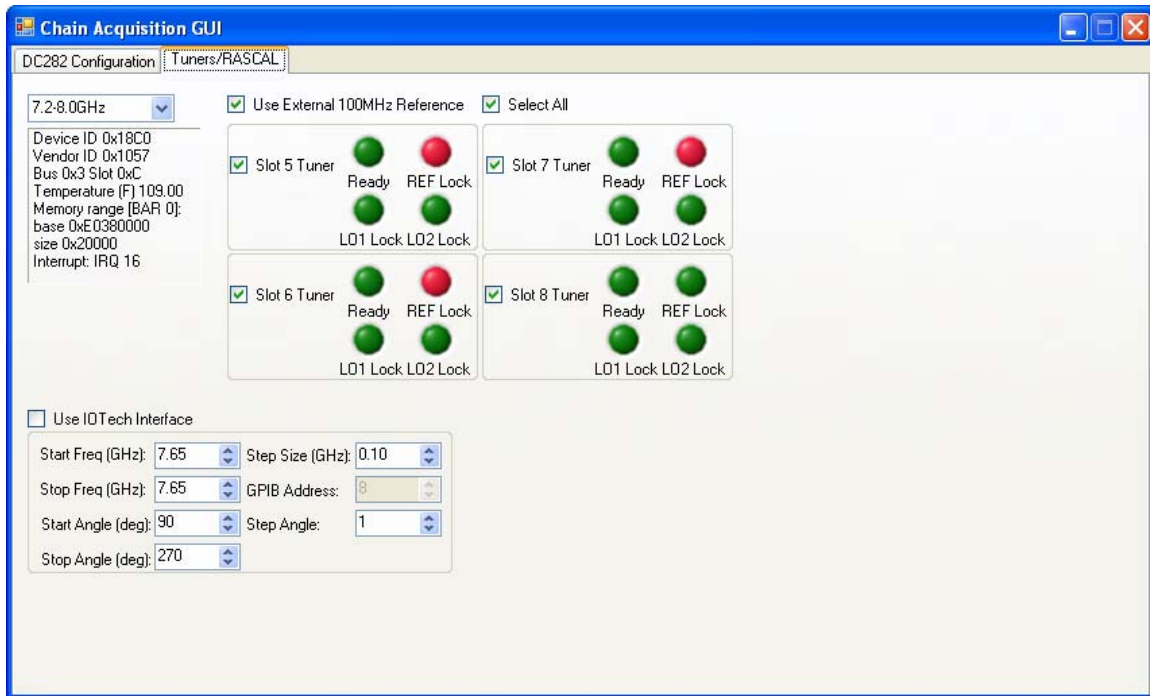


**Figure 4: SI-9250 Control GUI**

#### 4. RF System Modeling

A combination of linear and nonlinear RF modeling is essential for gaining an understanding of system performance issues and identifying possible improvements before implementation in hardware. Modeling can be performed in a hierarchical fashion depending on the desired accuracy of the simulation. A typical approach is to begin with cascaded 2-port analysis, then move towards behavioral modeling of components, and finally with circuit level modeling. Cascaded 2-port analysis is the least computationally expensive, but also the least accurate. Circuit level modeling is the most accurate, but the most computationally expensive. Behavioral modeling is a compromise between the two. All levels of modeling are useful, depending on where one is in the design cycle.

Cascaded 2-port and behavioral modeling and analysis of a single RF string, consisting of an antenna element (1x8 column), a Miteq LNA, and a DRS block downconverter, has been performed in order to provide the correct input signal levels to the Acqiris digitizer, as well as to assess performance parameters such as spurious-free dynamic range (SFDR), minimum detectable signal (MDS), noise figure (NF), gain, and receiver saturation characteristics. The SFDR is bounded in minimum signal detection by noise and maximum signal detection by unacceptable in-band distortion. In our case, this corresponds to the difference between the MDS and the input signal which produces third-order intermodulation (IM3) products which are equal the noise level at the output of the chain. Third-order intermodulation products are of primary importance because

they appear within the bandwidth of the desired signal and cannot be filtered out. For a more detailed discussion of receiver chain analysis see [Pozar]<sup>6</sup>. Once a sufficient level of modeling accuracy has been achieved, different operating scenarios can be simulated and performance can be assessed.

#### 4.1 Cascaded 2-Port Analysis

Initially, cascaded 2-port analysis of the Miteq LNA and the DRS downconverter was performed using a commercially available tool, Syscalc<sup>7</sup>, shown in Figure 5. In this manner, initial performance estimates were established. Datasheet parameters at an RF frequency of 5.2 GHz for the Miteq LNA (NF= 2 dB, gain= 33 dB, OIP3= 27 dBm) and the DRS downconverter (NF= 17.5 dB, gain= 9 dB, and OIP3= 16 dBm) were input into the program. The bandwidth was set at 880 MHz with an IF frequency of 1.6 GHz. Cascaded NF, gain, and OIP3 were 2.08 dB, 42 dB, and 15.96 dBm, respectively. The analysis shows a SFDR of 37.61 dB with a MDS of -82.46 dBm. In order to avoid distortion, the maximum input signal level is near -45 dBm. The output power for the -45 dBm input is -3 dBm which maps well to the maximum input signal of the digitizer of -2 dBm (500mV peak to peak, 50Ω). The SFDR is limited by two factors, the noise floor due to the large bandwidth and the low OIP3 of the downconverter.

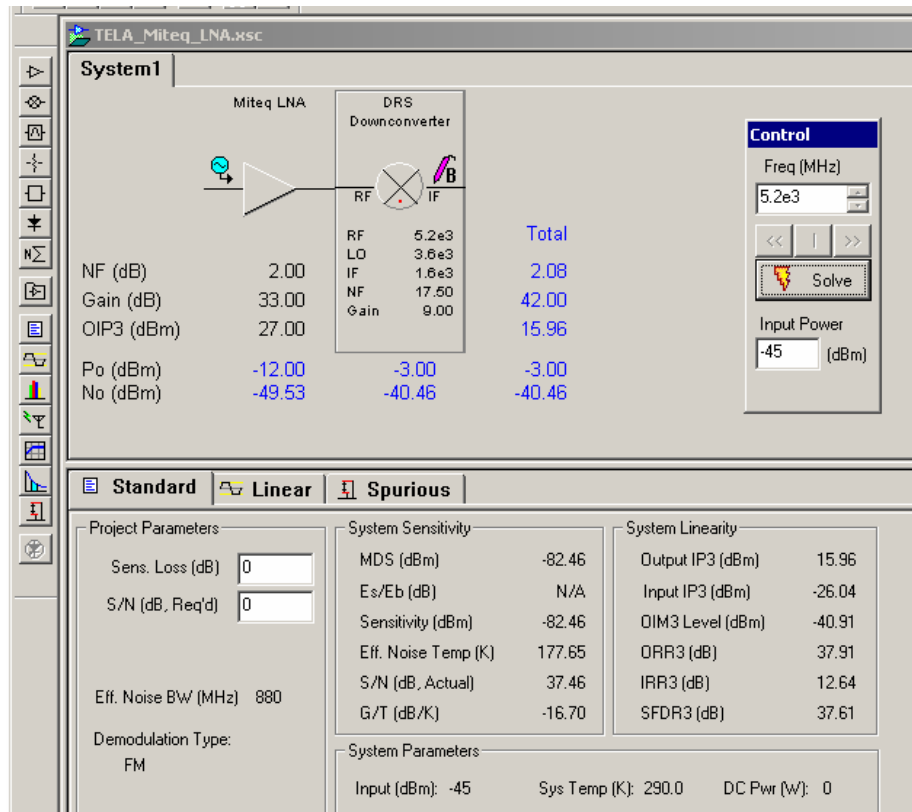
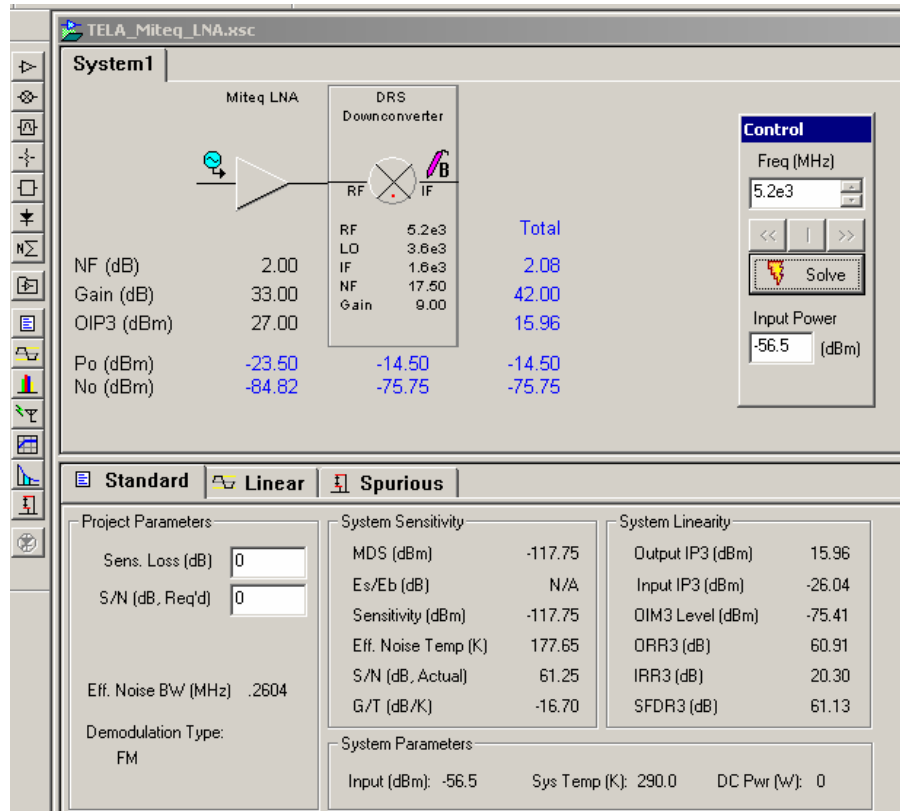


Figure 5: Cascaded 2-port analysis of LNA plus downconverter box

If instead of integrating the noise power over the full 880 MHz bandwidth one were to reduce the resolution bandwidth in the digitizer by using an FFT approach, the noise floor would be decreased, thereby improving, the SFDR significantly. The result is shown in Figure 6 with a resolution bandwidth of 0.2604 MHz, corresponding to a sampling frequency of 2.133 GHz using a 8192 sample FFT. The SFDR is now 61.13 dB with a MDS of -117.75 dBm. The maximum input signal for distortion free performance is now -56.62 dBm.



**Figure 6:** Cascaded 2-port analysis of LNA plus downconverter box with resolution bandwidth reduced from 880 MHz to 0.2604 MHz in the digitizer

## 4.2 Behavioral Modeling

While cascaded 2-port analysis provides valuable insights into expected system performance, it is limited in accuracy. A significant limitation for this work (2- 10 GHz) is the lack of frequency dependent analysis capability. Moving towards more accurate modeling over frequency, behavioral models were developed and analyzed in Agilent's ADS<sup>8</sup> CAD software.

Behavioral modeling of the Miteq LNA was accomplished using measured S-parameter data, NF data, power compression data, and 2-tone intermodulation data over the

frequency range of interest. Models were implemented with a table-based approach, utilizing interpolation between measured data points. Nonlinearities were modeled using 9th order polynomials. As an example of added model fidelity, Figure 7 shows simulated power compression curves at 2 GHz, 5GHz, and 8 GHz. Note that gain, compression characteristics, and nonlinear effects show some frequency dependency.

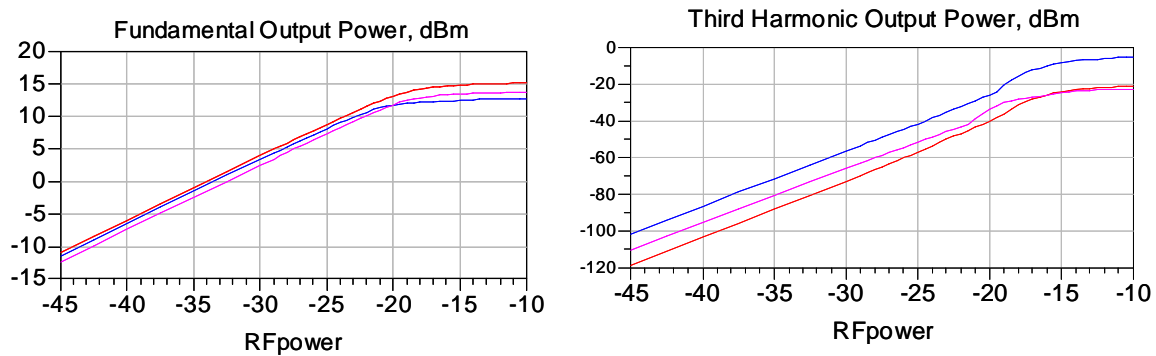


**Figure 7:** Fundamental and third harmonic power curves at 2 GHz, 5 GHz, and 8 GHz

The DRS downconverter has been modeled as an ideal mixer followed by a non-ideal amplifier, including second and third-order effects. Filters are also included to limit the bandwidth to that of the actual downconverter. In this manner, the fundamental and third-order intermodulation responses, which fall within the IF (output) bandwidth, can be accurately predicted. Modeling in this fashion is a reasonable approach due to the conversion process and filtering available in the downconverter. Detailed data regarding the individual components inside the unit were not available. Gain, NF, IP2, and IP3 measurements were taken in the various frequency bands of the downconverter and stored as a table-based model. The value of the parameters used is dependent on the specific downconverter unit and the frequency band chosen for analysis.

The behavioral models for the Miteq amplifier and the DRS downconverter have been combined and simulated using Harmonic Balance and Circuit Envelope methods available within Agilent ADS, as shown in Figure 8. As an example of the modeling capability, a 2-tone intermodulation analysis centered at a 5.1 GHz input frequency was run. Figure 9 shows the output of the simulation, where the X-axis represents the offset in MHz from the 1.6 GHz IF frequency. The input power for each carrier was -56 dBm and the tone spacing was set at 10 MHz. Markers 1 and 2 are the fundamental tones, while markers 3 and 4 are the third-order intermodulation tones. Resolution bandwidth for the noise floor is approximately 300 KHz. Simulated and measured results compare very well as demonstrated in Table 1. Also, results from a Syscalc analysis utilizing measured component parameters are also given for comparison.

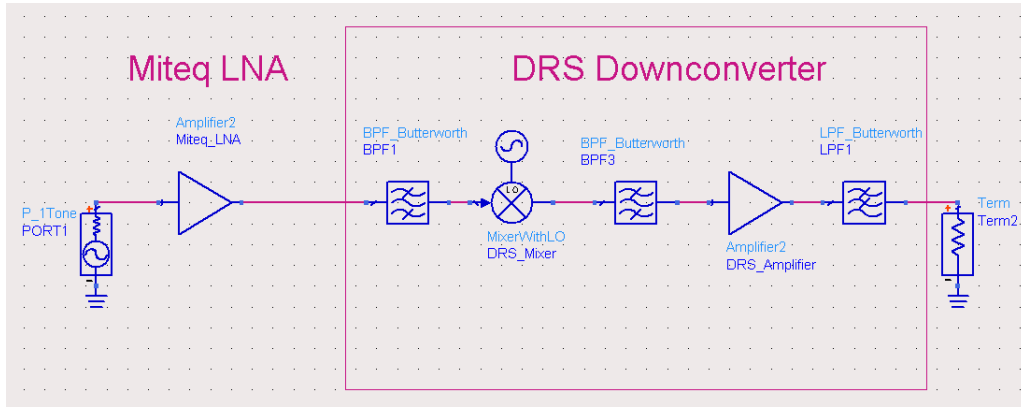


**Figure 8:** Simulation setup for behavioral modeling of LNA plus downconverter

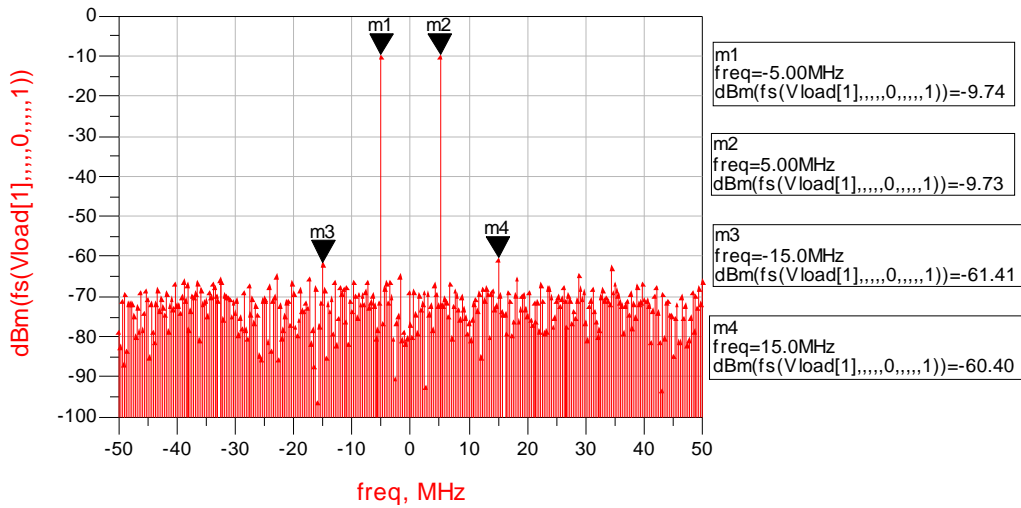


**Figure 9:** Simulated 2-tone response of Miteq LNA plus DRS downconverter. Input power is -56 dBm with a tone spacing of 10 MHz. Resolution bandwidth = 300 KHz

**Table 1:** Simulated and measured performance for the Miteq LNA plus DRS downconverter. Shown are gain, output noise power ( $N_o$ ), output third-order intercept point (OIP3), signal-to-noise ratio (SNR), spurious-free dynamic range (SFDR), and minimum detectable signal (MDS). Resolution BW = 300 KHz

	Gain (dB)	$N_o$ (dBm)	OIP3 (dBm)	SNR (dB)	SFDR (dB)	MDS (dBm)
Behavioral	46.4	-71.1	16.1	61.4	58.1	-117.5
Measured	46.7	-72 (Avg. 100)	16.2	62.7	58.8	-118.7
Cascaded 2-port	46.3	-70.5	16.3	60.84	57.9	-116.8

Even though there is not a large difference between the cascaded 2-port and behavioral modeling approaches, it must be noted that the input signals here are relatively simple 1-tone or 2-tone. Behavioral modeling will be much more valuable with complex signals which occupy a greater portion of the frequency spectrum (ex. LFM) or when examining effects of intentional or unintentional interfering signals.

Angle of arrival dependent effects can also be modeled for the antenna described in Section 2. Pattern measurements have been taken, as described in Section 5, and form the basis of a table-based behavioral model which can be incorporated into the RF string simulation as shown in Figure 10. Figure 11 shows a simulation of column 2 of the antenna over a frequency range of 5.1 GHz to 10.1 GHz in 1 GHz steps where 90° corresponds to broadside. Interpolation is utilized between measured points. Using this data, the dynamic range of the RF chain can be mapped to the range of electric field intensity present at the face of the antenna for desired operation characteristics.

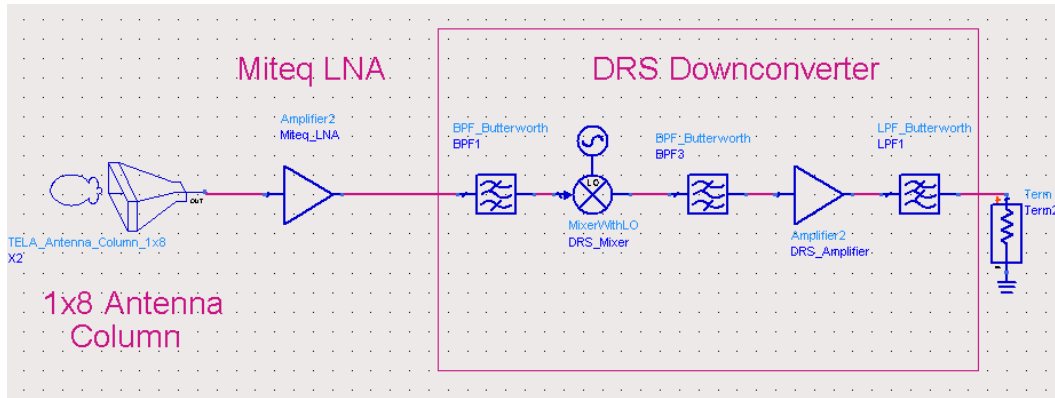


**Figure 10:** Simulation setup for behavioral modeling of 1x8 antenna column, Miteq LNA, and DRS downconverter

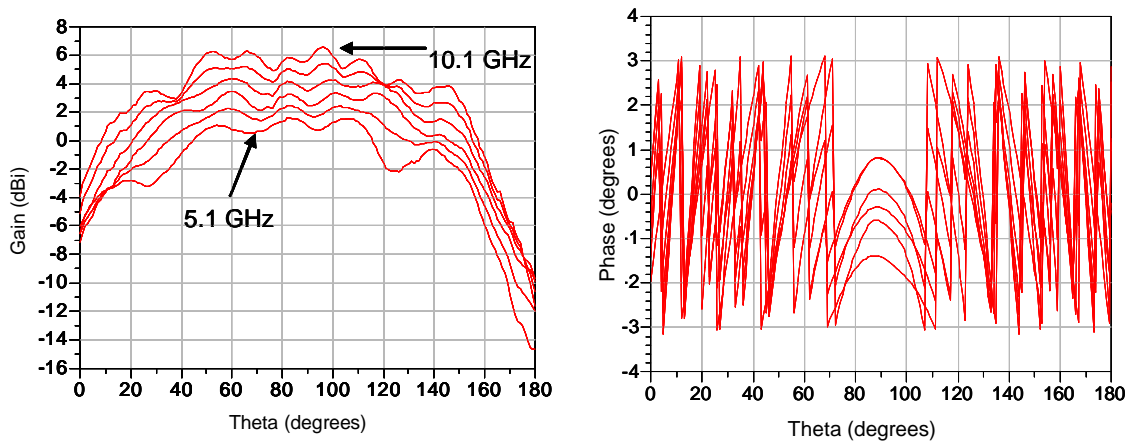


**Figure 11:** Simulated radiation pattern for column 2 of array over 5.1 GHz to 10.1 GHz



It must be noted that the current simulations do not include undesired effects introduced by the digitizer such as added noise and distortion when performing the analog-to-digital conversion. Effects such as these need to be taken into account and will degrade the performance of the receiver. Future work is planned in this subject area.

## 5. RF System Testing

### 5.1 Analog Testing & Beamforming

In order to test the integration of these multiple technologies, the ability to accurately characterize an antenna array is a necessity. Antenna measurements typically require that the source antenna and the antenna (or object) under test be separated by a large distance. This ensures that the target is illuminated by a locally planar wavefront, a condition that complies with definitions of antenna patterns and radar cross section. Furthermore, since antennas are designed to convey energy over large distances, the locally planar wavefront simulates real operating conditions. On the other hand, an indoor facility allows testing to take place in a secure environment, regardless of weather conditions. To generate a uniform plane wave in a limited amount of space, a compact range employs a feed-reflector system within an absorber-lined anechoic chamber. A diagram of a typical compact chamber is shown in Figure 12. AFRL's Radiation and Scattering Compact Antenna Laboratory (RASCAL) is equipped with a precision rolled-edge reflector that collimates the impinging spherical wave from an offset feed resulting into a uniform plane wave. The reflector is housed in an aluminum enclosure (24 feet long, 12 feet wide, and 9 feet high). In addition, the walls are lined with a curved pyramidal and curved wedge absorber. RASCAL currently has the capability to measure antenna gains and radiation patterns in the 2-18 GHz frequency band with high fidelity. RASCAL utilizes an Agilent 8362B Network Analyzer for fully automated data acquisition. RASCAL also uses an Agilent 8510 Vector Network Analyzer for S-Parameter measurements.

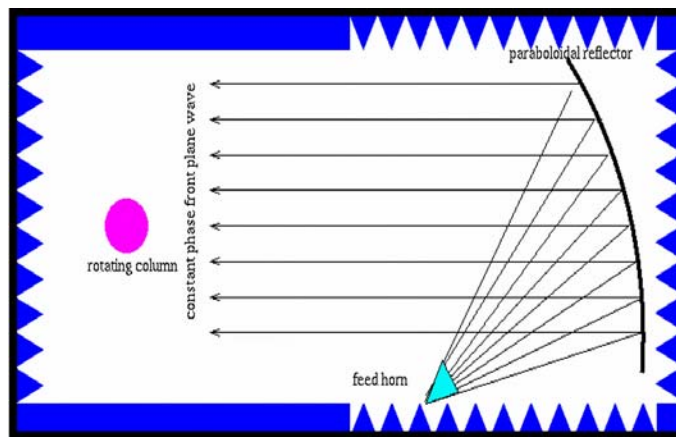


**Figure 12:** Depiction of a typical compact antenna range

As mentioned in Section 2, the antenna used in this effort is a wideband array procured from Raytheon. The Raytheon array employs a flared notch element. For full polarization selectability, a second set of boards is interleaved at ninety degree angles to the first. The result is the egg crate structure shown in Figure 13. Raytheon built and delivered an array with 16 x 21 dual polarized elements, yet only the 8 x 8 sub-array in the center was connectorized. With two separately fed polarizations, there are 128 connectors overall. The remaining elements were resistively terminated.

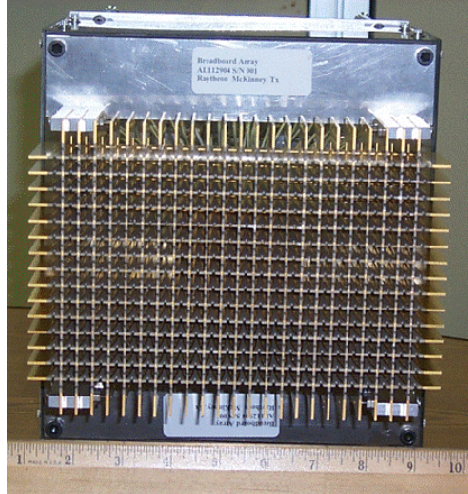


**Figure 13:** The egg crate structure of the front face of the Raytheon array.

The RF system testing in this effort required the configuration of the Raytheon array into four channels. The configuration chosen was four 8-element columns. As stated in Section 2, since these tests were performed at the low end of the array's operating frequency range, the array's eight columns alternated between feeds and terminations. A block diagram of the feed structure used in this effort is shown in Figure 14. It is broken down into three sections: the 32-element (four eight-element columns) array, the 8:1 combining network that defines the four channels, and the analog beamforming network. The analog beamforming network was used to take sum and difference antenna patterns of the entire array to compare to the results of the digital beamforming. Figure 15 shows a close-up view of the feed structure behind the array and the test setup in RASCAL.

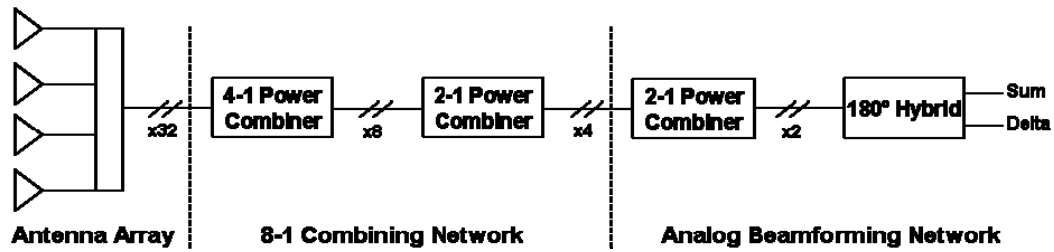


**Figure 14:** Block diagram of feed structure behind Raytheon array

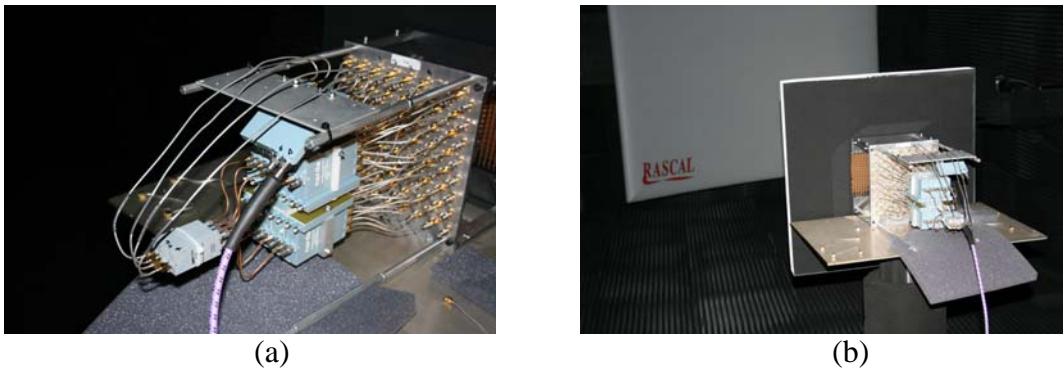
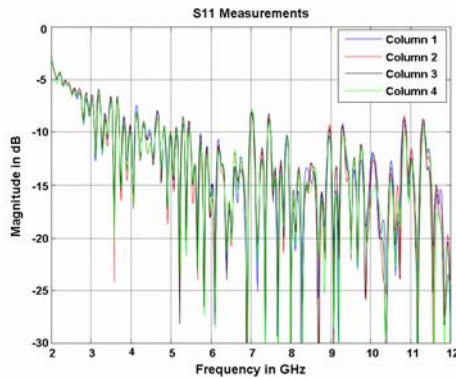
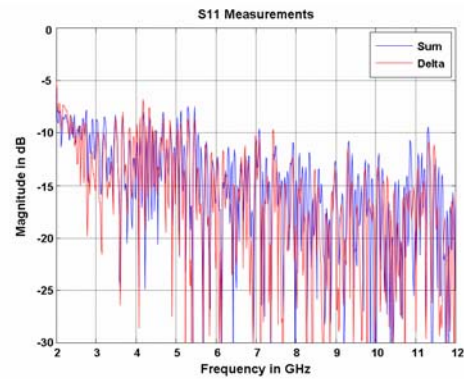


**Figure 15:** Close-up view of the feed structure behind the array (a) and the test setup in RASCAL (b)

In order to characterize the feed structure of the antenna, swept S-parameter measurements from 2-12 GHz were taken using RASCAL's Agilent 8510 Vector Network Analyzer. Return loss versus frequency of the four individual channels is shown in Figure 16a, and return loss of each of the sum and delta ports of the 180° hybrid is shown in Figure 16b. It is evident from Figure 16 that the antenna performance (with regards to matching) drops off at the lower frequencies (around 2-5 GHz). Figure 17a shows the insertion loss through one channel of the 8:1 combining network. The results are as expected, with loss being slightly over 9 dB and increasing with frequency. Figure 17b shows the insertion loss through both the analog beamforming network and the 8:1 combining network. These results are also as expected, with about 6 dB more loss coming from the extra 4:1 power dividing.

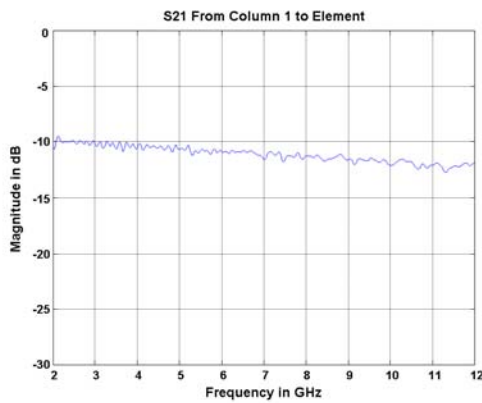


(a)

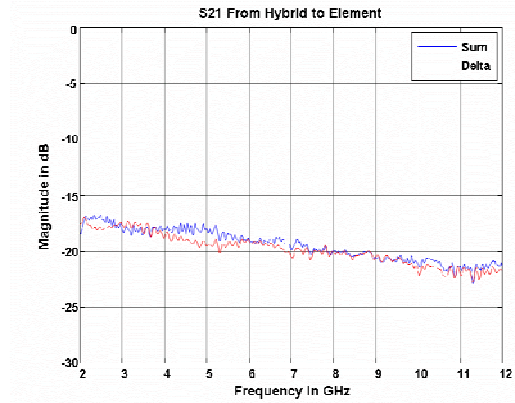


(b)

**Figure 16:** Return loss at each of the ports of the antenna feed structure, the four channels of the 8:1 combining network (a), and the two ports of the analog beamforming network (b)



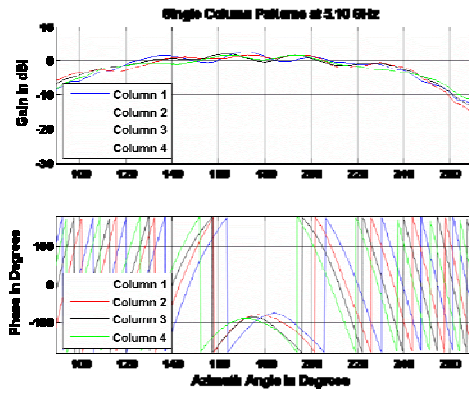
(a)



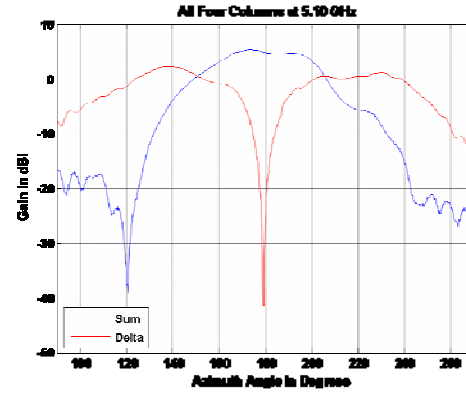
(b)

**Figure 17:** Insertion loss through one channel of the 8:1 combining network (a) and through both the analog beamforming network and 8:1 combining network

Antenna pattern measurements were conducted in RASCAL from 2-12 GHz, with the Raytheon array setup to scan at broadside. The orientation in the compact range is such that boresight (the antenna looking directly at the reflector) is labeled 180°. Elevation cuts of 90° to 270° were taken. Standard gain horn measurements were also taken to calibrate the gain of the antenna to dBi. This gain also includes the insertion loss discussed above. Figures 18, 19, and 20 show antenna patterns at 5.10 GHz, 7.5 GHz, and 10.2 GHz, respectively. The patterns included are calibrated gain and phase of each individual channel as well as the calibrated sum and difference patterns (the output of the analog beamforming network).

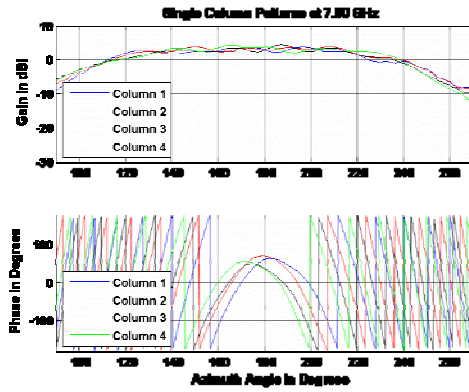


(a)

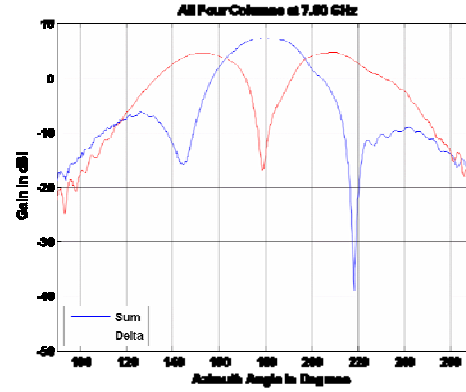


(b)

**Figure 18:** Single-column gain and phase (a) and combined sum and difference patterns (b) at 5.1 GHz

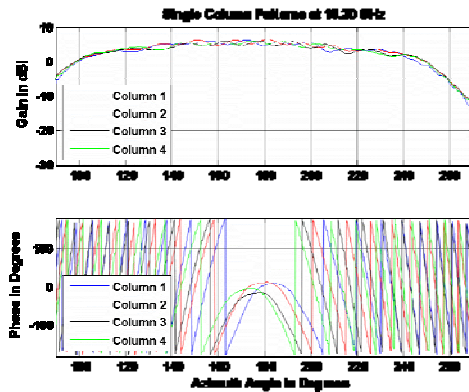


(a)

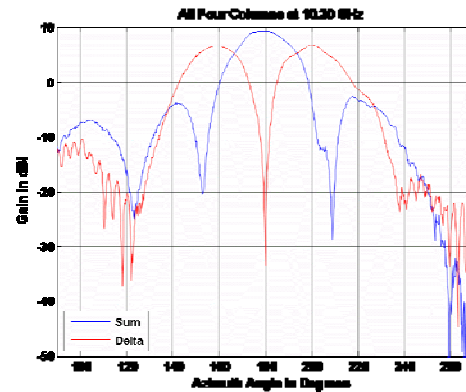


(b)

**Figure 19:** Single-column gain and phase (a) and combined sum and difference patterns (b) at 7.5 GHz



(a)



(b)

**Figure 20:** Single-column gain and phase (a) and combined sum and difference patterns (b) at 10.2 GHz

## 5.2. Digital Testing and Beamforming

Following the analog characterization of the antenna array, the full 4-channel digital receiver chain was set up in the RASCAL chamber. This included all of the RF String hardware as described in earlier sections. For digital testing purposes, a GPIB to Digital TTL converter box, manufactured by IOtech, was used to communicate with the range software. During a scan, the range software would send digital triggers to the IOtech box. These triggers were read over GPIB by the RF String control software and used to determine when the antenna was set at a specific angle/frequency so that data could be acquired. The current scan angle and frequency were also read over GPIB and incorporated into the filename for each data acquisition. A diagram of the test setup is shown in Figure 21.

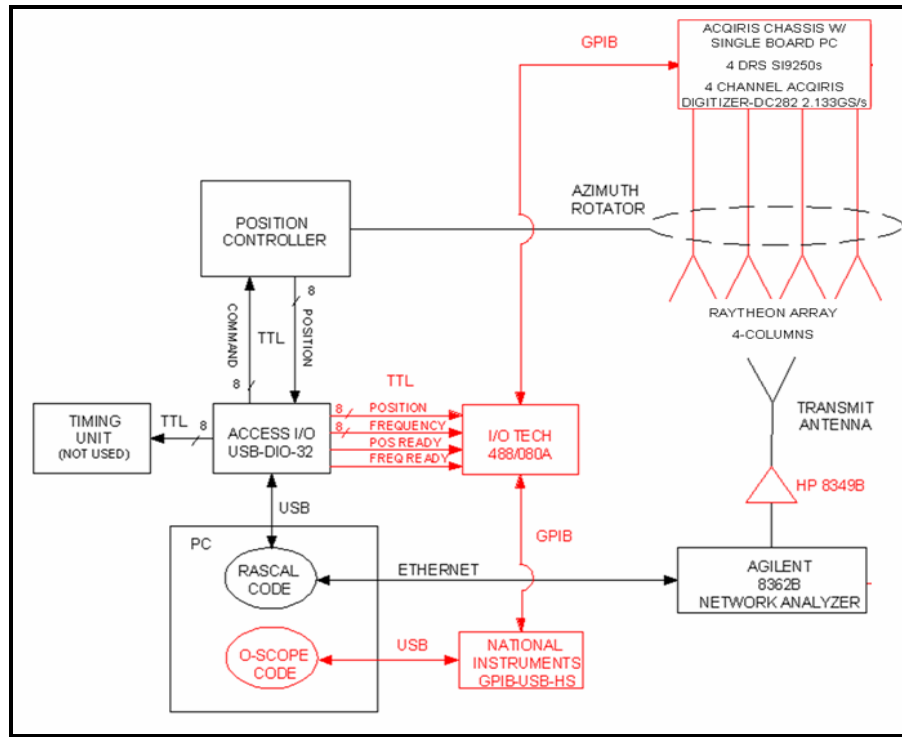


Figure 21: RASCAL Test Setup

### 5.2.1 Digital Calibration and Beamforming

As seen in the previous sections, the received signals from the phased-array are passed through wideband RF down-converters and then digitized at 2.133 GS/s with 10-bits of resolution. The digitized data is then recorded in a separate hard-drive to be processed off-line. This technique is often referred to as “poor-man’s DBF”, alluding to the fact that only a minimal amount of hardware is necessary since all processing is performed in software. This post-processing approach is appropriate for a laboratory environment, but in an operational environment it would be desirable to process the data in a near-real-time



fashion. This approach does lack the “real-time” feel of a digital beamforming system, but nonetheless provides a solid stepping stone in which to base initial system performance estimates and future directions for the testbed’s digital hardware.

The initial RF-string tests have solely focused on continuous-wave signals, enabling the processing algorithms to utilize the narrow-band array model common to the beamforming literature<sup>9</sup>. The model provides a great advantage for the initial tests in that array calibration and beam steering can be performed using phase shifts rather than fractional-delay sampling filters, integer-sample delays, or other wideband processing techniques. Due to the digitizer’s real output format, as opposed to a complex valued output stream, all calibration and weighting was performed in the frequency domain. This is a simple and well-known beamforming approach that, although requiring computationally intense Fast-Fourier-Transform (FFT) to extract the narrowband signal of interest, the resulting data can be simply weighted by a single complex multiplication. Once the data has been weighted, the user has the option to either continue processing in the frequency domain, or convert the data back into the time domain using the Inverse-Fast-Fourier-Transform (IFFT) for further processing. Figure 22 provides a basic block diagram of a beamforming system which processes the weighted data in the frequency domain.

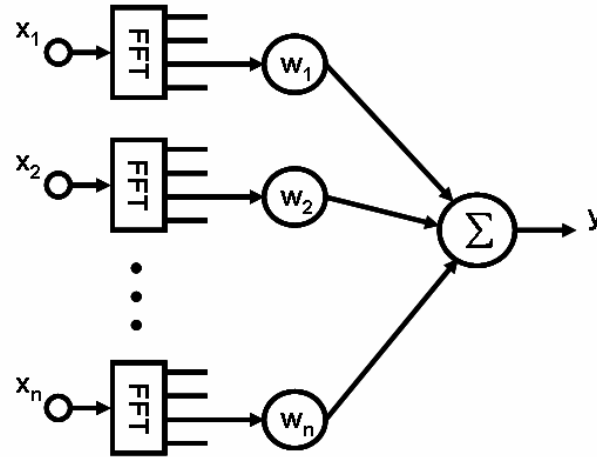


**Figure 22:** Narrowband Frequency Domain Beamformer

Although the analog components of the RF-String were demonstrated to have excellent magnitude and phase matching properties, the addition of the digital circuitry creates unacceptable phase and amplitude mismatches as seen in the top plot of Figure 23. Mismatches of these magnitudes are unable to produce the desired array patterns and thus need to be minimized using digital calibration. By applying the narrowband assumption, a similar calibration procedure as used in [5] was applied. Using the raw data collected at broadside, each channel’s narrowband response is measured using the FFT. One channel is then selected as the reference to which all channels are normalized resulting in a

uniform phase front at broadside as shown in the bottom plot of Figure 23. The center plot of Figure 23 shows the phase matching of the four channels prior to amplitude correction. The amplitude correction can be performed as a separate step or be included in the phase correction adjustment. The resulting normalization weights are then applied to their respective channel's recorded data at all other measured angles to correct for the phase and magnitude mismatches.

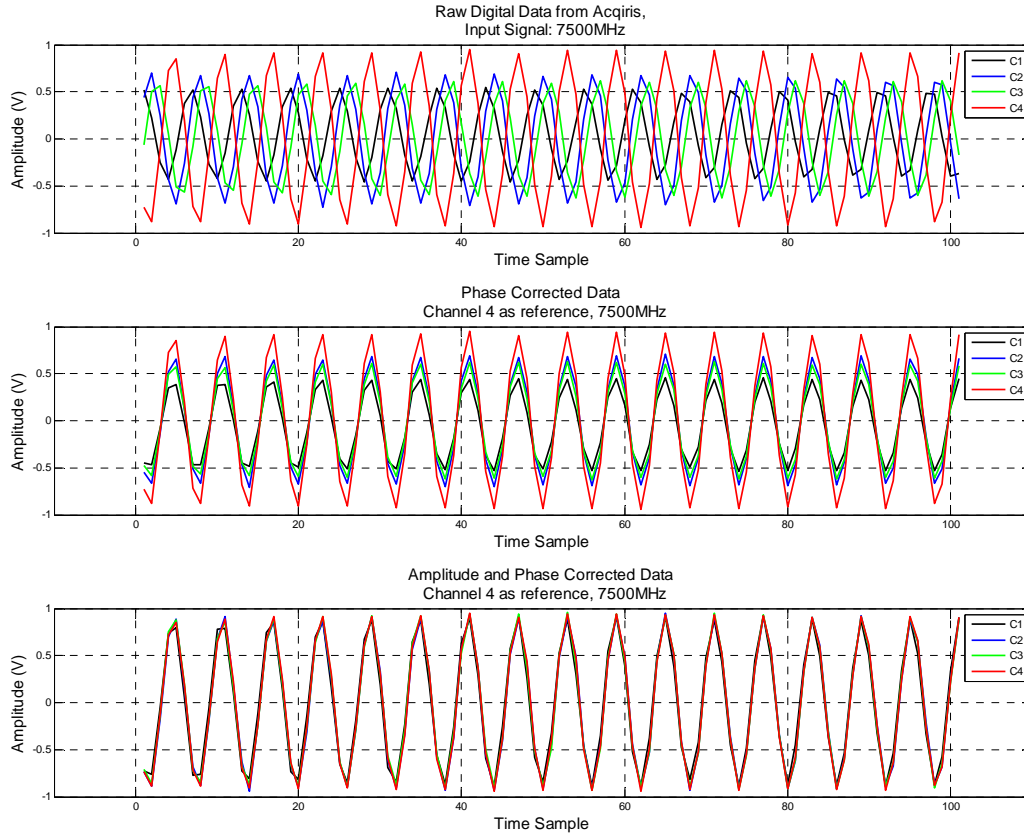


**Figure 23:** MATLAB Calibration Steps for Boresight Data at 7.5GHz

Due to the narrowband assumption, calibration was performed for each frequency in which the RF-string was tested. Once the calibration weights were calculated, it was possible to accurately apply linear-phase progressions across the array in order to perform beam steering. To ensure the calibration and beam steering was being performed accurately, the channel summation was processed in both the frequency and time domains. The resultant array patterns were then inspected and found to contain only slight differences, providing evidence that the implemented digital beamforming algorithms were working correctly.



## 5.2.2 Measured Results

Since the array was designed for 60-degree grating-lobe free scans at the upper-end of the system bandwidth, 18 GHz, and the array testing was performed in the lower-range of the system bandwidth, array patterns measured using consecutive columns lacked any clear array pattern definition. To present a more aesthetically pleasing final result, the spacing between columns was increased from using every consecutive output, to using every other column output. This technique doubled the spacing between the active columns and better approximated a half-wavelength spaced array for the frequencies under test. The measured array patterns for all frequencies were then compared to corresponding experimental simulations.

A subset of the measurements and simulations are shown below in Figures 24 and 25. For reference purposes, the measured and corresponding simulated array patterns are displayed on the same axes. The simulated patterns were modeled using a standard cosine element pattern along with the physical array architecture. The simulation versions did differ from the measured patterns, but provided a baseline as to the array pattern's basic shape and tendencies. It was noted that the measured and simulated patterns correlate well for all measured frequencies and steered look directions.

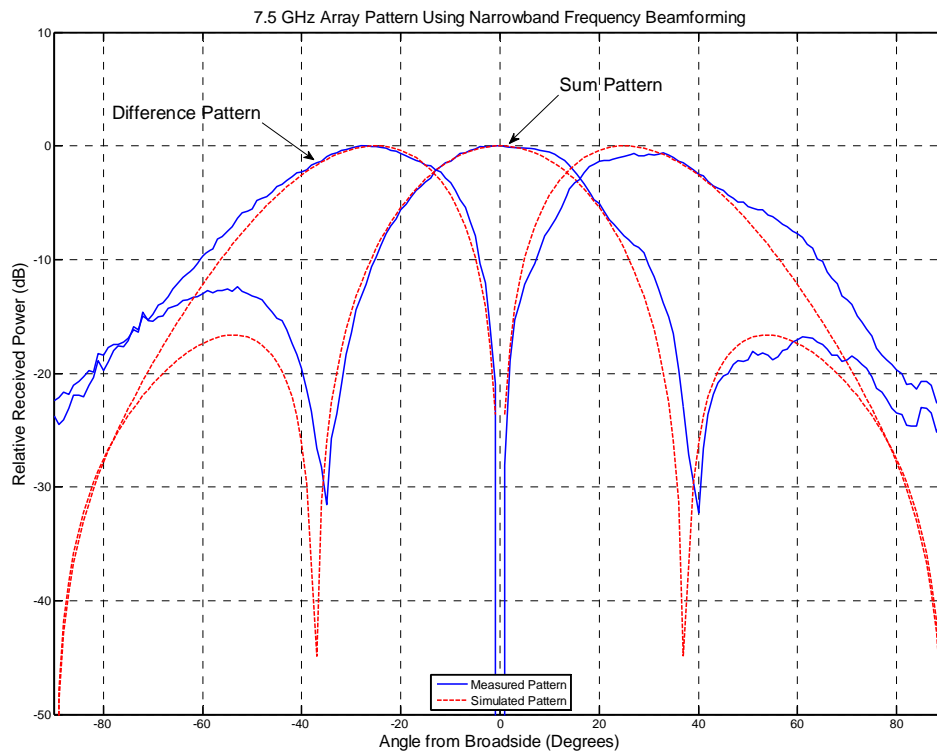


**Figure 24:** Broadside Array Pattern

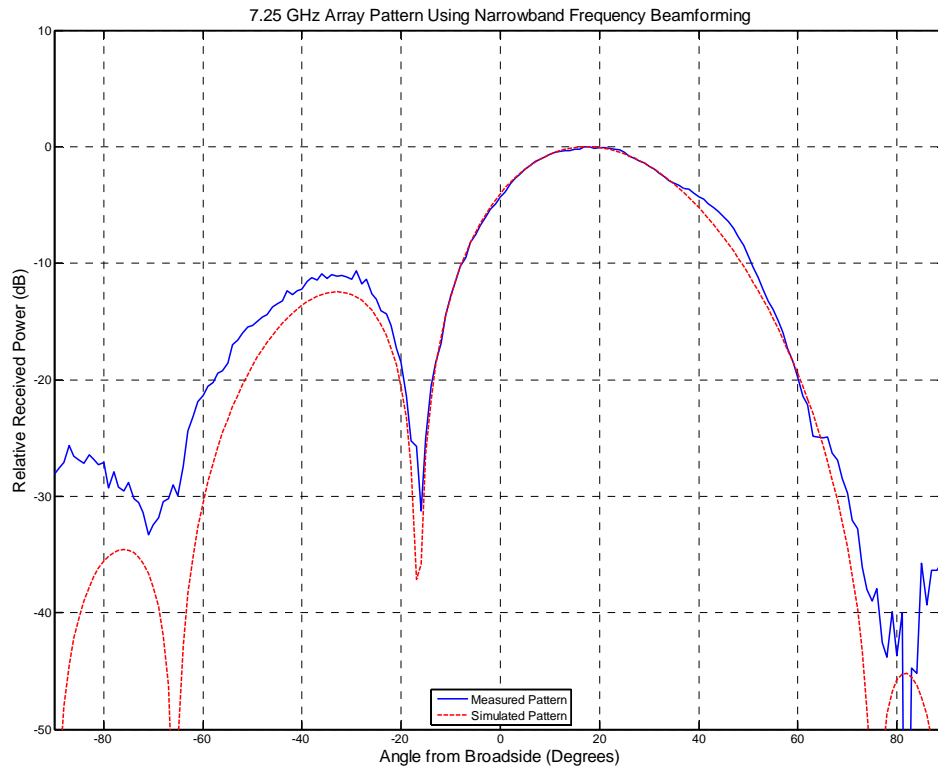


**Figure 25:** Scanned Array Pattern

For a direct comparison between analog and digital beamforming measurements, an attempt was made to replicate the sum and difference patterns shown in Figures 18-20 using digital beamforming. Figure 26-28 present the measured digital patterns overlaid onto the original analog measurements for a carrier frequencies of 5.2 GHz, 7.5 GHz, and 10.1 GHz. These measurements, along with similar patterns taken across the tested bandwidth, provide both proof and confidence that the wideband test bed is fully operational for our immediate testing purposes from 2 to 10 GHz.

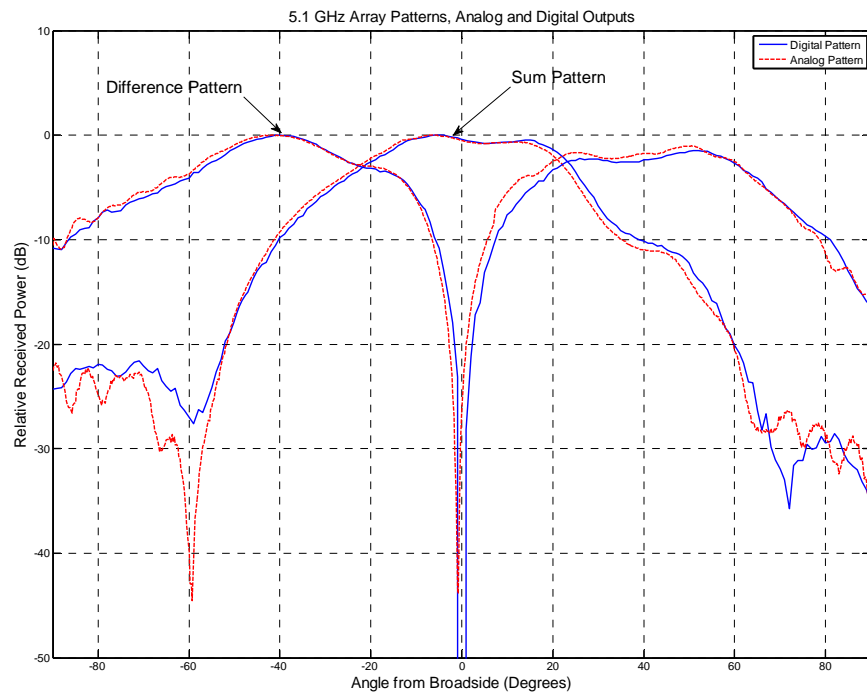


**Figure 26:** Direct comparison of analog vs. digital sum and difference patterns

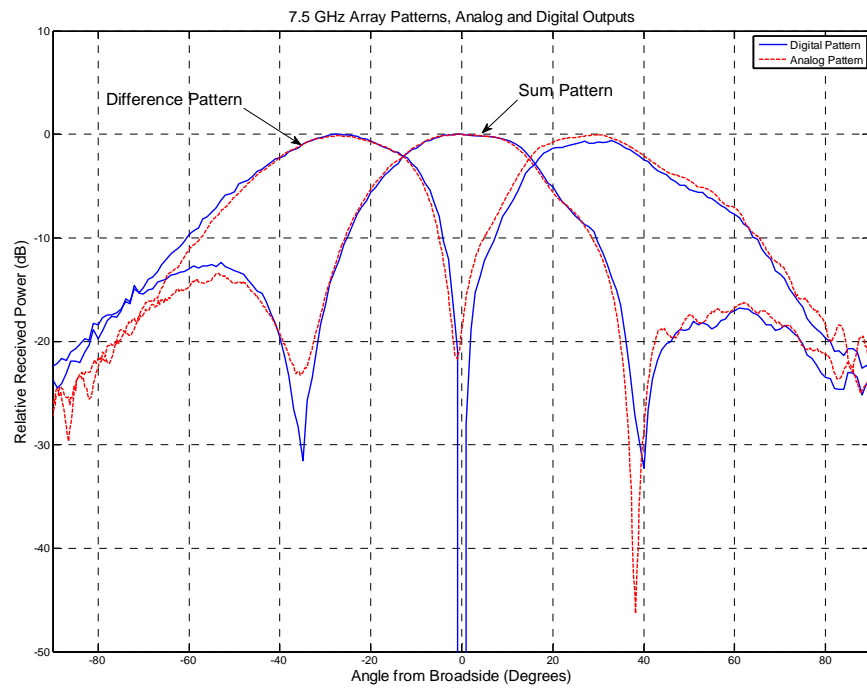


**Figure 27:** Direct comparison of analog vs. digital sum and difference patterns

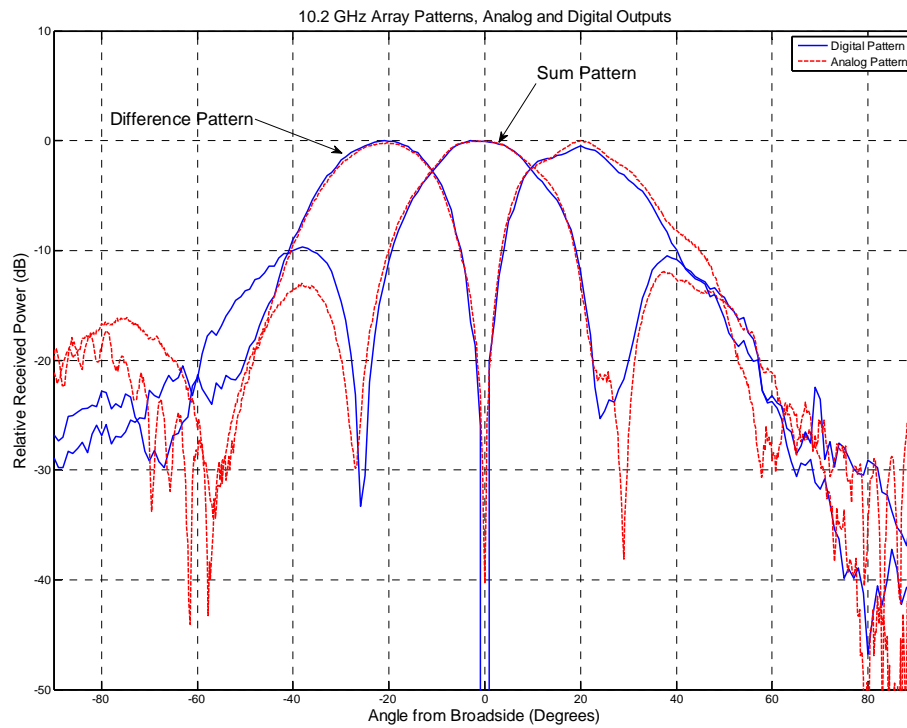


**Figure 28:** Direct comparison of analog vs. digital sum and difference patterns

## 6. Conclusions

A testbed system has been assembled that combines broadband phased arrays with multiple broadband digital receive channels. RF System Modeling, System Integration, and RF System Testing have been accomplished for this initial demonstration. Using data from the system, one can apply digital techniques to form digital antenna beams, as verified by comparison to analog antenna patterns.

The TELA testbed has been designed as an upgradeable system in order to assess current and future technologies at a system level. Future work planned includes the incorporation of broadband true time delay MMICs for analog calibration and beamsteering. The number of digital receiver channels will also be increased in order to increase the capability of the array. Future planned work also includes efforts to reduce the size and weight of the system while demonstrating even more advanced capabilities.

## 7. Acknowledgments

The authors wish to acknowledge the Dave Kuhl and the AFRL RASCAL facility for assistance in data collection.

## 8. References

- [1] B. A. Munk et al., “A low-profile broadband phased array antenna,” in *Proc. Antennas Propagation Soc. Int. Symposium*, Columbus, OH, Jun. 2003, pp. 448–451.
- [2] L. Corey et al, “Phased-array Development at DARPA,” *IEEE International Symposium on Phased Array Systems and Technology*, 14-17 Oct. 2003, pp. 9 – 16.
- [3] R. Mongia et al., “Wideband Plastic Packaged Highly Integrated TR MMIC with Variable Time Delay,” *GOMACTech-07 Proceedings*, March 2007.
- [4] T. Quach et al., “X-Band Receiver Front-End Components in Silicon Technology,” *GOMACTech-07 Proceedings*, March 2007.
- [5] D. Spendley et al., “Initial demonstration of an X-band digital beamforming (DBF) receive array,” *IEEE Aerospace Conference Proceedings*, March 2006.
- [6] Pozar, David M., *Microwave Engineering*, 3<sup>rd</sup> Edition, Wiley, 2005.
- [7] Syscalc Version 6.1.8, Arden Technologies Inc.
- [8] Advanced Design System (ADS) 2006A, Agilent Technologies.
- [9] Van Trees, Harry L., “Optimum Array Processing”, John Wiley and Sons, Inc, New York, 2002.

# **A Transportable VHF Ground Plane Antenna Range for Azimuthal Pattern Measurement**

Andrew Adrian, Texas Instruments and Joseph M. Huk, Visteon Corporation

## **Abstract**

Traditionally, automobiles have only had need for one antenna element that served a dual band use, MW-AM and VHF-FM. When the antenna elements consisted of single quarter-wave VHF monopoles using the vehicle sheet metal as a ground plane, electrical considerations related to the antenna pattern were not significant nor varied enough from installation to installation to justify antenna pattern measurements, even at VHF. In the last 20 years, significant effort in automotive antenna design has taken the AM/FM antenna from a quarter-wave monopole design to a variety of reduce height masts and concealed antenna element structures on many vehicle body styles. This is only possible with the use of an antenna range for pattern design. The antenna pattern information is also of interest to the rest of the radio reception system which needs the information in the process of the radio receiver design, especially for these vehicles with concealed antennas. Not only did this necessitate a technical challenge to make antenna pattern measurements at relatively low frequency on vehicles of significant electrical dimensions, but also maintaining the security of publicly unreleased automobile designs. Independent of this is the site improvement expense of a facility that is permanently installed. As a result, what is described in the following paper is a transportable VHF ground plane antenna range for azimuthal pattern measurement. This transportable facility is designed to successfully perform the technically challenging automobile VHF measurement after setup on an automotive manufacturer's premises where privacy and security are in the absolute unquestionable control of the automobile developer and manufacturer.

## **1 Motivation**

The need for automobile antenna pattern data has grown significantly in the last 20 years. As most vehicles came with AM/FM radios by the mid-1980's, car manufacturers sought ways to enhance the appearance of their vehicles while at the same time saving money. A resurgence back to concealed antenna designs began in that same time period. By 1995 teams at many original equipment manufacturers (OEM) had reintroduced AM/FM antenna systems with elements embedded in the rear glass. In order to avoid the pitfalls that some OEM's suffered in the 1970's with their windshield antennas, all the design teams understood that every vehicle body design needed a unique antenna element design



– this was overlooked in the past. Hence a need for automotive antenna pattern capability grew.

Not only did car manufacturers need the capability, but so did the antenna system suppliers. All automotive antenna ranges were built as permanently installed structures. This typically cost more than \$1M including land. Additional expense also was incurred with yearly property taxes due to the extensive site improvements incurred from buildings, and turntable installations.

With suppliers needing to use prototype vehicles at their facilities (away from the car manufacturer's secure proving grounds), issues of availability and security began to cause extreme hardship in the design process. Prototype Vehicles needed to be securely transported to the antenna supplier and left there for periods of 1 to 2 weeks. While the car was with the supplier, no one else could access the vehicle during off hours for other testing. The car manufacturer was also very uneasy about their secret prototype vehicle not being within OEM control.

If all of these needs are pulled together, the best solution is a transportable antenna test facility. It does not have a significant site improvement cost – no large property tax increase. The facility can be set up at the car manufacturer's secure proving ground for a short period (1 to 2 weeks) to allow for antenna element design using prototype vehicles. While the vehicles are not being used for antenna development (12 – 16 hours per day) other compatible testing can be performed using the same vehicle. No secure transportation is required. And finally, the initial capitalization cost for this type of facility is far less than the cost of a permanently installed facility.

## **2 Requirements**

Before commissioning such a facility, a baseline set of requirements need to be established. These requirements can be grouped into four categories. First is the pattern taking capability. The second requirement category is the facility transportability. Third there is the mass of a vehicle that can be tested. Fourth is the instrumentation that is required to perform the testing.

### **2.1 Patterns**

The minimum pattern testing capability required is vertical, horizontal, and circular polarization horizon cut patterns from 70 to 108 MHz. Performance down to 50 MHz and up to 2 GHz for horizon patterns would be useful and in all consideration, very achievable. Circular polarization patterns could be performed by coherent addition of a vertically and horizontally polarized antenna pattern.

### **2.2 Transportability**

It must be possible for the whole facility to be set up and operated in an open space area that is adequate in size to approximate a far field wave front. This means that it must be possible to set up the turntable with 2 trained people in a “short” period of time. In this case “short” is less than 1 day. Disassembly and storage should also take a “short” amount of time. The extreme majority of parts that need to be moved into place must be light enough for a single person to lift without the need for custom tools. Where necessary, the rest of the parts must be light enough for 2 people to maneuver. A minimum of transport trailers is required to move the facility. In this case 2 trailers are required, and they can each be individually pulled by the transmit and instrumentation van. All trailers and the tow vehicle cannot exceed 8 ½ feet wide.

### 2.3 Vehicle Capacity

Since the turntable must be capable of measuring the antenna patterns of antenna systems installed on vehicles, the system must have the capacity to load onto and rotate vehicles of significant weight and length. The heaviest vehicles typically are crew cab diesel powered pickups with dual rear wheels on each side (Fig. 1.) The longest vehicles are full size extended cargo vans (Fig. 1.). It is desirable to be able to place the antenna element of any vehicle in the center of the turntable even if this produces an asymmetric load on it. Gross vehicle weight to be turned is 5 to 6 ½ tons – although rarely. Typical usage is 0.75 to 3 tons. Since the turntable is above ground, a ramp system that is adequate to drive the vehicle up onto the turntable is necessary. The ramp system must accommodate the shortest wheel base vehicles with the lowest clearance (5 inches) (Fig. 1.) as well as the longest with the highest clearance.

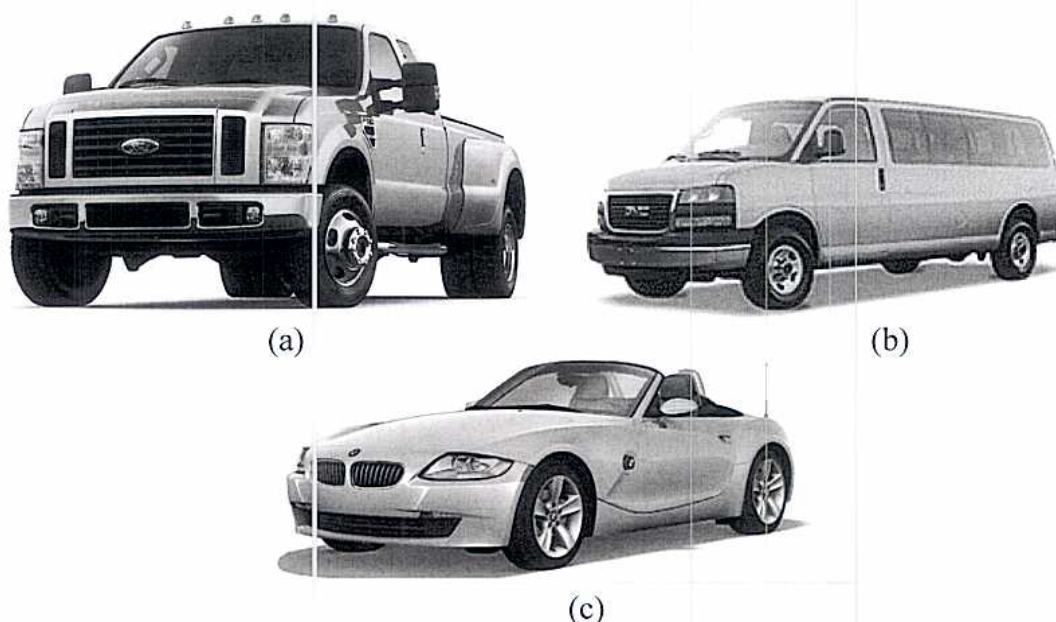


Figure 1. Vehicles exhibiting the limiting characteristics for the system capacity. (a) Heavy Vehicle. (b) Long Vehicle. (c) Low Vehicle



## **2.4 Instrumentation**

Instrumentation required for this mobile antenna measurement facility includes at least one network analyzer, one spectrum analyzer, an angular position encoder, manual turntable rotation control, automated data acquisition and processing, electrical power generation, external power input, transmit antenna, transmit antenna mast, and transmit antenna position control. The network analyzer allows for coherent range calibration and measurements to support circular polarization as well as amplitude with relative phase measurements. By receiving broadcast signals, the spectrum analyzer allows for a simple method for comparing AM antenna performance to a standardized antenna.

Minimum requirements for the angular position encoder are relative position location, direction of rotation, and zero setting. For safety, the turntable rotation control must be manually actuated. A controller for automated data acquisition and processing is required. For security, it must also be removable from the mobile environment. The facility must also have self contained power generation capability in the form of an AC generator as well as an inverter for operation of small electrical loads. 240 VAC must be available external to the vehicle as well as internally. The facility must also be able to utilize externally supplies 240 VAC.

The transmit antenna is linearly polarized because a cross polarized type of antenna could not be easily stowed for transport. Hence, two linear measurements are required to produce a circular polarized source pattern. The antenna also has to break down for transport to a width that is less than 8 ½ feet long. Its mast and positioning equipment are necessary to elevate and point it so it is oriented parallel to the range and can be simply rotated to change polarization.

## **3 Design**

In its completed form the transportable antenna range consist of 4 major components:

1. The Transmit and Instrumentation Van,
2. The Turntable,
3. The Supplemental Parts Trailer, and
4. The Data Acquisition Software.

### **3.1 Transmit and Instrumentation Van (TIV)**

The TIV is a 2003 Cargo Van with a 7.3L diesel engine. In addition, 4 Wheel Drive capability has been added along with enhanced rear suspension.

Between the rear fender wells on the floor of the chassis, a 30 foot pneumatic mast has been installed. (Fig. 2b.) A permanently installed rear door ladder and walking platform on top of the vehicle have been added for accessing the transmit antenna that resides on the top of the mast (Fig. 2.) On top of the mast is a positioning unit that can tilt the antenna in a vertical plane (pitch control), pan it in the horizontal plane (yaw control) or



rotate it on its axis (roll control). Additionally, a camera is installed at the top of the mast and provides video display in the direction that the antenna is pointed.

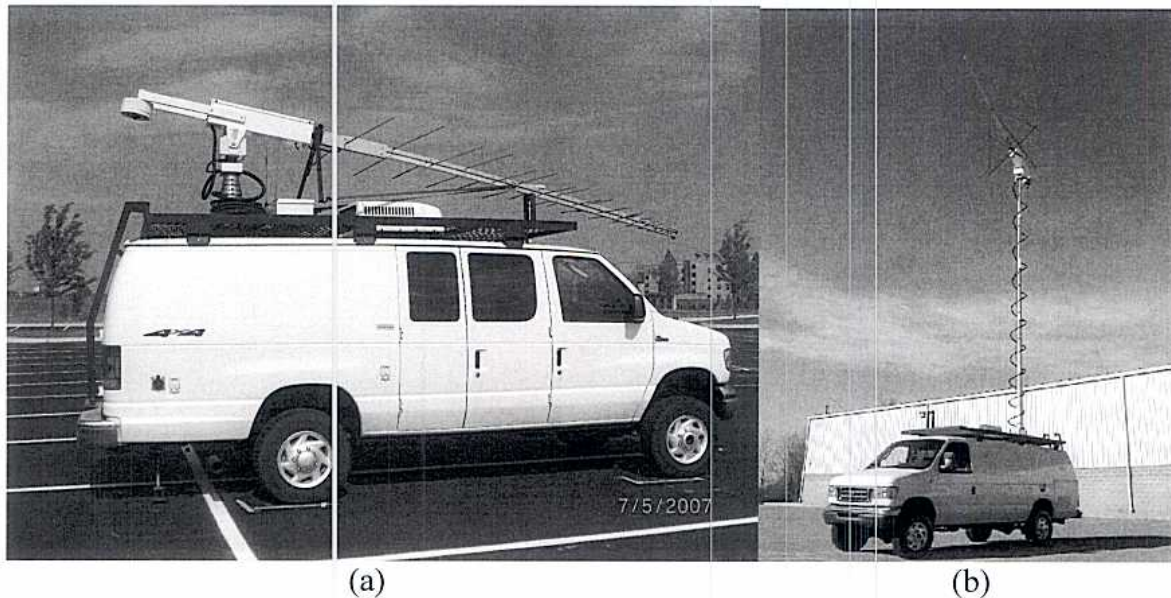


Figure 2. TIV with (a) mast stowed and (b) elevated.

The transmit antenna is installed at the top of the mast. It is a linearly polarized log periodic dipole array. It operates down to 50 MHz and up to 1300 MHz. Overall length is 12 feet. The longest element is 10 feet and the shortest is 5 ½ inches (Fig. 3.)

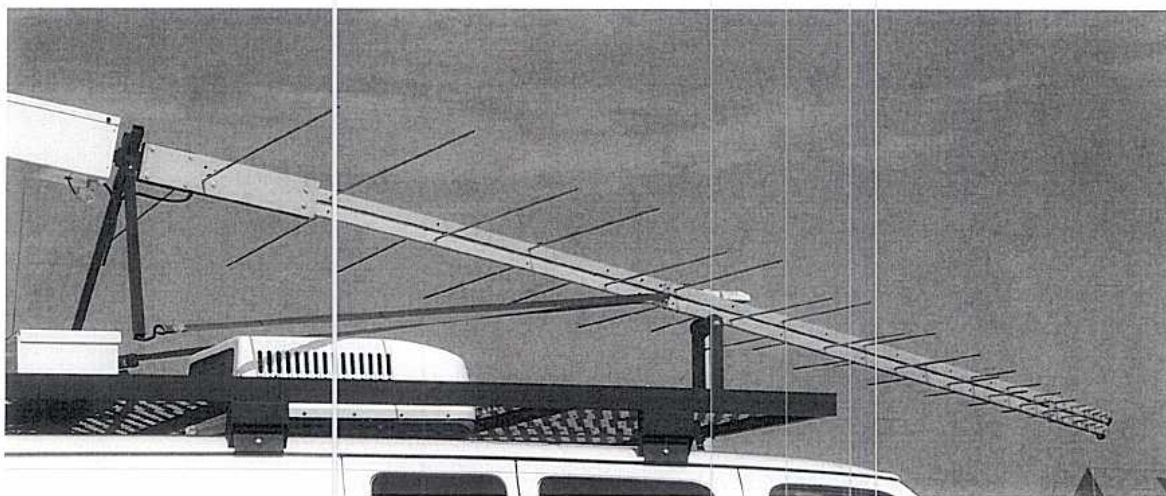


Figure 3. 50 to 1300 MHz LPDA used for signal transmit.

Inside the TIV, are 2 rows of bucket seating. The rear seats can be rotated to face 3 instrument racks that are located just forward of the mast installation. On the instrument racks are mast, power generation, camera, and antenna positioning controls. Test and measurement equipment is also installed on the racks. The test equipment is intended to



consist of 2 HP 8753 network analyzers, and 2 Agilent 8560 EC series spectrum analyzers.

AC power can be routed into and/or through the TIV in several ways. On board is a 7.2 KW, 240 VAC, 2-Pole generator. One pole is routed into the rack, and a 240 VAC output is available on the outside of the TIV. There is also an additional connector on the outside of the TIV for 240 VAC input. Power is automatically switched from external to on board generation when the generator is turned on. This controller is also mounted in the racks. On this controller are AC and DC voltage status meters. If 240 VAC is not available, and adaptor cord can be fitted from a 120 VAC outlet to one pole of the 240 VAC input connector in order to only power the racks. Finally there is an inverter in the racks that gets its power from the TIV batteries. It can only power the rack instrumentation. The same batteries are used to start the generator, or the TIV, and can be charged by either the vehicles alternator or the AC generator via a 12V battery smart charger.

### 3.2 Turntable (TT)

The first question with respect to the TT is how big can the diameter be made? Two competing requirements are the desire for an infinite ground plane and the need to be able to move and set it up. In the end the result was a 40 foot diameter ground plane. This size was chosen because it was as large of a structure that could be reasonably be set up, taken down, and moved. Since the geometry of the ground plane is circular, the entire surface of the TT need not be load bearing. A section of the turntable that is roughly 20 feet wide, and 32 feet long was designed to be load bearing. The rest of the turntable was made as light as possible (Fig. 4.)

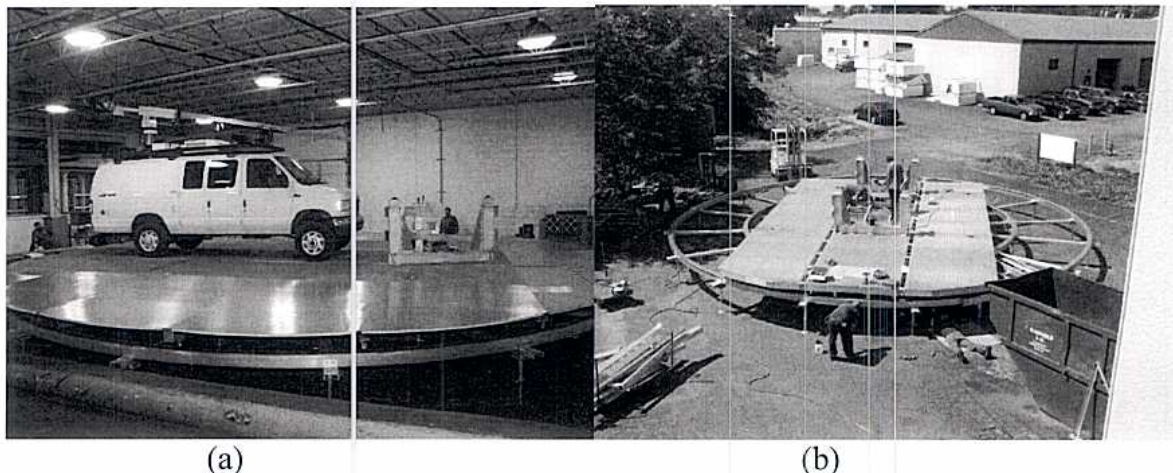


Figure 4. (a) Turntable with TIV. Dull areas are load bearing. (b) Turntable showing load bearing section without lighter ground plane areas installed.

In order to facilitate tear down and transport, the non-load bearing sections are removed and packed into the Supplemental Parts Trailer (SPT). The remaining load bearing



section is divided into 3 hinged sections. Two of the sections fold up and bolt into travel brackets. This entire stowed portion of the TT permanently lives on top of a trailer (Fig. 5a.) The entire rotating structure is then secured to the trailer and ready for transport (Fig. 5b.) Also permanently attached to the trailer are the motor, main drive gear, drive chain, gear box, and position encoder interface gear. Virtually all the components of the TT are made from aluminum stock to minimize weight.

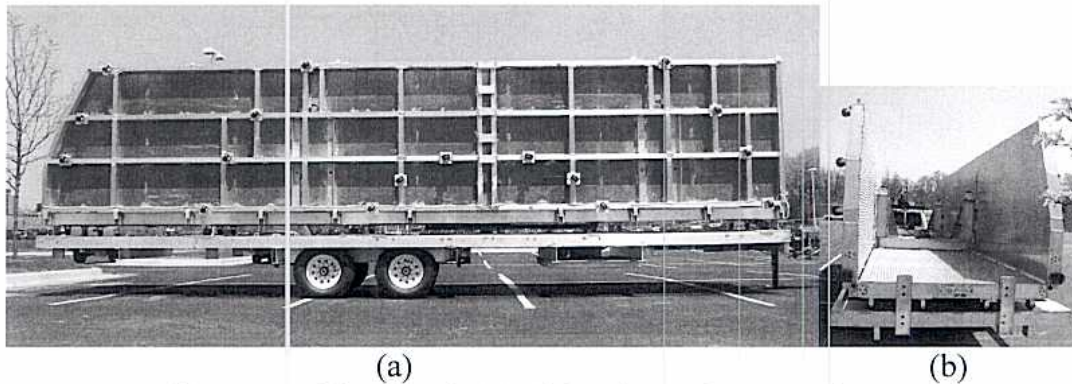


Figure 5. TT Trailer stowed for travel. (a) Side View. (b) Rear View.

During operation, the TT rides on a set of 3 concentric tracks. The tracks are either part of the permanent trailer structure or set up on the ground (Fig. 6.) Once the tracks are set up and leveled, the wings are folded down; additional support bracketing is installed along with the non load bearing sections of the ground plane. All ground plane sections have at least a 1 inch over lap to the next section. Once set up is complete, the ramp system is installed and the travel brackets are removed and stored in the SPT. When all is complete, the top of the TT is approximately 4 feet above the ground.

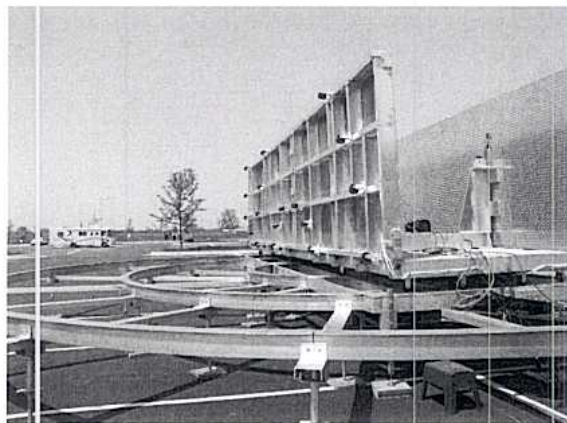


Figure 6. Tracks that the TT rides upon.

There are 3 major electrical interfaces between the TT and the TIV. The first is the turntable motor control. This consists of a multi-conductor cable that plugs into the 220VAC output of the TIV and routes to a relay matrix at the TT. Another multi-conductor cable set routes from the TT to a control switch panel on the racks in the TIV.



This control simply reverses the leads on the 240 VAC motor to control the direction of the TT rotation. The second electrical interface is the encoder output that is fed back to the TIV. The encoder is a quadrature encoder that provides output that triggers RF measurements at 1 or 2 degree intervals of TT rotation. Finally, the third interface is a low loss coaxial cable from the vehicle under test that is fed down through a hole in the center of the TT back to the instrumentation in the TIV.

### 3.3 Supplemental Parts Trailer (SPT)

The SPT was included in the design simply do to the real weight towing limitations of the TIV. With approximately 15,000 pounds of TT to move from place to place, it was divided into 2 loads – the load bearing folding part and the supplemental parts that were not part of the TT trailer. Consequently, an additional trailer was procured for the purpose of transporting the supplemental parts (Fig. 7.)



Figure 7. Supplemental Part Trailer behind a tow vehicle.

### 3.4 Data Acquisition Software (DAS)

DAS utilizes the angular information from the position encoder to trigger RF data sweep events. At uniform intervals of TT rotation, up to a 21 point  $S_{21}$  sweep of RF data can be taken with a network analyzer where the transmit antenna is connected to port 1 and the coaxial cable from the TT is connected to port 2. All instrumentation is GPIB interfaced with the controller using a LabView [1] operating environment. As the turntable makes one revolution, patterns for up to 21 frequencies can be acquired. This is the standard setup for measurements above 50 MHz.

Measurements are performed in vertical or horizontal polarization. Spin linear is not possible. If a circular polarized gain result is desired, a coherent sum with the appropriate  $90^\circ$  phase shift on one pattern is computed from the vertical and horizontal amplitude and phase measurement results. Slant polarization patterns can be computed in an analogous manner.

For AM pattern measurements, known broadcasts are used as the RF sources and a spectrum analyzer is used as the receiving instrument.



Typically, maximizing power gain (or directivity), as defined in the ANSI IEEE Std. 149-1979, for a VHF automotive antenna is not the desired goal. Traditionally, a minimum of azimuthal variation is desired and a statistical average gain figure of merit is computed. For each frequency, the amplitude pattern is converted to linear voltage units, integrated in a polar coordinate system and compared to a perfectly omni-directional pattern of equal area to determine the average voltage. The result is then converted to back into logarithmic units. The other figure of merit is a maximum-to-minimum ratio. As it sounds, it is simply to ratio of the pattern peak to its deepest null, again in log units. As a result, the desire is to maximize the average gain while minimizing the maximum-to-minimum ratio. Finally, the standard gain reference is a resonant dipole at the frequency of test. This results in gain units of dBd – dB relative to a dipole.

## **4 Geometry, Analysis, and Prove Out**

Range length can be set between 150 and 300 feet. The transmit antenna is approximately 32 feet above the ground. The top of the TT is 4 feet off the ground. The ground plane is 40 feet in diameter. And the phase center of the calibration antenna, a resonant dipole, is set at 4.6 feet above the center of the ground plane. This sets up the base line for analysis and expected performance of the measurement system.

### **4.1 Field Uniformity**

Field uniformity was not initially specified, and the system was not designed to directly meet a uniformity criteria. Certainly, the larger the ground plane, the more uniform the field distribution results become. As mentioned earlier, the diameter was chosen by the largest possible ground plane that could be taken down and set back up. Simulations were performed on the range geometry to be used as part of the verification process once the range was operational.

### **4.2 Computer Simulations**

Since the primary band of operation of this system is 87.9 to 107.9 MHz, these are the frequencies over which the electromagnetic simulations were carried out. Prior to publication, simulation was performed from 87.9 to 93.9 MHz. The simulations were performed using WIPL-D [2].

#### **4.2.1 Transmit Antenna**

The transmit antenna is a 28 element LPDA with a 12 foot boom. It has an average scale factor of 1.136. This would be a rather intense and time consuming simulation all by itself. However, including it as part of the range simulation was beyond the capability of the computer performing the simulation. Additionally, opportunity for error due to the transmit antenna model was great. The first engineering approximation was made. According to the histogram developed by Carrel [3], as published in Kraus [4] the LPDA should have a free space gain of approximately 6 dBi.

With this information, a dipole spaced a  $\frac{1}{4} \lambda$  in front of an infinite ground plane was used. As a result we have a source with gain that approximates the LPDA gain – approximately 7.5dBi.

#### **4.2.2 Vertical Polarization Simulation**

In the vertical polarization simulation, the range was set at 150 feet from the dipole source. The transmit antenna was 30 feet above the ground and oriented vertically. It was also placed a  $\frac{1}{4} \lambda$  in front of an infinite ground plane. The turntable was located 150 feet away, horizontally, from the transmit antenna. Co- and cross-polarized receive E-field distributions were calculated in a square from  $\pm 12$  feet of the center of the turntable. In elevation, the field was calculated at 4.6 feet above the turntable. A pec was used to simulate the earth below the turntable. The simulation was also performed without an earth ground in a effort to bound the results with a “real” ground. Results are illustrated in Table 1. and Figure 8.

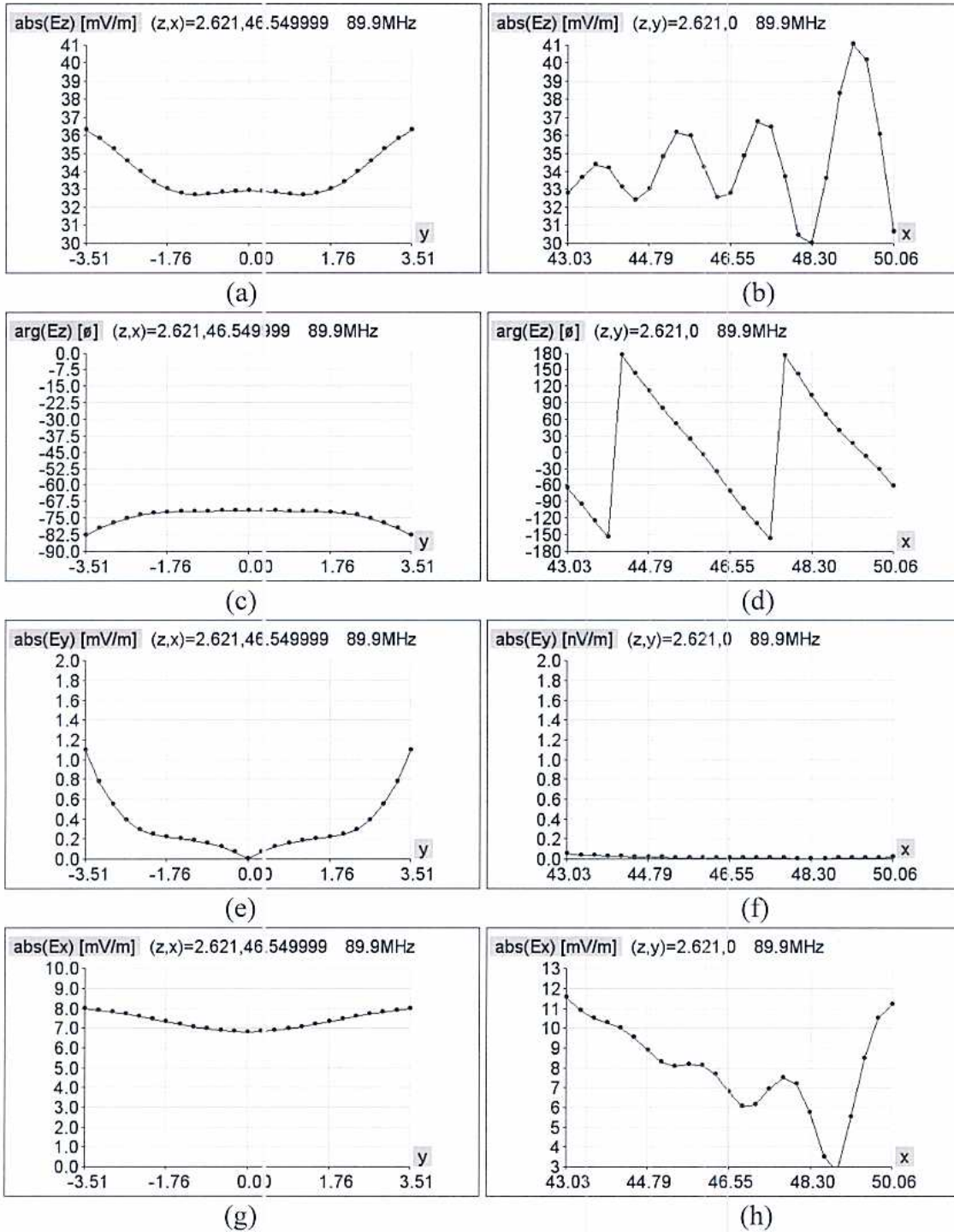
Table 1. lists the simulation conditions and the resultant field strength range over the  $\pm 12$  foot quiet zone over the center of the turntable. In the simulation, the +z-direction was up, and the +x-direction is the horizontal propagation direction from the transmit antenna to the turntable. The vertical co-polarization shows very good flatness for the portion of the band that is illustrated. Cross-polarization ( $E_y$ ) is also pretty good for such a low frequency measurement system.



Ground Type	Transmit Polarization	Receive Polarization												87.9	88.9		89.9		90.9		91.9		92.9		93.9	
		Ex (Long. X-pol)	Magnitude (mV/m)	Max (mV/m)	Min (mV/m)	(dBc)	12.51	-7.37	13.07	-7.31	13.45	-7.04	13.68		-6.59	13.59	-6.25	13.18	-6.03	12.58	-5.92					
PEC	Vertical	Ey (X-pol)	Magnitude (mV/m)	Max (mV/m)	Min (mV/m)	(dBc)	5.27	-14.88	5.46	-14.90	5.51	-14.79	5.39	-14.68	5.19	-14.61	4.93	-14.57	4.64	-14.58						
		Ez (Co-pol)	Magnitude (mV/m)	Max (mV/m)	Min (mV/m)	(± dB)	40.15	1.38	40.94	1.30	40.84	1.30	39.96	1.36	38.50	1.40	36.99	1.47	35.27	1.52						
		Ex (Long. X-pol)	Magnitude (mV/m)	Max (mV/m)	Min (mV/m)	(dBc)	29.24	-6.15	10.88	-6.46	10.84	-6.78	10.56	-7.08	9.99	-7.48	9.30	-7.93	8.59	-8.37						
	Horizontal	Ey (Co-Pol)	Magnitude (mV/m)	Max (mV/m)	Min (mV/m)	(± dB)	61.89	9.08	64.41	8.99	65.52	8.85	65.40	8.75	63.94	8.64	61.73	8.51	59.08	8.38						
		Ez (X-pol)	Magnitude (mV/m)	Max (mV/m)	Min (mV/m)	(dBc)	10.98	-5.94	11.68	-5.84	11.99	-5.90	11.91	-6.04	11.48	-6.27	11.15	-6.36	10.76	-6.41						
		Ex (Long. X-pol)	Magnitude (mV/m)	Max (mV/m)	Min (mV/m)	(dBc)	8.37	-11.00	8.62	-11.00	8.69	-10.97	8.60	-10.97	8.39	-11.00	8.08	-11.01	7.73	-11.00						
No Ground	Vertical	Ey (X-pol)	Magnitude (mV/m)	Max (mV/m)	Min (mV/m)	(dBc)	4.61	-16.18	4.73	-16.21	4.82	-16.09	4.76	-16.11	4.64	-16.15	4.48	-16.13	4.28	-16.14						
		Ez (Co-pol)	Magnitude (mV/m)	Max (mV/m)	Min (mV/m)	(± dB)	43.00	3.21	44.27	3.21	44.68	3.25	44.27	3.26	43.21	3.24	41.66	3.24	39.84	3.24						
		Ex (Long. X-pol)	Magnitude (mV/m)	Max (mV/m)	Min (mV/m)	(dBc)	29.70	-3.38	30.58	-3.74	30.73	-3.94	30.41	-4.24	29.77	-4.47	28.69	-4.62	27.43	-4.87						
	Horizontal	Ey (Co-Pol)	Magnitude (mV/m)	Max (mV/m)	Min (mV/m)	(± dB)	42.53	10.24	43.83	10.14	44.04	10.02	43.43	9.87	42.89	9.83	41.58	9.89	39.64	9.94						
		Ez (X-pol)	Magnitude (mV/m)	Max (mV/m)	Min (mV/m)	(dBc)	11.83	-0.87	12.14	-1.01	12.36	-1.01	12.25	-1.12	12.08	-1.18	11.70	-1.12	11.02	-1.18						
		Ex (Long. X-pol)	Magnitude (mV/m)	Max (mV/m)	Min (mV/m)	(dBc)	0.00		0.00		0.00		0.00		0.00		0.00		0.00		0.00	-1.18				



Table 1. Simulation results using WIPL-D. E-field variation is indicated in (mV/m) and for all the co-polarized cases, the  $\pm$  range in dB is also indicated. In the cross-polarized cases, the highest cross-polarized level below the lowest co-polarized level is indicated in dBc.



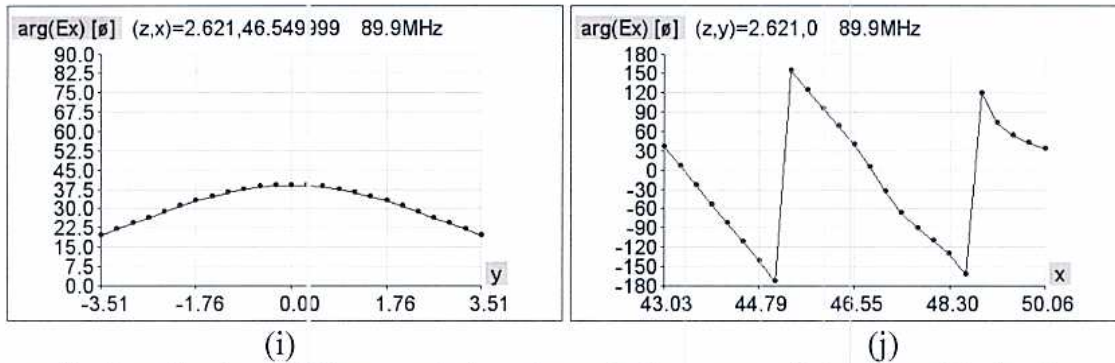
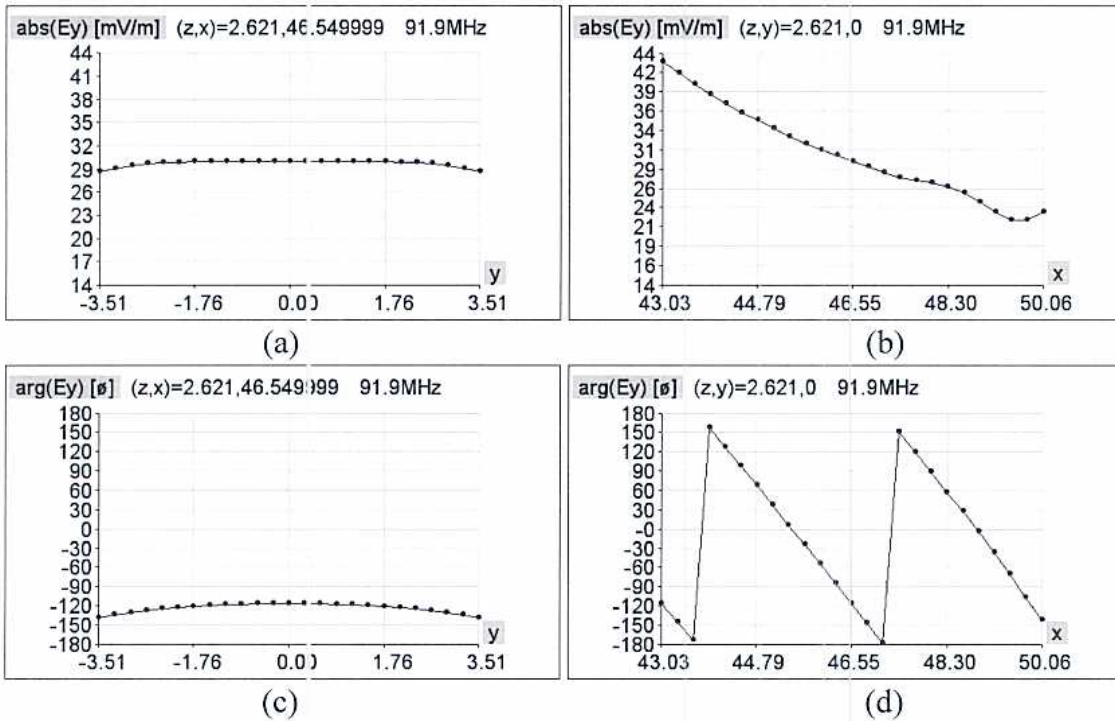


Figure 8. Amplitude and Phase variation through the center of the turntable for the vertically polarized transmitted signal with PEC ground plane at 89.9MHz. (a) Transverse Cut, Co-Pol. Magnitude. (b) Longitudinal Cut, Co-Pol Magnitude. (c) Transverse Cut, Co-Pol. Phase. (d) Longitudinal Cut, Co-Pol Magnitude. (e) Transverse Cut, Cross-Pol. Magnitude. (f) Longitudinal Cut, Cross-Pol Magnitude. (g) Transverse Cut, Longitudinal Cross-Pol. Magnitude. (h) Longitudinal Cut, Longitudinal Cross-Pol. Magnitude. (i) Transverse Cut, Longitudinal Cross-Pol. Phase. (j) Longitudinal Cut, Longitudinal Cross-Pol. Phase.

#### 4.2.3 Horizontal Polarization Simulation

The same simulation was performed for the horizontal polarization as was performed for the vertical polarization except for the alignment of the transmit antenna which was horizontally positioned in this case. Results are also illustrated in Table 1. and Figure 9.





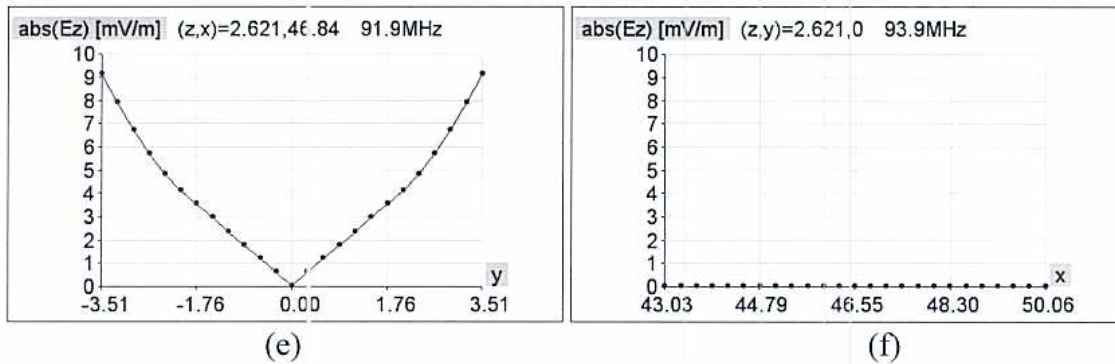


Figure 9. Amplitude and Phase variation through the center of the turntable for the horizontally polarized transmitted signal with no ground plane at 91.9MHz. (a) Transverse Cut, Co-Pol. Magnitude. (b) Longitudinal Cut, Co-Pol Magnitude. (c) Transverse Cut, Co-Pol. Phase. (d) Longitudinal Cut, Co-Pol Magnitude. (e) Transverse Cut, Cross-Pol. Magnitude. (f) Longitudinal Cut, Cross-Pol Magnitude.

### 4.3 Measurements

At this time, field distribution measurements have not yet been made.

### 4.4 Issues of Practicality

One of the major issues that need to be shaken out is the ground continuity of the TT. As it is designed, the various sections of the TT surface simply overlap with gravity as the only force pulling them together. Field uniformity and azimuthal symmetry tests need to be performed to determine whether a need exists for more significant fastening between neighboring ground plane sections.

Once the ground plane continuity issues are dealt with, the field uniformity needs to be measured in order to determine the absolute capability and measurement uncertainty of the system. The open space location at Visteon Corporation is still being upgraded, and hence no measurements are yet available.

## 5 Limitations

This system certainly has its limitations. At present, only azimuthal patterns can be taken at any frequency. In the future, it would be desirable to add an elevation capability for amplitude patterns at frequencies above 800 MHz.

The system measures vertical and horizontal polarized patterns and uses coherent summation to create responses for circular and slant polarizations. This adds time to the process, but is unavoidable for the measurements below 800 MHz. An upper frequency limit will also be reached where coherent combination of vertical and horizontal patterns cannot be performed. This frequency has not yet been determined. Above 800 MHz,

circular polarized sources are small enough to be set up without worrying about their moment of inertia. Spin linear at these frequencies also becomes feasible, however there are not any plans to include it in the future.

As this system is currently set up, it measures azimuthal patterns on antennas installed on vehicles. It currently does not have the capability to perform 3 dimensional patterns on antenna components such as GPS, SDARS, or cellular antennas. This can be easily added to the system with minimal hardware and software modification.

## **6 Future Work**

The primary area of future work involves verification completion. Ground continuity requirements need as they relate to field uniformity symmetry need to be determined. Another aspect of this system is safety. Safety enhancements to further prevent accidents need to be evaluated with respect to safety benefit versus field uniformity degradation. Finally, setup and tear down procedures as well as packing compartmentalization in the SPT need to be optimized and/or created.

## **7 Conclusion**

In conclusion, a transportable VHF ground plane antenna range for azimuthal pattern measurement has been presented. Motivation for this project along with its requirements, design, and analysis has been presented. The facilities have been built and undergone partial verification. Expected performance, has also been presented. Finally, limitations and future work for facility improvement have been identified and documented.

### **Acknowledgements**

The authors would like to recognize Dan Andres, Jim Brewer, and Fred Rhine for their significant contributions to this project and its success.

### **References**

- [1] National Instruments, LabView Software v.7.
- [3] B. M. Kolundzija, J. S. Ognjanovic, T. K. Sarkar, WIPL-D Professional Electromagnetic Analysis Software.
- [4] R. L. Carrel, "The Design of Log-Periodic Dipole Antennas," IRE Int. Conv. Rec., vol. 1, pp. 61-75, 1961.
- [5] J. D. Kraus, Antennas, pp. 704-7, New York: McGraw-Hill, 1988.

# **EXPONENTIALLY TAPERED AND FOLDED WIDEBAND TEM HORN ARRAY FOR 20 KV OF IMPULSE**

Young-Joon Ahn<sup>1\*</sup>, Jin-Seong Lee<sup>1</sup>, Sung-Joo Kim<sup>1</sup>, Frances J. Harackiewicz<sup>2</sup>, and  
Byungje Lee<sup>1</sup>

<sup>1</sup>Department of Wireless Communications Engineering  
Kwangwoon University  
447-1, Wolgye-Dong, Nowon-Gu, Seoul, 139-701, Korea

<sup>2</sup>Department of Electrical and Computer Engineering  
Southern Illinois University  
Carbondale, Illinois 62901-6603

**Abstract:** An exponentially tapered and folded wideband TEM horn array is proposed to reduce the overall dimension of the array. The proposed antenna can handle a 20 kV of the impulse input signal. The radiating elements are folded twice parallel to the direction of electric field to reduce the overall dimension of the exponentially tapered TEM horn array. A 20 kV of the impulse input signal is divided into the  $1 \times 16$  exponentially tapered TEM horn elements. The divider has the microstrip structure and is designed by using a triangularly taper transformer. To avoid the breakdown due to the high voltage of the 20 kV, the distance between metallic objects (feed points, microstrip lines, and ground plane) is determined to be more than 7 mm: the distances between the feed points and between the microstrip line and the ground plane are 10 mm and 15 mm, respectively. The overall dimension of the proposed array antenna is  $2700 \times 1900 \times 1100 \text{ mm}^3$  and its impedance bandwidth ( $\text{VSWR} < 2$ ) is 845 MHz (120 ~ 965 MHz). The proposed antenna is analyzed by CST (MWS), and its performance is measured and discussed.

## 1. Introduction

The explosive growth of electronic devices and wireless communication systems makes the human life very convenient, and they are necessities for today's human life. The wireless communications revolution has electromagnetics at its very core. However, we are immersed in electromagnetic fields. They are everywhere. The modern office, kitchen, and automobile are all stuffed full of electronic devices. With the anticipated continued growth in wireless technology, the study on electromagnetic interference (EMI), defined as the degradation in the performance of an electrical circuit or system resulting from electromagnetic noise, is greatly demanded. Noise can arise from other circuit components or systems or from natural phenomena. The impact of noise on performance of an electrical systems grows more important as the circuits get smaller and faster. This is especially true for digital circuits because high-speed digital signals with short rise times generate a broad spectrum of noise that lead to interference. For EMI test, the high voltage impulse is used as the interference source. In general, the high power system consists of a power supply generating the high power impulse signal and an antenna part transmitting it. A conventional TEM horn antenna is widely used because it is very useful to transmit the pulse signal and is non-dispersive, but it also has a disadvantage of large size in the low frequency band, that is, its size goes up as the frequency becomes lower [1]. To reduce the overall dimension of a conventional TEM horn antenna, the folded horn structures are studied [2]-[3]. In this work, the folded TEM horn array antennas are studied for the high power ultra wideband(UWB) system. The proposed antenna has an advantage of reducing the overall length of a conventional TEM horn antenna which is suitable for transmitting the UWB and high power impulses. Analyzing the performance of the folded radiator and considering air breakdown at peak 20kV impulse, an exponentially tapered and folded TEM horn array are proposed. First, a folded TEM horn antenna, which has triangularly tapered and folded radiating elements and is fed by a stripline power divider, is designed. Then, based on analysis of the triangularly tapered and folded TEM horn antenna, an exponentially tapered and folded TEM horn array antenna is proposed to further improve the impedance bandwidth at the lower frequency band. The proposed antenna can be applied for high power system using 20 kV of impulse with 700 ps of rising time and 1~2 ns of pulse width as an input signal. The proposed antenna is designed to operate from 200 MHz to 800 MHz.

## 2. Design of Triangularly Tapered TEM Horn Antenna

The folded TEM horn antennas are studied to reduce the size of a conventional TEM horn antenna with maintaining its wideband characteristics [2]-[3]. It is known that the basic operation principle of a folded horn antenna is similar to a waveguide slot coupler [2]. The proposed antenna in this work will be designed by applying an exponential taper theory [4] to a folded TEM horn in [3]. First, the dimension of a conventional TEM horn antenna will be determined. It is known [5] that the dimension of its aperture height ( $H$ ) and width ( $W$ ) should be greater than  $0.5 \lambda$ , and the length ( $L$ ) of a radiating element should be bigger than  $1.0 \lambda$  at the lowest operating frequency. Figure 1 shows the conventional structure of a TEM horn antenna. It has two radiating plates with a triangularly tapered structure and two angles,  $\theta_1$  and  $\theta_2$ . In this paper, by the simulation and experiment, the design parameter and dimensions are determined, and then a triangularly tapered conventional TEM horn antenna is designed as shown in Figure 2. A  $50\Omega$  probe feeds the antenna, and the dimension ( $H \times W$ ) of the aperture is  $1.2 \lambda \times 1.2 \lambda$  ( $377\Omega$ ) at the lowest frequency. The antenna length ( $L$ ) is  $2.8 \lambda$ , and the angle ( $\theta$ ) between two plates is  $24^\circ$ .

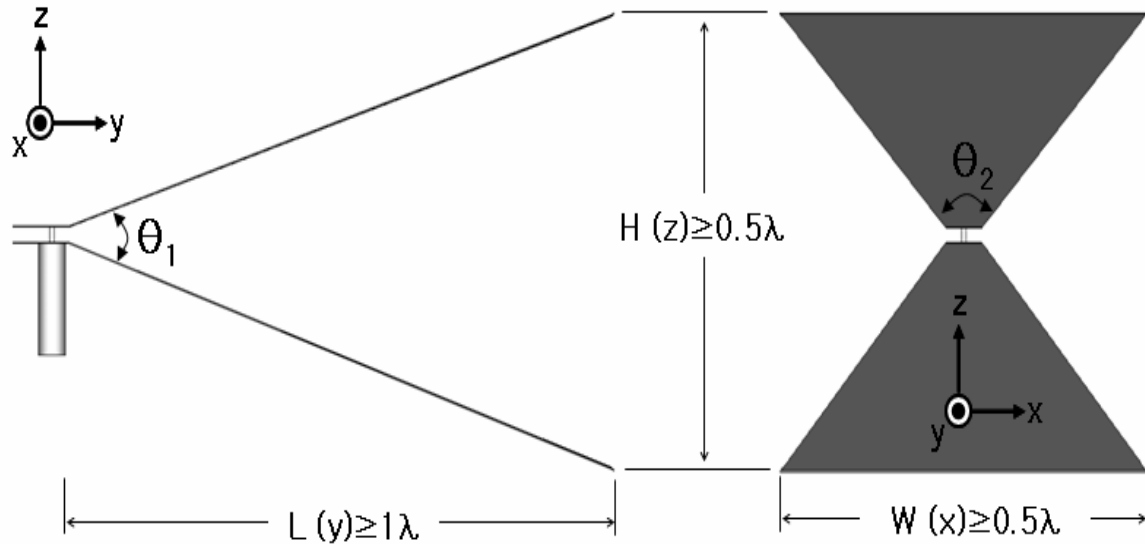


Figure 1. Structure of a conventional TEM horn antenna



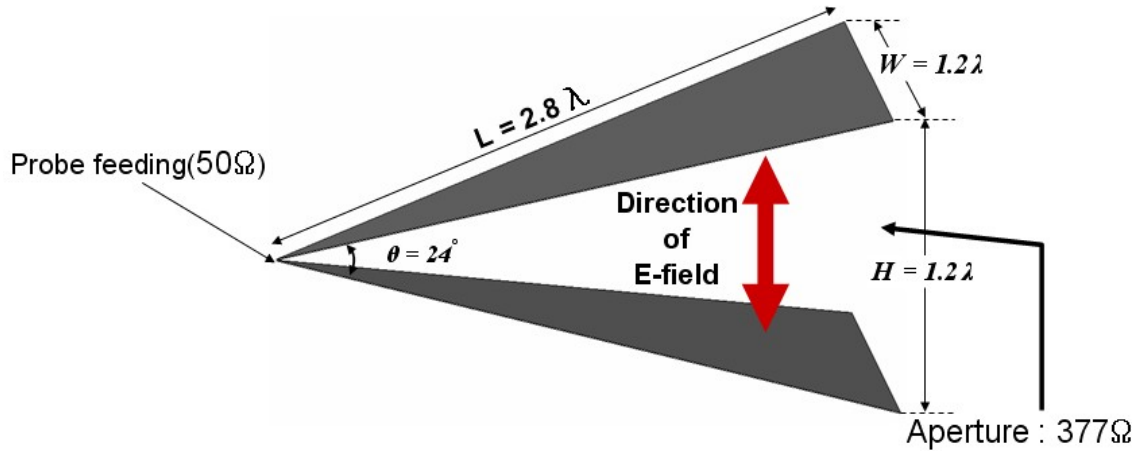


Figure 2. Designed triangularly tapered TEM horn antenna

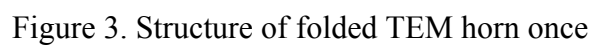
### 3. Triangularly Tapered and Folded TEM Horn Antenna

For a conventional TEM horn (segment  $h-a-j$  in Figure 3), an angle  $\theta$ , length ' $L$ ', and gap ' $H$ ' between two plates are determined by equations (1), (2), and (3) where  $f_H$  is the lowest operating frequency,  $k$  is a constant to determine the aperture size ( $H$ ), and  $c$  is the speed of light. To design folded TEM horn once, the length ( $L_1$ ) is determined by using equations (4), (5) and (6). Equation (7) is used to determine point  $P_\theta$  to fold a TEM horn radiator once. By folding TEM horn once with the segment  $h-b-y-d-j$  and two input ports, the length of the radiator is reduced up to 38 % of the length of the triangularly tapered but unfolded TEM horn antenna.

$$H = \frac{c}{f_H} \times k \quad (1)$$

$$\lambda_0 = \frac{c}{f_H} \quad (2)$$

$$L = \frac{\frac{H}{2}}{\tan \frac{\theta}{2}} \quad (3)$$



451

A folded TEM horn twice with four input ports can be designed by using equations (8) ~ (14) to further reduce the length of a folded TEM horn once as shown in Figure 3. By folding TEM horn twice with the segment  $r-e-j-y-p-g-m-h-t$  and four input ports as shown in Figure 4, the length of the radiator is reduced up to 52 % of the length of the triangularly tapered but unfolded TEM horn antenna.

$$E = 2D \times \tan \frac{\theta}{2} \quad (8)$$

$$f_E = \frac{c}{\lambda_0} \quad (9)$$

$$\lambda_0 = \frac{E}{k} \quad (10)$$

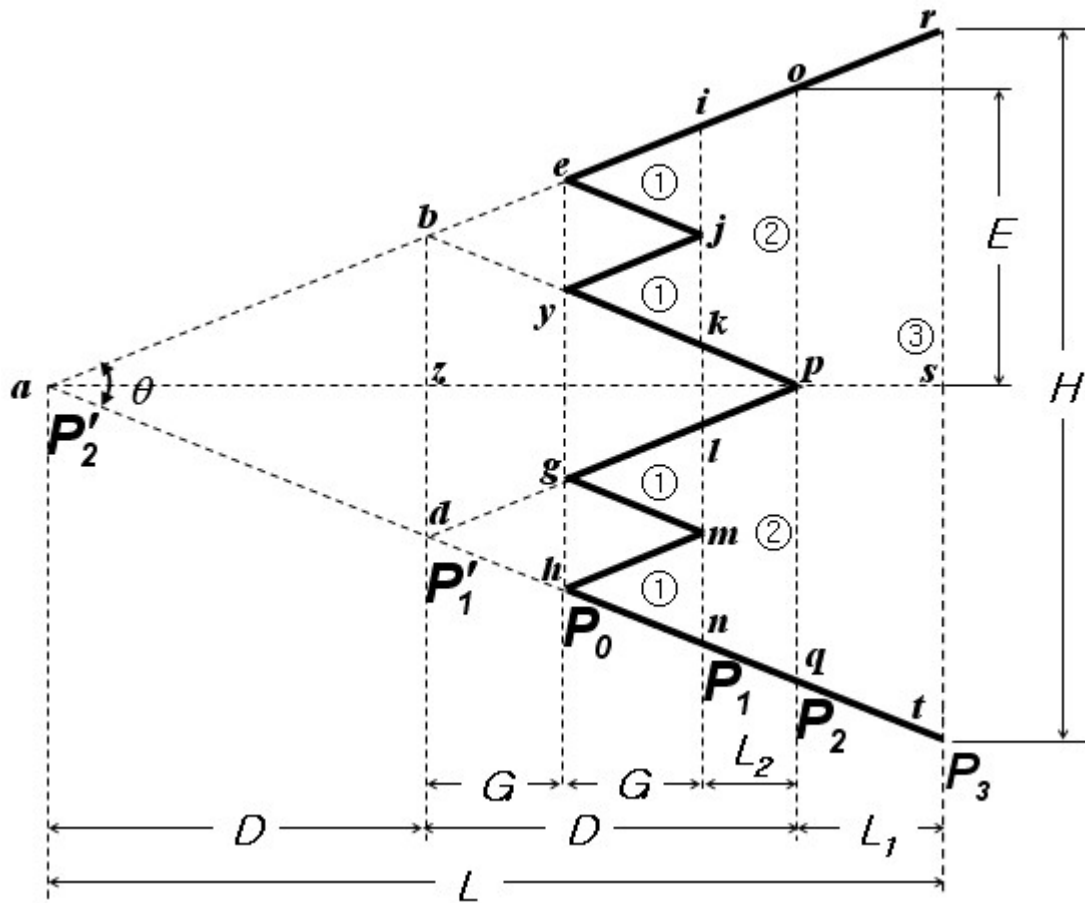


Figure 4. Structure of folded TEM horn twice

$$\lambda_E = \frac{\lambda_0}{\sqrt{1 - \left(\frac{\lambda_0}{2E}\right)^2}} \quad (11)$$

$$\lambda_{\frac{E}{2}} = \frac{\lambda_0}{\sqrt{1 - \left(\frac{\lambda_0}{E}\right)^2}} \quad (12)$$

$$L_2 \leq \frac{\sqrt{\lambda_E \times \lambda_{E/2}}}{2} \quad (13)$$

$$G = \frac{D - L_2}{2} \quad (14)$$

#### 4. Exponentially Tapered and Folded TEM Horn Antenna

Based on analysis of the triangularly tapered and folded TEM horn array in Section 3, then an exponentially tapered and folded TEM horn array antenna is newly proposed to further improve the impedance bandwidth at the lower frequency band. When a TEM horn antenna is designed to improve the impedance bandwidth, the most important factor is that the impedance should vary slowly from transition part to aperture part so that discontinuity and reflected waves at the radiating element can be minimized. Exponentially tapered and folded TEM horn structure is designed by applying exponentially tapered structure [6] to each sector ( $P_0$ - $P_1$ ,  $P_1$ - $P_2$ , and  $P_2$ - $P_3$ ) of the folded TEM horn structure as shown in Fig. 4. Figure 5 represents a cross-section of exponentially tapered and folded TEM horn. In order to increase a gain, exponentially tapered and folded TEM horn array, which has four array elements along y-axis and maintains  $1.2 \lambda \times 1.2 \lambda$  of the aperture dimension, is designed. The final designed array has 16 input ports fed by a microstrip line type of the power divider. The gap between the metal strip and the ground plate for the stripline structure maintains 15 mm to prevent the air breakdown for peak voltage 20 kV impulse. Length of the radiating element is optimized to have more than 10 dBi of the gain for all operating frequencies

by using MWS CST [7]. Then, its length is reduced up to about 78.6 % of the length of a conventional unfolded TEM horn antenna. The final dimensions of the radiating element are  $1800 \times 1800 \times 900$  (mm<sup>3</sup>).

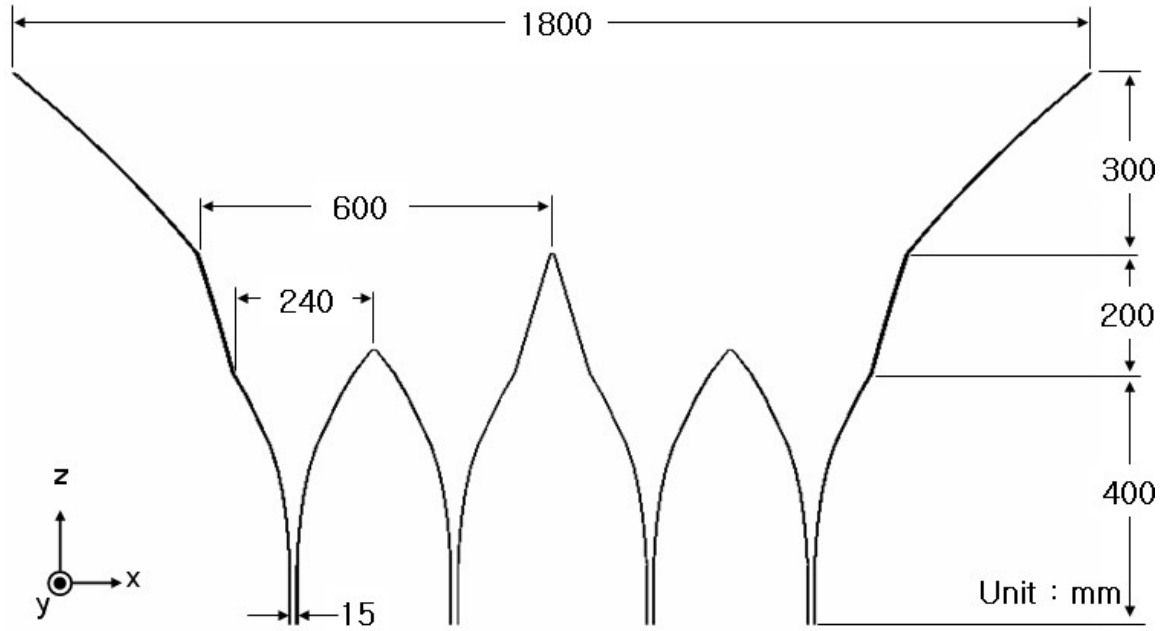


Figure 5. Structure of exponentially tapered and folded TEM horn

## 5. Design of the Power Divider

A microstrip line type of power divider is designed to feed 16 input ports of the proposed antenna with uniform amplitude and in phased current. A triangularly tapered transformer is used to obtain the wide impedance bandwidth, and  $50 \Omega$  DIN type connectors are used to prevent the air breakdown from the input ports. The power divider is designed to have  $100 \Omega$  at all output ports. The gap between each metallic part (feed point, microstrip line, and ground) in power divider maintains 15 mm to prevent itself from the air breakdown. Figure 6 shows the structure of a microstrip line power divider. Figure 7 shows the simulated dB magnitude of S parameters for the part of the proposed power divider. As shown in Figure 7(a), it operates from 120 MHz to 1,000 MHz (VSWR<2). Also, Figure 7(b) shows that it operates from 50 MHz to 980 MHz (VSWR<2).

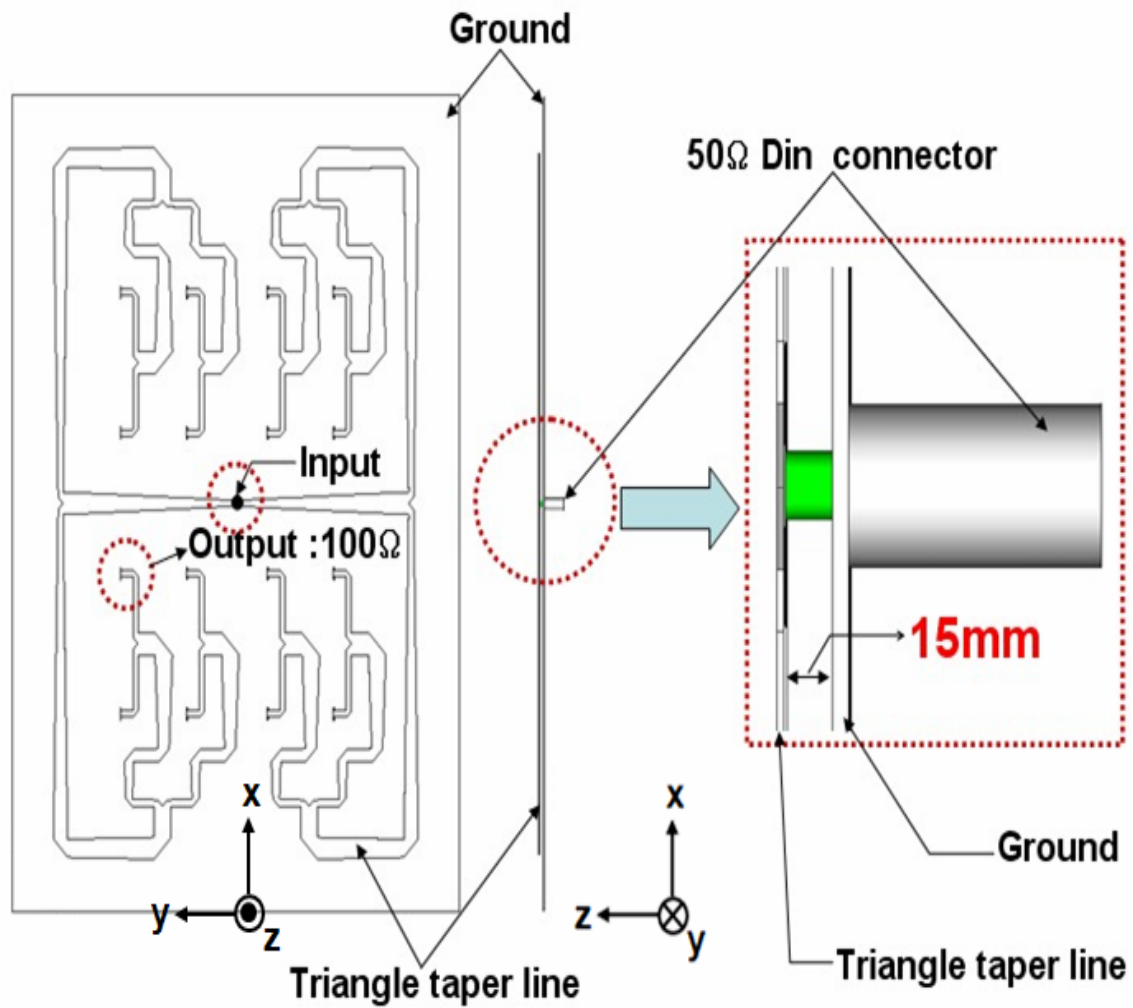
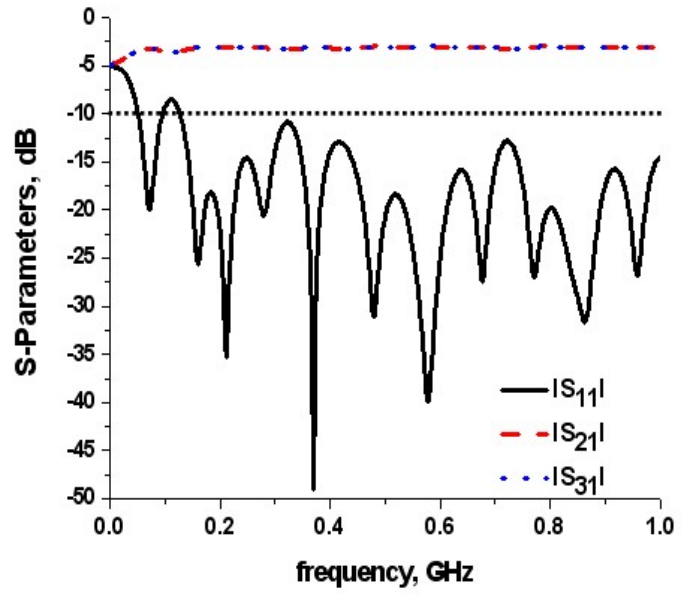
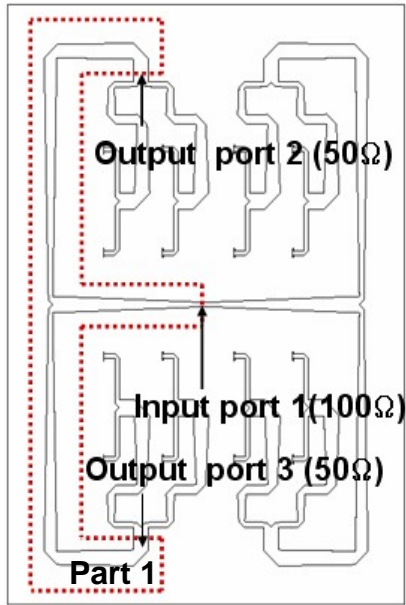
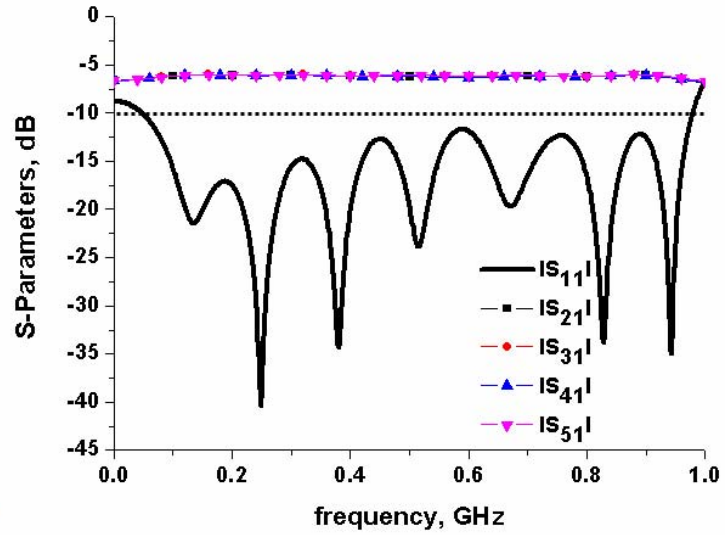
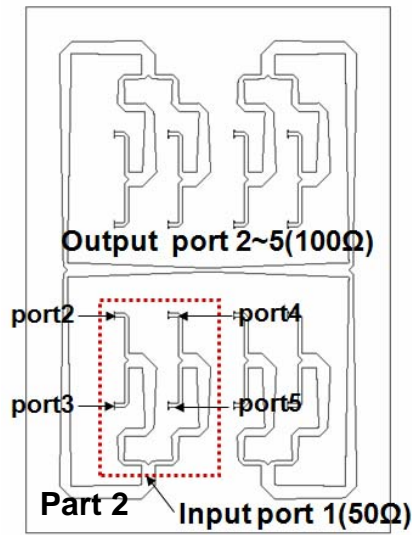


Figure 6. Structure of microstrip line power divider



(a)



(b)

**Figure 7. Simulated dB magnitude of S parameters for the part of power divider**  
**(a) Part 1, (b) Part 2**

## 6. Proposed Exponentially Tapered and Folded TEM Horn Array Antenna

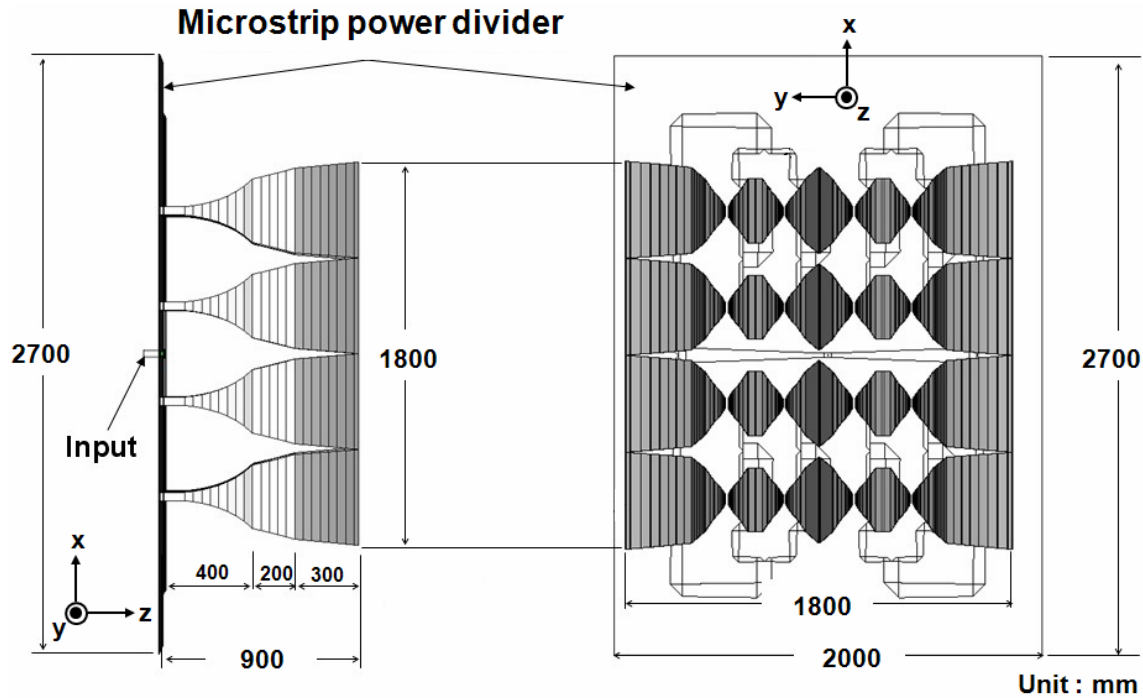


Figure 8. Overall view of the proposed array antenna

Figure 8 shows the overall view of the proposed array antenna with dimensions. The array has 16 input ports ( $100 \Omega$ ) to feed exponentially tapered and folded TEM horn elements. The dimension of radiating part is  $1800 \times 1800 \times 900 \text{ mm}^3$ . The dimension of a microstrip line power divider is  $2700 \times 2000 \times 200 \text{ mm}^3$ . Figure 9 shows the photograph of the proposed antenna. The proposed antenna mainly consists of the exponentially tapered and folded TEM horn array radiators and the microstrip line type power divider. The ground of the power divider is formed by Duralumin (thickness = 3 mm), and copper (thickness = 1 mm) is used for microstrip line. At the input port of the power divider,  $50 \Omega$  of the DIN type connector is used. The Duralumin (thickness = 2 mm) is used for the radiating elements since it is very light and has a high conductivity. To maintain the antenna elements firmly, the support-1(Mono cast nylon:  $\epsilon_r = 3.1$ ) is used. The overall dimension of the proposed antenna is  $2700 \times 1900 \times 1100 \text{ mm}^3$ , and the weight is about 190 kg.



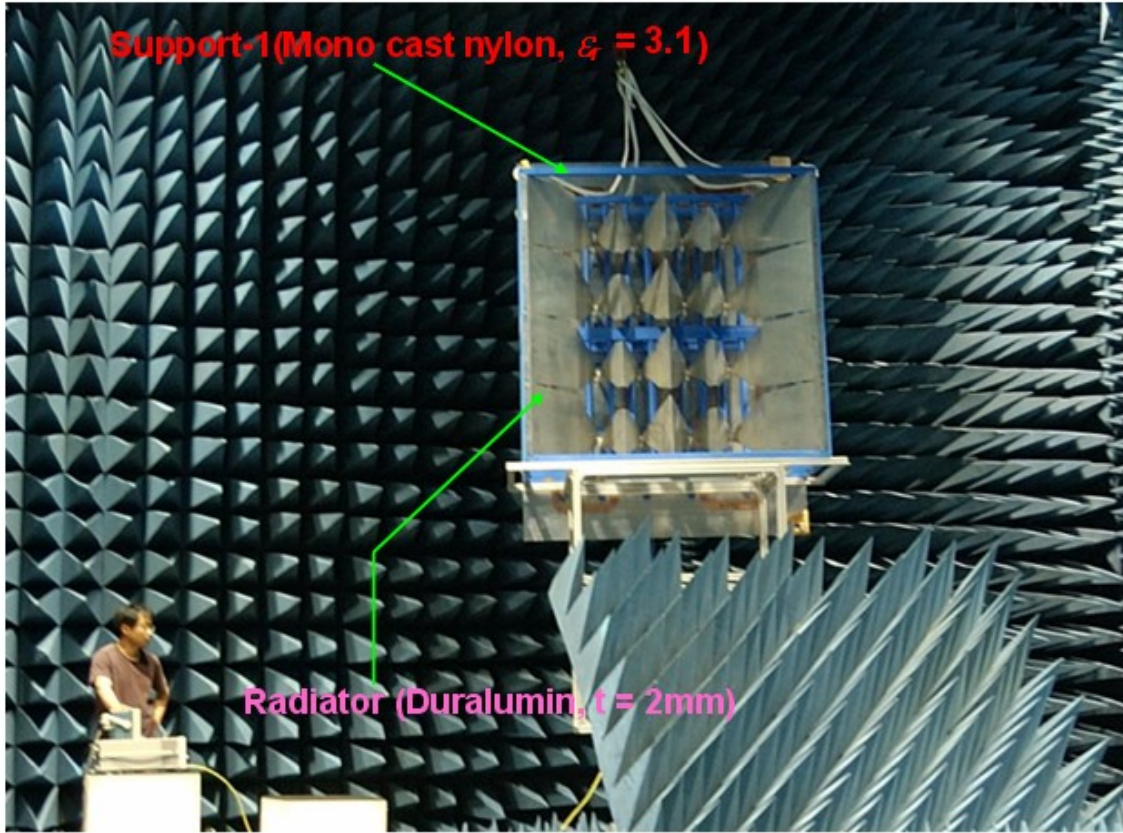


Figure 9. Photograph of proposed antenna

## 7. Simulation and Experimental Results

Figure 10 shows the simulated and measured dB magnitude of  $S_{11}$  of the proposed antenna. The solid line indicates the measured results of the antenna shown in Figure 9, and the dashed line shows the simulated result for Figure 8. The measured bandwidth of the proposed antenna is 845 MHz (120 ~ 965 MHz,  $VSWR < 2$ ). It is noticed that there is a small difference between the measured and simulated results. Figure 11 shows the simulated and measured radiation patterns in the y-z plane and z-x plane. Table 1 shows the measured gains and HPBW of the proposed antenna. A peak gain of the proposed antenna is 20.75 dBi (at 800 MHz). HPBW is  $43.44^\circ \sim 7.65^\circ$  at y-z plane, and  $51.43^\circ \sim 11.41^\circ$  at z-x plane.

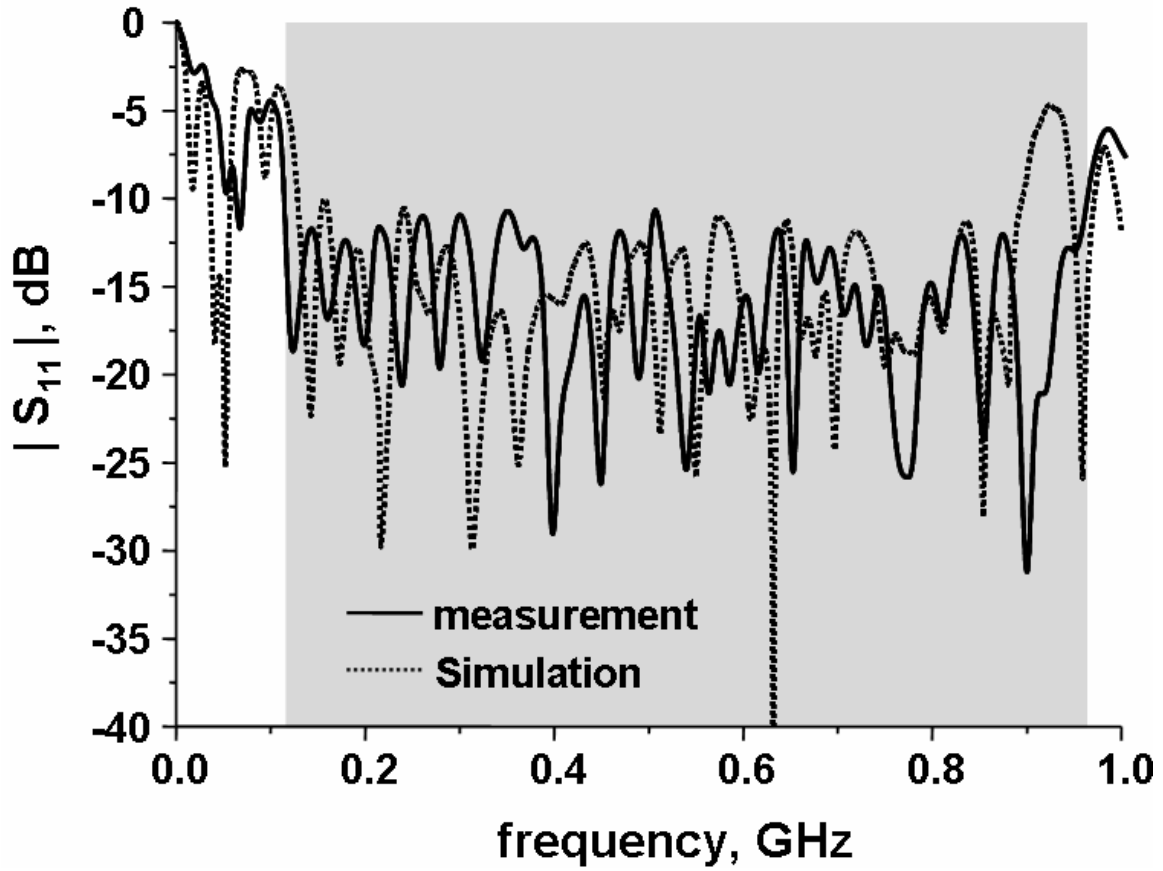
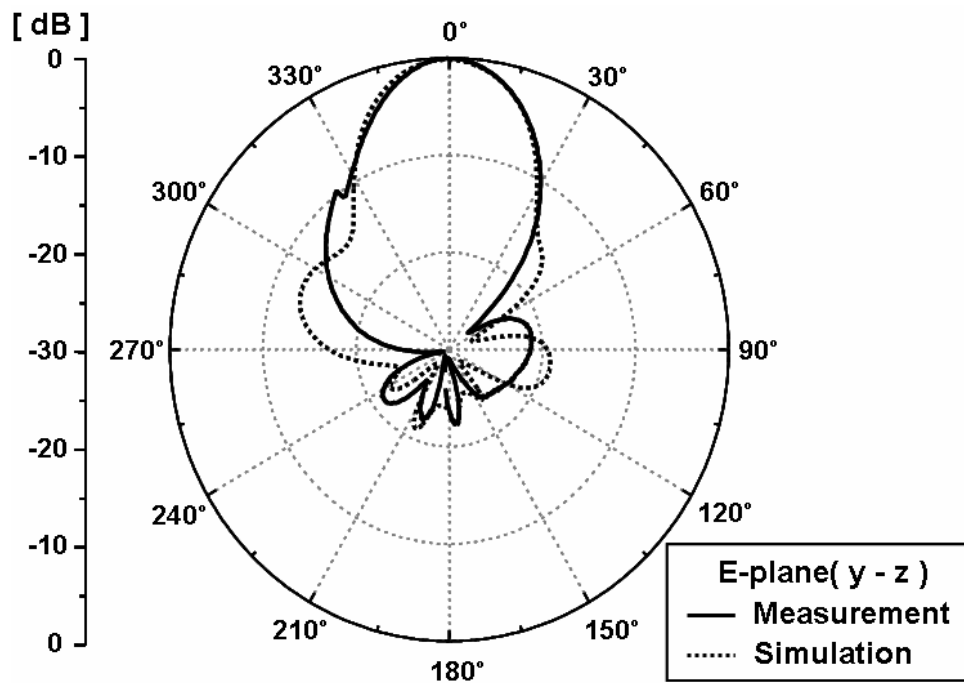
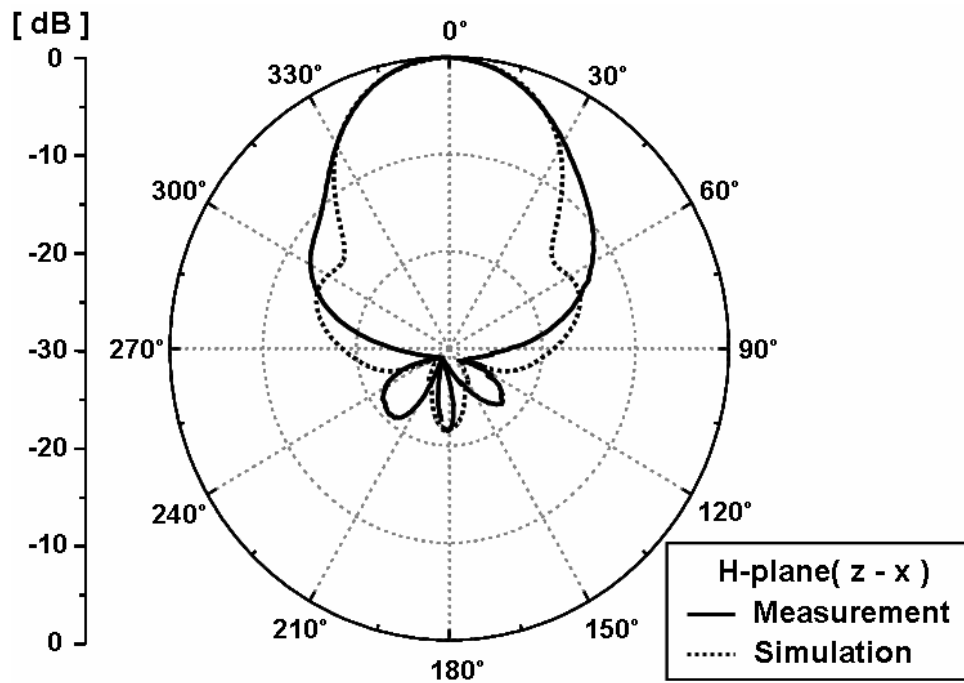


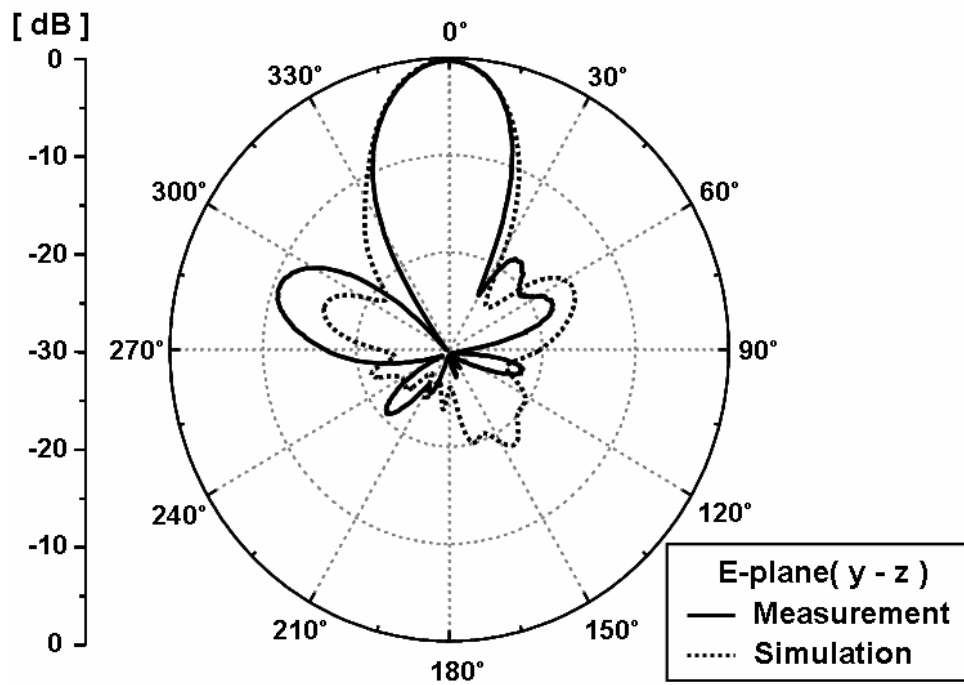
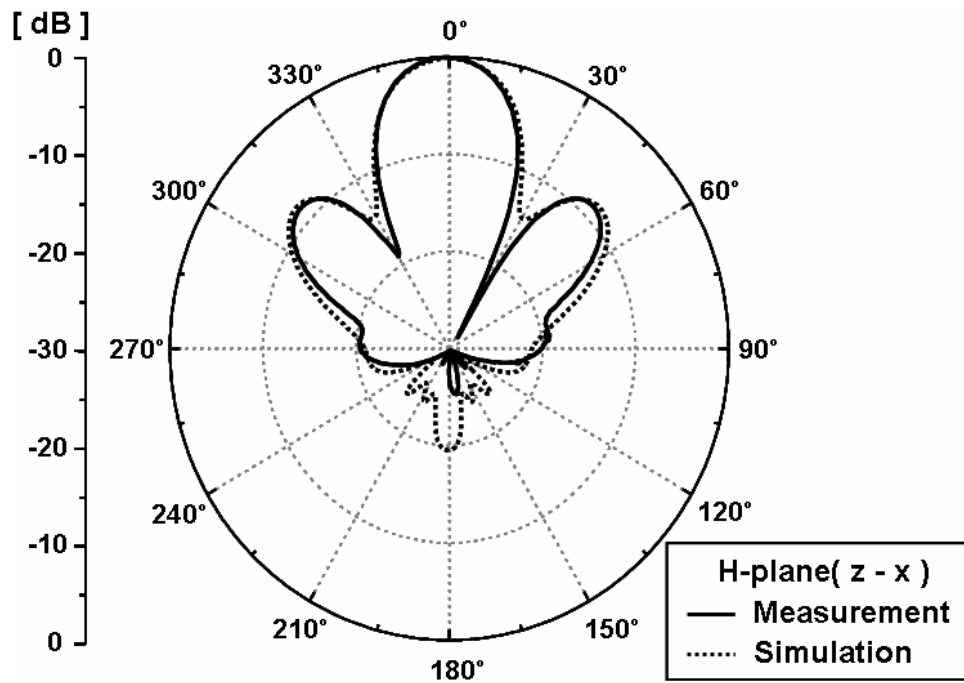
Figure10.  $S_{11}$  for the proposed horn array

## 8. Conclusion

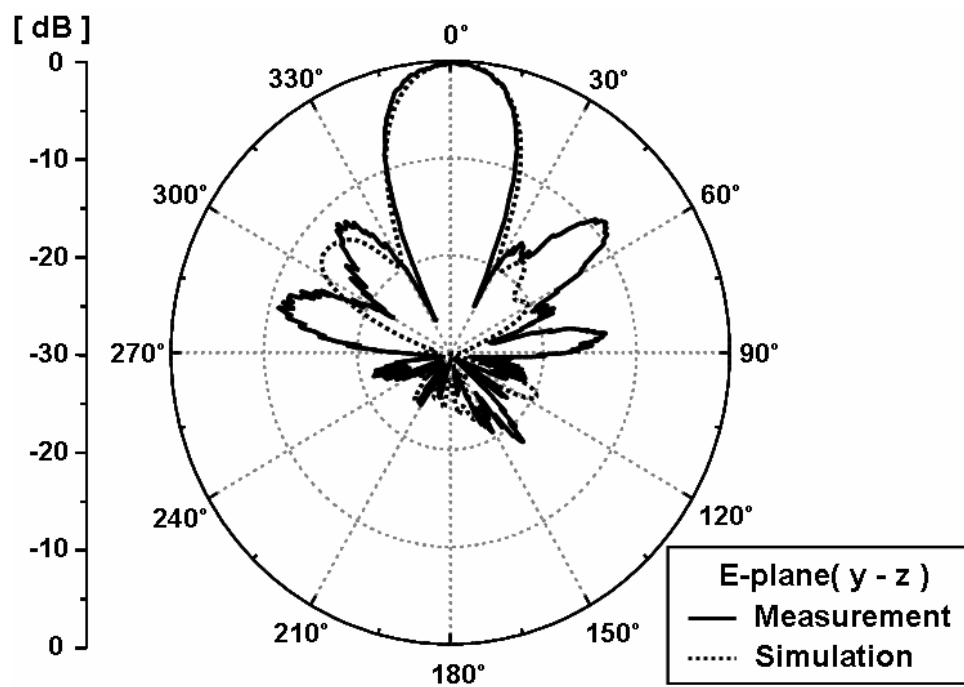
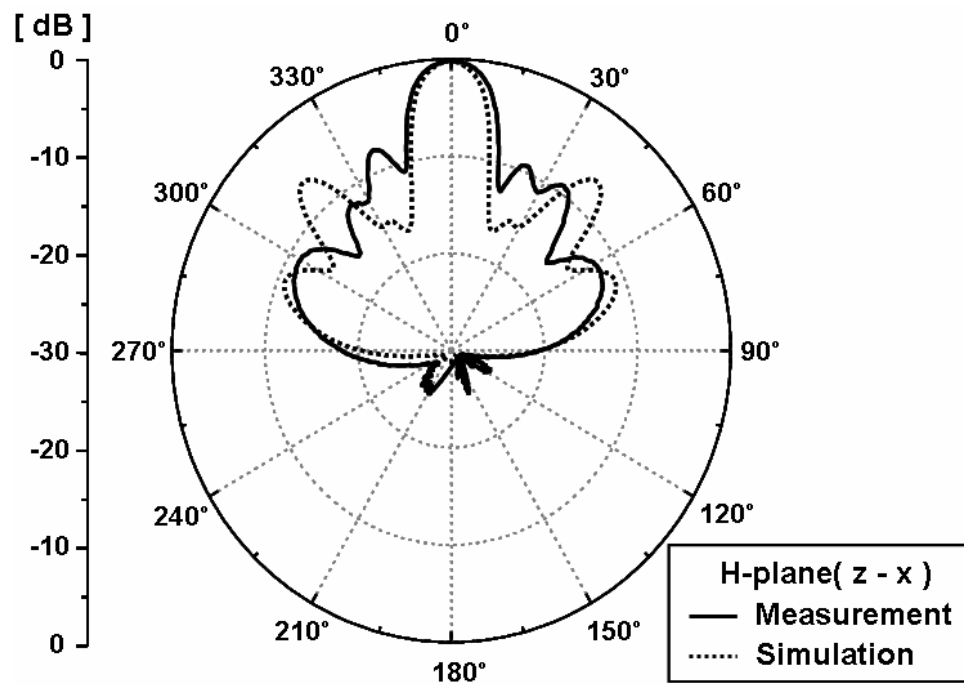
The exponentially tapered and folded TEM horn array antenna is proposed to reduce the length of the conventional TEM horn antenna and improve the impedance bandwidth. The proposed antenna has a wide bandwidth (120 ~ 965 MHz, VSWR<2), and its length is reduced up to about 78.6 % of the length of a conventional unfolded TEM horn antenna. The proposed antenna is designed to resist against 20 kV impulse in the air. In future, the proposed antenna will be studied for wider impedance band operation, higher gain, and higher power handling up to 100 kV impulse.



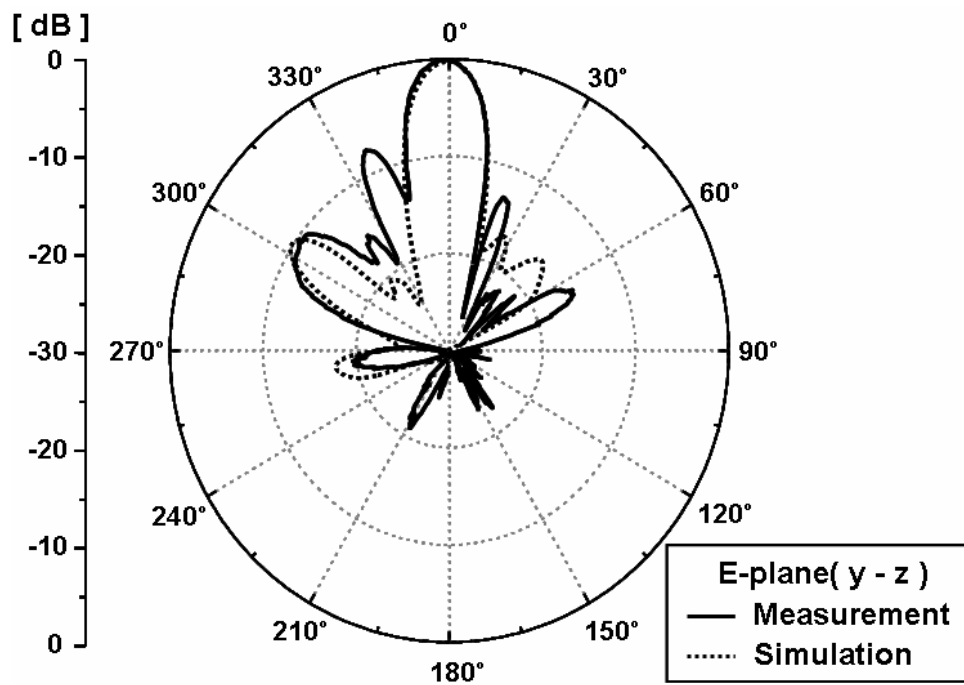
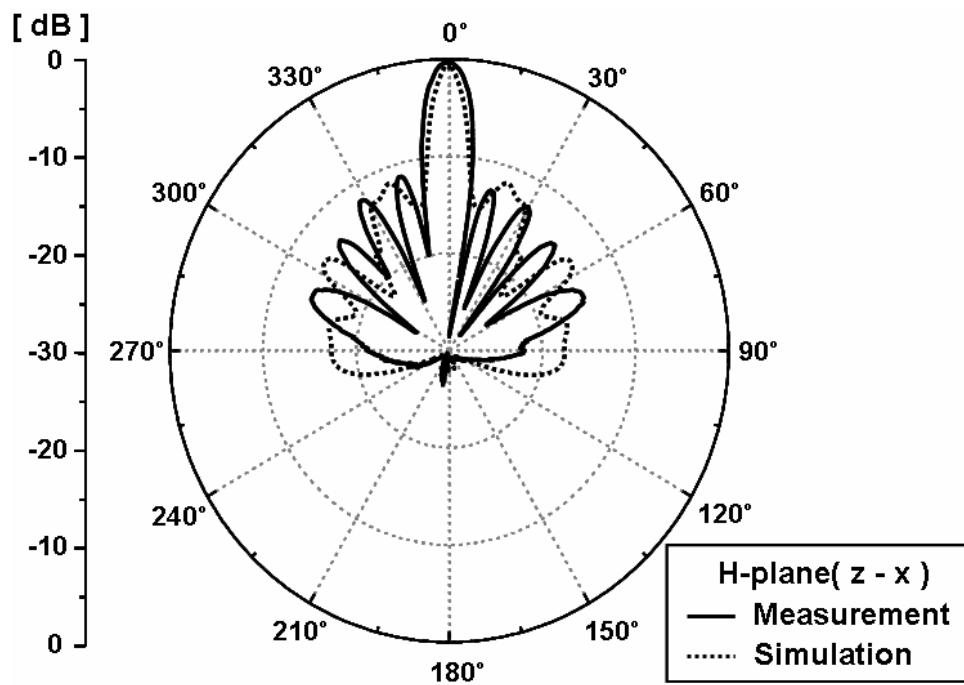
a) 200 MHz



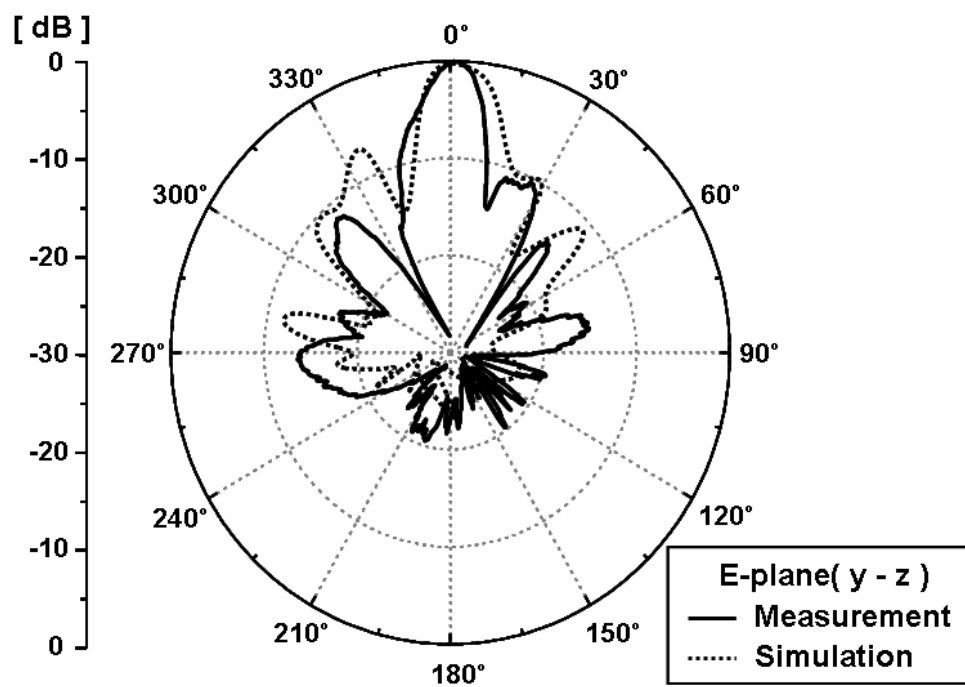
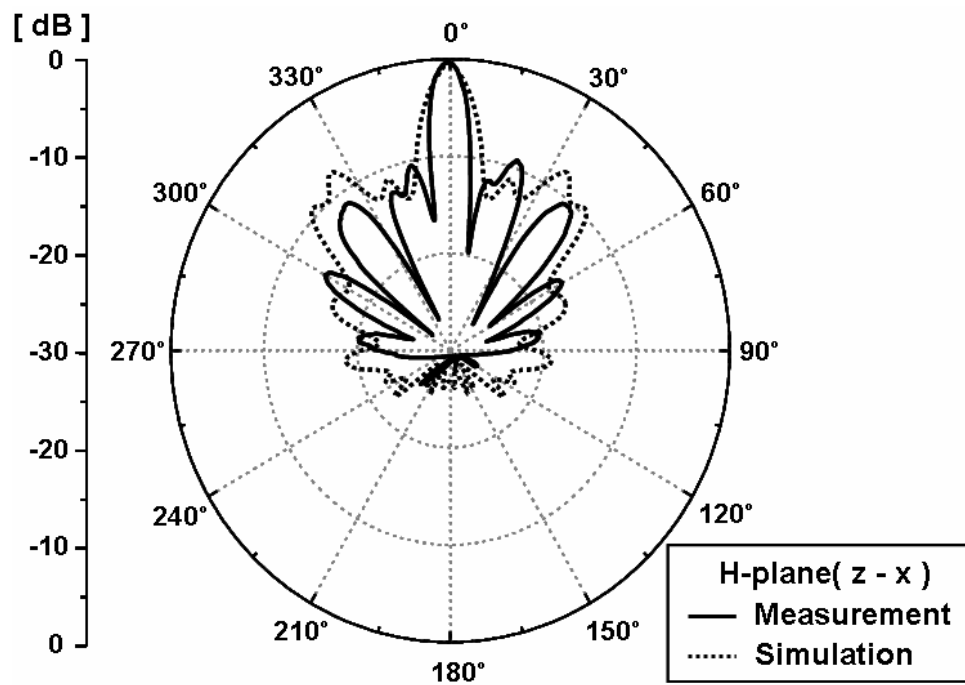
b) 400 MHz



c) 600 MHz



d) 800 MHz



e) 1,000 MHz

Figure 11. Simulated and measured radiation patterns.

Table 1 Measured result of proposed antenna

Freq. (MHz)	$G_{\max}$ (dBi)	HPBW ( Degree)	
		z-x plane	y-z plane
<b>200</b>	10.50	31.10	43.44
<b>300</b>	10.75	24.10	40.75
<b>400</b>	12.90	23.22	26.65
<b>500</b>	14.11	25.00	20.91
<b>600</b>	16.01	26.50	18.50
<b>700</b>	17.18	20.40	10.62
<b>800</b>	20.75	15.16	9.52
<b>900</b>	18.85	11.88	8.50
<b>1,000</b>	16.29	13.66	7.65

## 9. Acknowledgments

This work is financially supported by the Ministry of Education and Human Resources Development (MOE), the Ministry of Commerce, Industry and Energy (MOCIE) and the Ministry of Labor (MOLAB) through the fostering project of the Lab of Excellency, and supported in part by the post BK21.

## 10. References

- [1] J. D. Taylor, Introduction to Ultra-Wideband Rader Systems, pp. 176-183, Florida: CRC Press, Inc., 1995.
- [2] V. B. Braude, S. B. Sukhovetskaya, and B. J. Sukhovetsky, "Wide-band Folding Horn Type Microwave Antennas", Antennas and Propagation for Wireless Communications, IEEE-APS Conf., pp. 143-146, 2000.



- [3] J. S. Lee, J. W. Park, B. Jung, F. J. Harackiewicz, and B. Lee, "Wideband folded horn antenna array for 20kV impulse", *Antenna Applications Symp.*, pp. 314-329, 2006.
- [4] D. M. Pozar, *Microwave Engineering*, 2nd Edition, John Willy & Sons, 1998.
- [5] D. A. Kolokotronis, Y. Hung, and J. T. Zhang, "Design of TEM Horn Antennas for Impulse Radar", *IEEE High-Freq. Postgrad. Student Colloq.*, pp. 120-126, Sep. 1999.
- [6] H. Choi and S. Lee, "Design of an exponentially-tapered TEM horn antenna for the wide broadband communication", *Microwave and Optical Technology Letters*, Vol. 40, Mar. 2004.
- [7] CST Microwave Studio, Version X, CST GmbH, Darmstadt, Germany.

# Multipath rejection by virtue of a choke ring for a broadband droopy turnstile antenna

Sergey N. Makarov<sup>(1)</sup> and Francesca Scire' Scappuzzo<sup>(2)</sup>

(1) Worcester Polytechnic Institute, Worcester, MA 01609

(2) Physical Sciences Inc., Andover, MA 01810

[makarov@wpi.edu](mailto:makarov@wpi.edu), [fss@psicorp.com](mailto:fss@psicorp.com)

**Abstract:** The choke ring is a well known tool for shaping radiation patterns of a GPS base station antenna. In view of the development of Modernized GPS and Galileo, the GPS base station antenna should have a wider polarization and impedance bandwidth than at present, ideally from 1.15 to 1.60 GHz. Such a bandwidth may require some modifications of the choke ring ground plane. This study investigates the performance of a droopy bowtie turnstile antenna in the presence of a choke ring ground plane of variable geometries in the band 1.15-1.60 GHz. Two simple choke ring configurations are potentially possible – the standard choke ring with “tall” teeth (the cutoff corrugated surface at all frequencies of interest) and a choke ring with “short” teeth that still supports slow or surface waves and uses the cancellation principle in order to shape the pattern. These two types are discussed in the present study. Both simulation results for the first and second type, and prototype measurements (second type only) are presented and discussed. The paper also contains an introduction to corrugated surface and choke ring operation as applied to pattern shaping.

## Content

1. Properties of metal corrugation - an introduction
2. GPS cutoff choke ring
3. Cutoff choke ring performance over the band 1.15-1.60 GHz
4. Non-cutoff choke ring performance over the band 1.15-1.60 GHz
5. Acknowledgements
6. References

## 1. Properties of metal corrugation - an introduction

### *1.1. Plane wave propagation*

First, let's combine multiple quarter-wave parallel-plate resonators and form a corrugated metal surface as shown in Fig. 1 that follows. Is this combination of any practical interest for GPS circularly-polarized antennas? To answer this question we compare the

performance of the corrugated surface with that of the solid metal surface – see Fig. 1a. We consider two plane wave types labeled as I and II in Fig. 1, which potentially might propagate along both surfaces. Oblique plane wave of type I is often designated as a TE to  $z$  or, shortly,  $TE_z$  plane wave since it does not have a  $E$ -field component in the  $z$ -direction. Similarly, the oblique plane wave of type II is the TM to  $z$  or  $TM_z$  plane wave.

The metal surface shorts out signal I since  $E_z = 0$  but still allows for signal II to propagate. For the corrugated surface, the metal teeth require  $E_z = 0$  at top and will still short out the signal I very efficiently [1]. At the same time, the waveguide openings require  $H_y = 0$  at their top and will short out the signal II, for which it must be  $H_y \neq 0$ .

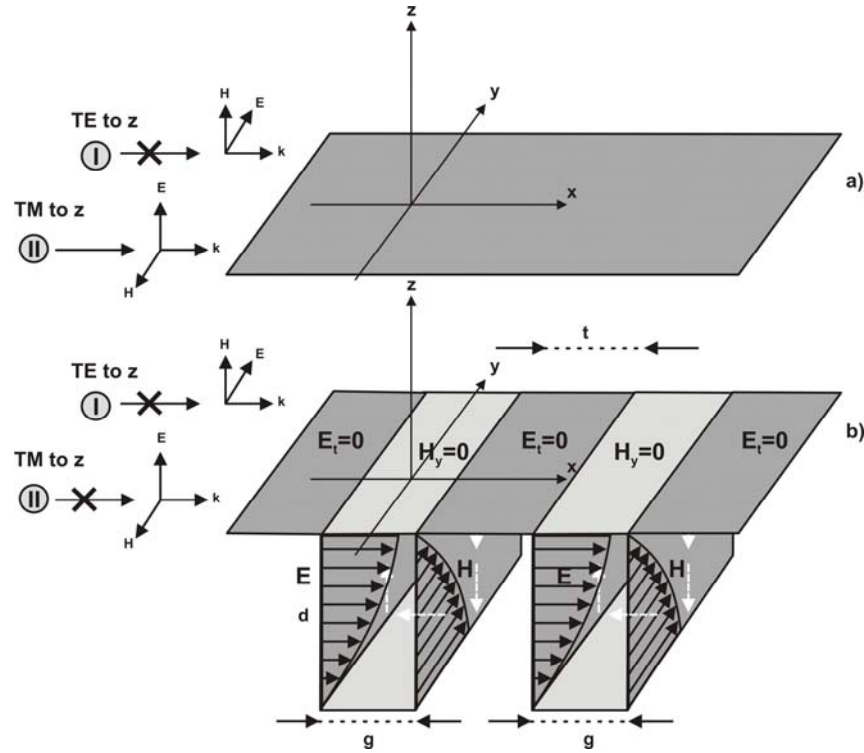


Fig. 1. A corrugated surface on the base of quarter wave resonators.

Thus, neither mode I nor mode II can propagate along the corrugation in contrast to the solid metal. Such a reasoning was used in a classic reference [2] devoted to artificial *soft* and *hard* surfaces. One condition for it to be valid is the geometry inequality [2]

$$g + t < \frac{\lambda}{2} \quad (1)$$

which implies that the parallel-plate waveguide cannot be very wide. The definition of a soft surface given in [2] implies that, for two plane waves propagating *along* that surface and *perpendicular* to corrugation, one has the related surface impedances in the form

$$Z_y \equiv + \frac{E_y(z=0)}{H_z(z=0)} = 0 \quad (2a)$$

$$Z_x \equiv - \frac{E_z(z=0)}{H_y(z=0)} = \infty \quad (2b)$$

which is again equivalent to shorting out modes I (Eq. (2a)) and II (Eq. (2b)), respectively. Thus, the quarter-wave corrugated surface is a soft surface.

Since any oblique plane wave with wave vector perpendicular to corrugation is a combination of I and II modes (TE<sub>z</sub> and TM<sub>z</sub> modes), we conclude that the planar corrugated surface blocks out any oblique plane wave whose wave vector is perpendicular to corrugation, independent of the direction of the electric field. In that sense, it becomes the *polarization-independent* soft surface according to terminology adopted from Ref. [2]. Such a property of corrugated surfaces is critical and allows us to use it as a special finite ground plane, in particular for circularly-polarized antennas with both modes potentially present.

### 1.2. On surface waves

Thus, no plane wave can propagate along the corrugated surface in the direction perpendicular to corrugation if the corrugation depth is exactly quarter wavelength. But what happens for other corrugation depths? To answer this question let's define the proper boundary conditions on the top of corrugation teeth, i.e. formalize the problem as shown in Fig. 2.

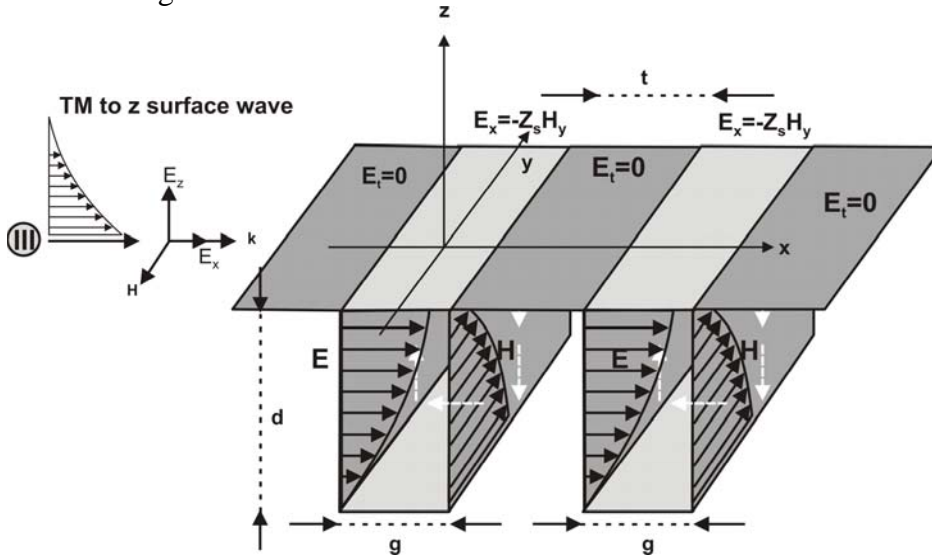


Fig. 2. Corrugated surface of arbitrary depth and the corresponding boundary conditions.

The surface impedance of open waveguides  $Z_s$  should be directly related to the slot termination (circuit) impedance in the form ( $w$  is the length of corrugation)

$$Z_{\text{ter}} \equiv -\frac{g}{w} \frac{E_x(z=0)}{H_y(z=0)} = \frac{g}{w} Z_0 \frac{Z_{\text{bottom}} + jZ_0 \tan kd}{Z_0 + jZ_{\text{bottom}} \tan kd} \quad (3a)$$

with  $Z_{\text{bottom}}$  being zero for metal bottom corrugation, in which case one has

$$Z_{\text{ter}} \equiv \frac{g}{w} jZ_0 \tan kd \quad (3b)$$

$E$  and  $H$  in Eq. (3a) denote total field components of the waveguide field in the opening of the parallel-plate resonator. For the entire surface, with relatively small tooth width,  $t$ , one may use the *average* termination impedance (reactance) in the form (see [3], p. 798)

$$Z_{\text{ter}} \equiv jZ_0 \frac{g}{w} \frac{g}{g+t} \tan kd \quad (3c)$$

Oblique plane wave of type I or, which is the same, TE to  $z$  or  $\text{TE}_z$  plane wave in Fig. 1 cannot exist for the same reason as that given above, for any value of  $Z_s$ . So is the oblique plane wave II (TM to  $z$  or  $\text{TM}_z$ ) since it does not have a  $E$ -field component in the propagation direction, which is required by the corresponding boundary condition. But how about a solution III in Fig. 2? This potential solution does have a  $E$ -field component in the direction of propagation – it is therefore not TEM but a TM to  $x$  wave (and simultaneously TM to  $z$  wave). At the same time, such a wave is expected to decay far way from the surface, which means that the solution is becoming a *surface non-leaky*<sup>1</sup> wave. The surface impedance  $Z_s$  is thus

$$Z_s \equiv -\frac{E_x(z=0)}{H_y(z=0)} = \frac{w}{g} Z_{\text{ter}} \quad (4a)$$

$$Z_s = jZ_0 \tan kd \quad \text{or} \quad Z_s = jZ_0 \frac{g}{g+t} \tan kd \quad (4b)$$

where  $E$  and  $H$  now denote the field components of the *surface wave field* in the opening of the parallel plate resonator. In other words, the surface wave impedance looking into

---

<sup>1</sup> The surface leaky waves have a small non-zero wave vector component in the- $z$ -direction. In other words, a part of the energy trapped close to the surface is being radiated away. Otherwise, they are similar to standard (non-leaky) surface waves. In particular, a layer of dielectric with metal backing is a “competitor” to metal corrugation – it may support both surface waves and leaky surface waves.

the top of the corrugated surface is equal the termination impedance of the parallel plate transmission line looking into the corrugation bottom, to within a factor of  $g/w$ .

### 1.3. Solution for a slow surface wave [1]<sup>2</sup>

The problem shown in Fig. 2 is further simplified as shown in Fig. 3. The corrugation boundary condition is extended to the entire surface, which corresponds to metal teeth that are infinitely thin but still could block out plane wave of type I. Furthermore, Eq. (1) needs to be satisfied in order to enable Eqs. (3) to be valid for the fundamental TEM mode of the resonator.

Now, however, we are no longer interested in the parallel plate resonators that have all been replaced by the corresponding boundary condition on the top of corrugation – see Fig. 3. This is a reasonable approximation that is commonly used in practice. If necessary, the exact mathematical analysis of the external field coupled to all modes in the inner corrugation waveguide can be done – the so-called *space harmonic approach* – see Ref. [4] for the planar corrugation or Ref. [9], Appendix, for cylindrical corrugation.

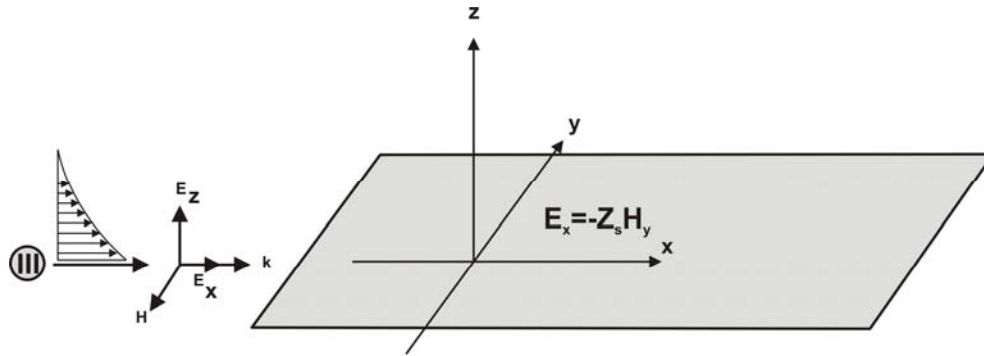


Fig. 3. Simplified problem geometry. The corrugation with thin teeth is replaced by uniform boundary conditions Eqs. (4).

We further seek a solution for the surface wave of type III in the form

$$\begin{aligned} E_x &= E_{x0} \exp(-jk_x x - \alpha z) \\ E_z &= E_{z0} \exp(-jk_x x - \alpha z) \\ H_y &= H_{y0} \exp(-jk_x x - \alpha z) \end{aligned} \tag{5}$$

with an a priori unknown positive decay factor  $\alpha$ . The first step is to express the amplitudes of the electric and magnetic field through each other. For this purpose, it is

<sup>2</sup> In this section, we follow the derivation given in Ref. [1] although the acoustic and electromagnetic surface waves have been known since Lord Rayleigh and the corresponding derivation for an electromagnetic surface wave, which is supported by an impedance boundary, can indeed be found in earlier sources.

wise to use Maxwell's curl equation since the curl of the  $H$  field is calculated most straightforwardly, i.e.

$$\nabla \times \vec{H} = j\omega\epsilon\vec{E}, \quad \nabla \times \vec{H} = \left[ \frac{-\partial H_y}{\partial z}, 0, \frac{\partial H_y}{\partial x} \right] = [\alpha, 0, -jk_x] H_{y0} \exp(-jk_x x - \alpha z) \quad (6)$$

That yields

$$E_{x0} = \frac{\alpha}{j\omega\epsilon} H_{y0} \quad (7a)$$

$$E_{z0} = -\frac{k_x}{\omega\epsilon} H_{y0} \quad (7b)$$

The next step is to substitute Eqs. (5) into any of the vector Helmholtz equations

$$\Delta \vec{E} + k^2 \vec{E} = 0 \quad (8a)$$

$$\Delta \vec{H} + k^2 \vec{H} = 0 \quad (8b)$$

This gives us the dispersion relation in the form

$$k^2 - k_x^2 + \alpha^2 = 0 \quad (9)$$

The dispersion relation in general allows us to express the propagation wavenumber (in this case just  $k_x$ ) through frequency  $\omega$  or, which is the same, through free-space wavenumber  $k = \omega/c$ . The decay factor  $\alpha$  is yet to be determined. To find  $\alpha$ , we finally plug the anticipated solution (5) into the boundary condition (4) to obtain

$$\frac{d\alpha}{j\omega\epsilon} = -Z_0 \frac{Z_{\text{bottom}} + jZ_0 \tan kd}{Z_0 + jZ_{\text{bottom}} \tan kd}, \quad \alpha = -\frac{j\omega\epsilon Z_0}{g} \frac{Z_{\text{bottom}} + jZ_0 \tan kd}{Z_0 + jZ_{\text{bottom}} \tan kd} \quad (10)$$

The result simplifies for  $Z_{\text{bottom}} = 0$  (metal corrugation with no bottom load) and takes the form

$$\alpha = \frac{\omega\epsilon Z_0}{g} \tan kd = \eta\epsilon\omega \tan kd = k \tan kd \quad (11)$$

where, according to Eq. (9),

$$k_x = k\sqrt{1 + \tan^2 kd} \quad (12a)$$

When the corrugation teeth are considered to be of finite width, an approximate solution can be obtained by replacing Eq. (3b) by the average surface impedance Eq.(3c). It has the form [1]

$$k_x = k\sqrt{1 + \left(\frac{g}{g+t}\right)^2 \tan^2 kd} \quad (12b)$$

The propagation or phase speed of the surface wave thus becomes

$$c_p \equiv \frac{\omega}{k_x} = c \frac{k}{k_x} \quad (13)$$

Now, we will summarize the above results for a planar corrugated surface in the form of a chart that uses the corrugation depth as a varying parameter.

**Case a).** Zero corrugation depth,  $d = 0$ . The decay factor  $\alpha$  from Eq. (11) becomes zero, the  $E$ -field component in the propagation direction given by Eq. (7a) is also zero. The surface wave transforms into a non-decaying plane wave of type II. The corrugation surface becomes the solid metal surface.

**Case b).** Small corrugation depth, less than quarter wavelength,  $0 < kd < \pi/2$  or  $d < \lambda/4$ . The decay factor  $\alpha$  from Eq. (11) is positive; the slow surface wave with the propagation speed (metal teeth are infinitely thin)

$$c_p = \frac{c}{\sqrt{1 + \tan^2 kd}} < c \quad (14)$$

being less than speed of light in the medium may exist. No other modes of type I or II can propagate along the surface. The surface wave is “bonded” to the corrugated surface and formally exists only for an infinite such surface.

**Case c).** Large corrugation depth, greater than or equal to quarter wavelength,  $\pi/2 \leq kd < \pi$  or  $\lambda/4 \leq d < \lambda/2$ . The decay factor  $\alpha$  from Eq. (11) is negative; the decaying surface wave cannot therefore exist. No modes of type I or II or III can therefore propagate along the surface. This case – the *surface wave cutoff region* – is perhaps most interesting from the viewpoint of practical applications.



**Case d).** Larger corrugation depths, greater than or equal to half wavelength,  $kd > \pi$  or  $d > \lambda/2$ . The process repeats periodically according to sign of the tangent function in Eq. (11).

#### **1.4. Corrugated surface as an antenna ground plane**

The idea of the corrugated surface as a ground plane is perhaps best explained on the base of Fig. 4 that is partially adopted from Ref. [5]. Consider a monopole-like antenna located in the middle of a metal (Fig. 4a) or corrugated (Fig. 4b) finite ground plane. The metal ground plane supports the plane wave of type II that travels all the way toward the surface edge and then is being radiated from the edge as if the edge tip would be somewhat similar to a point source. Note that the uniform theory of diffraction (UTD) is commonly used to analyze the edge diffraction – see, for example, Ref. [6].

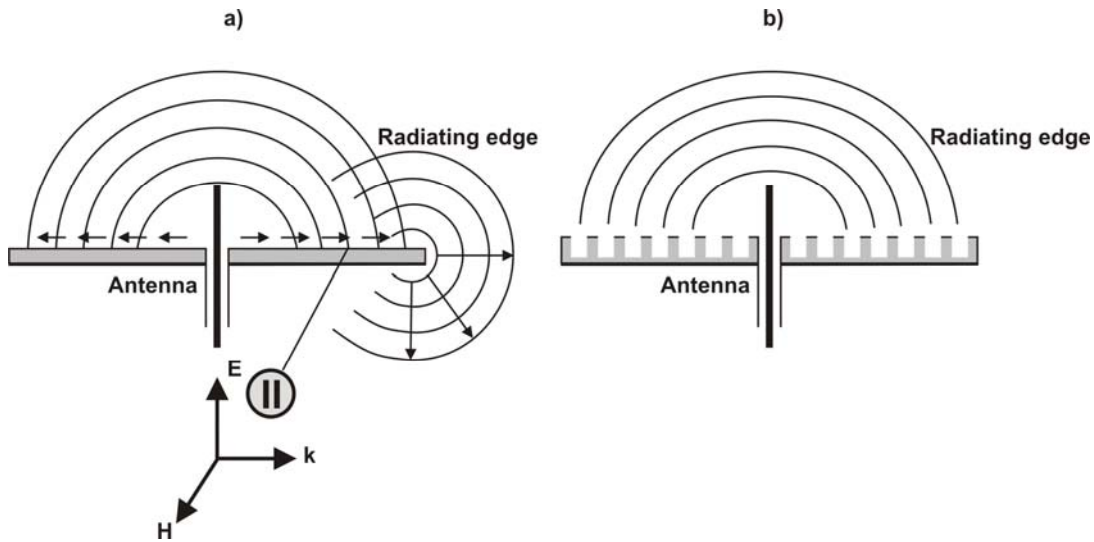


Fig. 4. A monopole-like antenna in the middle of a finite ground plane; a) –finite metal ground plane; b) – finite cutoff corrugation surface. The signal radiated from ground plane edge is schematically shown.

The edge radiation is in particular directed downwards, which means a significant antenna backlobe. Due to reciprocity, the same pattern holds for the receiving antenna. The receiving antenna will thus not only receive the useful signal from a positive elevation angle but also will receive all the electromagnetic noise that is emitted by ground and, what might be more important, the noise emitted by possible interference sources located close to horizon. These sources could be due to a residential activity for larger UHF or L/S band antennas. For an antenna printed on a chip, these sources could be due to neighbor on-chip components.

On the other hand, the cutoff corrugated surface shown in Fig. 4b will suppress either plane or surface wave and will thus prevent the edge radiation. Hence, the backlobe

radiation and radiation at very low elevation angles (from horizon) should be significantly reduced. Indeed, the present property of the corrugated surface holds only for a certain band of frequencies.

At this point one may ask a question: what happens to a plane wave that is incident upon the corrugated surface at a nonzero incidence angle? Such a plane wave may be generated by a taller antenna similar to a monopole. If the direction of incidence is still transversal to the corrugation, the plane wave at any non-oblique incidence is to be separated into two components: with the wave vector being parallel and perpendicular to the ground plane, respectively. The former component is the plane wave of type I or II in Fig. 4 and can be treated accordingly. The latter is of little interest for the present study since it will be reflected back vertically.

## 2. GPS cutoff choke ring

### **2.1. Note on GPS navigation and base station (high-performance) antennas<sup>3</sup>**

Along with the corrugated horn [10]-[16] and the monopole above the corrugation [7], an important example of an antenna with the cylindrical corrugated ground plane is given by a GPS base station antenna. The Global Positioning System (GPS) is a receive-only continuous (CW) signal, spread spectrum radio navigation system operating at L-band. In the ultimate configuration, 24 satellites in approximately 12,000 miles altitude orbit provide navigation capability by any number of users. Continuous position fixing is achieved by range tracking (in general) for satellites. Each satellite also transmits its orbit parameters (for calculating the satellite position as a function of time), which when used in conjunction with the range measurements allow the users position and system time of day to be calculated. The patterns of the GPS coverage require almost uniform coverage from the horizon to zenith<sup>4</sup>.

The GPS is supported by the United States government and enables satellite navigation for military and civilian users alike. Two codes:

- i. coarse grained acquisition code (C/A-code)
- ii. fine-grained precision code (P-code)

are transmitted on two L-band microwave frequencies, e.g. L1 on 1575.42 MHz and L2 on 1.227.6 MHz, and each provide ranging and GPS-system time information. The C/A code is available to civilian users and the P-code is available primarily to authorized users.

---

<sup>3</sup> Materials of this sections are based on public sources including but not limited to those referenced in this text.

<sup>4</sup> For NAVY antennas and other ship antennas, because of ship roll, coverage must be extended to 30 deg below the horizon.

The L1 and L2 carrier frequencies are sufficiently separated in the radio spectrum as to usually require separate antennas for their reception. The related GPS band chart is shown in Fig. 5 that follows and in Table 1. Microwave patch antennas to receive L-band radio transmissions are a conventional inexpensive solution. They comprise a rectangular conductive foil on a flat ceramic substrate, with typically a high dielectric constant. The dual-band and multiple-band operation is achieved by using stacked patches.

Furthermore, all GPS signals are right-hand circularly-polarized (RHCP) signals – so are the GPS antennas. The circular polarization has several advantages, among them:

- i. orientation of the receiving antenna on earth is no longer important; the receiving antenna plane should be perpendicular to a vertical but can be rotated, dynamically or statically, to any azimuthal angle.
- ii. a better signal-to-noise ratio (SNR) compared to linear polarization as the environmental noise is rather linearly than circularly polarized and is more efficiently filtered out by the antenna.

Table 1. Center frequencies and bandwidth of some public GPS SATCOM bands.

<b>Modernized GPS</b>		
L1=1575.42 MHz	Bandwidth=24 MHz	[1563-1578] MHz
L2=1227.60 MHz	Bandwidth=24 MHz	[1215-1237] MHz
L5=1176.45 MHz	Bandwidth=20 MHz	[1164-1186] MHz
<b>GALILEO</b>		
E1 =1589.742 MHz	Bandwidth=4 MHz	[1587-1591] MHz
E2 =1561.098 MHz	Bandwidth=4 MHz	[1559-1563] MHz
E5 =1191.795 MHz	Bandwidth=24 MHz	
E5a =1176.45 MHz	(=L5)	
E5b =1207.14 MHz		
E6 =1278.75 MHz	Bandwidth=40 MHz	[1260-1300] MHz

A GPS modernization effort was announced in 1999 for the benefit of the military and civilian communities. Two navigation signals will be available for civilian use. The first signal (L2C) is allocated in the current L2 band and the second signal will be available in the new L5 band. The L5 signal, combined with current L, and L2 signals, will provide the extended capabilities of navigation, positioning and timing services. The 24MHz bandwidth extensions for the current L1 and L2 signals are also proposed to carry new codes.

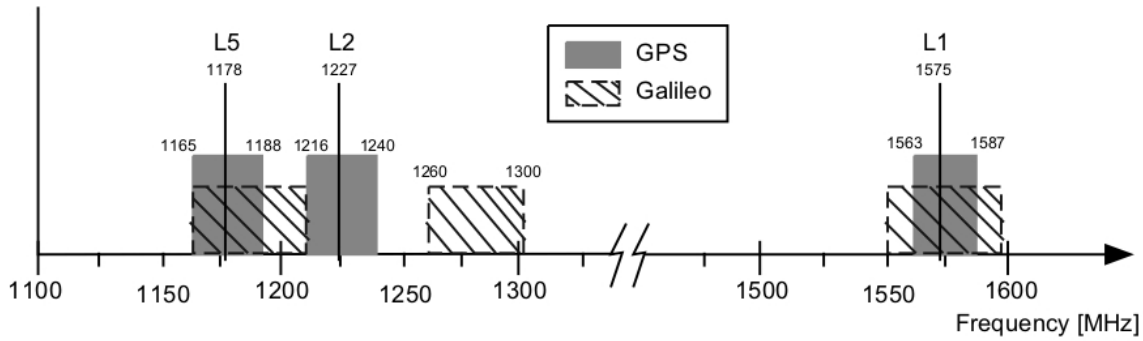


Fig. 5. GPS bands and prospective Galileo (EU) bands; see also Table 1.

The GPS base station antenna is considerably different from an antenna used in the existing car GPS receiver. It needs to satisfy a number of pattern criteria in L1 and L2 bands - see [19], [20] and also other related references [19]-[42] - which are mostly related to the pattern shaping in order to provide with multipath rejection and be able to track up to 12 satellites simultaneously. The most important ones are

- i. the absence of significant RHCP and LHCP sidelobes and backlobes at any negative elevation angles (directed to ground or to nearby scatterers);
- ii. a good polarization isolation over the upper hemisphere;
- iii. a sufficiently large and possibly uniform RHCP gain over the upper hemisphere.

The multipath signals from below horizon due the reflections from ground and mounting structure are main concerns because the antenna usually is mounted less than two meters above the ground and it is difficult for signal processing at the receiver to mitigate the effect of short-distance multipath, less than 10m [34]. The ideal GPS antenna would thus have a uniform gain for the upper hemisphere and block the signal coming from below the horizon. In other words, we attempt to design an ideal "band-pass filter" but in angular domain rather than in frequency domain<sup>5</sup>.

The pattern shaping thus becomes the main goal for the high-performance GPS antenna; the size of the antenna becomes a secondary issue. The pattern control is achieved by the proper ground plane. Since we need a circular polarization at low elevation angles, we need both TM to z and TE to z plane waves shown in Fig. 1 just above the ground plane. On the other hand we need none of them in the direction below horizon, neither we need all of them along the ground plane to eliminate the edge diffraction. Fig. 6 shows a pattern shaping concept that again utilizes the corrugated disk. In the GPS community, such a ground plane is commonly referred to as a *choke ring*.

<sup>5</sup> Similar to the ideal band-pass filter that is not realizable as being a non-causal system, the ideal GPS pattern can hardly be realized in practice.

Fig. 7 shows a typical to date antenna design from Trimble Navigation Limited intended for existing L1/L2 GPS bands [17],[18]. The center radome shown in Fig. 7 typically covers a Dorne-Margolin split-loop antenna<sup>6</sup> or a (droopy) dipole turnstile, or a circularly polarized patch antenna on a metal pedestal, with a dual or single feed, etc.<sup>7</sup>

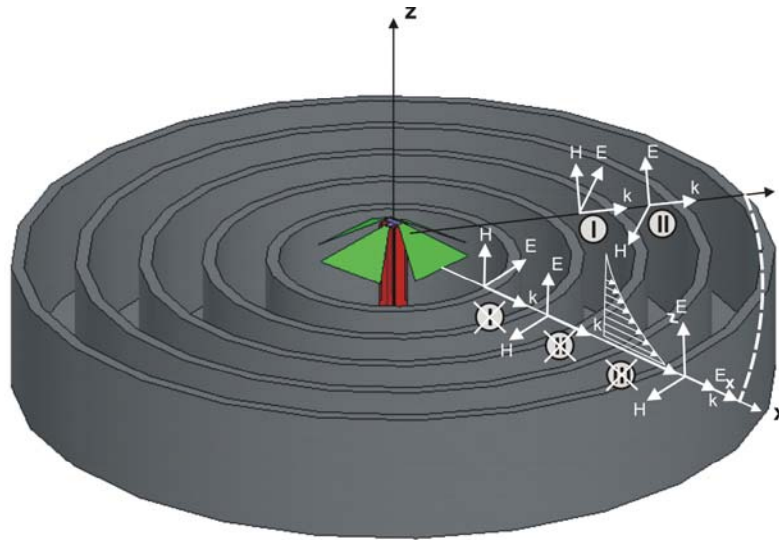
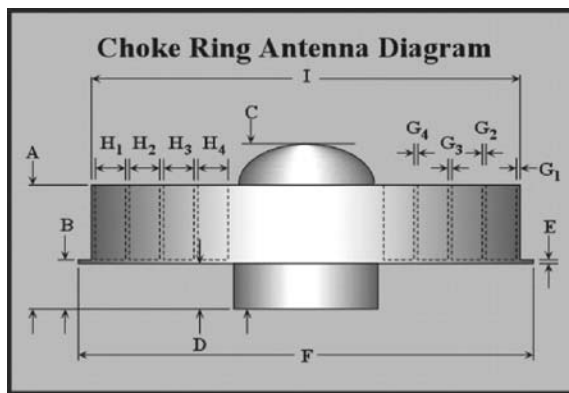


Fig. 6. A pattern shaping concept for the circularly-polarized antenna over a corrugated disk at cutoff. TE to  $z$  plane wave (I), TM to  $z$  plane wave (II), and surface wave (III) cannot propagate along the cutoff corrugated surface – the edge diffraction is thus eliminated or reduced. Such a ground plane is referred to as a *choke ring*.



H-1146

Fig. 7. A generic diagram of the choke ring antenna [18] and a L1/L2 Choke Ring Antenna from Trimble Navigation Limited [17].

<sup>6</sup> See, for example, Ref. [37] for a linearly-polarized Dorne-Margolin antenna operation.

<sup>7</sup> The related antenna elements are not reviewed in this study.

When the depth of the corrugated surface,  $d$ , in Fig. 6 exceeds  $\lambda/4$ , more specifically,  $\lambda/4 < d < \lambda/2$ , the corrugated surface presents a capacitive series reactance to the  $E$ -plane incident field, with no planar or surface wave propagation along the corrugated surface – see case c) in section 1.3 above. The cutoff corrugated surface thus again serves as a way to reduce or eliminate the fields associated with the oblique wave propagation.

According to the theory of planar corrugation, the conventional Trimble's choke ring becomes a cutoff corrugated surface when the depth of the corrugation becomes greater than the largest quarter wavelength – in this case – the quarter wavelength in L2 GPS band centered at 1.227 GHz.

$$d > \lambda_{1.227 \text{ GHz}} / 4 = 61 \text{ mm} \quad (15a)$$

At the same time, the depth still should be less than  $\lambda/2$  at a highest frequency – in this case – the half wavelength in L1 band centered at 1.575 GHz, which yields

$$d < \lambda_{1.575 \text{ GHz}} / 2 = 95 \text{ mm} \quad (15b)$$

In fact, these values will be a bit altered by the corrections to planar corrugation discussed above. A certain value in between these two from Eqs. (15) could be chosen. It makes sense to choose a lower depth in order to reduce the ground plane height. In particular, the depth of 61 to 64 mm will give good results for a wideband base station GPS turnstile according to full-wave numerical simulations – see below. Other parameters of the choke ring then need to be optimized properly. There is no exact recipe, however. The corrugation width should be large enough to ensure proper boundary conditions at cutoff whereas the tooth width may be small.

Dual frequency (L1/L2) choke ring base station antennas provide geodetic-quality GPS measurements for surveying, mapping, and research applications. Typical dual-frequency choke ring antennas maintain a stable phase center that has less than 1 mm of drift. The choke ring antenna is based on the geodetic research standard and features aluminum choke rings and the Dorne-Margolin antenna element. These antennas are durable, have a low power consumption, and have excellent multipath rejection characteristics [19]-[18]. The extensive use of this type of the antenna in the IGS global network makes it a de-facto standard in the GPS community [26]. A list of companies involved in the GPS base station antennas along with the corresponding abbreviations is given below in Table 2 [18].

Table 2. Manufacturers of base station GPS antennas [18].

AER	Aeroantenna
AOA	Allan Osborne Associates

ASH	Ashtech
JPL	Jet Propulsion Lab
JPS	Javad
LEI	Leica
MAC	Macrometer
MAG	Magellan
MPL	Micro Pulse
NAV	NavCom
NOV	NovAtel
SEN	Sensor Systems
SOK	Sokkia
SPP	Spectra Precision
TOP or TPS	Topcon
TRM	Trimble
NGS	National Geodetic Survey

Fig. 8a below shows RHCP (solid curve) and LHCP (dashed curve) gain patterns adopted from Ref. [21] for L1 band (1.57542 GHz) for three antenna types:

- (a) with the 76 cm in diameter aluminum circular ground plane;
- (b) with the same ground plane but covered by a 5.6 cm thick untuned layered absorbing material;
- (c) and with a four-slot non-tapered uniform choke ring ground plane of 37 cm in diameter.

The feeding antenna under consideration was a Dorne-Margolin antenna Model C146 [21] in all three cases. It is seen from Fig. 8a that the choke ring ground plane clearly outperforms the flat ground planes of a larger diameter.

Quite often, a tapered choke ring is used – see below. The principal effect of tapering can be seen in Fig. 8b [21], where a comparison is made of the uniform choke ring (4 slots) with 37 cm in diameter and of a tapered choke ring with the same diameter. The antenna phase center *rms* deviations are hardly affected by tapering [21].

A major disadvantage of the choke ring antenna is seen directly from Fig. 6 and Fig. 8a and 8b – not only the backlobe radiation is suppressed, but also radiation (RHCP gain) at low but positive elevation angles, typically 20 deg and lower [26]. Another drawback is a large size; the Trimble choke ring, for example, is about 360mm in diameter.

The antenna *phase center* will depend on both the azimuth and elevation angle, additionally; it will vary with frequency for every particular direction in the upper hemisphere. Such a variation should indeed be minimized for TOA- based measurements. The phase center dynamics is also critical for the high-precision GPS antennas.

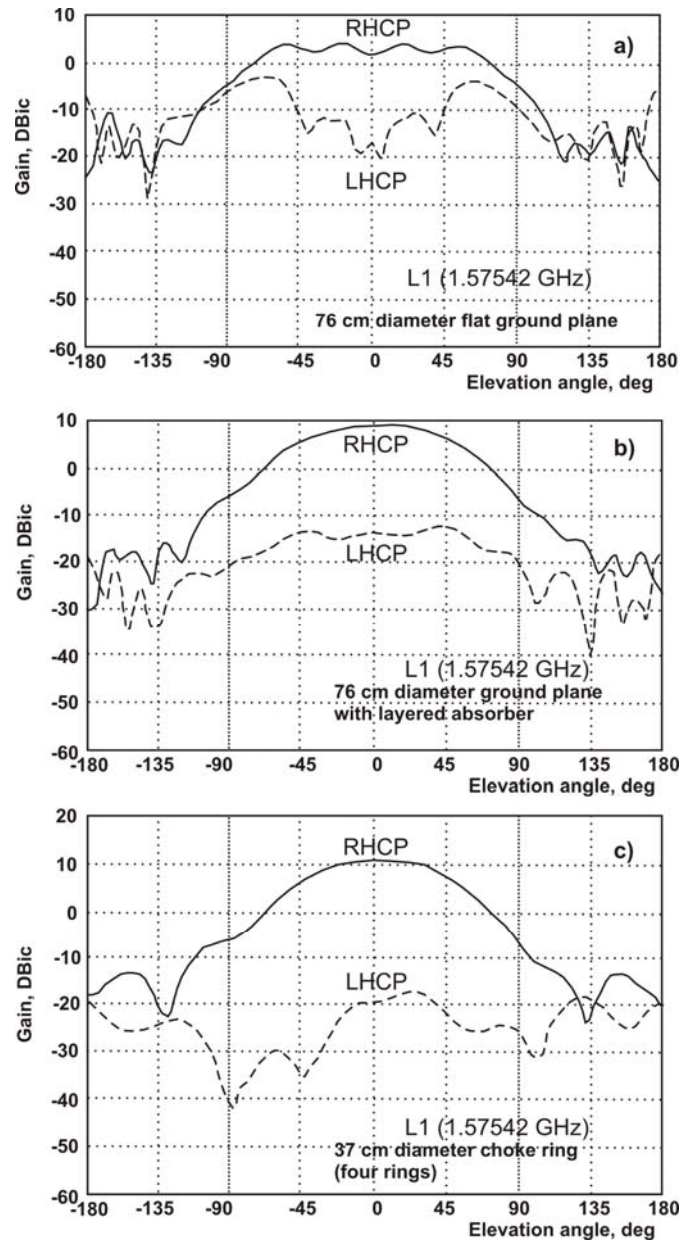


Fig. 8a. L1 RHCP and LHCP gain patterns for three antenna ground planes [21]: (a) with the 76 cm in diameter aluminum circular ground plane; (b) with the same ground plane but covered by a 5.6 cm thick untuned layered absorbing material; (c) and with a four-slot non-tapered uniform choke ring ground plane of 37 cm in diameter.

It is suggested in [21] to determine the *best-fit* phase sphere first by a least-mean square fit to the measured (or calculated) hemispherical phase data. Then, a local *rms* deviation from that value can be estimated, which gives the average error estimate. For the choke



ring ground plane, the rms phase deviation of about 5 deg (approximately 3mm at L1) is typical [21].

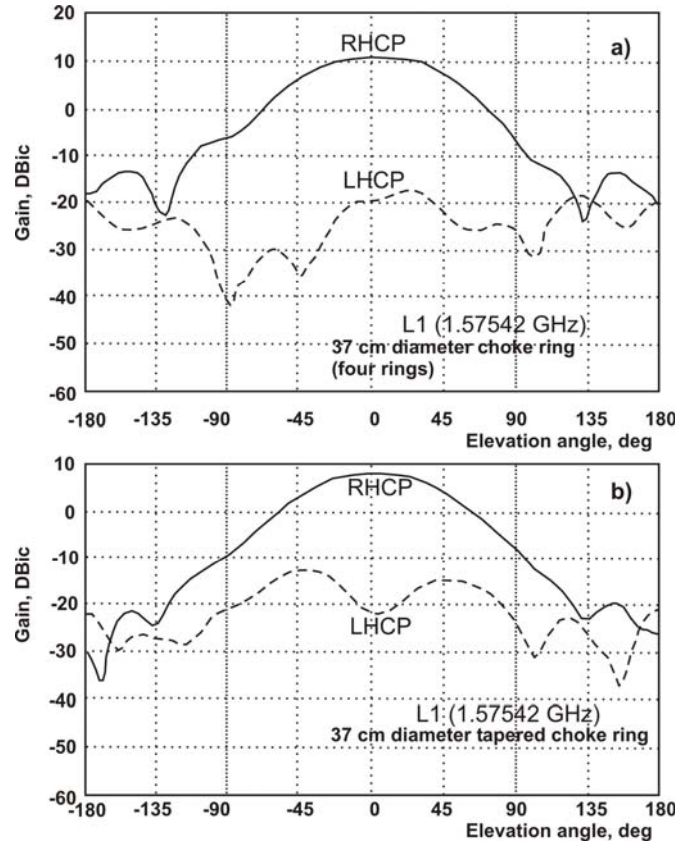


Fig. 8b. Comparison of the uniform choke ring (4 slots) with 37 cm in diameter (a) with a tapered choke ring having the same diameter (b) – Ref. [21].

## 2.2. Choke ring modifications and extensions

A lot of modifications/extensions of the choke ring and the radiating antenna element have been proposed and realized [17]-[36], along with the extensive measurements on different prototype and commercial antennas - see [17]-[36], [38]-[41]. Among them:

- i. Standard non-tapered choke ring with typically 3-5 corrugation grooves, each of them is about 63 mm in depth – Fig. 9a;
- ii. Tapered choke ring – Fig. 9b;
- iii. Dual-frequency choke ring – Fig. 9c;
- iv. Dielectric-filled choke ring – Fig. 9d;
- v. Resistive tapered ground plane – Fig. 9e;
- vi. Horizontal corrugation – Fig. 9f.

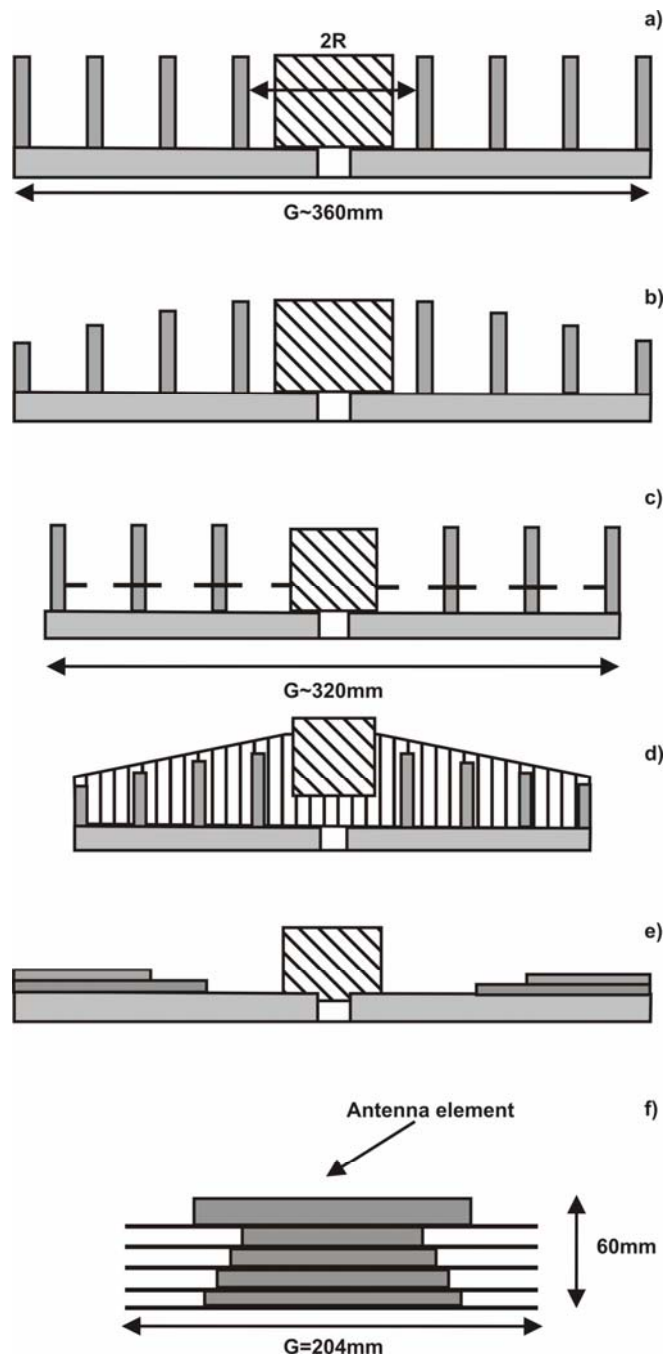


Fig. 9. Different modifications of the choke ring: a) – uniform; b) – tapered; c) – dual-frequency; d) – dielectric-filled; e) – resistive taper; f) –horizontal corrugation.

Not shown in Fig. 9 are the pinwheel GPS base station antenna [27],[33], the GPS antennas with the conical ground planes [24], p. 231-234, [43], and the rolled-edge cavity antenna with a reflector [45]. These variations are briefly reviewed in the following text.

*Tapered choke ring* – see [21],[26]

One possible effect of tapering is shown in Fig. 8b [21]. The conical choke ring ground plane was proposed for GPS antennas used in precise geodetic applications [26]. It is claimed that the proposed choke ring configuration allows better reception of low elevation angle GPS satellites and improved multipath rejection. The proposed ground plane does not degrade other performance characteristics (i.e. pattern symmetry) that are typically associated with 2D choke ring (standard) ground planes [26].

*Dual-frequency choke rings* [32], [28]

A filter in the choke ring groove is introduced to make it exactly resonant ( $\lambda/4$  resonance) at two frequencies (L1 and L2). The filter or diaphragm blocks (reflects) the high frequency but passes low frequencies. The invented design is claimed to have equally good performance for L1 and L2 bands and has a reduced size (320 mm total length) compared to the standard choke ring<sup>8</sup>.

*Dielectric-filled (tapered) choke ring* [29]

A low-profile dielectric –filled (tapered) choke ring is less bulky and is smaller in size and the use of ceramics as a high dielectric constant material promotes fabrication by molding and mass production techniques.

*Resistive tapered ground plane (R-card)* [30],[31]

The peripheral region of the ground plane comprises at least one conductive layer that extends radially beyond the radiating element and provides a sheet resistivity higher than that of the radiating element. Different geometry distributions of the resistive spots are invented. Though physically small, the ground plane structure reduces multipath signals caused by reflections from the Earth.

*Horizontal corrugation* [34],[25]; see also [43], pp. 231-234 and p. 361

In [34],[25], a triple stacked patch antenna as a radiating element for L1, L2, and L5 bands is proposed and realized. The corresponding edge diffraction reflector uses the plurality of conducting plates, preferably circular in shape, instead of using ring-type walls as with the conventional choke ring. The depth of the grooves (typically five stacked grooves has been considered) was optimized using Ansoft HFSS – the depth is typically 0.2 wavelength at the operating frequency. The resulting design is small (204×60mm versus approximately 360×63 mm for the standard choke ring) but its performance, with regard to polarization isolation, is a bit lowered.

*Pinwheel antenna/ground plane* [27],[33]

The entire ground plane is replaced by a microstrip-coupled slot-array antenna that includes a nonconductive planar substrate and a transmission line disposed on a rear substrate surface. A conductive layer on the front substrate surface includes a plurality of

---

<sup>8</sup> The present design is somewhat questionable as the metal corrugation is inherently broadband and using its exact tuning at two relatively close resonant frequencies could perhaps give merely a modest improvement.

slotted openings arrayed about an antenna axis. A surface-wave suppression region encloses the array of slotted openings, and a plurality of peripheral openings are disposed between the surface-wave suppression region and the peripheral edge of the antenna.

*Slotted cone with dipole turnstile* [43], p. 231-234 and *truncated cone with a patch antenna at L1, L2* [24]

For the truncated cone with the patch antenna feeding element; the performance in L1 and L2 bands is good; the ground plane size is also considerably smaller than that of the choke ring.

*Rolled-edge cavity-backed turnstile antenna* [45]

This cavity antenna has a broadband crossed dipole and a rolled edge cavity termination to reduce illumination loss resulting from feed backlobes. This design motivated by a future GPS monitoring application covers the L5 (1176 MHz) to L1 (1575 MHz) frequencies. The antenna is used as a *compact feed* in a relatively small (4 ft) reflector.

It is not the goal of this study to present a comprehensive review of different feeding elements. One can mention the Dorne-Margolin antenna element briefly discussed above and

- curved dipole turnstile with dipole wing tips closely spaced to the ground plane [35];
- a patch antenna assembly when two antennas (L1 and L2) are mounted flat and adjacent to one another [36];
- volute (or quadrifilar helix) antenna [42], etc.

### **3. Cutoff choke ring performance over the band 1.15-1.60 GHz**

Even though the cutoff corrugated surface is rather bulky, it's major advantage compared to the conformal frequency-selective surfaces (a mushroom surface) is a large frequency bandwidth [7]. The present example relates to the GPS base station antenna and provides a confirmation to this fact. We will not be able to obtain the choke ring performance over a large band of frequencies as good as in Fig. 8a and 8b, indeed. However, we will show that a properly designed choke ring ground plane performs reasonably well in the frequency band from 1.15 GHz to 1.60 GHz, which simultaneously covers L1, L2, and L5 GPS bands as well as prospective Galileo bands.

#### **3.1 Radiating element and choke ring setup**

Below, we present typical simulated performance results for a wideband choke ring ground plane with a circularly-polarized *droopy turnstile radiating element*. The sketch of the setup and the dimensions are shown in Fig. 10 that follows.

The choice of the turnstile element instead of the more common patch antenna and the further choice of the bowtie shape of the turnstile dipole is made to increase the antenna

impedance bandwidth [46]-[48]. The choice of the droopy turnstile is made to improve the RHCP pattern (or more general dual polarization) of the antenna close to horizon, where one of the ordinary straight turnstile dipoles has a null and thus does not contribute to circular polarization. On the other hand, the (smaller) vertical field component created by the droopy element allows us to maintain the circular polarization at low elevation angles. The choke ring ground plane should operate at cutoff frequency everywhere within the desired band. One more important antenna component is the turnstile balun; the balun is not the subject of the present study and is to be considered separately.

It is less challenging to achieve the necessary pattern performance in a single frequency band or for a dual-band narrowband operation. It however more challenging to achieve a comparable performance over a wide frequency bandwidth. Below, we will present some results for a broadband choke ring ground plane. These results are not expected to give a very sharp drop off for the RHCP gain close to horizon or completely eliminate the backlobe. At the same time, they may guarantee us an acceptable performance uniformly over the band 1.15-1.60 GHz that includes L1, L2, and L5 GPS bands as well as anticipated Galileo bands - see above.

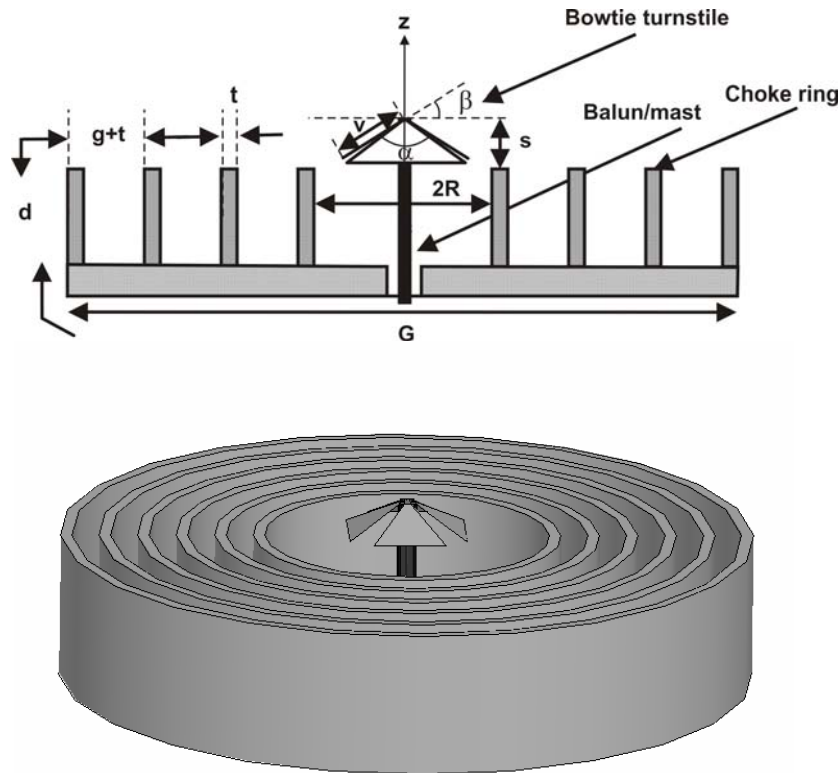


Fig. 10. Top - geometry of the choke ring with bowtie turnstile; bottom - a more generic structure with variable number of rings created in Ansoft HFSS.

### 3.2 Ground plane modeling

Since the analytical corrugation model could give qualitative estimates and an initial guess only (even though it may be quite correct), the fine tuning of the ground plane with a cavity and antenna radiating element should be done with the help of numerical modeling software, e.g. Ansoft HFSS.

Table 3 and Fig. 11 provide with the parameters for some selected geometry designs. The number of corrugation rings is the rounded ratio of the choke ring radius,  $G/2$ , minus the cavity radius,  $R$ , to the ring period,  $g+t$ . It is equal to 2-5 for all the geometries listed in Table 3. The presence of a sufficiently large and deep central cavity is a necessary condition for the good choke ring operation with the turnstile element. Further shaping the cavity shape (e.g conical bottom) has little or negative influence on the patterns. For  $v$ ,  $s$ , and  $t$ , Table 3 gives the most appropriate parameter values; other tested configurations are not reported. The droop angle  $\beta$  should be close to 30-45 deg. The presence of the turnstile balun (a mast) affects the polarization isolation at higher elevation angles and cannot be ignored.

Table 3. Geometry parameters for selected antenna configurations. Angles  $\alpha$  and  $\beta$  are equal to 60 and 30 deg, respectively. Numerical FEM solution (Ansoft HFSS) is obtained after 18-20 mesh refinement steps (default linear size of  $0.333\lambda$  for the initial mesh), with the final mesh size of 250,000-350,000 tetrahedra. The PML box size is 550×550×550mm. Only the discrete frequency sweep has been used. The antenna is fed at the balun bottom using two in-quadrature lumped ports.

Geometry	G, mm	R, mm	v, mm	s, mm	g+t, mm	t, mm	d, mm
Design #1 Flat ground plane	360	--	30	ant. height: 50:5:70mm	--	--	--
Design #2 Two rings, wide cavity	360	80	30	14	100	6	65-69
Design #3 Three rings, narrow cavity	360	60	30	14	60	6	65-69
Design #4 Three rings, wide cavity	360	80	30	14	50	6	65-69
Design #5 Four rings, wide cavity	360	80	30	14	34	6	65-69
Design #6 five rings, narrow cavity	360	60	30	14	30	6	65-69

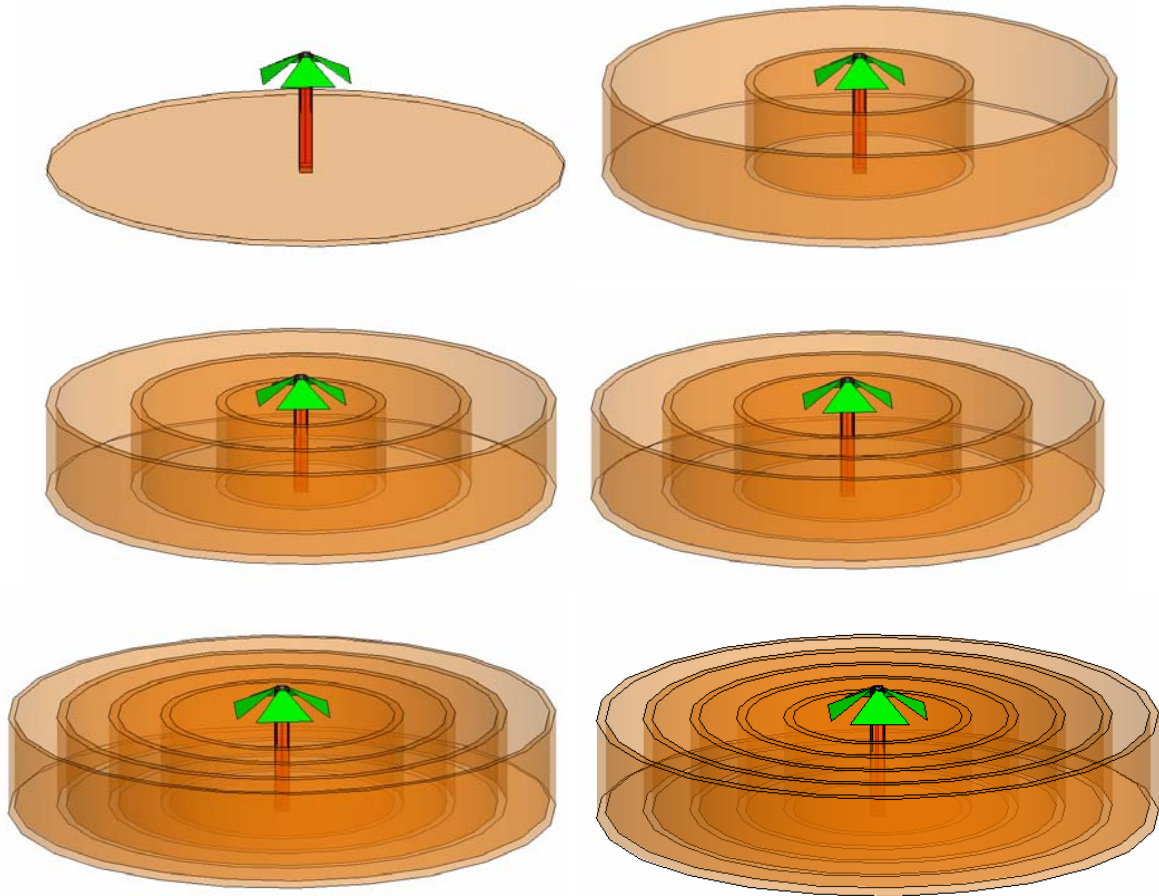


Fig. 11. Choke ring geometry (all rings are 360mm in diameter; with the total height of 65mm; corrugation depth is always 61mm). From left to right and from top to bottom: antennas #1-6 - see Table 3 above.

Fig. 11 only depicts some selected geometries that give a relatively good performance; a large number of other geometries were tested as well, but they are not included into the present text.

Also note that the performance of virtually any choke ring is visibly improved by rolling the outer edge - see Fig. 12. The remaining surface wave is not being radiated from the surface at a certain angle but rather stays bounded to that and spreads out at different angles. However, this modification also increases the ground plane size. Such a method is very similar to that used for the turnstile in a rolled cavity [45].

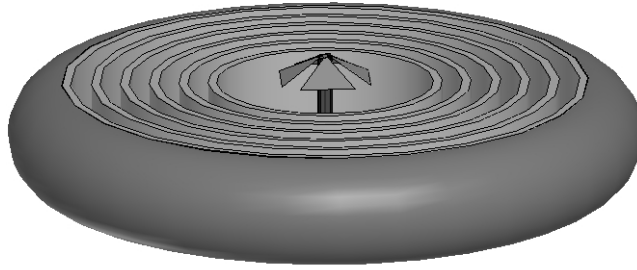


Fig. 12. Possible shaping the choke ring with the rolled edge – an Ansoft HFSS project. Although improving the pattern, this modification may lead to a significant size increase of the ground plane and is therefore ignored in the present study.

### 3.3. *Modeling results*

We present here the complete modeling results for the cases given in Table 3 and Fig. 11, over the band 1.15 GHz to 1.60 GHz. Again, only the pattern information is given, for the absolute antenna gain (RHCP or LHCP). Phase center dynamics and the impedance matching problems of the corresponding feeding element are not considered.

One reason for choosing the set of parameters from Table 3 is a desire to maximize the polarization isolation over the upper hemisphere. Reducing a (relatively narrow) antenna backlobe at 180 deg was a secondary priority<sup>9</sup>.

The RHCP/LHCP patterns are given in Fig.13a to Fig. 13f that follow. Every figure corresponds to a separate case from Table 3, in consecutive order. Variation of parameter  $d$  in Table 3 from 65mm to 69 mm is included. This data – choke ring depth – is labeled on every separate pattern plot for the choke ring. For the flat ground plane (Fig. 13a), the varying separation distance from the ground plane is given. All gain curves are given for a droopy turnstile bowtie over the band 1.15-1.60 GHz, in steps of 0.05 GHz. The following observations can be made from the figures:

- i. The flat ground plane (Fig. 13a) at any separation distance has a poor polarization isolation (less than 10 dB) at elevation angles above 60 deg and a large LHCP backlobe (- 7 dB or so) at 180 deg elevation angle. Furthermore, RHCP gain considerably changes with frequency, which points toward a potential problem with the phase center fluctuations.
- ii. The two-ring choke with a wide cavity (Fig. 13b) improves the polarization isolation to a minimum of about 10 dB for elevation angles above 100 deg. The LHCP backlobe still remains, about -12 dB. The RHCP gain variation with frequency greatly stabilizes.

<sup>9</sup> One way to reduce the backlobe is a tooth at the ring edge bottom.



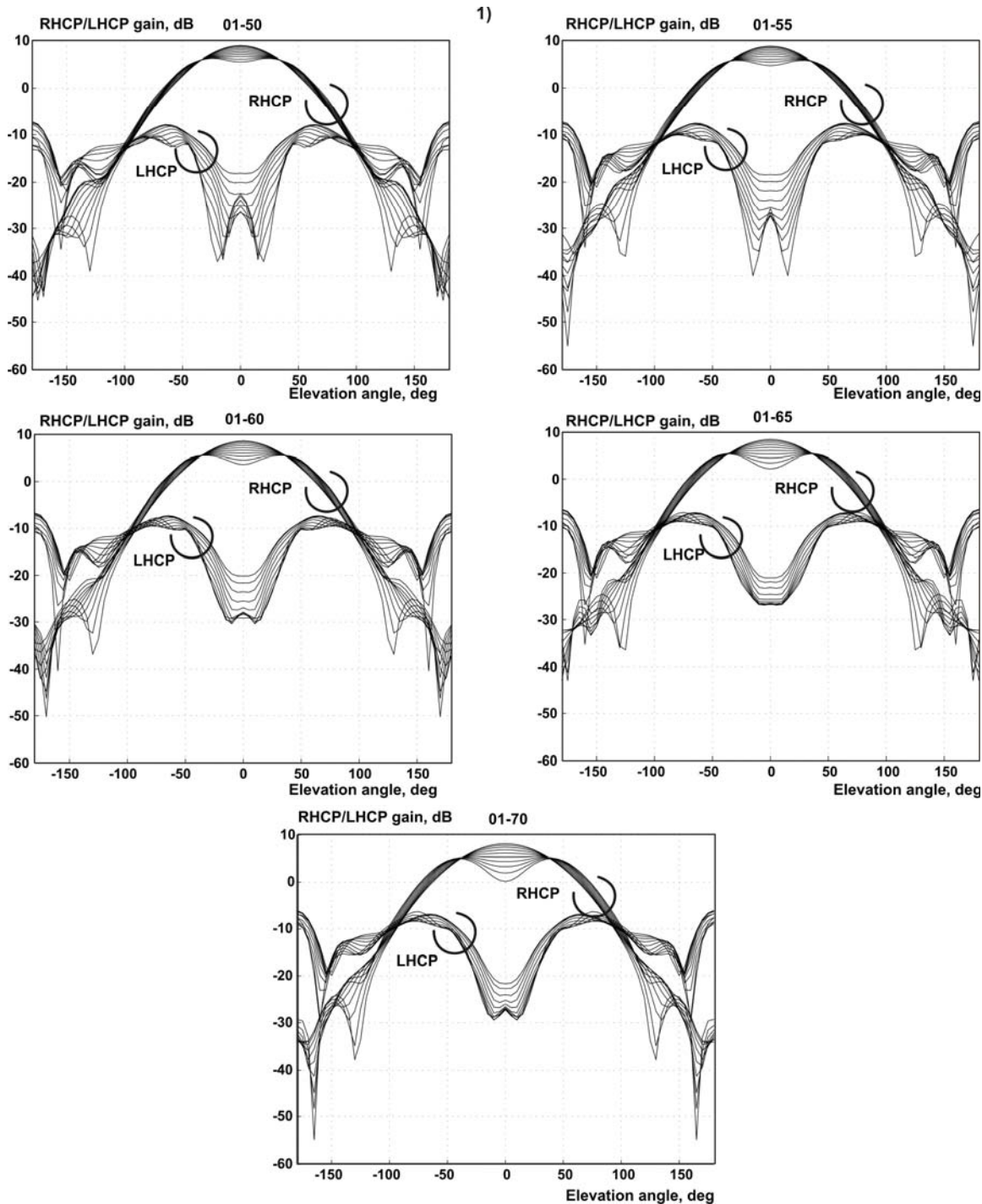


Fig. 13a. RHCP and LHCP gain curves (absolute gain) in the E-plane of one turnstile element – Design #1 in Table 3 (flat ground plane). The gain curves are given for a droopy turnstile bowtie over 1.15-1.60 GHz, in steps of 0.05 GHz. Different plots correspond to different chore ring depths.

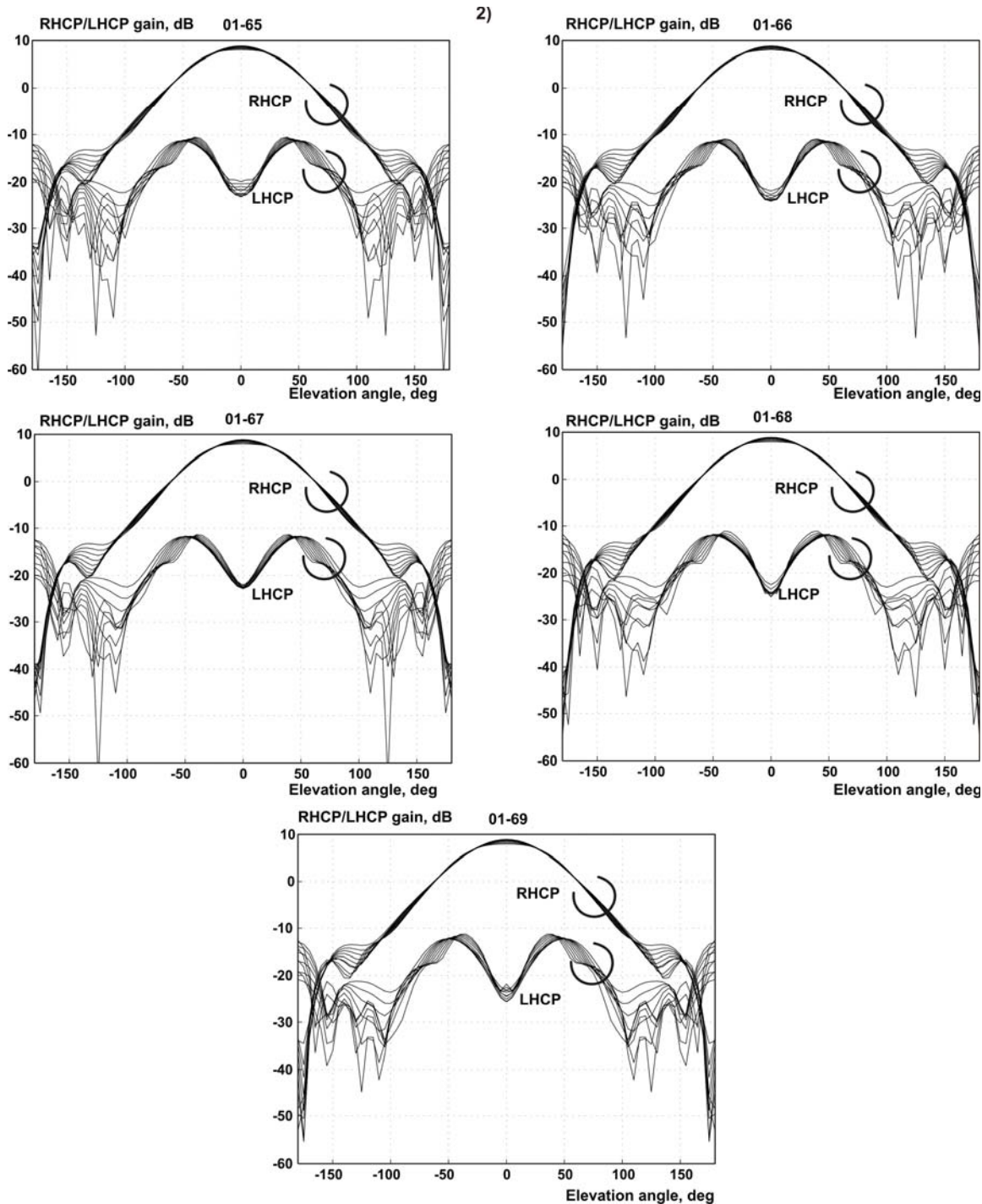


Fig. 13b. RHCP and LHCP gain curves (absolute gain) in the E-plane of one turnstile element – Design #2 in Table 3 (two rings; wide cavity). The gain curves are given for a droopy turnstile bowtie over 1.15-1.60 GHz, in steps of 0.05 GHz. Different plots correspond to different chore ring depths.

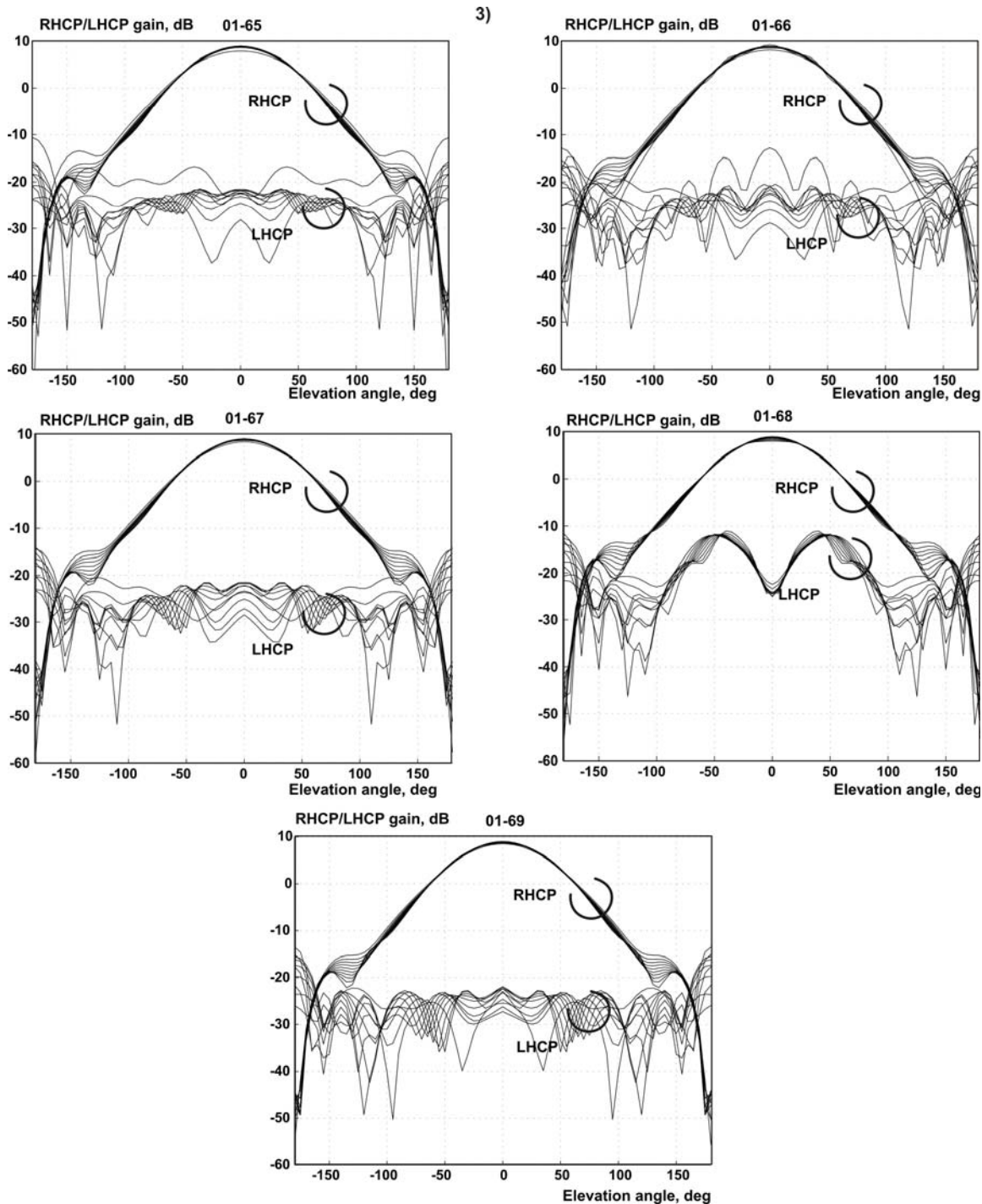


Fig. 13c. RHCP and LHCP gain curves (absolute gain) in the E-plane of one turnstile element – Design #3 in Table 3 (three rings; narrow cavity). The gain curves are given for a droopy turnstile bowtie over 1.15-1.60 GHz, in steps of 0.05 GHz. Different plots correspond to different chore ring depths.

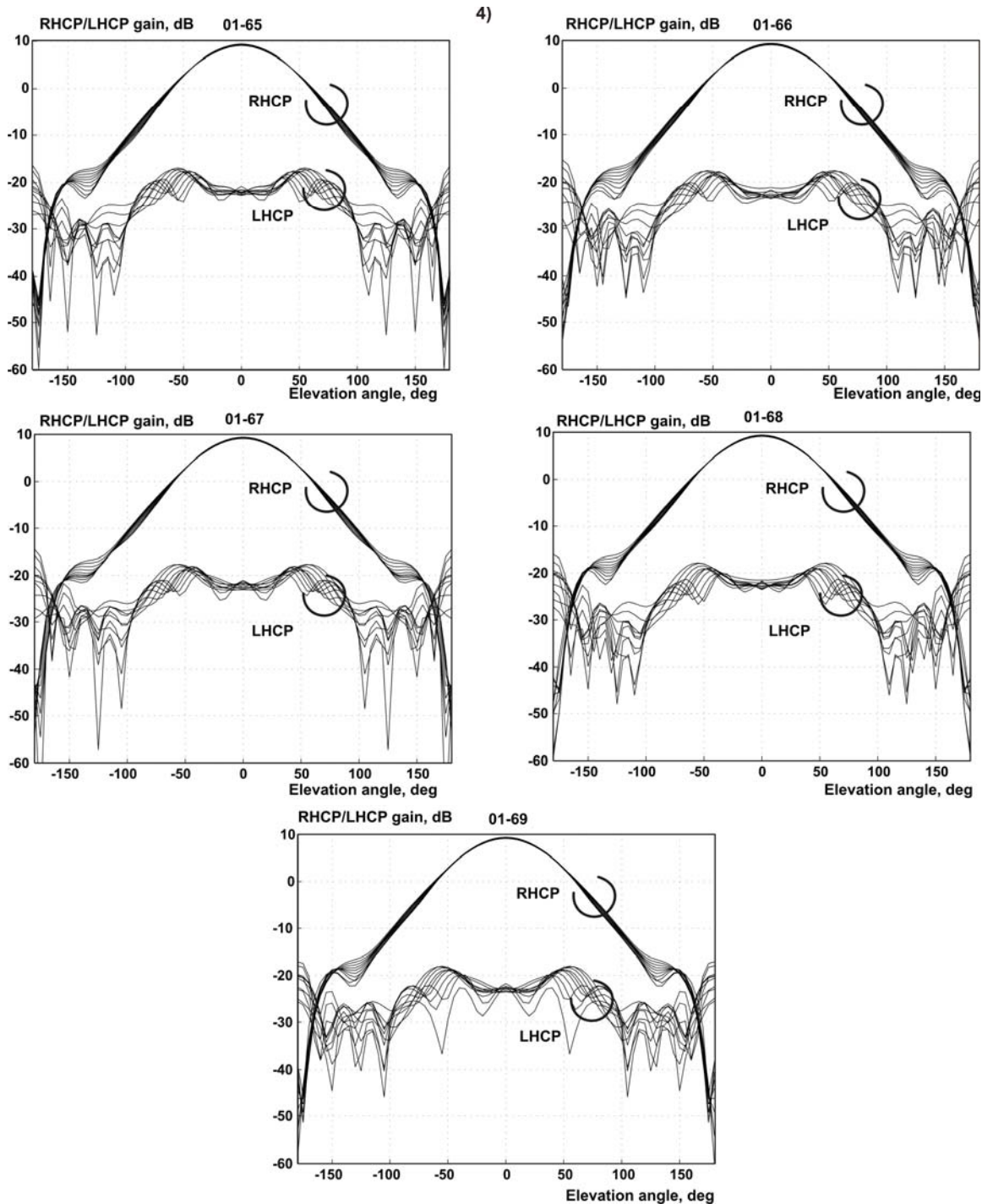


Fig. 13d. RHCP and LHCP gain curves (absolute gain) in the E-plane of one turnstile element – Design #4 in Table 3 (three rings; wide cavity). The gain curves are given for a droopy turnstile bowtie over 1.15-1.60 GHz, in steps of 0.05 GHz. Different plots correspond to different chore ring depths.



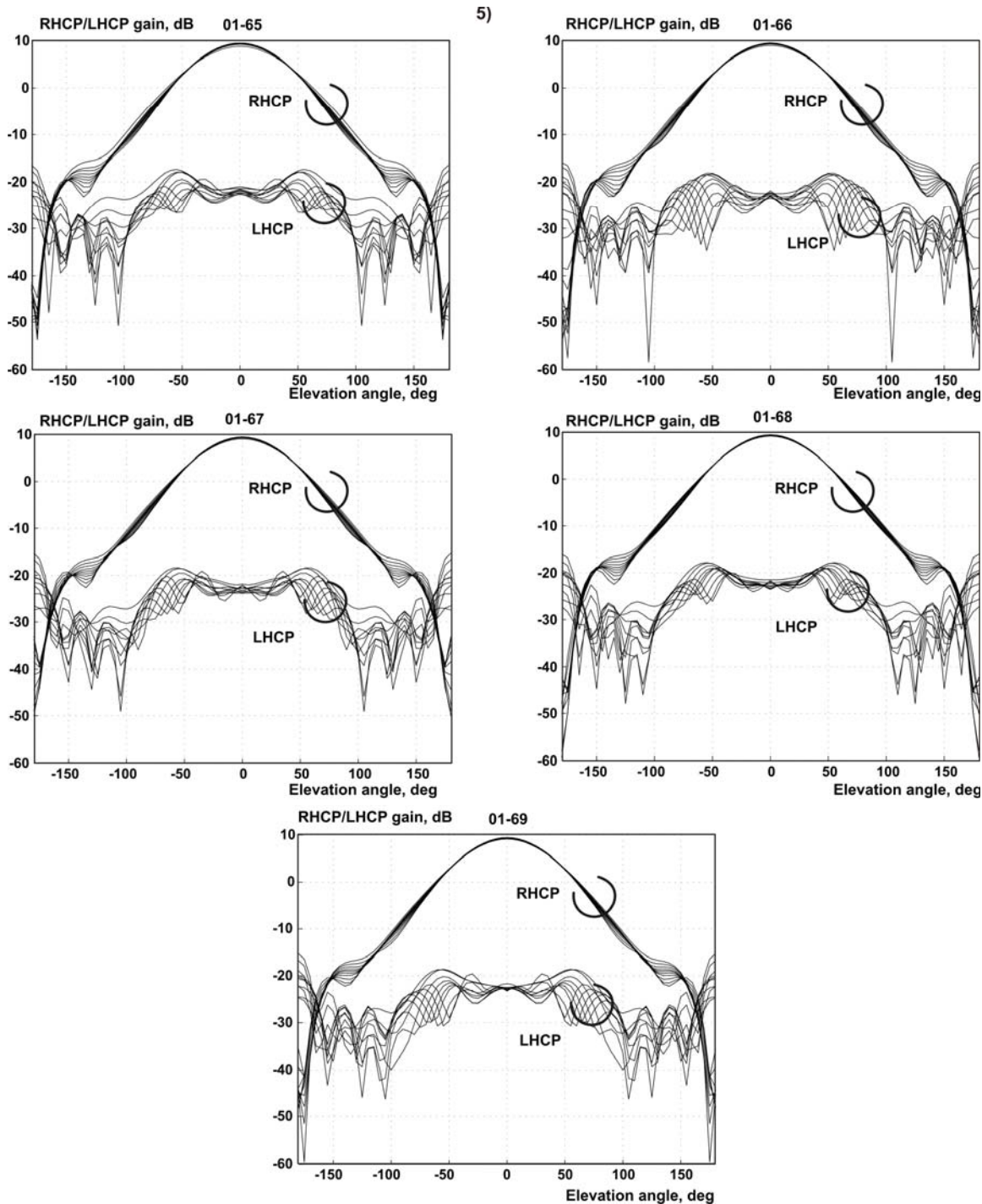


Fig. 13e. RHCP and LHCP gain curves (absolute gain) in the E-plane of one turnstile element – Design #5 in Table 3 (four rings; wide cavity). The gain curves are given for a droopy turnstile bowtie over 1.15-1.60 GHz, in steps of 0.05 GHz. Different plots correspond to different chore ring depths.

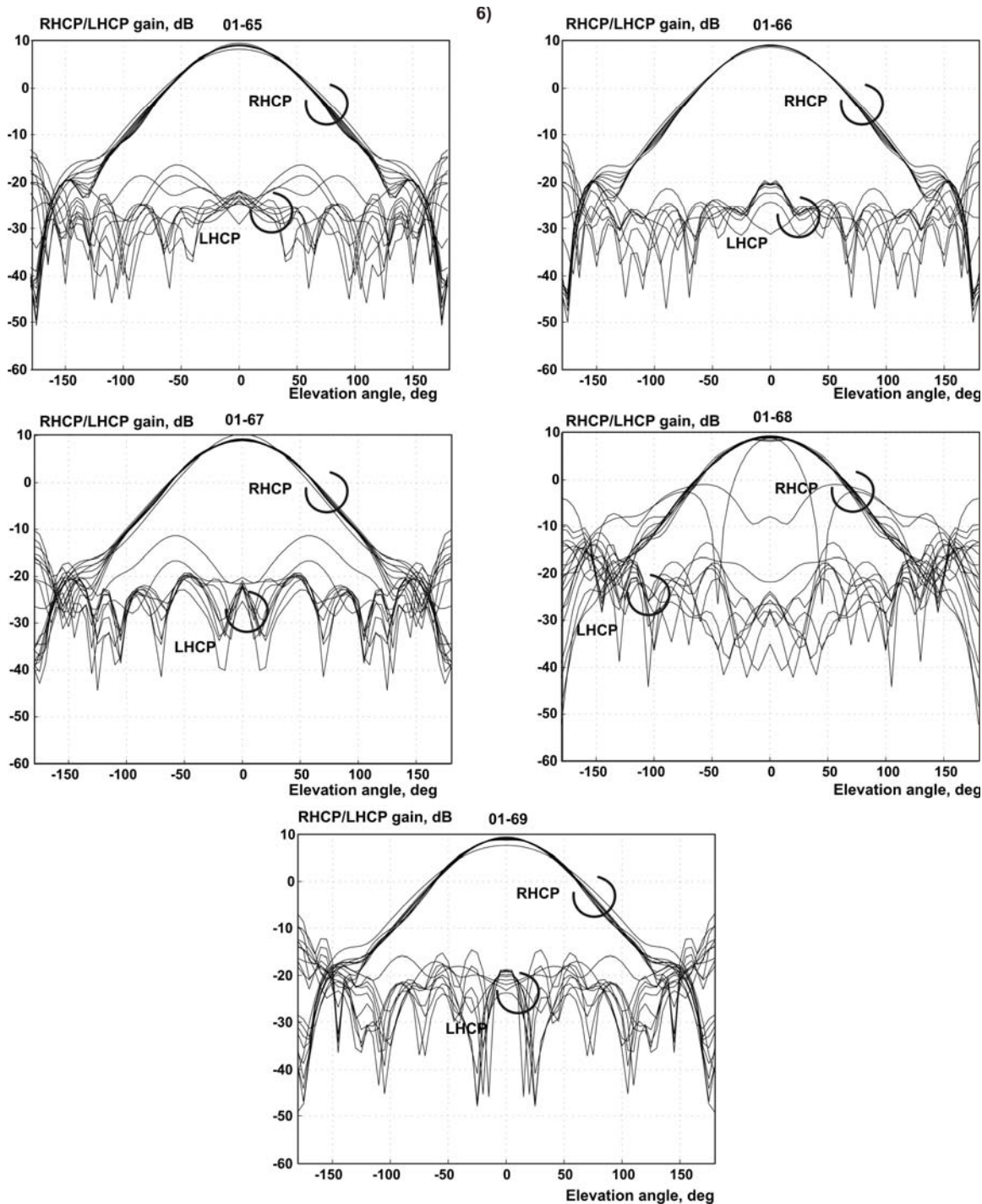


Fig. 13f. RHCP and LHCP gain curves (absolute gain) in the E-plane of one turnstile element – Design #6 in Table 3 (five rings; narrow cavity). The gain curves are given for a droopy turnstile bowtie over 1.15-1.60 GHz, in steps of 0.05 GHz. Different plots correspond to different chore ring depths.

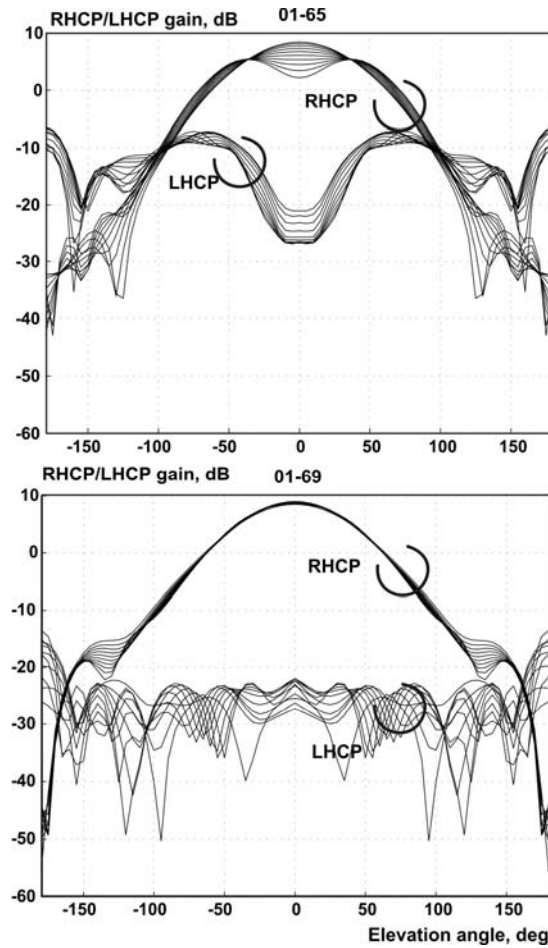


Fig. 13g. RHCP and LHCP gain curves (absolute gain) in the E-plane of one turnstile element; top – flat ground plane spaced by 65 mm from Fig. 13a (Design #1); bottom - Design #3 in Table 3 (three rings; narrow cavity) at 69 mm corrugation depth. The gain curves are given for a droopy turnstile bowtie over 1.15-1.60 GHz, in steps of 0.05 GHz.

- iii. The three-ring choke with a wide cavity (Fig. 13d) very considerably improves the polarization isolation to a minimum of about 15 dB for elevation angles above 100 deg. The LHCP backlobe is on the order of -15 to -17 dB. The RHCP gain variation with frequency greatly stabilizes.
- iv. The four-ring choke with a wide cavity (Fig. 13e) is quite similar to the three-ring choke in Fig. 13d. Therefore, one may conclude that further increase in the number of rings can only have a minor effect on the pattern performance.
- v. The three-ring choke (Fig. 13c) and five-ring choke (Fig. 13f) with a *narrow cavity* still may have an excellent performance at certain turnstile heights. However, these results are very strongly dependent on the turnstile antenna

height: the variation of 1mm in the height may lead to a significant change in the pattern. The narrow cavity may thus have undesired narrowband resonant properties. This effect becomes more dramatic when the number of rings increases – see Fig. 13f.

Thus, the choke ring with three-to four thick rings, tooth height of 65 to 69 mm, and the droopy turnstile element in a reasonably wide cavity may be a reasonable candidate to uniformly cover the band from 1.15 GHz to 1.60 GHz. To again appreciate the value of corrugation Fig. 13g shows the choke ring performance (from Fig. 13c) versus the flat ground plane performance (from Fig. 13a).

## 4. Non-cutoff choke ring performance over the band 1.15-1.60 GHz

### 4.1. Concept

In this section, we discuss a new concept of choke ring operation – as a non-cutoff FSS that may support the slow surface wave – see Fig. 14. We let the surface wave to be excited, as shown in Fig. 14. Therefore, the signal at low elevation angles becomes a combination of the direct LOS signal from the turnstile (TM to z plane wave II) and the slow wave supported by the corrugation surface (surface wave III). The plane wave I (TE to z) is not excited as it is shorted out by the corrugation.

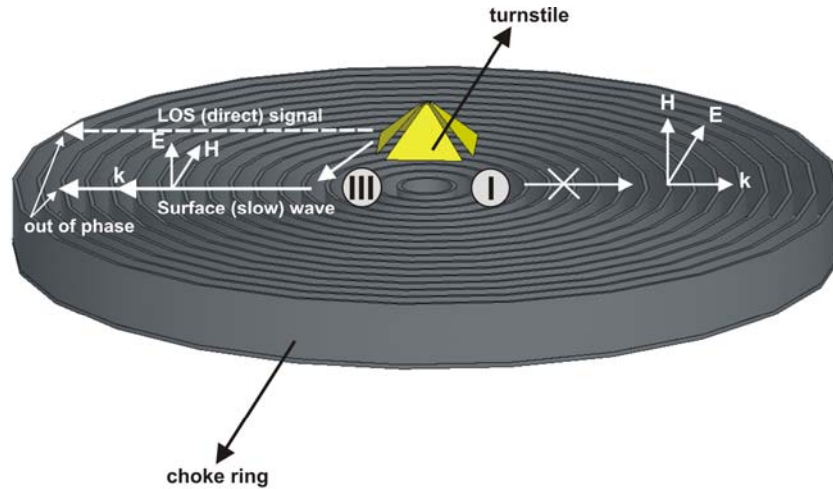


Fig. 14. The concept of phase cancellation for the surface wave and the LOS signal for the turnstile antenna above the choke ring. The phase cancellation is expected close to the choke rim.

We request that the LOS signal and the surface wave are cancelled at the end of the ring, i.e. have almost equal amplitudes and the phase difference of multiple  $\pi$ . Such a cancellation would imply that the major source of edge diffraction – the quasi TM to z wave may be reduced or eliminated. This idea of pattern control is partially adopted from



radar cross-section manipulation at oblique incidence, by virtue of corrugated surfaces [9].

The motivation for the non-cutoff choke ring ground plane is a desire to reduce its height as the non-cutoff corrugated surface is more conformal than the deeper cutoff corrugation.

For a planar infinite corrugated surface one obtains the cancellation condition by comparison of the phases for both waves at the ring edge. It is assumed that the initial phase at the ring center is the same. The cylindrical divergence does not contribute into the phase difference. From Eq. (12b) and Eq. (13), the phase cancellation condition is thus obtained in the form:

$$k_x R - k_0 R = n\pi, \quad \sqrt{1 + \left( \frac{g}{g+t} \tan k_0 d \right)^2} - 1 = \frac{n\pi}{k_0 R}, \quad n = 1, 3, \dots \quad (16)$$

where  $R$  is the distance from the antenna to the rim of the choke ring (choke ring radius). Eq. (16) is indeed an approximation that does not take into account corrections for the rings of constant curvature, variable nonzero incidence angles, divergence, and amplitude taper.

At the same time, the corresponding full-wave simulation test performed for a finite exactly planar corrugated surface excited by a simple dipole indicated that Eq. (16) at  $n = 1$  does predict the pattern cancellation at oblique radiation angles of about 18 dB for a single frequency band.

For a wideband operation, it may be suggested to setup the ring gap in order to achieve a phase cancellation at the higher frequency (1.6 GHz) as being more sensitive to the ring size. For example, at

$$f = 1.60\text{GHz}, d = 33\text{mm}, g = 6\text{mm}, t = 4\text{mm} \quad (17)$$

the required radius value according to Eq. (16) approaches 170mm. In practice, a slightly lower corrugation depth,  $d$ , may be chosen. The dipole height above the corrugation is critical for the subsequent analysis.

#### **4.2. Antenna setup**

A choke ring antenna built according to the above model is shown in Fig. 15 that follows. Fig. 16 depicts the antenna feeding element (turnstile) and the rear of the ground plane with a quadrature hybrid. We have used a split-coaxial balun with four slots and two inner transmission lines. Details of the balun operation may be found elsewhere. The dipole height (from top) above the ground plane is typically around 60mm.



Fig. 15. Non-cutoff ground plane setup; the ground plane diameter is 338 mm. The ground plane has a conical shape with a semi-flare angle close to 85 deg. The corrugation depth (about 30mm) is kept the same along the radius.

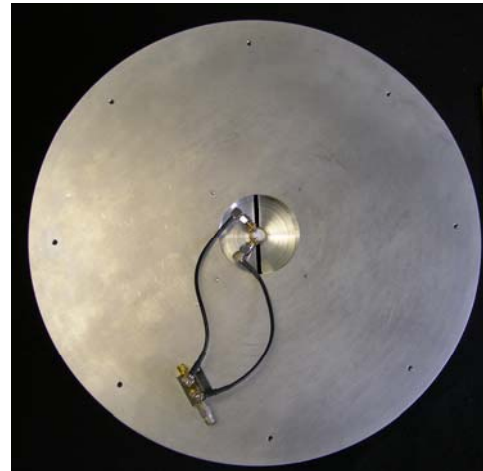
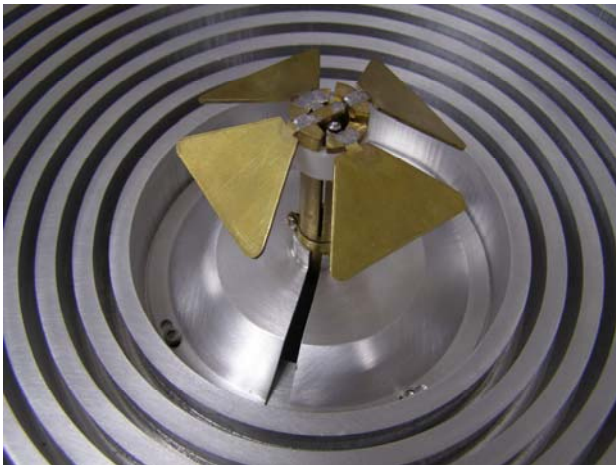


Fig. 16. Antenna element (droopy turnstile bowtie) with the balun and the rear of the ground plane with a quadrature hybrid.  
Two dipole element pairs have been used while testing the antenna:

- i. a pair of shorter dipole turnstiles with a reduced dipole length and with a considerable impedance mismatch at a lower frequency of 1.15 GHz. Also,

- individual dipole impedances have been found to be considerably different at lower frequencies;
- ii. a pair of longer dipole turnstile elements with better absolute impedance matching properties and with a better agreement between two individual impedances.

Fig. 17 shows RHCP and LHCP antenna patterns in the *E*-plane of one dipole (top) and in the *D*-plane (45 deg cut between two dipoles) – bottom. The left column gives the measured data for the smaller dipole turnstile (realized gain)<sup>10</sup>; the right column shows the corresponding numerical simulations (Ansoft HFSS; absolute gain with no impedance mismatch correction). Whilst the simulations for the absolute gain are weakly affected by the dipole size(s), the relative impedance mismatch between two individual dipoles clearly leads to a larger LHCP front lobe at zenith measured in Fig. 17.

To improve the antenna performance, the feeding elements were rebuilt and made longer. Fig. 18 shows similar RHCP and LHCP antenna patterns, but for a pair of longer-dipole feeding elements, with better impedance matching at lower frequencies. The agreement between theory (simulations) and measurements becomes better. Note that the antenna still has a certain impedance mismatch (the return loss approaches -5 to -7dB at low frequencies and then decreases toward high frequencies).

Note, however, that the longer dipoles perform well mostly within the band 1.20 GHz – 1.55 GHz – see Fig. 18. If we add the patterns at 1.15 GHz and 1.6 GHz as shown in Fig. 19 then the antenna performance at zenith (polarization isolation) starts to become worse compared to simulations. It is believed that a not perfect impedance matching of the feeding element is one reason for that.

Both in theory (simulations) and in experiment, the non-cutoff choke ring has a somewhat larger RHCP gain at low elevation angles compared to that for the cutoff choke ring. It also has a somewhat faster decay of the RHCP gain at elevation angles just below the horizon. At the same time, the backlobe at 180 deg is higher than for the cutoff choke ring. It is believed that the performance of the present antenna can be further improved.

Finally, Fig. 20 shows the relative size of the non-cutoff choke ring versus the Trimble Navigation choke ring assembly. One could see a considerable reduction in the size, both in vertical and in horizontal dimensions.

---

<sup>10</sup> All measurements for the present antenna have been done at ElectroScience Lab, Ohio State University, Columbus, Ohio.

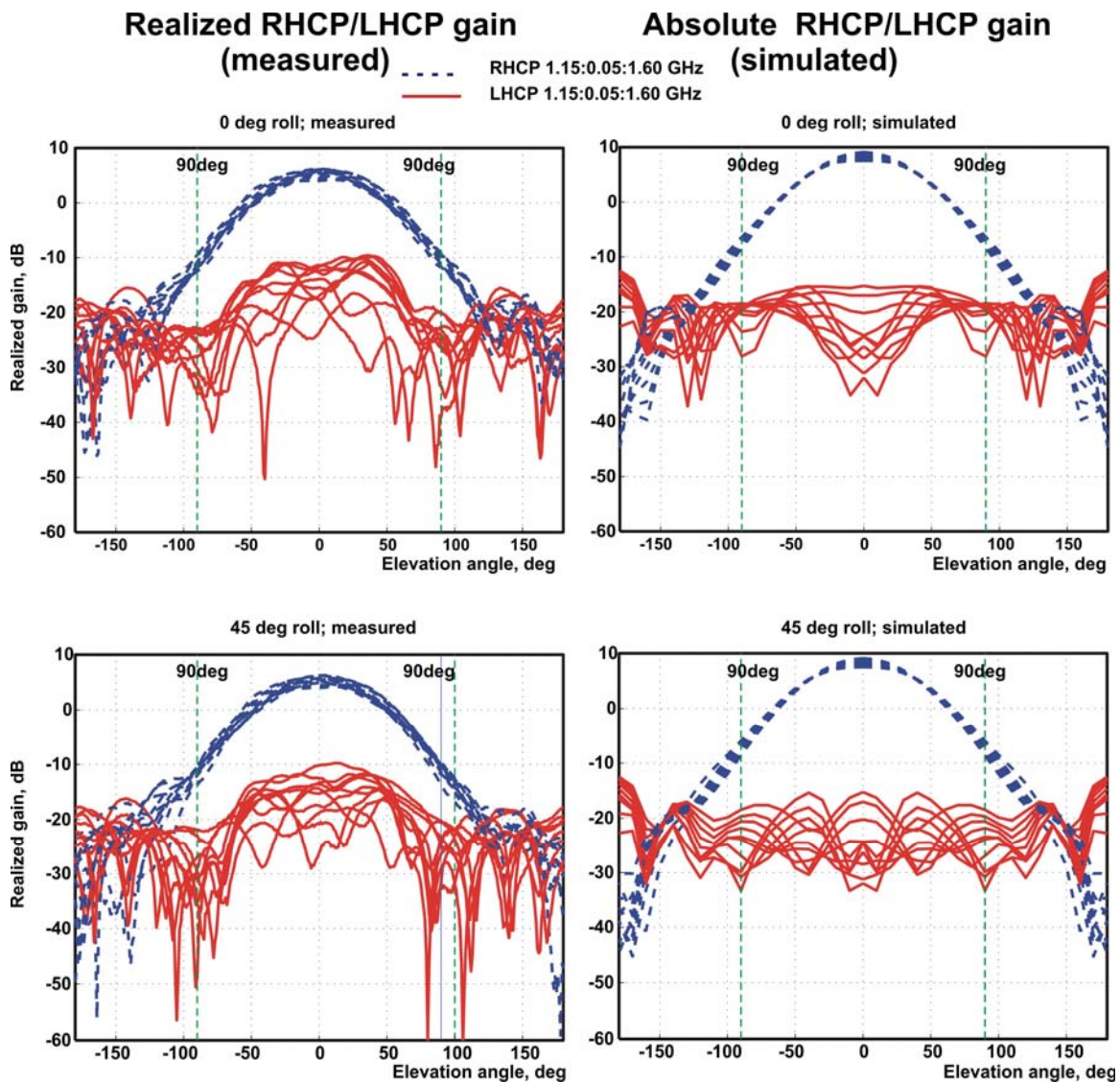


Fig. 17. RHCP and LHCP antenna patterns in the  $E$ -plane of one dipole (top) and in the  $D$ -plane (45 deg cut between two dipoles). Left column – measured; right column – simulated. The shorter dipole elements are used in the measurements. Both the measurement data and the simulations are given for 1.15:0.05:1.60 GHz.

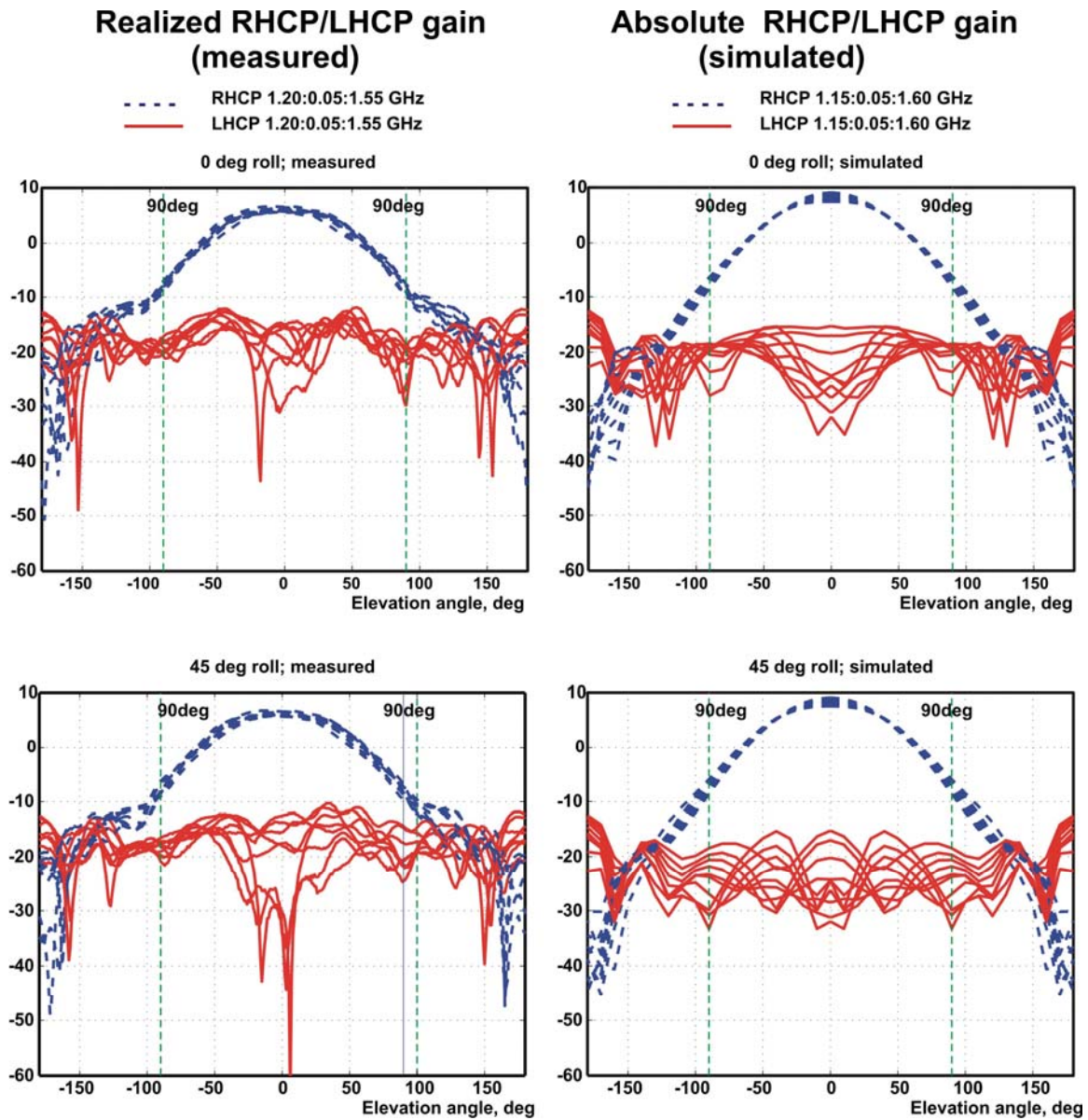


Fig. 18. RHCP and LHCP antenna patterns in the *E*-plane of one dipole (top) and in the *D*-plane (45 deg cut between two dipoles). Left column – measured; right column – simulated. The longer dipole elements are used in the measurements. The measurement data is given for 1.20:0.05:1.55 GHz only.



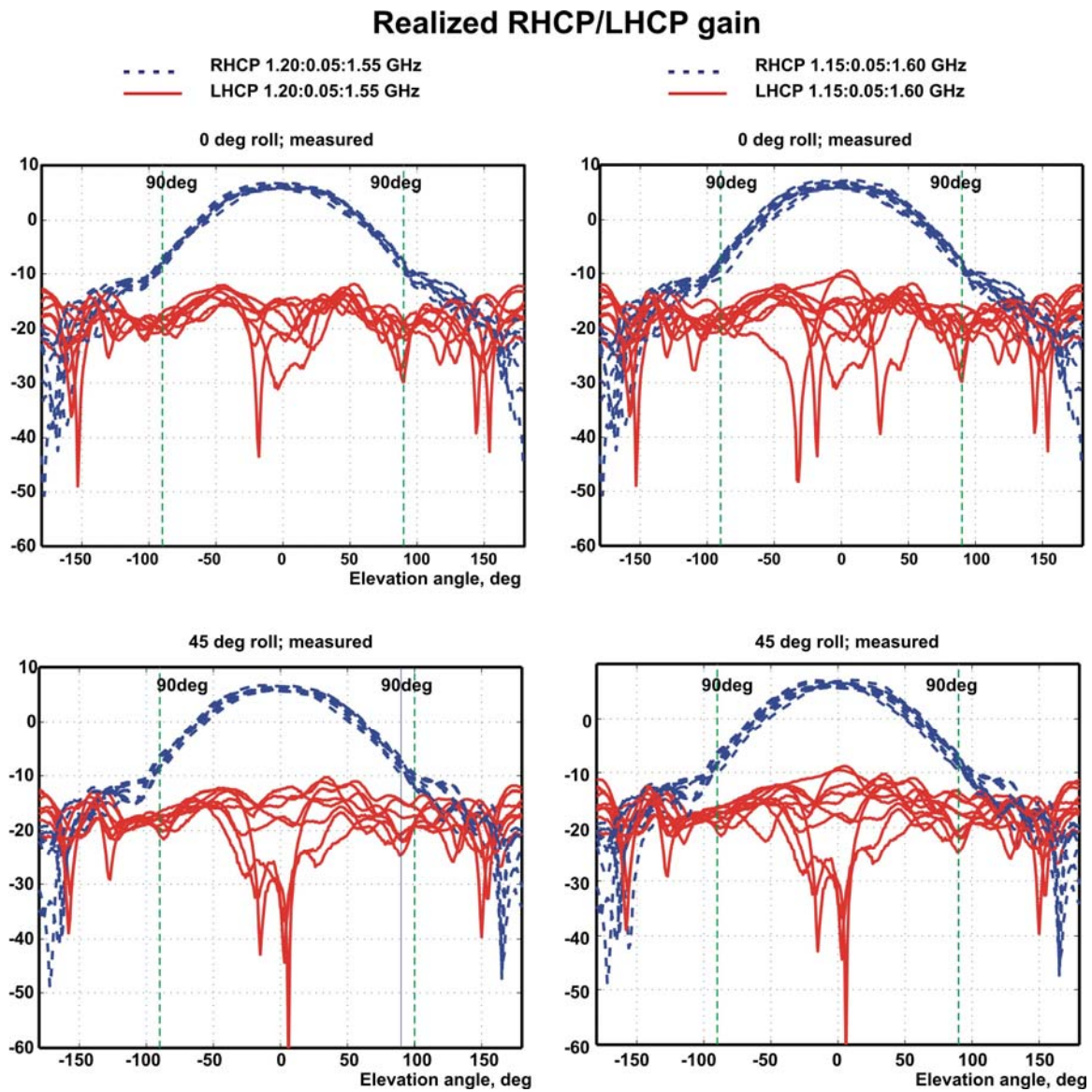


Fig. 19. RHCP and LHCP antenna patterns in the *E*-plane of one dipole (top) and in the *D*-plane (45 deg cut between two dipoles). Left column – measured at 1.20:0.05:1.55 GHz; right column – measured at 1.15:0.05:1.60 GHz. The longer dipole elements are used in the measurements.



Fig 20. Comparison of the dimensions of the present antenna with those of the Trimble Navigation choke ring.

## 5. Acknowledgements

The authors thank Patrick Morrison of WPI for hardware support, Bernard Kaswarra and Wasim Quddus of WPI for modeling support, Dr. Jonathan P. Towle of PSI Inc. for help with measurements, Ray Sprungle, and Dr. Chi-Chih Chen of OSU for help with measurements.

This work has been supported by National Science Foundation, NSF grant DMI-0450524.

## 6. References

- [1] R. F. Harrington, *Time-Harmonic Electromagnetic Fields*, McGraw Hill, New York, 1961, pp. 170-171.
- [2] P. S. Kildal, "Artificially soft and hard surfaces in electromagnetics," *IEEE Trans. Antennas Propagation*, vol. 38, no. 10, pp. 1537-1544, Oct. 1990.
- [3] C. A. Balanis, *Antenna Theory. Analysis and Design*, Wiley, New York, 2005 3<sup>rd</sup> ed., pp. 785-791.
- [4] G. A. Kriegsmann and B. J. McCartin, "Scattering by a rectangularly corrugated surface: an approximate theory," *IEEE Trans. Antennas and Propagation*, vol. 44, no.8, Aug. 1996, pp. 1193 – 1194.
- [5] D. Sievenpiper, Zhang Lijun, R.F.J. Broas, N. G. Alexopolous, and E. Yablonovitch, "High-impedance electromagnetic surfaces with a forbidden frequency band," *IEEE Trans. Microwave Theory and Techniques*, vol. 47, no.11, Nov. 1999, pp. 2059 – 2074.
- [6] R. G. Kouyoumjian and P. H. Pathak, "A uniform geometrical theory of diffraction for an edge in a perfectly conducting surface," *Proc. IEEE*, vol. 62, Nov. 1974, pp. 1448-1461.
- [7] Z. Ying, Per-Simon Kildal, and A. A. Kishk, Study of different realizations and calculation models for soft surfaces by using a vertical monopole on a soft disk as a test bed, *IEEE Trans. Antennas and Propagation*, vol. 44, no.11, Nov. 1996, pp. 1474 – 1481.
- [8] D. M. Pozar, *Microwave Engineering*, Wiley, New York, 2005, third edition.
- [9] R. Lawrie and Leon Peters, "The control of the echo area of ogives by cutoff corrugated surfaces," *IEEE Trans. Antennas and Propagation*, vol.14, no.6, Nov. 1966, pp. 798 – 799.
- [10] P. J. B. Claricoats and A. D. Olver, *Corrugated Horns for Microwave Antennas*, Perter Peregrinus Ltd., London, UK, 1984.
- [11] Carl A. Mentzer and Leon Peters, "Properties of cutoff corrugated surfaces for corrugated horn design," *IEEE Trans. Antennas and Propagation*, vol. 22, no.2, March 1974, pp. 191 – 196.
- [12] M. E. J. Jeuken, "*Frequency independence and symmetry properties of corrugated conical horn antennas with small flare angles*," Ph.D. Dissertation, Eindhoven University, The Netherlands, 1970.
- [13] M. E. J. Jeuken and V. J. Vokurka, "Multi - Frequency Band Corrugated Conical Horn Antenna," 3<sup>rd</sup> *European Microwave Conference*, 1973, vol 2, Oct. 1973, pp.1– 4.
- [14] M. Jeuken and L. Thurlings, "The corrugated elliptical horn antenna," *IEEE Antennas and Propagation Society International Symposium*, 1975, vol. 13, Jun. 1975, pp. 9 – 12.



- [15] Y. Beniguel, A. Berthon, C. V. Klooster, and L. Costes, "Design realization and measurements of a high performance wide-band corrugated horn," *IEEE Trans. Antennas and Propagation*, vol. 53, no.11, Nov. 2005, pp. 3540 – 3546.
- [16] R. Lawrie and L. Peters, Jr., "Modifications of horn antennas for low sidelobe levels," *IEEE Trans. Antennas Propagation*, vol. 14, no. 5, pp. 605-610, Sep. 1966.
- [17] Trimble Navigation Limited online at <http://www.trimble.com/1112chokering.shtml>
- [18] The University NAVSTAR Consortium (UNAVCO); online at [http://facility.unavco.org/project\\_support/permanent/equipment/antennas/antennas.html](http://facility.unavco.org/project_support/permanent/equipment/antennas/antennas.html)
- [19] C. C. Counselman, "Multipath rejecting GPS antenna," *IEEE Proceedings, Special Issue on GPS The Global Positioning System*, vol. 87, no.1, Jan. 1999, pp. 92-110.
- [20] James M. Tranquilla, J. P. Cam, and Hussain M. Al-Rizzo, "Analysis of a Choke Ring Groundplane for Multipath Control in Global Positioning System (GPS) Applications," *IEEE Trans. Antennas Propagation*, vol. 42, no. 7, pp. 905-911, July 1994.
- [21] James M. Tranquilla and B. G. Colpitts, "Development of a class of antennas for space-based NAVSTAR GPS applications," *6th Int. Conference on Antennas and Propagation, ICAP 89*, Conf. Publ., No. 301, vol. 1, pp. 65-69, April 1989.
- [22] J. I. Ortigosa, N. Padros, and M. F. Iskander, "Comparative study of high-performance GPS receiving antenna designs," *IEEE AP-S International Symposium*, July 1996, pp. 1958-1961.
- [23] L. I. Basilio, J. T. Williams, David R. Jackson, and M. A. Khayat, "A comparative study of a new GPS reduced-surface-wave antenna," *IEEE Antennas and Wireless Propagation Lett.*, vol. 4, pp. 233-236.
- [24] T. Milligan and P. K. Kelly, "Optimization of ground plane for improved GPS antenna performance," *IEEE AP-S Int. Sym. 1996*, vol. 2, pp. 1250-1253, July 1996.
- [25] Y. Lee, S. Ganguly, and R. Mittra, "Multi-band L<sub>5</sub>-capable GPS antenna with reduced backlobes," *IEEE AP-S Int. Sym. 2005*, vol. 1A, pp. 438-441, July 2005.
- [26] Waldemar Kunysz, *A Three Dimensional Choke Ring Ground Plane Antenna*, NovAtel Inc. Application Note.
- [27] Waldemar Kunysz, *High Performance GPS Pinwheel Antenna*, NovAtel Inc. Application Note.
- [28] Vladimir Philippov, Igor Sutiagin, and Javad Ashjaee, "Measured Characteristics of Dual Depth Dual Frequency Choke Ring for Multipath Rejection in GPS Receivers," Application Note, Javad Positioning Systems.
- [29] S. H. Huynh and G. Cheng, *Low Profile Ceramic Choke*, US Patent # 6,040,805, March 21<sup>st</sup>, 2000, Antcom Corp.
- [30] B. G. Westfall, *Antenna with R-Card Ground Plane*, US Patent # 5,694,136, Dec. 2, 1997, Trimble Navigation.
- [31] B. G. Westfall and K. B. Stephenson, *Antenna with Ground Plane having Cutouts*, US Patent # 5,986,615, Nov. 16, 1999, Trimble Navigation.
- [32] J. Ashjaee, V. S. Filippov, D. V. Tatarnikov, A. V. Astakhov, and I. V. Sutjagin, *Dual-Frequency Choke-Ring Ground Planes*, US Patent #6,278,407, Aug. 21<sup>st</sup>, 2001, Topcon Positioning Systems, Inc.

- [33] W. Kunysz, *Slot array antenna with reduced edge diffraction*, US Patent # 6,452,560, Dec. 8<sup>th</sup>, 2000, NovAtel, Inc.
- [34] Y. Lee, S. Ganguly, and R. Mittra, *Multi Frequency Antenna with Reduced Rear Radiation and Reception*, US Patent #6,940,457, Sep. 6<sup>th</sup>, 2005.
- [35] E. B. Rodal, M. C. Detro, D. R. Gildea, and J. M. Janky, *Antenna with Curved Dipole Elements*, US Patent # 5,173,715, Dec. 22<sup>nd</sup>, 1992.
- [36] P. K. W. Tom and V. L. Denninger, *Dual Frequency Microwave Radio Antenna System*, US Patent #5,625,365, April 29<sup>th</sup>, 1997, Trimble Navigation.
- [37] D. J. Goodman, *Direction finding antenna and system*, US Patent #4,161,736 July 17<sup>th</sup>, 1979.
- [38] B. R. Schupler, R. L. Allshouse, and T. A. Clark, "Signal characteristics of GPS user antennas," *Navigation: J. Inst. Navigation (ION)*, vol. 41, no. 3, pp. 277–295, Fall 1994.
- [39] A.-M. Dinius, "GPS antenna multipath rejection performance," Massachusetts Inst. Technol. Lincoln Laboratory, Cambridge, MA, Report ATC-238, vol. 70, p. 7, Aug. 1995.
- [40] P. El'osegui, J. L. Davis, R. T. K. Jaldehag, J. M. Johansson, A. E. Niell, and I. I. Shapiro, "Geodesy using the global positioning system: The effects of signal scattering on estimates of site position," *J. Geophys. Res.*, vol. 100, no. B7, pp. 9921–9934, June 10, 1995.
- [41] B. R. Schupler and T. A. Clark, "High Accuracy Characterization of Geodetic GPS Antennas Using Anechoic Chamber and Field Tests," *13th International Technical Meeting of the Satellite Division of the Institute of Navigation (ION)*, Sept. 20, 2000, Salt Lake City, 7 p.
- [42] S. G. Moore, V. A. Marotti, and K. Plate, *Combination GPS and VHF Antenna*, US Patent #5,650,792, July 22<sup>nd</sup> 1997. Dorne and Margolin, Inc.
- [43] T. A. Milligan, *Modern Antenna Design*, Wiley-IEEE Press, New York, 2005, 2<sup>nd</sup> edition.
- [44] S. Maci, M. Leoncini, A. Neto, R. Tiberio, and A. Toccafondi, "Diffraction at artificially soft and hard edges by using incremental theory of diffraction", *IEEE AP-S International Symposium*, June 1994, vol. 3, pp. 1464-1467.
- [45] D. E. Ping, J. T. Shaffer, L. U. Brown, and R. B. Dybdal, "A broadband rolled edged cavity antenna," *IEEE AP-S International Symposium*, June 2004, vol. 1, pp. 787-790.
- [46] M. S. Gatti and D. J. Nybakken, "A circularly polarized crossed drooping dipole antenna," *IEEE AP-S International Symposium*, May 1990, vol. 1, pp. 254-257.
- [47] A. Kerkhoff, and S. Ellingson, "A wideband planar dipole antenna for use in the long wavelength demonstrator array (LWDA)," *IEEE AP-S International Symposium*, July 2005, vol. 1B, pp. 553-556.
- [48] S. Ellingson and A. Kerkhoff, "Comparison of two candidate elements for a 30-90 MHz radio telescope array," *IEEE AP-S International Symposium*, July 2005, vol. 1A, pp. 590-593.

## LEAKY WAVE ANTENNA RESEARCH AT AFRL

Dan Janning<sup>1</sup>, John McCann<sup>1</sup>, Michael Corwin<sup>1</sup>, Thomas Dalrymple<sup>1</sup>, Leo Kempel<sup>1,2</sup>,  
Daniel Killips<sup>2</sup>, Krishna Pasala<sup>1,3</sup>, Robert Penno<sup>1,3</sup>, Joshua Radcliffe<sup>1</sup>,  
Stephen Schneider<sup>1</sup>, and Kyle Zeller<sup>1</sup>

<sup>1</sup>Air Force Research Laboratory  
2241 Avionics Circle, Bldg 620  
Wright Patterson AFB, Ohio 45433

<sup>2</sup>Michigan State University  
2120 Engineering Building  
East Lansing, MI 48824-1226

<sup>3</sup>University of Dayton  
300 College Park  
Dayton, OH 45469-0226

**Abstract:** Printed leaky wave antennas offer the potential for a low-profile, wide bandwidth antenna element. Microstrip leaky wave antennas rely on the suppression of the familiar  $\text{EH}_0$  mode and the propagation of the radiating  $\text{EH}_1$  mode. Previous work at AFRL has resulted in the development of a half-width design for a leaky wave antenna, using a shorting strip along the length of the antenna to suppress the dominant mode. Furthermore, termination of the end of the antenna with a resistive load reduces the reflected wave on the microstrip, largely eliminating the corresponding backlobe in the radiation pattern. Antennas for this research are designed with the aid of commercially available CEM tools and validated through in-house fabrication and testing. Different fabrication techniques have been employed, using alternate feeding mechanisms and various implementations of the shorting strip. An effort is underway at AFRL to develop an array of leaky-wave antennas in order to enhance efficiency and bandwidth. The impact of coupling has been explored through the use of parasitic elements.

### 1. Introduction

Microstrip leaky wave antennas offer the potential for a low-profile antenna with greater bandwidth than microstrip patch antennas. The improved bandwidth is principally due to the fact that a greater area on the circuit board is utilized in order to create a traveling wave. Traditional microstrip leaky wave antennas are wide microstrip structures fed in such a way that enhances the first higher order leaky wave mode ( $\text{EH}_1$ ) while suppressing the transmission line mode ( $\text{EH}_0$ ). This mode suppression is rather challenging in traditional leaky wave antennas because feed structures must be designed to preferentially excite the leaky wave mode. Menzel [1] utilized periodic slots to suppress

the dominant mode while Lin [2] investigated various feed structures for preferentially exciting the chosen mode. Oliner [3] made significant contributions to the theory of leaky wave structures as antennas. The primary motivation for this research is the desire to create designs that retain the low-cost, low-profile properties of a patch antenna, but have significantly wider bandwidth. Previous investigations have also centered on increasing the bandwidth by tapering the microstrip structure [4-5].

This paper presents a survey of the last four years of leaky wave antenna research conducted at AFRL. Much of the material has been previously released in various journals, conferences and symposia, including IEEE/APS, AMTA, and ACES.

## 2. Full-Width Leaky Wave Antenna

The type of leaky wave antenna under consideration is characterized by the constant cross section shown in Figure 1. As seen in Figure 1a, energy in the dominant  $EH_0$  mode is tightly bound to the structure and does not radiate. On the other hand, the  $EH_1$  (or first higher order) mode exhibits an electric field distribution that is odd about the y-axis, and will shed energy as the wave propagates down the z-axis. Furthermore, the existence of a null in the electric field under the strip in the y-z plane suggests that a metallic short placed in the location of the dotted line in Figure 1b will prevent propagation of the fundamental mode while having no effect on any leaky-wave mode that is present.

This centerline short along the length of the antenna, together with an offset feed that excites the anti-symmetric  $EH_1$  mode, forms the basis of the “full-width” leaky wave antenna. A purely anti-symmetric field distribution could also be obtained with a differential feed, but in many cases this approach would require an external balun.

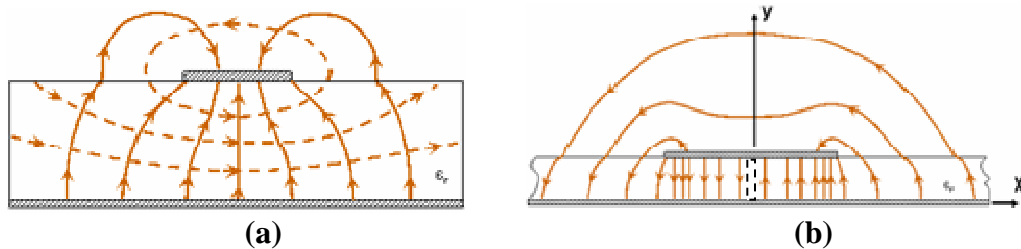


**Figure 1: Field diagram for the (a)  $EH_0$  mode and (b)  $EH_1$  mode (E-field = solid, H-field = dashed)**

Other means of preferentially exciting the  $EH_1$  mode have been investigated (see for example [5] and the references contained within that manuscript). Most notably, Menzel [1] placed small transverse slots in the microstrip structure near the feed region and an offset feed (including a quarter wave transformer to improve the match to a 50  $\Omega$  port).

These slots interrupt the strong  $z$ -directed  $EH_0$  electric current at the center of the microstrip, causing this mode to be suppressed. Figures 2a and 3a illustrate Menzel's design. The short circuit proposed here is implemented with closely spaced metal posts along the centerline of the microstrip between the top conductor and ground plane, as illustrated in Figure 2b. Figure 3 shows Menzel's antenna design and the alternative design as fabricated in AFRL/SNDR's Radiation and Scattering Compact Antenna Laboratory (RASCAL). Figure 4 shows pattern measurements taken in the RASCAL compact range. These results indicate that the alternate configuration produces a similar radiation pattern as the Menzel design.

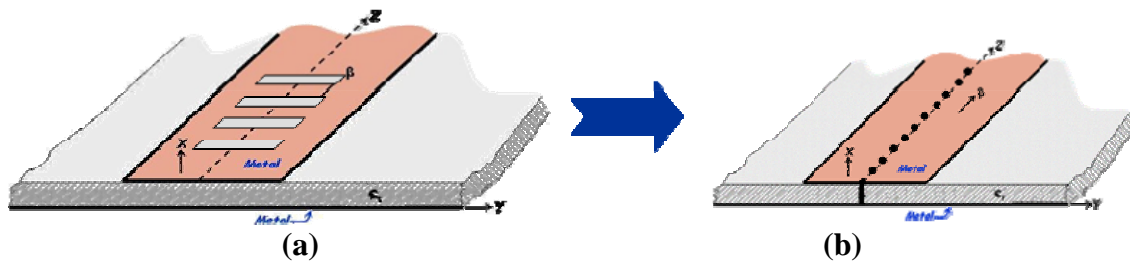


**Figure 2: Two alternate methods of suppressing the dominant  $EH_0$  mode in a microstrip: (a) Menzel's use of transverse slots and (b) shorting pins along the centerline**

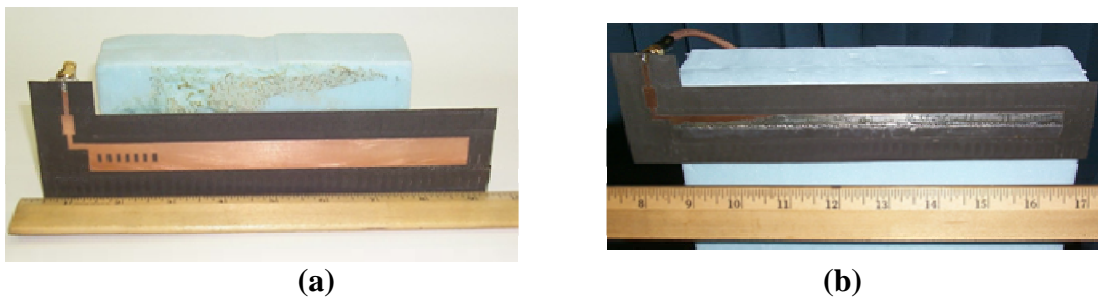


**Figure 3: Menzel's (a) antenna design and (b) the alternate design as fabricated at AFRL**

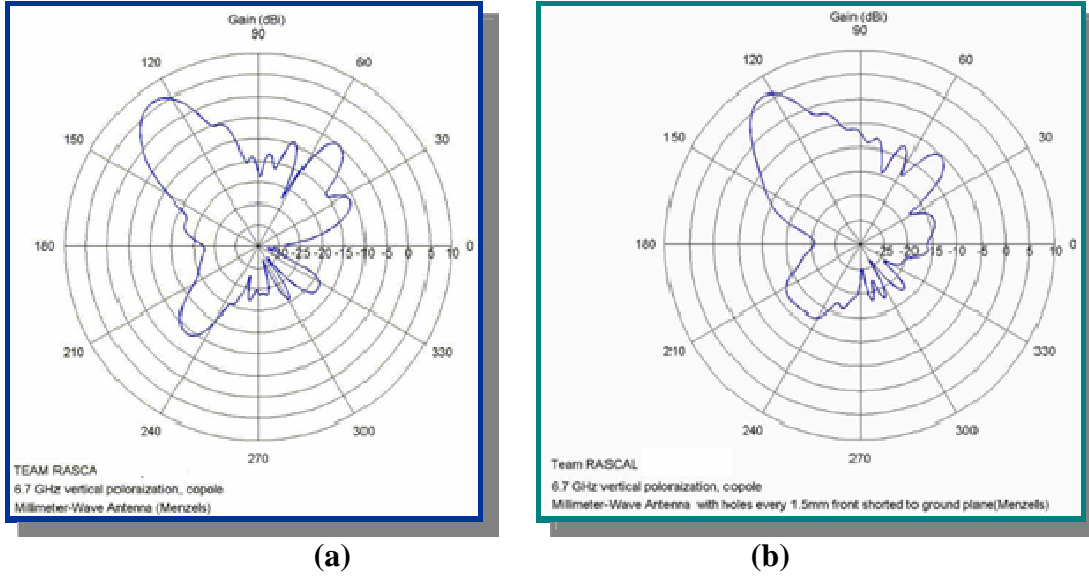


**Figure 4: Radiation pattern measurements taken at AFRL of the (a) Menzel antenna and (b) the alternate configuration**

A common method for estimating the radiation bandwidth of an  $EH_1$ -mode antenna is based on a waveguide model [6-7]. The bandwidth of such an antenna is determined by the cut-off frequency for the  $EH_1$  mode and the frequency where the phase constant equals  $k_0$  (e.g. above this frequency, the bound mode propagates and the fields evanesce away from the structure). This frequency range is given by

$$f_c = \frac{15}{w_{\text{eff}} \sqrt{\epsilon_r}} < f < \frac{f_c \sqrt{\epsilon_r}}{\sqrt{\epsilon_r} - 1} = \frac{15}{w_{\text{eff}} \sqrt{\epsilon_r} - 1} \quad (1)$$

where the zero-thickness effective width of the microstrip (in centimeters) is given by Wheeler [8-9]

$$w_{\text{eff}} = h \left\{ \frac{w}{h} + \frac{2}{\pi} \ln \left[ 2\pi e \left( \frac{w}{2h} + 0.92 \right) \right] \right\} \quad (2)$$

Operation of the microstrip in the range of frequencies specified by (1) will allow the propagation of the  $EH_1$  leaky wave mode. The  $EH_0$  will also propagate in this range, and may dominate in the absence of suppressive measures, such as those outlined above.

### 3. Half-Width Leaky Wave Antenna

Returning to Figure 1b, one notes that the tangential electric fields are zero everywhere in the plane that bisects the strip. This suggests that one-half of the structure can be removed with little effect on the fields, at least in the region away from the feed, where a pure  $EH_1$  mode can be said to exist. The result is the “half-width” leaky wave antenna [10], the concept of which is illustrated in Figure 5b. A fabricated half-width leaky wave antenna is shown in Figure 6. This antenna is terminated with a  $50\ \Omega$  load in order to reduce reflection. Reflection in this case would result in a wave traveling towards the feed and consequently create a significant backlobe in the radiation pattern, in a direction mirror opposite to the main lobe. A major advantage of the half-width design is the reduced footprint. An array of such elements can be packed closer together without increasing the mutual coupling between elements.

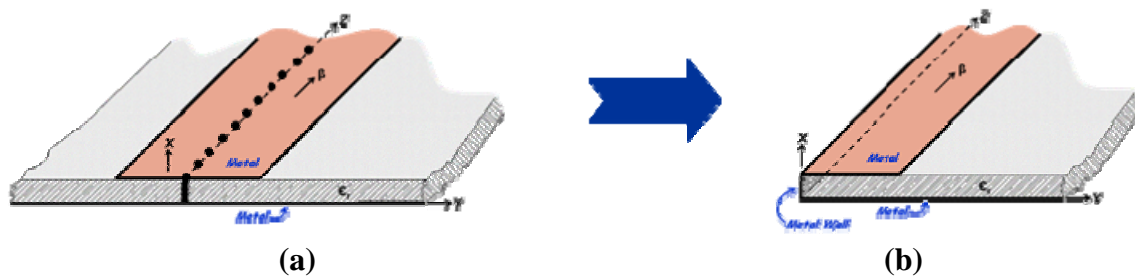


**Figure 5: Full-width leaky wave design (a) using shorting pins along the centerline and (b) half-width design developed at AFRL**



**Figure 6: Half-width leaky wave antenna designed and fabricated at AFRL**

## 4. Leaky Wave Antennas in Array Environments

To date, much work has been accomplished at AFRL regarding the effects of arraying leaky wave antennas. This includes using the hybrid finite element-boundary integral (FE-BI) method to analyze coupling between elements and calculate radiation and impedance properties of linear arrays [11-12]. More recently, antennas with parasitic elements have been fabricated and tested [13]. This section outlines this research.

### 4.1 Finite Element-Boundary Integral Model

The hybrid finite element-boundary integral (FE-BI) method is widely understood to be an accurate and efficient method for modeling planar, microstrip apertures. The assumed geometry is a cavity-backed aperture recessed within an infinite metallic plane. The FE-BI formulation is an integro-differential equation representing a weak enforcement of the relevant boundary conditions applied to the vector wave equation. This FE-BI expression is given as

$$\begin{aligned} \int_V [(\nabla \times \mathbf{W}_i) \cdot \bar{\bar{\mu}}_r^{-1} \cdot (\nabla \times \mathbf{E}^{\text{int}}) - k_0^2 \mathbf{W}_i \cdot \bar{\bar{\epsilon}}_r \cdot \mathbf{E}^{\text{int}}] dV + \\ k_0^2 \iint_S \mathbf{W}_i \cdot [\hat{\mathbf{z}} \times \bar{\bar{G}}_{e2} \times \hat{\mathbf{z}}] \cdot \mathbf{E}^{\text{int}} dS' dS = \\ - jk_0 Z_0 \int_V \mathbf{W}_i \cdot \mathbf{J}^{\text{imp}} dV \end{aligned} \quad (3)$$

where  $\mathbf{W}_i$  is a vector testing function,  $\bar{\bar{G}}_{e2}$  is the half-space dyadic Green's function, and  $\mathbf{J}^{\text{imp}}$  is an impressed current used to represent the antenna feed. The material in the computational volume (that is, the antenna cavity), is represented by the relative permittivity tensor ( $\bar{\bar{\epsilon}}_r$ ) and the inverse of the relative permeability tensor ( $\bar{\bar{\mu}}_r^{-1}$ ). The FE-BI formulation is reduced to a linear system via Galerkin's procedure resulting in the following linear system

$$[\mathbf{Y}_{ij}^{\text{FE}}] \{E_j\} + k_0^2 \begin{bmatrix} \mathbf{Y}^{\text{BI}} & 0 \\ 0 & 0 \end{bmatrix} \begin{Bmatrix} E_j^s \\ E_j^v \end{Bmatrix} = \{f_i^{\text{int}}\} \quad (4)$$

In this, the unknown coefficients associated with the expansion functions ( $\mathbf{w}_j$ ) are represented by ( $E_j$ ). For the unknown coefficients, ( $E_j^s$ ) represents unknowns associated with the surface while ( $E_j^v$ ) represent unknowns not associated with the surface. This system can efficiently be solved, both in terms of memory consumption and wallclock



time, using an iterative solver such as the biconjugate gradient method [14].

By utilizing a fast Fourier transform (FFT) method to accelerate the computation of matrix-vector products in an iterative solution of the FE-BI linear system, simulation of a large antenna is feasible within practical design time limits. Hence, brick elements were used to discretize the computational volume [15]. The shorted side of the HWLW antenna is modeled using an infinitesimally thin perfectly conducting wall running along the length of the strip. The lumped loads were modeled as infinitesimally thin loads placed midway between the shorted edge and the open edge of the half-width antenna. The feeds are modeled likewise as infinitesimally thin probe feeds placed midway between the shorted edge and the open edge of the antenna.

In addition, the computer program was parallelized using OpenMP [16] and run on a dual-core AMD 64-bit system with a total of four cores per node. The program has also been used on an SGI Altix 3700 Bx2 using 64-bit Itanium processors [17]. The primary routine that was parallelized was the iterative matrix solvers (the biconjugate gradient and transpose-free QMR algorithms are implemented) and fast Fourier transforms. For this work, the BiCG algorithm [15] was used.

#### 4.2 Computed Data for a Five-Element Linear Array

To validate the computational model discussed above, an experiment was conducted in a compact anechoic chamber using a single HWLW antenna. The shorting wall in the half-width antenna was approximated using shorting pins running the length of the antenna strip, spaced 5 mm apart. The ports were attached to an HP-8510 vector network analyzer. A representative radiation pattern, comparing computed and measured data, is shown in Figure 7. The agreement is reasonably good considering that the shorting wall in the prototype was not solid, and that the FE-BI model used a probe feed and an infinite ground plane.

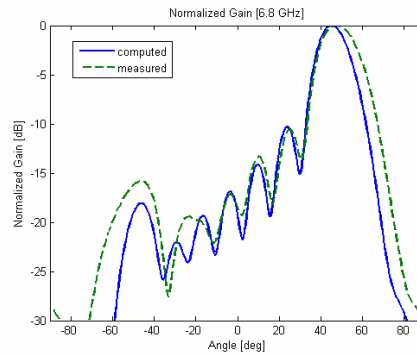


**Figure 7: Comparison of computed and measured radiation patterns from a half-width, leaky-wave antenna at 6.8 GHz**

Next, the FE-BI model was used to determine the impact of leaky wave coupling on adjacent microstrip elements. Figure 8 illustrates a representation of coupling between a driven element (the lower one in the figure) and an unfed element that is terminated on both ends with  $50\ \Omega$  loads, spaced 1.95 cm (center-to-center) from the lower element. The simulation was conducted with a single cavity containing both the driven element and the passive element. In this manner, coupling between elements can occur via substrate, across the surface of the aperture, and via space-wave mechanisms. For an aperture where each element is contained within individual cavities, coupling via the substrate is suppressed. Because this is assumed to be the dominant mechanism and the  $EH_1$  mode is a leaky wave mode, this geometric arrangement is appropriate.

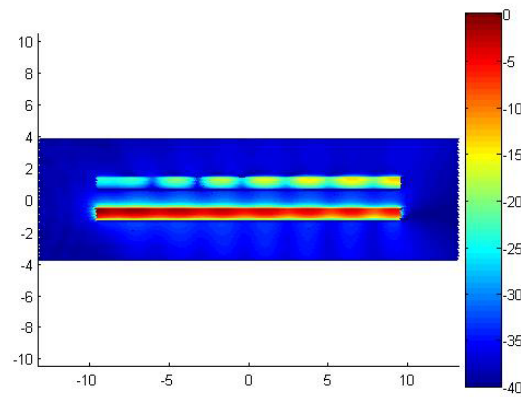


**Figure 8: Normal fields in cavity for driven lower element and passive upper element**

It is clear that the leaky wave from the driven lower element is coupled into the upper element. Notice that the fields in the upper element are strongest in the end of the element opposite the driving point in the lower element, a phenomenon expected from leaky wave coupling because the driven leaky wave will have a directional component from left to right in the figure. To assess the impact of this coupled field to the radiating current (and hence the fidelity of the radiation pattern to predictions based on a single traveling wave), the coupling ratio was determined for various separations. The coupling ratio is defined as the ratio of the maximum field strength in the region of the passive antenna to the maximum field strength in the region of the driven element. It is a measure of how strong one leaky wave couples, and hence corrupts, the leaky wave propagating in another microstrip. As a function of the center-to-center separation distance, the coupling between these elements at 7 GHz is given in Figure 9. As can be seen, the coupling remains fairly strong even out to a distance of 6.45 cm. For 7 GHz, the free space wavelength is 4.29 cm, where a separation of 6.45 cm would result in grating lobes. This result demonstrates that to accurately assess the radiation properties of a leaky wave array, consideration of mutual coupling is essential.

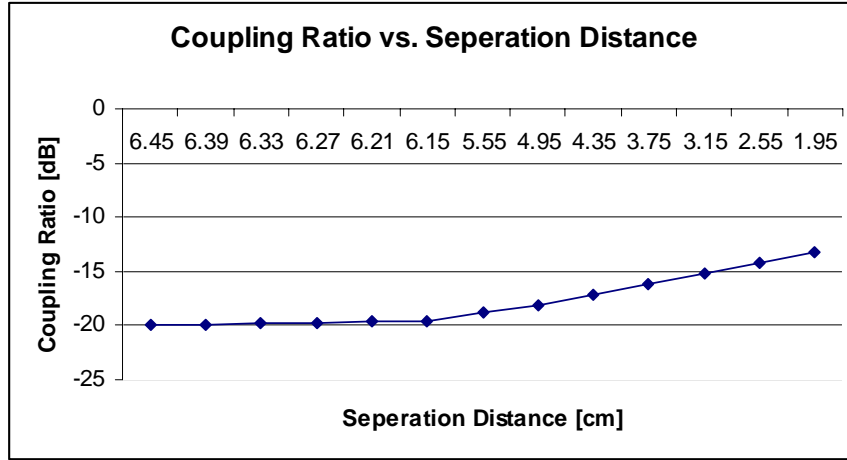


**Figure 9: Coupling ratio between elements versus separation distance.**

A five-element array was simulated using the FE-BI model. The array elements have a separation of 1.2 cm between elements, which is less than one-third of the free-space wavelength. The theoretically predicted radiation patterns for a uniformly illuminated array are shown in Figure 10. The corresponding patterns as computed by the FE-BI model are shown in Figure 11.

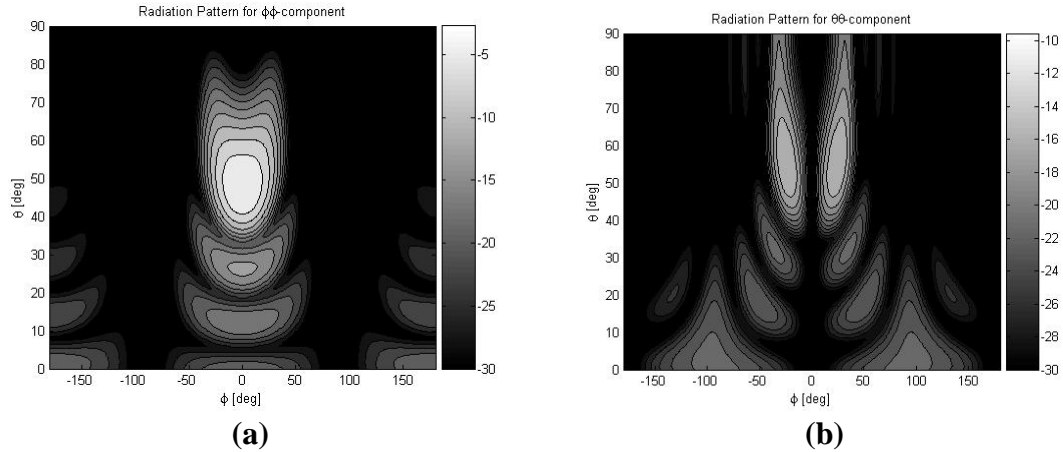


**Figure 10: Theoretical (a)  $\phi$ - $\phi$  and (b)  $\theta$ - $\theta$  radiation pattern for a uniformly illuminated array**

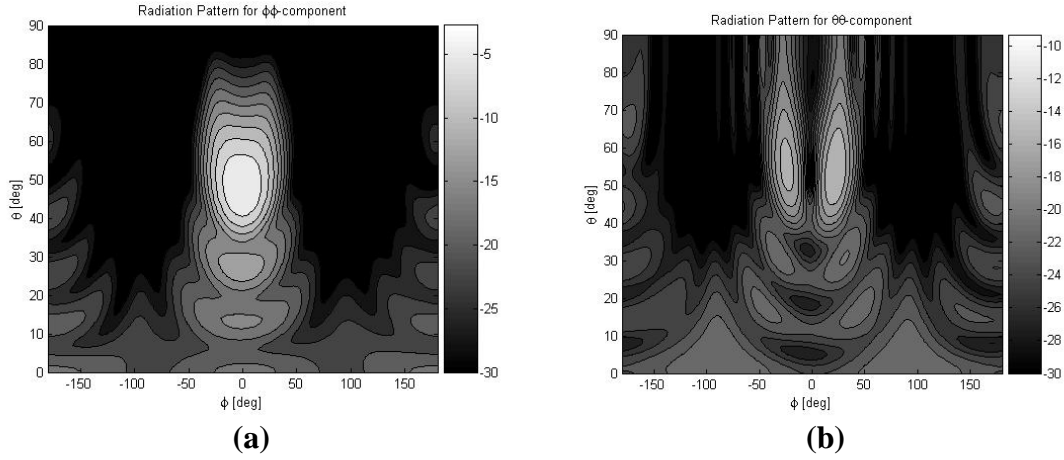


**Figure 11: Numerical (a)  $\phi\phi$  and (b)  $\theta\theta$  radiation pattern for a uniformly illuminated array**

For all of the contour plots, each contour line represents 3 dB of change. As seen by comparing Figure 10a to Figure 11a and Figure 10b to Figure 11b, the agreement is quite good with the exception of the somewhat diffused sidelobes for the numerically computed results. This is presumably due to the leaky wave coupling that is neglected in the theoretical results.

#### 4.3 Fabricated Parasitic Antennas

The fabricated leaky wave antennas measured were printed on Duroid 5870 (31 mils thick,  $\epsilon_r = 2.33$ ,  $\tan \delta = 0.0005$ ). The half-width strip width is 7.5 mm. The strip is 190 mm long and terminated with a lumped 50  $\Omega$  load placed midway between the shorted edge and the free edge of the antenna. The placement of the load was determined using transverse resonance methods and confirmed using numerical techniques [18]. The parasitic elements are terminated at both ends with a 50  $\Omega$  lumped load placed midway between the shorted edge and the free edge of each element.

Three antennas were fabricated to determine the effects of mutual coupling: a single active element half-width antenna (shown previously in Figure 6), a single active element antenna with one parasitic element (Figure 12a) and a single active element antenna with two parasitic elements, one on each side (Figure 12b). The yellow arrows in Figure 12 indicate the active element. The measured results from the two antennas with passive parasitic elements are then compared to the single active element half-width leaky wave, as well as the computed results using CST Microwave Studio, a commercial code that employs the Finite-Integration Technique.

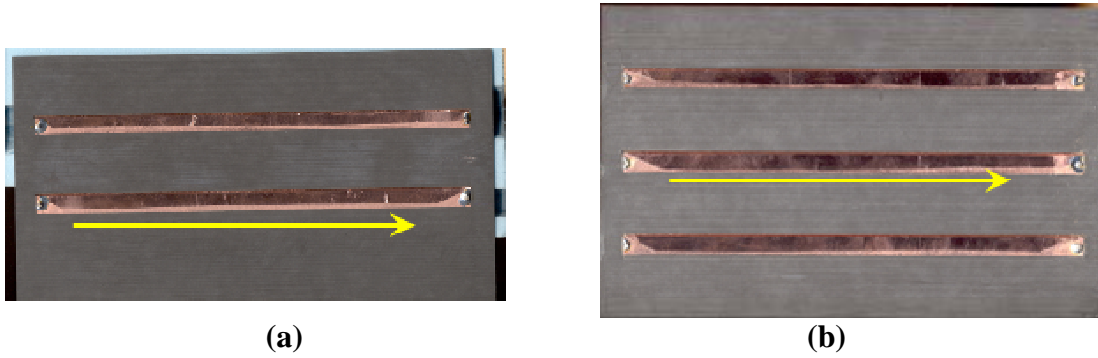


**Figure 12: Fabricated (a) single-parasitic element and (b) dual-parasitic element**

#### 4.4 Experimental Results

Antenna patterns and S-parameter measurements were taken on the three antennas described above. When measured, the parasitic elements were each loaded (on each end) with  $50\ \Omega$ , mimicking the performance improvement in pattern and VSWR determined in [18-19]. From the results shown in Figure 13a, it is observed that the impedance bandwidth increases by approximately 1.5 GHz for the single-parasitic antenna and approximately 2.0 GHz for the dual-parasitic antenna. Pattern results, shown in Figure 13b, display that as parasitic elements are added, the resulting pattern becomes more directive, as would be expected, and subsequently scanned. The latter result indicates a modification of the complex propagation constant associated with the leaky wave propagating now in the presence of nearby parasitic elements. It may also be noted that the dual parasitic antenna has increased gain (about 5 dB) compared with the single element and single parasitic antenna at 7.25 GHz.

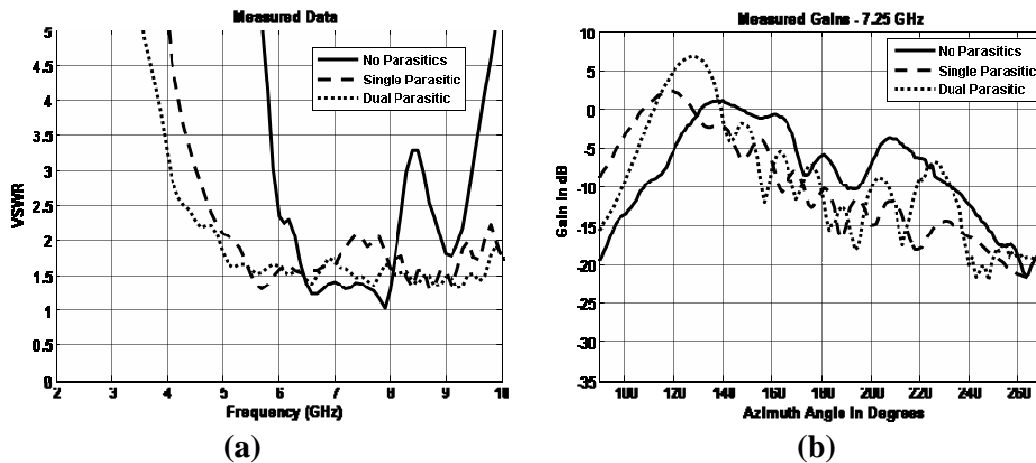


**Figure 13: (a) VSWR data and (b) pattern measurements from the three antennas**

CST Microwave Studio was used initially to determine the theoretical antenna patterns of the parasitic element antennas. Figure 14 shows the results of the comparison between results from CST Microwave Studio and the actual data measured in the RASCAL compact range at AFRL. It is observed from the plots that the measured data for the dual-parasitic case agrees well with the results from CST Microwave Studio, with the exception of a slightly reduced backlobe. The results for the single parasitic case are similar, but with a more greatly reduced backlobe and a main beam that is shifted approximately  $10^\circ$  from the computational model. This shift in the main beam for the single-parasitic case indicates a change in the complex propagation constant that apparently does not occur when the one parasitic is balanced by another on the opposite side.

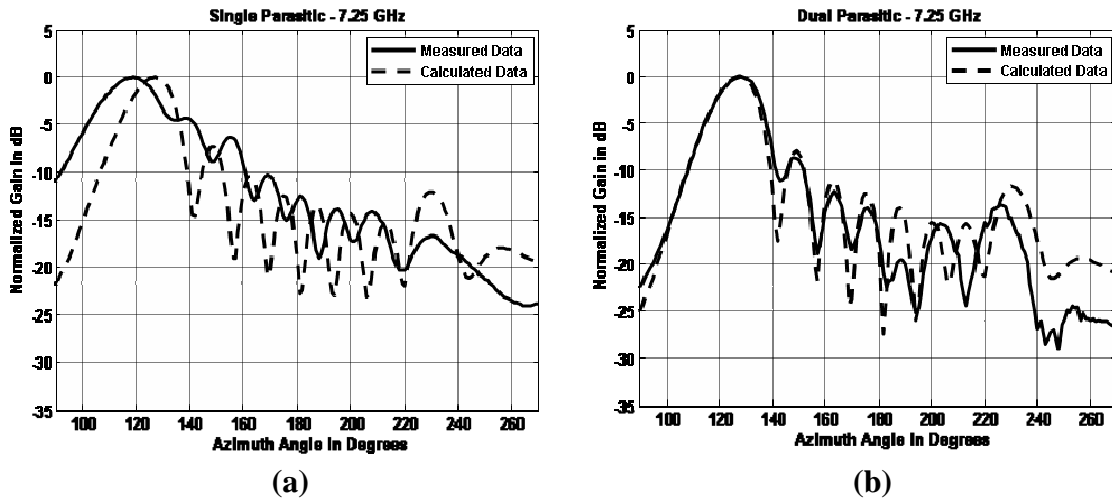


**Figure 14: CST MS results compared with measured data for the (a) single-parasitic and (b) dual-parasitic antennas**

## 5. Leaky Wave Antennas on Curved Surfaces

Research into the performance of leaky wave antennas on a curved surface has also been accomplished at AFRL. In [20], a full-width, dual port, tapered, leaky wave antenna design on a curved surface is modeled using a conformal FE-BI computer program. The FE-BI program makes use of an asymptotic evaluation of the appropriate dyadic Green's function in its formulation [21]. It was found in [20] that a constant width leaky-wave antenna on a curved surface will have a very broad pattern due to wave shedding with curvature. This is shown in Figure 15 for the antenna design used in [22], but with the antenna conformed to right circular cylinders of various radii. The normalization factor is the directivity for the largest cylinder.

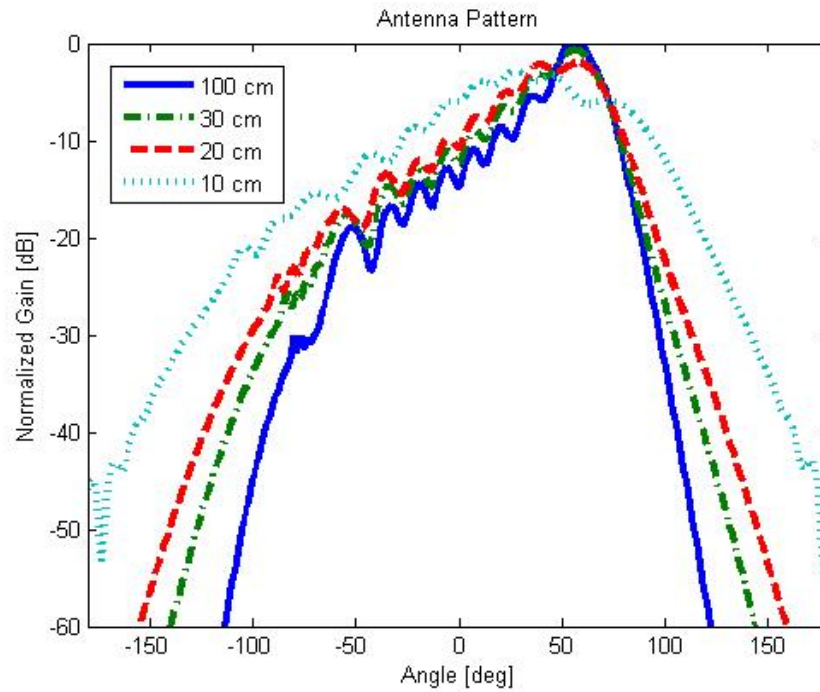


**Figure 15: Comparison of normalized radiation pattern for a leaky wave antenna on cylinders of various radii**

It is observed that the more the antenna is curved (smaller cylinder radius), the directivity of the antenna pattern decreases. In order to increase directivity, a tapered antenna design is employed. Tapered leaky-wave antennas are not novel. In [4-5], they are used to enhance the bandwidth of a planar design. The antenna design used here is the same as that in [23-24]. It is a full-width leaky wave antenna, with a strip width of 8.32 mm tapering to 5.98 mm. The strip is 190 mm long for the simulations and measurements. The antenna is fed with two microstrip lines, excited with opposite phase. Because the feed locations at the edge of the full-width antenna are high impedance points, there is a need for a quarter-wave transformer. This antenna was designed for operation at a frequency of 14 GHz. This tapered width design and the subsequent varying propagation constant allow for a desired change in the leakage constant. As the width decreases towards the end of the antenna, the leakage constant increases and leaves a very small amount of energy left to reflect as a backward traveling wave. The curved surface was modeled as a cylinder with a radius of 20 cm. The radiation pattern for this antenna, evaluated at 14 GHz, is shown in Figure 16. As seen, this antenna has fairly good directivity, even though it is mounted on a curved surface.

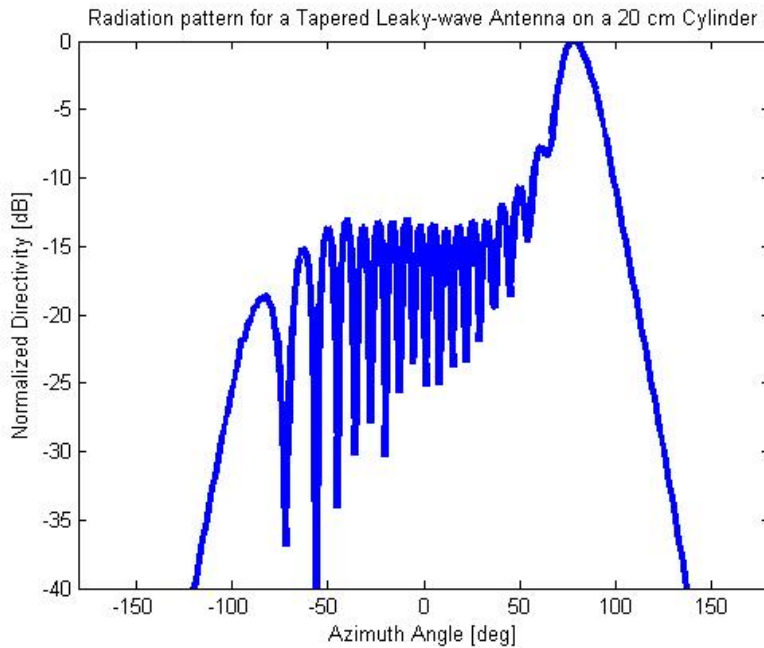


**Figure 16: Normalized radiation pattern for a tapered leaky-wave antenna mounted on a metallic cylinder with a radius of 20 cm.**

## 6. Methods of Fabrication

One of the advantages of leaky wave antennas is the ease with which they can be manufactured using mainstream techniques. Such antennas could readily be integrated into more complex structures, such as phased array antennas, by merely adding an extra layer or two to the RF and digital control distribution layers of a printed circuit board (PCB) based design. Leaky wave antennas for this study were built using AFRL's in house fabrication facilities.

Three methods have been used to implement the shorting wall along the length of the half-width leaky wave antenna. The first is shown in Figure 6, where metal pins have been manually inserted along the structure and soldered in place to complete the connection. This technique is electrically effective but rather labor-intensive. A second method is to mill out a strip completely through the substrate along the antenna and fold copper tape over the structure to short out that side, as pictured in Figure 17. This is a simpler process than the metal posts and more aesthetically pleasing, but the electrical performance of the copper tape is unreliable and degrades over time. The most recent method, and the method currently being used at AFRL, is to use copper-plated vias along the length of the antenna. This method is described further below.



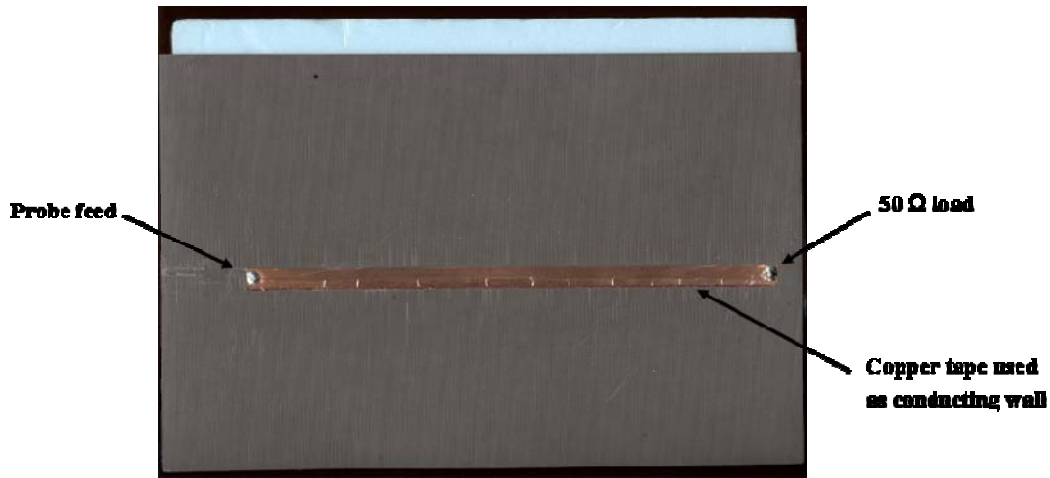


**Figure 17: Half-width leaky wave antenna fabricated using copper tape as a conducting wall**

Simulations are performed in CST Microwave Studio. The layouts are exported into the AutoCAD DXF format, and set up for fabrication in CircuitCAM. The CircuitCAM software forms the milling bit traces and paths for the LPKF PCB milling system to follow.

The PCB used in all prototypes is Rogers Duroid RT/5870. RT/5870 is procured in a 31 mil thickness with ½ oz. copper on both sides. The substrate is laid out on a LPKF 95s/II milling system platen, and holes are drilled for top to bottom electrical connections. The holes are coated with a carbon loaded, electrically conductive ink, and the PCB is subsequently electroplated with copper. The copper is deposited using a state of the art pulse-pulse reverse electroplating system. This system is able to plate various size features and uniformly plate copper onto the through holes as well as the top and bottom surfaces of the board. Following plating, the vias are inspected to ensure proper copper coverage (see Figure 18). At this point, the PCB is returned to the milling machine, where endmill style bits remove copper from the surface, leaving the antenna circuit features behind (Figure 19).

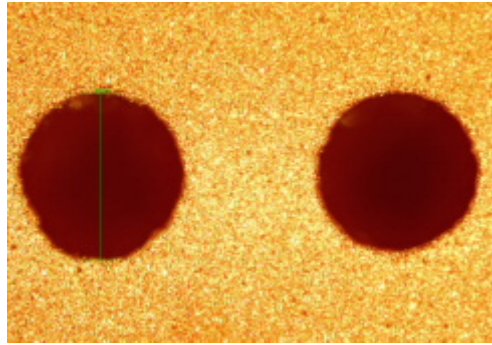


**Figure 18: Copper plated through holes**

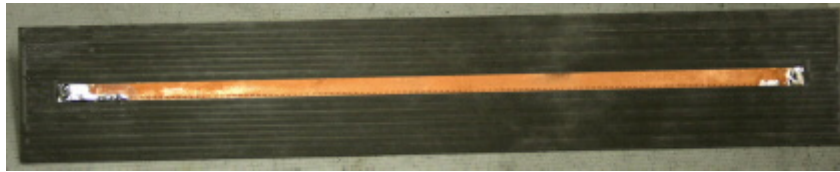


**Figure 19: Completed half-width leaky wave antenna using copper plated through holes along the length of the antenna**

## 7. Acknowledgements

The authors wish to acknowledge Gary Thiele, Jim Mudd, Ken Coss, Dave Kuhl and the AFRL RASCAL facility for assistance in design, fabrication, and data collection.

## 8. References

- [1] W. Menzel, "A New Traveling-Wave Antenna in Microstrip", *Archiv fur Elektronik und Ubertragungstechnik (AEU)*, Band 33, Heft 4:137-140, April 1979.
- [2] Y-D Lin, J-W Sheen, and C-K. C. Tzuang, "Analysis and design of feeding structures for microstrip leaky wave antennas," *IEEE Trans. Microwave Theory Tech.*, 44, pp. 1540-1547, Sept. 1996.
- [3] A. Oliner, "Leakage from Higher Modes on Microstrip Line with Applications to Antennas", *Radio Science*, 22, pp. 907-912, Nov. 1987.
- [4] J-W Sheen, W. Hong, and Y-D Lin, "Wide band tapered microstrip leaky-wave antenna," *Proc. 30<sup>th</sup> European Microwave Conf.*, 2, pp. 234-237, 2000.
- [5] W. Hong, T-L Chen, C-Y Chang, J-W Sheen, and Y-D Lin, "Broadband tapered microstrip leaky-wave antenna," *IEEE Trans. Antennas Propagat.*, 51, pp. 1922-1928, Aug. 2003.

- [6] C.S. Lee, V. Nalbandian, and F. Schwering, "Planar dual-band microstrip antenna," *IEEE Trans. Antenna. Propagat.*, 43, pp. 892-895, Aug. 1995.
- [7] C.S. Lee and V. Nalbandian, "Planar leaky-wave microstrip antenna," *Proc. IEEE AP-S Int. Symp. Dig.*, pp. 1126-1129, 1997.
- [8] H.A. Wheeler, "Transmission line properties of parallel wide strips by conformal mapping approximation," *IEEE Trans. Microwave Theory Tech.*, 12, pp. 280-289, 1964.
- [9] H.A. Wheeler, "Transmission line properties of parallel strips separated by a dielectric sheet," *IEEE Trans. Microwave Theory Tech.*, 13, pp. 172-185, 1965.
- [10] D. Janning and G.A. Thiele: "Conformal microstrip leaky wave antenna". U.S. Patent Application, 9 February 2005.
- [11] D. Killips, J. Radcliffe, L. Kempel, and S. Schneider, "Radiation by a Linear Array of Half-Width Leaky-Wave Antennas," *ACES Journal*, November 2006, Vol. 21, No. 3, pp. 248-255.
- [12] M. Corwin, L. Kempel, and S. Schneider, "Driving Point Impedance for a Linear Array of Half-width Leaky-wave Antennas," *IEEE Antennas and Propagation Society Symposium*, Albuquerque, NM, July 2006.
- [13] J. Radcliffe, H. Griffith, J. McCann, K. Zeller, K. Pasala, S. Schneider and L. Kempel, "Empirical Analysis of the Effects of Parasitic Elements on the Half-Width Leaky Wave Antenna," *IEEE Antennas and Propagation Society Symposium*, Honolulu, HI, June 2007.
- [14] C.F. Smith, A.F. Peterson, R. Mittra, "The biconjugate gradient method for electromagnetic scattering," *IEEE Trans. Antennas Propagat.*, 38, pp. 938-940, June 1990.
- [15] J.L. Volakis, A. Chatterjee, and L.C. Kempel, *Finite Element Methods for Electromagnetics*, IEEE Press: Piscataway, N.J., 1998.
- [16] H.F. Jordan and G. Alaghband, *Fundamentals of Parallel Processing*, Prentice Hall: Upper Saddle River, NJ, 2003.
- [17] MSU High Performance Computing Center, <http://www.hpc.msu.edu>.
- [18] D. Killips, M. Corwin, L. Kempel, and S. Schneider, "Termination of Half-width Leaky-wave Antennas," *IEEE Antennas and Propagation Society Symposium*, Albuquerque, NM, July 2006.
- [19] L. Kempel, S.W. Schneider, J.S. Radcliffe, D.S. Janning, and G.A. Thiele, "FE-BI Analysis of a Leaky Wave Antenna with Resistive Sheet Termination," *2005 IEEE/ACES (Applied Computational Electromagnetics Society) Conference*, Honolulu, Hawaii, Apr. 2005.
- [20] J. Radcliffe, S. Schneider, L. Kempel, and R. Penno, "Finite Element-Boundary Integral Simulation of a Conformal Microstrip Leaky-wave Antenna", *2007 IEEE Antennas and Propagation Society Symposium*, Honolulu, HI, June 2007.
- [21] L.C. Kempel, J.L. Volakis, and R.J. Sliva, "Radiation by cavity-backed antennas on circular cylinder," *IEE Proc.-Microw. Antennas Propag.*, 142, pp. 233-239, June 1995.

- [22] L. Kempel, S. Schneider, T. Kastle, and G. Theile, "Comparison of two termination schemes for a half-width leaky-wave antenna," *URSI National Radio Science Mtg.*, Washington DC, July 2005.
- [23] R.P. Penno, G. Thiele, J. Reynolds, and S. Schneider, "Back lobe elimination using a conformal microstrip leaky-wave antenna," *2006 IEEE Conf. on Radar*, 24-27 Apr 2006.
- [24] J. Radcliffe, G. Thiele, R. Penno, S. Schneider, and L. Kempel, "Microstrip leaky-wave antenna performance on a curved surface," *2006 IEEE Antennas and Propagation Symposium*, Albuquerque, NM, July 2006.

# Scalar and Tensor Artificial Impedance Surface Conformal Antennas

J. S. Colburn, D. F. Sievenpiper, B. H. Fong, J. J. Ottusch, J. L. Visher and P. R. Herz  
HRL Laboratories LLC  
3011 Malibu Canyon Road  
Malibu, CA, USA, 90265

©2007 HRL Laboratories, LLC All rights reserved.

**Abstract:** Conformal antennas can be realized with artificial impedance surfaces. By modulating the wave impedance on a structure's surface the energy in a surface wave traveling on that surface can be radiated away at a prescribed rate and angle. The required impedance distribution for a desired radiation pattern can be determined with microwave holography and realized with artificial impedance structures. Polarization control can be achieved by realizing full tensor impedances. This technology offers a new approach to achieve high directivity antennas patterns with minimal affects on the host vehicle aesthetics or aerodynamics by utilizing the surface of structure to achieve collimation.

## 1. Introduction

Conformal antenna can be realized with artificial impedance surfaces. As first reported by Oliner *et al.* [1], by modulating the wave impedance on a structure's surface the energy in a surface wave traveling on that surface can be radiated away at a prescribed rate and angle. The required impedance distribution for a desired radiation pattern can be determined with microwave holography [2] and realized with artificial impedance structures. In the approach we have been investigating, the complex object of interest is coated with an artificial impedance surface consisting of a lattice of sub-wavelength metal patches on a grounded dielectric substrate [3,4]. The effective surface impedance depends on the gap between the metal patches, which is varied as a function of position to realize the proper surface impedance distribution in order to achieve the desired radiation/scattering characteristics.

Previously we reported on demonstrations of directive radiation from a dipole source located on a flat artificial impedance surface [3], radiation into the "shadow region" of a cylinder from a dipole feed [3], and a higher order surface impedance design approach using an iterative procedure [4]. In this work we discuss our recent demonstrations of controlled surface wave radiation with the modulated scalar artificial impedance surface approach. The demonstrations discussed include a waveguide feed tapered modulation impedance surface antenna with 58% aperture efficiency, the redirection of plane waves around solid objects with reradiation at a prescribed angle and the realization of an impedance surface on a structure with two dimensions of curvature.

In addition to our work on scalar impedance surfaces, we have extended our study of artificial impedance surfaces to tensor impedance surfaces which accounts for the true vector nature of both the fields and the currents. Through this more complete tensor representation of the problem complete polarization control of the radiation from surface wave propagation on modulated impedance surfaces is possible.

## 2. Scalar Impedance Surfaces

Microwave holograms are created using the interference pattern between the expected bound surface wave and the desired outgoing field. In the scalar impedance case, electric field and surface current are related via

$$\mathbf{E}_t = Z(\mathbf{x}_t)\mathbf{J} \quad (1)$$

for scattering of bound TM modes the artificial impedance function derived from the holographic interference is

$$Z(\mathbf{x}_t) = -i\left(X + M \operatorname{Re}\left[\psi_{out}(\mathbf{x}_t)\psi_{surf}^*(\mathbf{x}_t)\right]\right) \quad (2)$$

, where  $X > 0$  and  $M$  are normalized to the free space impedance, and the wave quantities contain only phase information. We assume the surface lies in the x-y plane and  $\mathbf{x}_t$  gives the tangential x-y coordinates. The impedance modulation created by the interference pattern generalizes the one-dimensional impedance modulation and radiation analysis given by Oliner [1].

The scalar artificial impedance function is implemented with a pattern of subwavelength square metal patches on dielectric, on a square lattice. To determine the relationship between metal patch size and artificial surface impedance we use the full wave electromagnetic simulator FastScat [5] to compute the TM surface mode wavenumbers for an infinite array of square metal patches. The TM surface mode has spatial dependence

$$\exp(i\mathbf{k}_t \cdot \mathbf{x}_t) \exp(-k_z z) \quad (4)$$

where the wavenumbers are related to the surface impedance via

$$k_t = k\sqrt{1 + X^2} \quad (5)$$

$$k_z = kX \quad (6)$$

$$Z = -iX \quad (7)$$

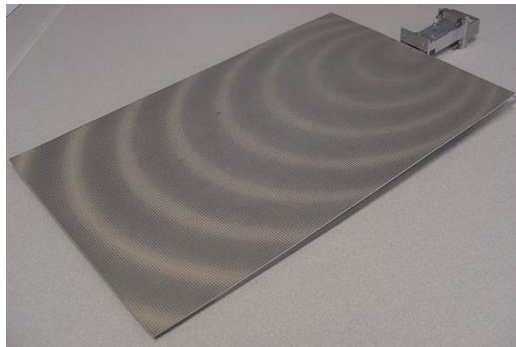
and  $k$  is the free space wavenumber. By computing the impedance for a range of metal patch sizes, we determine the mapping between impedance and patch size. Sampling the

hologram impedance function at each unit cell center gives the local impedance value and hence the local metal patch size.

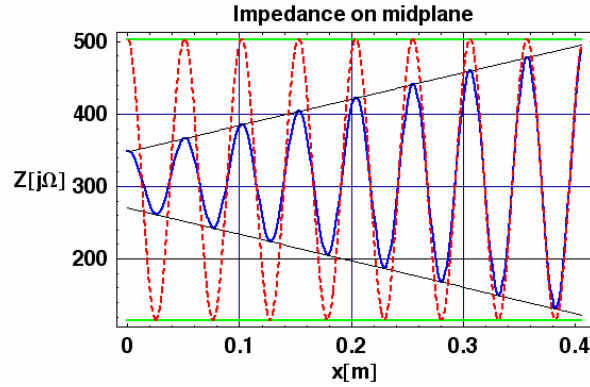
## 2.1 Waveguide Excited Tapered Modulation Impedance Surface

Figure 1 contains a picture of an X-band artificial impedance surface antenna excited by a reduced height waveguide feed at one end. The surface is 254mm by 400 mm and fabricated with 1.27 mm thick Rogers 3010 microwave substrate material. The opening of the reduced height waveguide feed only extends 1.27 mm above the top of the artificial impedance. This surface impedance pattern was determined with the holographic approach and the impedance modulation was tapered from a small amplitude at the feed end to a large amplitude at the opposite end. Figure 2 contains plots of the impedance along the center line of two conformal directive antennas with beam peaks 45 degrees from the surface normal, one for the case of a constant impedance modulation, solid curve, and the tapered modulation case, dashed curve. The radiation efficiency scales with modulation depth. We taper the profile away from the source so that the scattering efficiency is lower at the feed end where there is more energy in the surface wave and it is higher at the opposite end where there is less energy in the surface wave since most of the feed energy has been radiated away.

Figure 3 is a contour plot of the measured near field distribution of the electric field strength polarized parallel to the long side of the artificial impedance surface for the case of the tapered impedance modulation function at 10 GHz. In the figure, the feed location and edge of the artificial impedance surface are indicated. This plot indicates efficient utilization of the radiating aperture with a peak in the radiated field in the center of the aperture. In Figure 4 are plots of the measured far field pattern at 10 GHz in the cut parallel to the long side of the artificial impedance surface again for the case of the tapered impedance modulation function. The measured patterns show a well defined beam peak at 45 degrees, with relatively low sidelobes and low cross polarization radiation. The aperture efficiency of this antenna is 58%. The measured beamwidth for the tapered modulation artificial impedance surface antenna was approximately 50% less than for the constant modulation artificial impedance surface.



**Figure 1: Photo of taper modulated artificial impedance surface with reduced waveguide feed.**



**Figure 2: Plot of a constant modulation impedance surface profile (dashed) and tapered modulation impedance profile (solid ) along the midplane of the surface.**

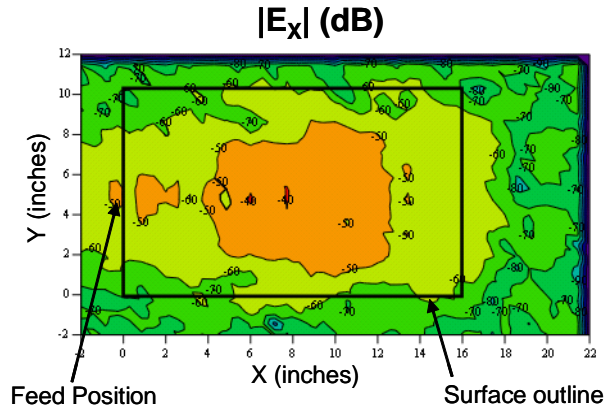


**Figure 3: Measured near field electric field distribution polarized parallel to the x-axis of the modulation taper impedance modulation surface at 10 GHz.**

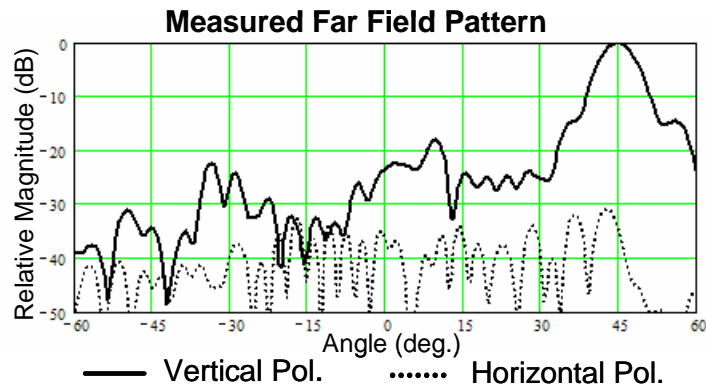


**Figure 4: Measured far field pattern at 10 GHz of taper modulated impedance surface in the cut parallel to x-axis. Horizontal polarization is parallel to y-axis in this cut and the vertical polarization is perpendicular to the y-axis in this cut.**



## 2.2 Redirection of Plane Waves Around Solid Objects

We have also demonstrated redirection of a plane wave around a solid object with the scalar holographic artificial impedance approach. In this demonstration, impedance patterns were designed to capture plane wave energy incident on one side of a solid cylinder into a surface wave that traveled around the cylinder and then reradiated on the opposite side of the cylinder at a prescribed angle. Thus we were affectively able to “see through” a solid object at microwave frequencies at one particular incident angle. This capability to direct incident plane wave energy around a solid object enables the location of antennas in locations previously not possible due to blockage issues in the required coverage area.

Figure 5 contains a photograph of the experimental setup, which consists of an illuminating horn situated in front of a metal cylinder with an artificial impedance surface wrapped around it, both of which are mounted on a rotating stage. The metal cylinder is 254 mm in length and 813 mm in circumference, and the impedance surfaces were fabricated with 1.27 mm thick Rogers 3010 microwave substrate material. Figure 6 contains plots of the measured patterns at 11 GHz when the illuminating horn and cylinder were rotated, for the case of a metal cylinder only (dotted curve), in addition to when the cylinder was wrapped with two different impedance surfaces, one designed for reradiation in the same direction of the incident plane wave (solid curve) and one 30 degrees (dashed curve) with respect to the incident plane wave. Superimposed on the measured results in Figure 6 is a top down view of the experimental setup. For the results shown in Figure 6, the incident wave was blocked by absorber on half of the cylinder in order to reduce interference effects from surface waves traveling in both directions around the cylinder. From the results shown in Figure 6 it is clear that when a solid metal cylinder is illuminated the majority of the incident energy is scattered back in the lit side direction, but when the cylinder is wrapped in the artificial impedance surfaces the peak in the patterns are in the forward direction on the shadowed side of the cylinder.

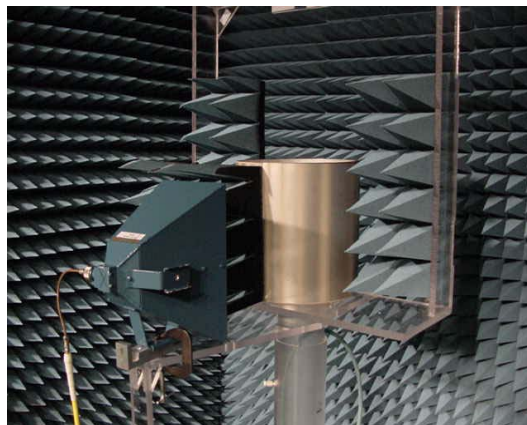


**Figure 5: Photograph of experimental setup used to illustrate capability of "seeing through" a solid cylinder.**

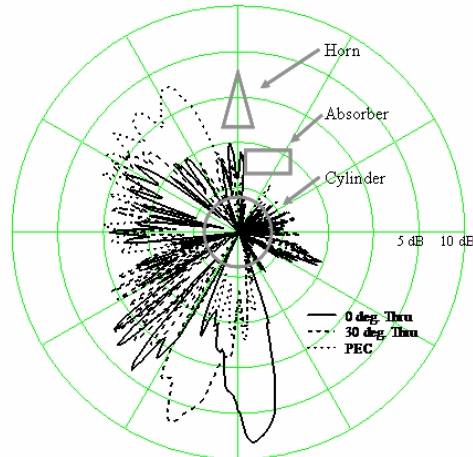


**Figure 6: Measured patterns at 11 GHz for experimental setup shown in Figure 5 for a metal cylinder only (dotted), plus when impedance surfaces were wrapped around the cylinder designed for reradiation at 0 (solid) and 30 (dashed) degrees relative to the incident plane wave.**

### 2.3 Artificial Impedance Surface Antenna on Partial Sphere

Figure 7 is a photograph of an artificial impedance surface fabricated on a portion of a 10.56 cm radius sphere. The previously reported cylindrical artificial impedance surface antennas were realized by wrapping a flat artificial impedance sheet around a cylinder. But this approach is not possible for surfaces with two dimensions of curvature which would require some stretching or compression of a flat surface to truly conform to the structure. Since the artificial impedance surface requires precise gap spacing between the subwavelength metal patches used to realize the required impedance pattern, any stretching or compression is not acceptable. The artificial impedance antenna shown in Figure 7 was fabricated directly on a partial sphere shell made of polycarbonate material.



**Figure 7: Photograph of artificial impedance surface fabricated directly on sphere shell.**

The first step in the design and fabrication was to compute the surface impedance verses gap size for the polycarbonate shell, which requires the thickness (2 mm) and dielectric constant (2.7) of the shell material. Once the surface impedance versus gap size was characterized, the metal pattern for the sphere surface was computed with the holographic approach. The impedance pattern was designed to produce a beam peak at 10 degrees from the apex of the shell from a monopole source located 20 degrees from the apex on the opposite side of the shell. The required shell was then machined from a piece of polycarbonate material, both sides of which were covered with a 2  $\mu\text{m}$  layer of copper and the required gaps were realized by patterning photoresist and etching.

Figure 8 contains plots of the measured pattern from the sphere section with the artificial impedance surface (solid) and the measure pattern from a monopole source located at a similar position on a metal shell (dotted) of the same size. The enhanced radiation at 10 degrees from the artificial impedance surface compared to the metal surface is clearly seen.

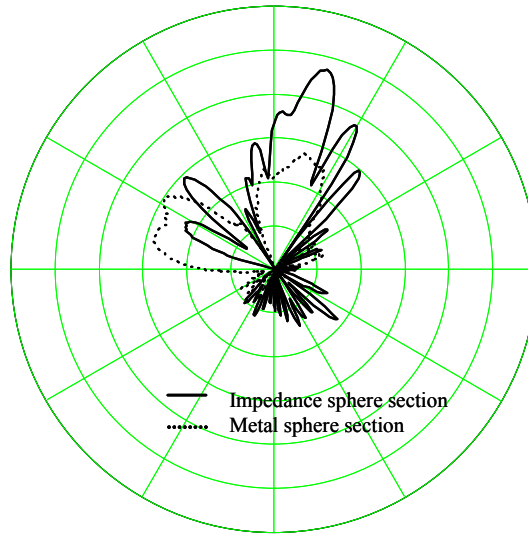


**Figure 8: Measured radiation pattern from monopole source located on a metal (dotted) and artificial impedance surface (solid) partial sphere.**

### 3. Tensor Impedance Surfaces

The tensor impedance hologram generalizes the scalar impedance hologram method described above. In the tensor impedance case, surface electric field and surface current are related through

$$\begin{pmatrix} E_x \\ E_y \end{pmatrix} = \begin{pmatrix} Z_{xx} & Z_{xy} \\ Z_{yx} & Z_{yy} \end{pmatrix} \begin{pmatrix} J_x \\ J_y \end{pmatrix}. \quad (8)$$

The tensor impedance function is constructed from the outer product of the expected vector surface current and the desired outgoing electric field vector; the outer product

generalizes the simple multiplicative scalar interference above. For an energy conserving reciprocal artificial impedance surface, the impedance tensor must additionally be made anti-Hermitian and pure imaginary [6]. The impedance tensor is then given by

$$\mathbf{Z}(\mathbf{x}) = -i \begin{pmatrix} X & 0 \\ 0 & X \end{pmatrix} - i \frac{M}{2} \text{Im}(\mathbf{E}_{out}(\mathbf{x}) \otimes \mathbf{J}_{surf}^\dagger(\mathbf{x}) - \mathbf{J}_{surf}(\mathbf{x}) \otimes \mathbf{E}_{out}^\dagger(\mathbf{x})), \quad (9)$$

where the dagger gives the Hermitian conjugate. As in the scalar case the diagonal  $X$  part of the impedance tensor binds a TM surface wave, but the modulated impedance components now scatter the *vector* surface wave into the desired *vector* outgoing wave.

### 3.1 Simulated Radiation from Tensor Impedance Surface

Artificial tensor impedance surfaces with holograms generated using the above procedure were simulated using FastScat. Figures 9 and 10 show the impedance components and computed far field for a tensor artificial impedance surface designed to scatter a vertically polarized TM surface wave from a point source located at the far left side of the impedance surface at 10 GHz into a circularly polarized plane wave at  $45^\circ$ . The impedance surface has dimensions 25.4cm by 40cm and an impedance range of  $136j\Omega$  to  $369j\Omega$ . The computed far field beam has a peak left hand circular polarization (LHCP) directivity of 26.8 dBi at  $45^\circ$ , with the right hand circular polarization component down by 14.3 dBi. The tensor impedance function generated by the outer product interference procedure successfully converts a vertically polarized excitation into circularly polarized

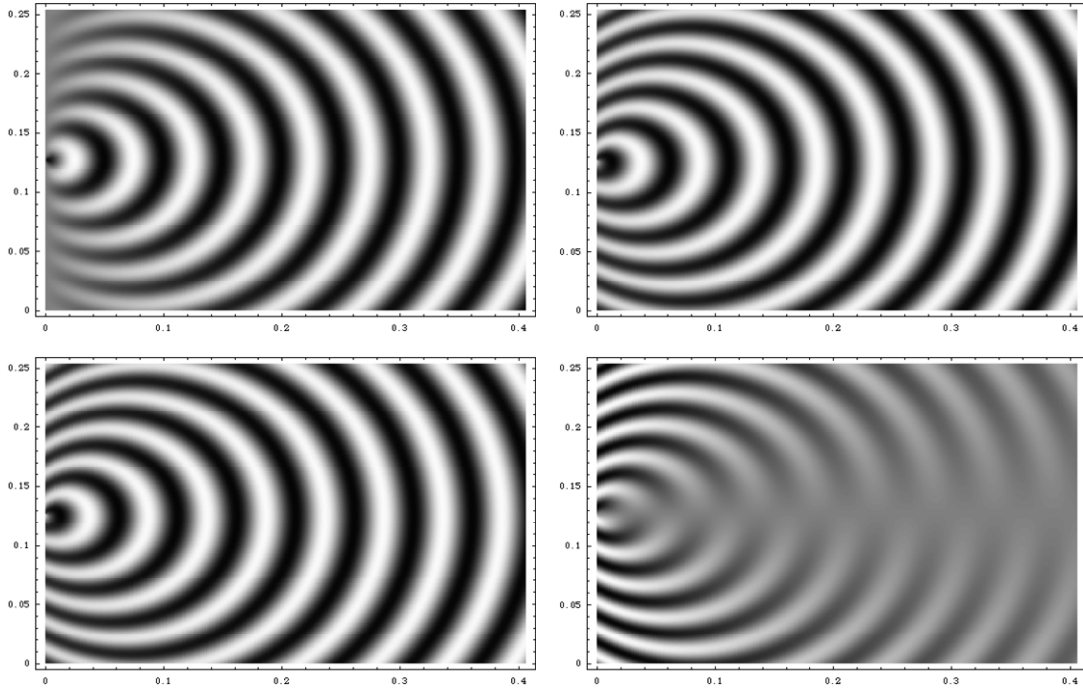


**Figure 9: Tensor impedance components  $Z_{xx}$ ,  $Z_{xy}$ ,  $Z_{yx}$ ,  $Z_{yy}$  for scattering a vertically polarized surface wave into a circularly polarized plane wave.**

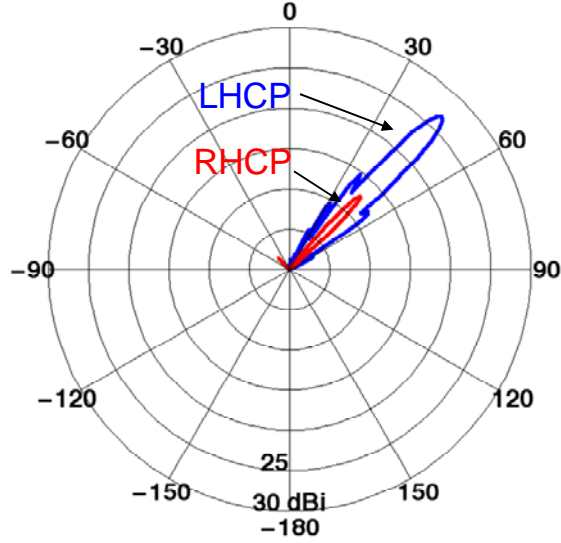


**Figure 10: Computed far field from artificial tensor impedance surface scattering a vertically polarized surface wave into a circularly polarized plane wave.**

radiation.

### 3.2 Tensor Impedance Surface Design and Characterization

In the scalar impedance case the relationship between impedance and geometrical parameter (metal patch size) is mapped out by determining the TM (or alternatively TE) bound mode wavenumber. In the tensor impedance case, the relationship between tensor impedance components and geometrical parameters is similarly determined. For a constant tensor impedance surface, a bound mode with spatial dependence  $\exp(i\mathbf{k}_t \cdot \mathbf{x}_t) \exp(-k_z z)$  has wavenumber  $k_z$  given by

$$\begin{aligned} \frac{k_z}{k} = & \left[ i(1 - Z_{xy}^2 + Z_{xx}Z_{yy}) \right. \\ & \pm \left\{ (1 - Z_{xy}^2 + Z_{xx}Z_{yy})^2 + 4(Z_{yy} \cos^2 \theta_k - Z_{xy} \sin 2\theta_k + Z_{xx} \sin^2 \theta_k) \right. \\ & \times (Z_{xx} \cos^2 \theta_k + Z_{xy} \sin 2\theta_k + Z_{yy} \sin^2 \theta_k) \left. \right\}^{1/2} \left. \right] \\ & \times \left[ 2(Z_{yy} \cos^2 \theta_k - Z_{xy} \sin 2\theta_k + Z_{xx} \sin^2 \theta_k) \right]^{-1} \end{aligned} \quad (10)$$

where  $\theta_k$  gives the propagation direction of the bound mode; the minus sign corresponds to a TM-like mode, and the plus sign to a TE-like mode. Unlike the scalar case, the tensor impedance bound modes are no longer pure TM or pure TE. Because the scalar case has the  $k_z/k$  ratio giving the constant scalar impedance, in the tensor impedance case one can interpret the  $k_z/k$  ratio as giving an *effective* scalar impedance that is propagation direction dependent. (This interpretation does not extend to the surface electric field and current since they are not generally aligned.) Eq. 10 also implies that

the mode phase velocity is direction dependent, as is generally true in an anisotropic medium.

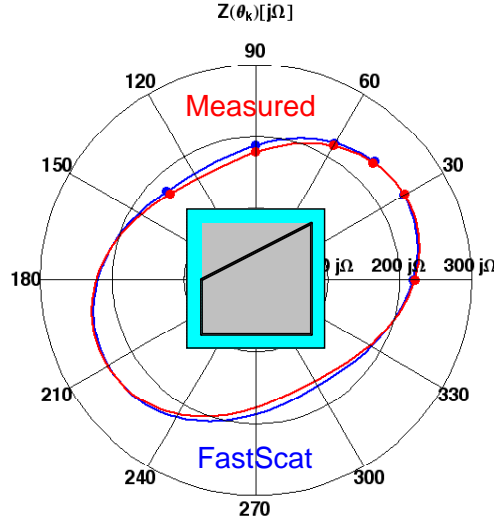


**Figure 11: Trapezoidal metal patch (inset) and measured (gray dots) and FastScat computed (black dots) effective scalar impedances. Gray and black lines give effective scalar impedances as a function of propagation angle via Eq. 10.**

Eq. 10 gives the effective scalar impedance as a function of tensor impedance components and propagation direction. To determine the impedance tensor components using Eq. 10 requires computing or measuring the effective scalar impedance at three different propagation directions and then solving for the three unknowns  $Z_{xx}$ ,  $Z_{xy}$ , and  $Z_{yy}$  from the three nonlinear constraint equations. If data from more than three different propagation directions is available, a least squares solution to the constraint equations derived from Eq. 10 is used.

Figure 11 (inset) shows a square unit cell containing a trapezoidal metal patch on dielectric, creating a TM-like tensor artificial impedance surface. Figure 11 also shows the FastScat computed and measured effective scalar impedances as a function of propagation direction  $\theta_k$  for the trapezoidal patch geometry. FastScat computations include an empirical scaling function derived from true, i.e., non-effective, scalar impedance measurements and computations. The trapezoidal patch geometry clearly gives a non-scalar impedance since the effective scalar impedance varies with propagation direction. Measured best fit impedance components are ( $Z_{xx}=+222.7j\Omega$ ,  $Z_{xy}=+31.2j\Omega$ ,  $Z_{yy}=+179.1j\Omega$ ) and computed best fit impedance components are ( $Z_{xx}=+220.5j\Omega$ ,  $Z_{xy}=+29.0j\Omega$ ,  $Z_{yy}=+188.5j\Omega$ ). Good agreement is thus found between the analysis and both the measured and computed data.

For a given metal patch geometry, we are able to compute the associated impedance tensor using this characterization method. Implementing a tensor impedance hologram function given by Eq. 9 requires the solution of the inverse problem: for a given tensor impedance determine the metal patch geometry. We solve the inverse problem by

constructing a database of metal patch geometries and associated impedance tensors, and subsequently numerically inverting this mapping. A given impedance tensor may not be implementable with a given type of metal patch geometry, in which case alternative geometries must be considered. Unit cells for metal patch geometries that have been investigated are shown in Figure 12. The unit cell geometries we have studied so far

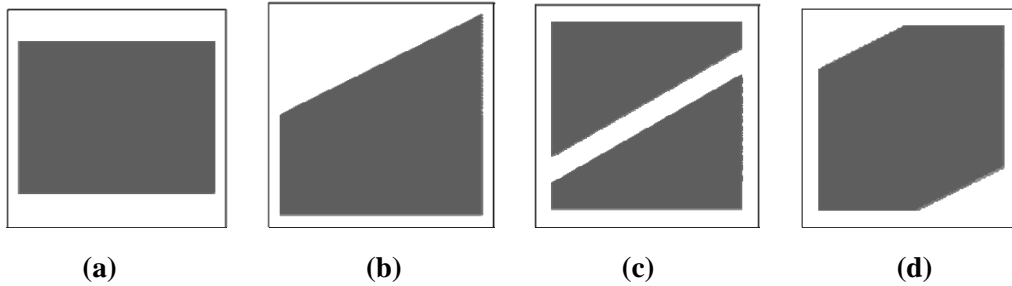


**Figure 12. Unit cells for metal patch geometries creating TM-like tensor artificial impedance surfaces. Shaded areas are metal. Impedance tensor components vary with geometrical parameters, i.e., gaps between metal and angles of cuts.**

conform to a rectangular grid which makes tiling simple and have either two or three degrees of freedom to vary to achieve the desired tensor impedance properties.

### 3.3 Waveguide Excited Tensor Impedance Surface

Figure 13 contains a drawing of a tensor impedance surface designed to realize the tensor impedance functions shown in Figure 9, which is intended to convert the excitation of a rectangular waveguide feed into circular polarization radiation. The unit cell structure utilized is a square patch with a slot cut in it, as shown in Figure 12 (c). The width of the patch to patch gap, the width of the slot cut into the patch and the angle of the slot are all parameters which can be varied to achieve a specified tensor impedance function. Figure 14 contains plots of the desired (solid) lines and computed (dashed) lines of the tensor components ( $Z_{xx}$ ,  $Z_{xy}$  and  $Z_{yy}$ ) along the line S drawn on the surface in Figure 13. As can be seen in this figure, we are not able to exactly reproduce the desired tensor impedance pattern, although the general trends can be achieved.

The impedance surface design shown in Figure 13 was fabricated and measured. The surface was realized on 1.27 mm thick Rogers 3010 microwave substrate material and the overall size is 25.4 cm x 40 cm. The feed was a WR90 (x-band) waveguide and was located at the center of the left side of the surface. Figure 15 contains plots of the measured far field patterns, in terms of left hand and right hand circular polarization components. The measured left hand circular polarization beam peak gain was 21.8 dB at 38 degrees from the surface normal. At the left hand circular polarization beam peak the right hand circular polarization peak was down by 19.6 dB. This measured far field data shows good agreement in terms of polarization purity compared to the computed pattern for the ideal tensor impedance surface, but the beam peak is off by 7 degrees.



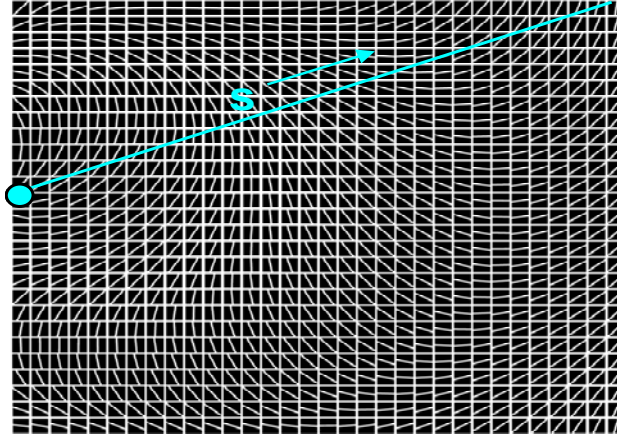


Figure 13: Tensor impedance surface design that converts a waveguide excitation at the left side into circular polarization radiation based on the unit cell shown in Figure 12 (c).

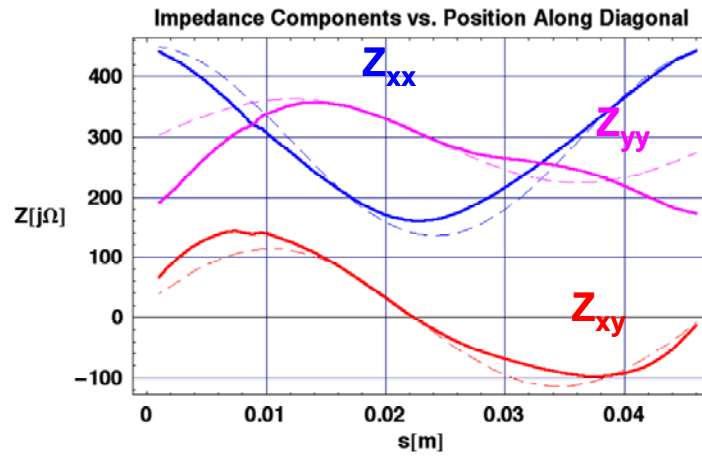


Figure 14: Plots of the desired (solid lines) and computed (dashed lines) tensor components along the line S in Figure 13.

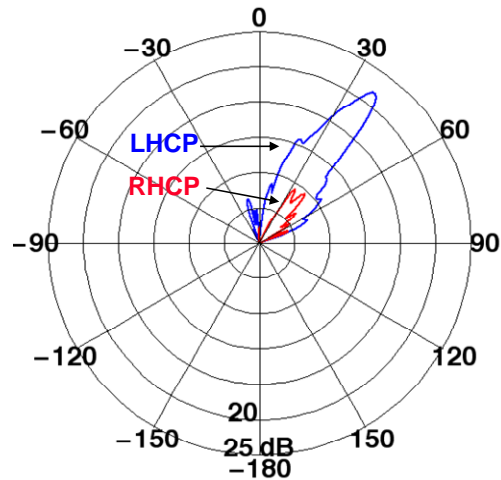
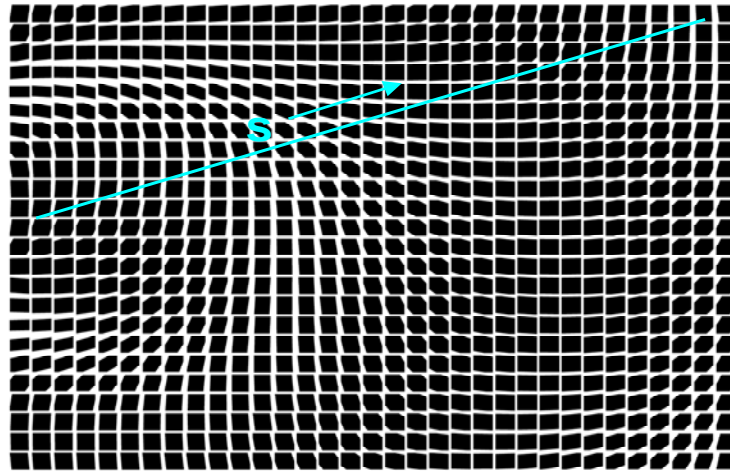


Figure 15: Measured far field radiation pattern of the tensor impedance surface shown in Figure 13 excited with a rectangular waveguide.

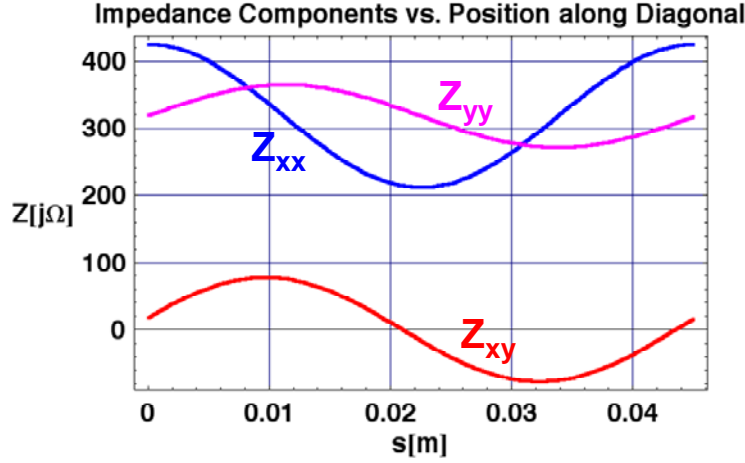


Figure 16 contains a drawing of a second tensor impedance surface designed to realize the tensor impedance functions shown in Figure 9. The unit cell structure utilized in this design is a square patch with parallel cuts introduced to remove a portion of the metal on the patch perimeter, as shown in Figure 12 (d). The width of the patch to patch gap, the size of the cuts and the angle of the cuts are all parameters which can be varied to achieve a specified tensor impedance function. Figure 17 contains plots of the desired (solid) lines and computed (dashed) lines of the tensor components ( $Z_{xx}$ ,  $Z_{xy}$  and  $Z_{yy}$ ) along the line S drawn on the surface in Figure 13. As can be seen in this figure, we are able to closely reproduce the desired tensor impedance pattern with this unit cell geometry.

The impedance surface design shown in Figure 16 was fabricated and measured. The surface was realized on 1.27 mm thick Rogers 3010 microwave substrate material and the overall size is 25.4 cm x 40 cm. The feed was a WR90 (x-band) waveguide and was located at the center of the left side of the surface. Figure 17 contains plots of the measured far field patterns, in terms of left hand and right hand circular polarization components. The measured left hand circular polarization beam peak gain was 17 dB at 45 degrees from the surface normal. At the left hand circular polarization beam peak the right hand circular polarization peak was down by 14.2 dB. In this realization of the tensor impedance we were able to exactly achieve the angular location of the beam peak and good polarization purity, but the gain is lower than expected.



**Figure 16:** A tensor impedance surface design that converts a waveguide excitation at the left side into circular polarization radiation based on the unit cell geometry shown in Figure 12 (d).



**Figure 17: Desired and simulated tensor impedance components along the line S in Figure 16.**

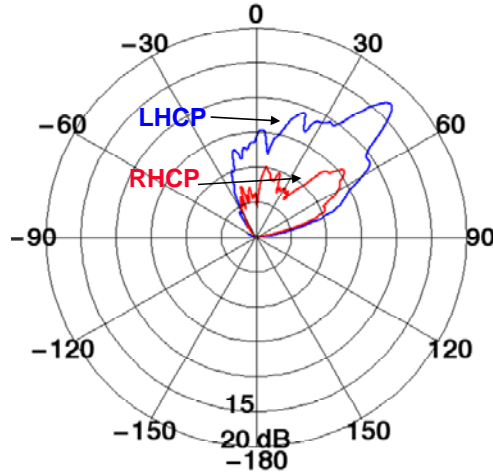


**Figure 28: Measured far field radiation pattern of the tensor impedance surface shown in Figure 16 excited with a rectangular waveguide.**

#### 4. Summary

In this paper we detailed our recent advances in utilizing impedance surfaces for advanced conformal antenna applications, based both the scalar surface impedance formulation and new the tensor surface impedance model. Scalar surface impedance results shown include a taper modulation impedance surface, redirection of plane waves around solid objects and realizing an impedance surface on a structure with two degrees of curvature. For the tensor impedance model, we have introduced the necessary components for designing and constructing polarization controlling holographic tensor artificial impedance surfaces, and presented measured data showing conversion of a vertically polarized source into a circularly polarized pencil beam. These demonstrations illustrate how to achieve high directivity antennas patterns with a structure that has

minimal affects on the host vehicle aesthetics or aerodynamics by utilizing the surface of structure to achieve collimation.

## **5. References**

- [1] A. Oliner and H. Hassel, "Guided Waves on Sinusoidally-Modulated Reactance Surfaces", IEEE Trans. on Antennas and Prop., vol. AP-7, no. 5, pp. 201-208, December. 1959.
- [2] W. Kock, "Microwave Holography", Microwaves, vol. 7, no. 11, pp. 46-54, November, 1968.
- [3] D. Sievenpiper, J. Colburn, B. Fong, J. Ottusch and J. Visher., 2005 IEEE Antennas and Prop. Symp. Digest, vol. 1B, pp. 256-259, 2005.
- [4] J. S. Colburn, D. F. Sievenpiper, B. H. Fong, J. J. Ottusch and J. L. Visher, 2006 URSI International Symposium Digest, pp. 412, 2006.
- [5] L. F. Canino, J. J. Ottusch, M. A. Stalzer, J. L. Visher, and S. M. Wandzura, "Numerical Solution of the Helmholtz Equation in 2D and 3D Using a High-Order Nyström Discretization," J. Comput. Phys., vol. 146, no. 2, pp. 627-663, November. 1998.
- [6] D. J. Hoppe and Y. Rahmat-Samii, Impedance Boundary Conditions in Electromagnetics, pp. 135-137, Washington, DC: Taylor & Francis, 1995.

# THREE-DIMENSIONAL ELECTROMAGNETIC BAND GAP (3-D EBG) STRUCTURES FOR ADVANCED CONFORMAL ANTENNAS

Francesca Sciré-Scappuzzo<sup>1</sup>, Jonathan P. Towle<sup>1</sup> and Marianne Lazzaro<sup>2</sup>

<sup>1</sup> Physical Sciences Inc., 20 New England Business Center, Andover, MA 01810  
[fss@psicorp.com](mailto:fss@psicorp.com), [towle@psicorp.com](mailto:towle@psicorp.com)

<sup>2</sup> US Army CERDEC, Fort Monmouth, NJ 07703  
[Marianne.Lazzaro@mail1.monmouth.army.mil](mailto:Marianne.Lazzaro@mail1.monmouth.army.mil)

**Abstract:** Within the commercial and military antenna market there is a pressing demand for small, conformal broadband antennas for many applications. In this work we propose to use Inner Cross-Split Ring Resonator (IC-SRR) (3-D EBG surfaces) for performance enhancement of conformal antennas and antenna arrays. Through numerical simulations using HFSS we have demonstrated that the proposed 3-D EBG structure works extremely well on curved surfaces and is considerably smaller than common flat surface EBG structures. Moreover, it is possible to achieve broadband frequency performance when the surface is properly designed in a hybrid configuration. These properties, together with excellent antenna pattern control, mutual coupling reduction, and EMI mitigation, make this 3-D EBG structure an ideal antenna technology enhancement for soldiers' uniforms, ground vehicles, UAVs, airplanes, and panels on space frames.

## 1. Electromagnetic Band-Gap Metamaterials

Electromagnetic Band-Gap (EBG) structures are metamaterials designed to have a periodically structured dielectric constants so that, they have frequency domains where electromagnetic fields cannot propagate (forbidden band-gaps). The position and width of these forbidden gaps can be controlled via the geometrical parameters of the structures. Introduced first in Optics as Photonic Band-Gap [1], EBG materials have application to a variety of devices in the microwave domain; such as waveguides, couplers, reflectors and antenna substrates.

Recently it has been shown that metamaterials can prevent propagation of surface radiation on planar structures. This can be extremely useful when trying to minimize mutual coupling between antennas, improve radiation efficiency of low profile antennas, or reduce EMI between components. Traditionally, the design and implementation of EBG have been focused on planar structures. However, EBG materials with

substructures of planar periodic forms might not fit to a curved surface and might not retain the desired electromagnetic properties for conformal antennas.

There are many important applications for antennas curved surfaces. Modern airplanes are equipped with a large number of antenna systems for communication, navigation, landing, radar altimetry, etc. These antennas usually protrude from the body of the aircraft and cause undesired drag that causes higher fuel consumption. Moreover, protruding antennas can act as backscatters of microwave radiation when illuminated by radars, impairing the aircraft stealth properties in military applications. Therefore, it is desirable to design antenna systems with radiating elements mounted conformal to the structure of the air platform on a smoothly curved surface and - if possible - integrated into the structure of the aircraft. Conformal antennas are especially desirable for large apertures necessary for satellite communication and military airborne surveillance radars. The US Army Future Combat System modernization program will require ensuring tight network communications between soldiers, commanders, artillery, and ground/air vehicles. Therefore, antenna systems are required in which broadband antennas cover several frequency ranges that can be mounted on small curved surfaces.

The lack of non-flat EBG configurations and the computational difficulties involved with modeling in a curved surface environment make it difficult to extend the benefits of BEG materials to conformal antennas. In response to the demand and to overcome these difficulties we propose a three dimensional EBG structure designed to enhance the performance of conformal antennas thanks to its isotropic nature. This structure is a combination of concentric “split-rings” opportunely sized and distributed to act as an EBG metamaterial in a desired frequency range. Due to the 3-D configuration of the proposed *Inner Cross Split Rings Resonator (IC-SRR) metamaterial*, the proposed EBG material is suitable to curved surface applications, as we will demonstrate in this paper.

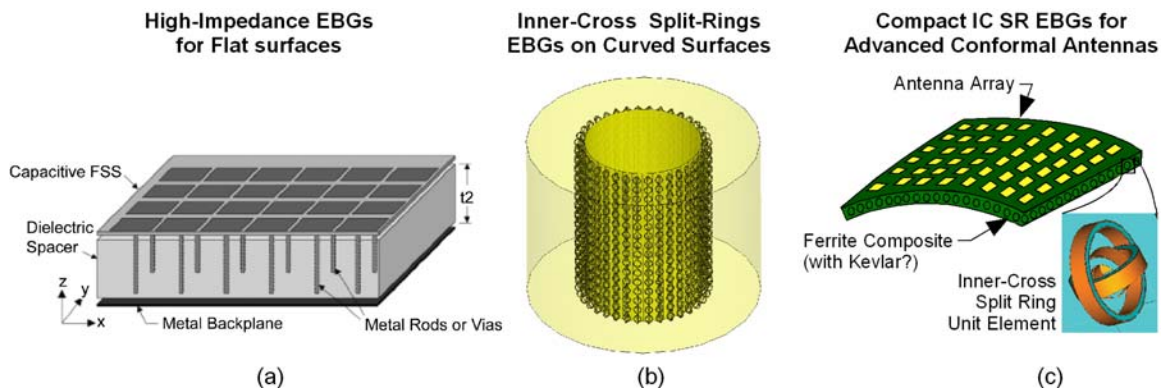


Figure 1. Research and Development roadmap from the classic EBGs structures [2] (a) to an example of conformal antennas on EBG substrate prototype under Army SBIR contract (c).

Table 1. Summary of performance. Comparison between classic and 3D EBGs.

Metamaterial: EBG Structures	Performance	Curved Surfaces	Wide Bandwidth	Size	Isotropy	Mechanical properties
<b>Classic EBGs: High-Impedance Surfaces</b>	Excellent BandGap Performance	Not suitable for curved surfaces	from ~1.0 GHz to 1.5 GHz	<b>Small:</b> ~ 1 cm	Not an isotropic structure	<b>Low:</b>  Usually imbedded in a dielectric foam
<b>Novel 3D EBGs: Inner-Cross Split-Rings Surfaces</b>	Excellent BandGap Performance	Works very well for curved surfaces	from ~200 MHz to 1.5 GHz (hybrid)	<b>Smaller</b> < 2.5 smaller than classic EBGs	<b>Quasi- Isotropic structure</b>  The single cells can be randomly oriented	<b>High:</b> Good mechanical and impact resistance: Ferrite/Kevlar composite

## 2. Surface and Volumetric EBG Structures

The EBG metamaterials are traditionally designed for flat surfaces, as in Figure 2, where the classic Sievenpiper's high-impedance surface is shown. The structure consists of a lattice of metal plates connected to a solid metal sheet by vertical conducting vias. Although it is made of continuous metal and conducts dc currents, it does not conduct ac currents within a forbidden frequency band. It does not support propagating surface waves, and its image currents are not phase reversed. The geometry is analogous to a corrugated metal surface in which the corrugations have been folded into lumped-circuit elements, and distributed in a 2-D lattice.

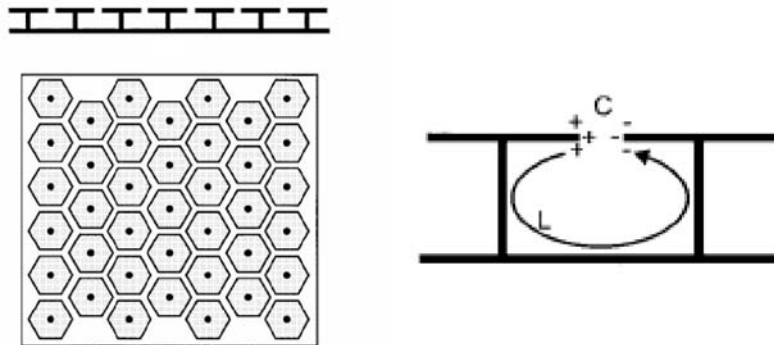


Figure 2. Simple structure of a High-Impedance surface and origin of C and L for the unit cell (Sievenpiper et al., 1999) [3].

This structure functions as the ideal antenna ground plane, because it simultaneously enhances gain of the antenna and it suppresses the surface waves (reducing the back-lobe and the reactive coupling to nearby circuits). These structures have been demonstrated for

flat surfaces, and to our knowledge there is no known EBG structure suitable for curved surfaces in literature.

Recent studies have shown that a microstrip antenna phased array embedded in a uniplanar EBG substrate has a reduction in mutual coupling between elements as much as 8dB [4] and provides a possible solution to the “blind spots” problem in phased array applications with printed elements.

Our proposed approach to be applied to curved surface utilizes a different basic component with respect to the Sievenpiper’s “mushroom” structure of Figure 2. We propose to use the split-ring, which can also be consider as a lumped-circuit element. A split ring is planar structure that acts as an EBG structure for waves in the direction of the ring plane, with in a certain frequency range (Figure 3).

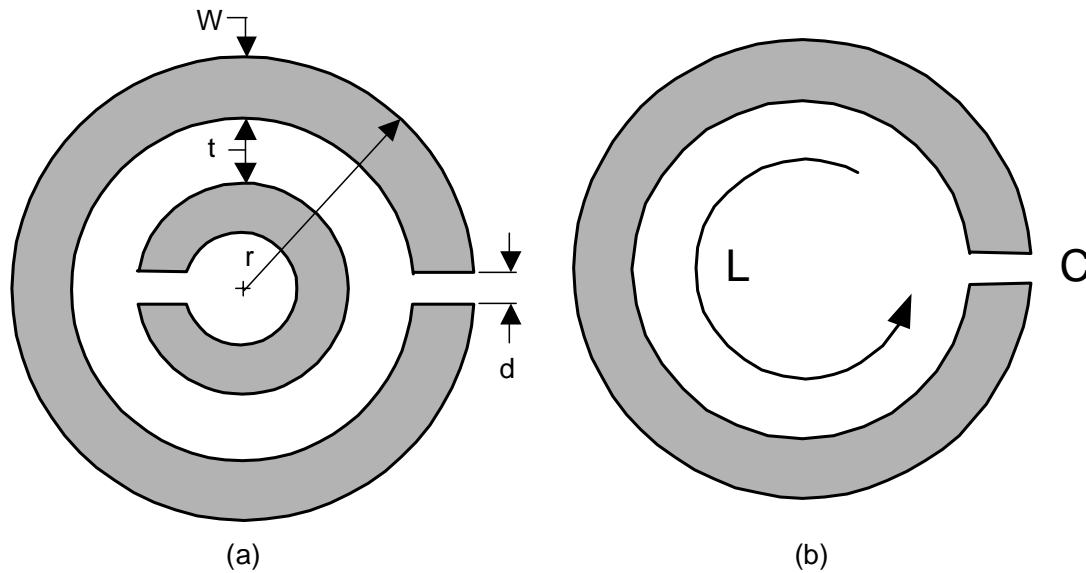


Figure 3. (a) Basic 1D split-ring geometry:  $r$ =outer ring diameter,  $d$ =split width,  $t$ =gap between outer and inner ring,  $w$ =ring width. (b) Origin of  $C$  and  $L$  for the unit split ring cell.

## 2.1 Approximate Formula and Equivalent Circuit

The frequency of resonance depends of several parameters, included the diameter of the ring (inner and outer), the split, the width of the ring, the thickness of the metal, and the spacing between inner and outer ring [5]-[6]. Therefore, the size of the structure can be reduced sensibly with a proper geometrical design. For a thin inner-cross structure as the double split ring of Table 1 (the Finger SRR), an approximate expression for the resonant frequency has been derived in [7]:

$$\omega_r = \sqrt{\frac{3d}{\pi^2 r}} \cdot \left(\frac{c}{r}\right) \quad (1)$$

where  $d$  is the difference between inner and outer radius, and  $r$  is the average radius (average between the inner and outer radius).

Table 1. 1-D Split Rings Geometries (from [5]).

Type (thick)	Single Split Finger Ring (big)	Single Split Double Finger Rings	Shielded Finger Rings	Finger SRR	Single Split Finger Ring (small)
Geo.					
$f_{\text{meas}}$	1.86	2.03	2.96	1.53	2.78
$f_{\text{sim}}$	1.955	2.071	2.926	1.562	2.829
$Q_{\text{meas}}$	16.9	19.6	89.2	39.4	15.4
$Q_{\text{sim}}$	17.3	21.3	272.1	44.5	14.9

Table 1: Five configurations of Finger Rings

This structure showed to be the smallest configuration to achieve a given resonance. Equivalently, a double split ring provides the smallest resonance for a given external diameter.

A more complex model relying on an equivalent circuit was proposed by in [8]. The equivalent circuit is a combination of lumped elements. The equivalent circuit is turned into a set of differential equations, which needs to be solved and subject to the boundary conditions. the resonant frequency is obtained as the solution of a transcendental characteristic equation.

An approximate formula for the resonant frequency for a double split ring (Figure 3) is as follows:

$$\omega_r = \sqrt{\frac{I}{2\pi L_{av} \left( \frac{\pi C}{2} + C_{G1} + C_{G2} \right)}} \quad L_{av} = \frac{L_1 + L_2}{2}$$

where:



$C_{G1}, C_{G2}$  = Gap Capacitances for the outer and inner rings, respectively (per unit radian)  
 $C$  = Inter-ring Capacitance  
 $L_1, L_2$  = Outer-ring and inner-ring inductance, respectively.  
 $L_{12}$  = Mutual Inductance between the rings

## 2.2 Proposed 3D Configuration

In order to model an omni-directional material that rejects or attenuates the propagating surface waves on curved surfaces, we propose to introduce a new combination of 3-D structures that we refer to as *Inner Cross-Split Ring Resonators*, shown in Figure 4.

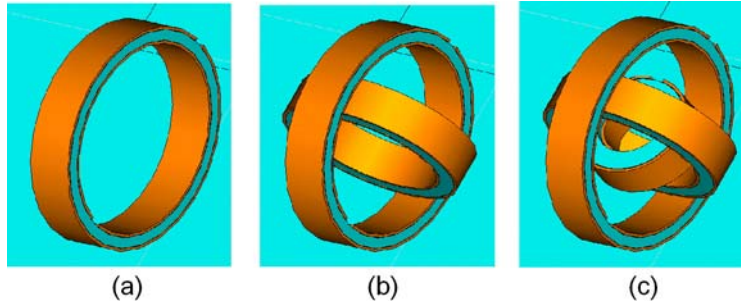


Figure 4. a) One-axis, b) two-axes and c) three-axes (Proposed 3-D) inner-cross split-ring structure, modeled at PSI with CST microwave studio.

Due to the inherent 3-D nature of the inner-cross split-ring structure, it is intuitive that EBG metamaterials are likely to be isotropic, especially when considered in bulk. Due to its 3-D nature, this structure is also likely to maintain its properties on curved surfaces as opposed to flat surfaces (Figure 5a), as function of the relative curvature, frequency, and ring diameters (Figure 5b).

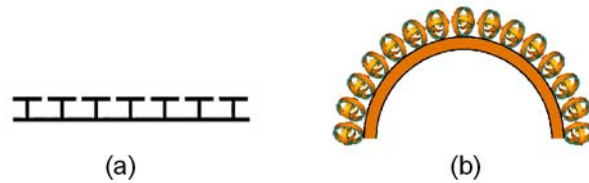


Figure 5. a) Flat surface Seivenpiper High Impedance surfaces b) Proposed Curved surface IC-SRR (Inner Cross-Split Ring Resonator) surfaces for conformal antennas.

Preliminary experimental and theoretical results for three dimensional Crossed Split Ring Resonators were first shown in [9] to demonstrate a new left-handed medium. This magnetic resonator structure demonstrated to have high isotropy, with response independent of the illumination direction in a specific plane.

Because of the complexity of the proposed inner cross double split ring structure, we propose to adopt “lump” parameter representation for the 3-D model. In [10] the effective constitutive parameters (permittivity and permeability) of a slab of metamaterial are retrieved from the measurements of S parameters. This method has proven effective and robust: however, the sensitivity to the accuracy of the S parameters measurements needs to be taken into account.

### 3. Modeling Curved Surfaces with EBG Materials

The goal of this work is to compare the performance of different FSS designs on curved surfaces.

Our first step is to actually define what “curved surfaces” mean from an electromagnetic point of view. The effect of surface curvature is clearly more profound at lower frequencies, when the wavelength approaches the cylinder radius (or, which is the same, the curvature radius). On the other hand, this effect should become less important at higher frequencies, when the wavelength is small compared to the curvature radius of the target. In the latter case, the surface becomes “quasiplanar” from the viewpoint of the incident field.

To compare the performance of different EBG materials/structures for curved surfaces, we have considered first the classic problem of plane wave scattering by an infinite PEC cylinder schematically shown in Figure 6. The frequency varies within the limits

$$3 < ka < 10 \quad (2)$$

where  $a$  is the cylinder radius, and  $k$  is the free-space wavenumber.

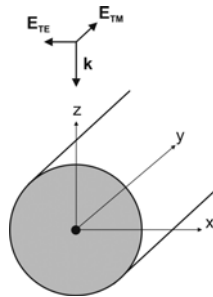


Figure 6. TM/TE scattering of the infinite cylinder.

The far-field solution to the problem shown in 6 is well-known [11] and [12]. For the TM excitation (incident  $\mathbf{E}$ -field is parallel to the cylinder axis) of the PEC cylinder, one has for the 2D radar cross-section (RCS),  $\sigma$ ,

$$\sigma_{2D} = \lim_{R \rightarrow \infty} \left( 2\pi R \frac{|E_y^s|^2}{|E_y^i|^2} \right) = \frac{2\lambda}{\pi} \left| \sum_{n=0}^{\infty} \varepsilon_n \frac{J_n(ka)}{H_n^{(2)}(ka)} \cos n\theta \right|^2, \quad \begin{cases} \varepsilon_n = 1 & n = 0 \\ \varepsilon_n = 2 & n > 0 \end{cases} \quad (3)$$

For the TE excitation, one similarly obtains

$$\sigma_{2D} = \lim_{R \rightarrow \infty} \left( 2\pi R \frac{|H_y^s|^2}{|H_y^i|^2} \right) = \frac{2\lambda}{\pi} \left| \sum_{n=0}^{\infty} \varepsilon_n \frac{J'_n(ka)}{H_n^{(2)'}(ka)} \cos n\theta \right|^2, \quad \begin{cases} \varepsilon_n = 1 & n = 0 \\ \varepsilon_n = 2 & n > 0 \end{cases} \quad (4)$$

Equation (3) predicts an almost constant monostatic RCS at backscattering over the band of interest (2) as a function of frequency. Equation (4) predicts some slow periodic variations of the corresponding monostatic RCS over the band. An extension to the case of a finite cylinder is given by [11].

When the PEC cylinder is coated by an EBG layer, the overall RCS should decrease, at least in the frequency band of the EBG, this is in particular true for the monostatic RCS (backscattering). However, for different EBG material types the corresponding frequency bands are quite different. We have analyzed two different EBG types: one of them was claimed to work better for the curved surfaces; whereas the other has a proven good performance for planar surfaces. The former EBG is the inner-cross split-ring based frequency-selective surface. The other is the well-known “mushroom” High-Impedance surface introduced by Sievenpiper [3].

There is no EBG structure that can perform equally well at all frequencies. For the present problem, we want to determine which EBG, performs better at small values of  $ka$ , for example, at

$$3 < ka < 5 \quad (5)$$

We expect that, the Inner Cross-Split Ring Resonator EBG structure will give the smallest RCS when the curvature radius is relatively small, i.e. on the order of wavelength. On the other hand, the “classic” mushroom-like structure may still perform better at higher frequencies, i.e. for quasi-planar surfaces. The corresponding frequency domain may be given by inequality

$$ka > 5 \quad (6)$$

After establishing this criterion, we need to check the corresponding EBG performance for both frequency domains. This was done using numerical modeling on fine meshes, and employing the periodic boundary conditions.

A high-impedance flat surface EBG (Figure 7a) was wrapped around a finite PEC cylinder with the radius  $a = 60$  mm (Figure 7b). The top square of the mushroom structure has dimension  $a=3.6$  mm. The height of the vias is 1.8 mm, for bandgap operation at 1.0 GHz. The solid cylindrical vias have the diameter of 0.5 mm.

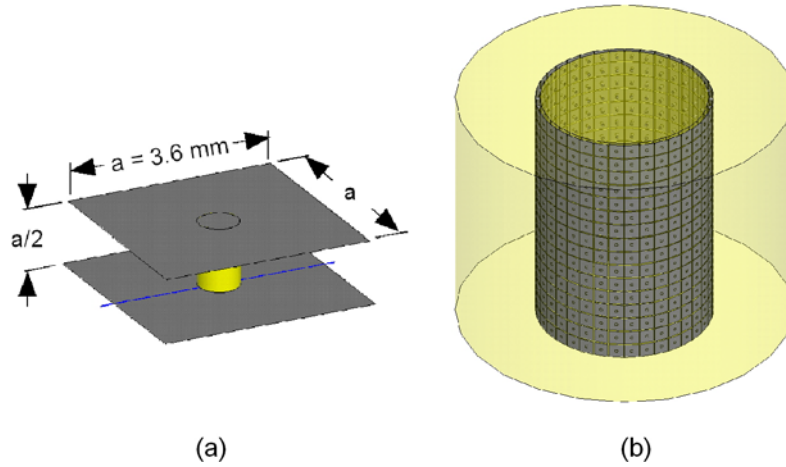


Figure 7. (a) Example of classic EBGs. The top square has dimension  $a=3.6$ mm. The height of the vias is 1.8 mm –about 3% of the cylinder radius, for bandgap operation at 1.0 GHz. The solid cylindrical vias have the diameter of 0.5 mm. (b) The classic Sievenpiper high-impedance surfaces on a finite PEC cylinder. The outer cylinder is the radiating boundary. Both TM and TE excitations are possible, depending on incident plane wave.

For the IC-SRR structure, as a first approximation, we have considered 2-D split-ring elements, which include *two* perpendicular rings, as in Figure 8a. We expect the results to improve when using a 3-D inner-cross split-ring structure. The intra ring material is air. The corresponding EBG cylindrical structure is shown in 8b.

In order to reduce the processing time and obtain the reliable preliminary results, we have considered only one “ring” elements as shown in Figure 9, then use the periodic boundary conditions implemented in Ansoft HFSS. The reason for this step is that the EBG will be in fact periodic along the axis of an infinite cylinder, with the period being equal to the cell size.

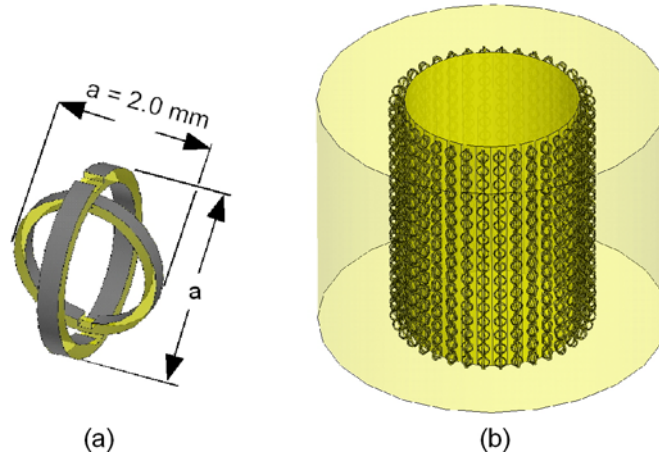


Figure 8. (a) A 2-D split-ring resonator element. For demonstration purposes have considered a simplified split-ring element structure, which include two perpendicular rings. In this example, the diameter of the outer ring is 2.0 mm, for band gap operation at 1.0 (b) The split-ring EBG surface. The individual elements are “embedded” into the artificial dielectric material wrapped around the cylinder.

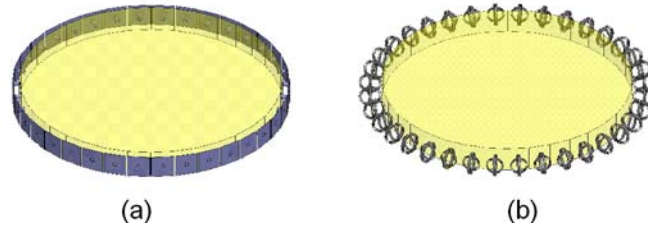


Figure 9. (a) One “ring” of the periodic High Impedance EBGs for the infinite cylinder. (b) One “ring” of the periodic Split-ring structure. periodic boundary conditions were used in conjunction with the plane wave excitation and with the radiation boundary.

#### 4. Results for Quasi-planar EBGs surfaces ( $ka > 5$ )

We ran several simulations to evaluate the performance of mushroom EBGs and split-ring EBGs for flat or (more appropriate definition) quasi-planar surfaces. Figure 10 shows the normalized backscattering RCS for the higher frequency band, for  $ka > 5$ . Our study shows that the mushroom EBGs work well at higher frequencies (Figure 10a). At higher frequencies, given the smaller wavelength, the surface is recognized as flat, as long as  $ka > 5$ . The smaller is the radius of curvature (more curved surfaces) the higher is the frequency of resonance for which the structure can work effectively. For comparison, Figure 10b shows the normalized backscattering RCS for the higher frequency band,  $ka > 5$  for the Split-ring structure.

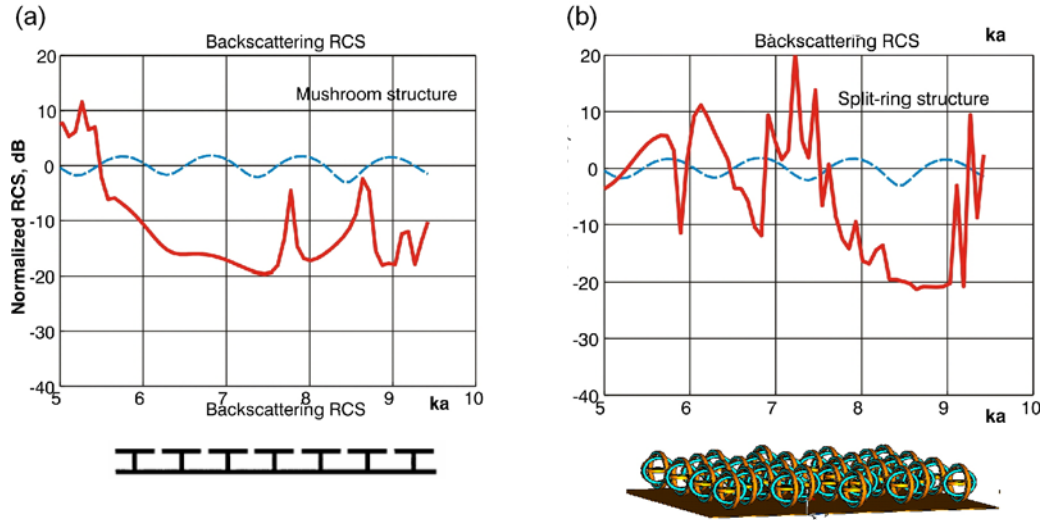


Figure 10. (a) Normalized backscattering RCS (thick solid line) for the mushroom structure as a function of  $ka$ . The dashed line is the RCS of an infinite PEC cylinder computed with the same numerical model. The minor oscillations around 0 dB may be associated with the numerical inaccuracy of the periodic Boundary Conditions. (b) Normalized backscattering RCS (thick solid line) for the mushroom structure (top) and for the split-ring structure (bottom) as a function of  $ka$ . The dashed line is the RCS of an infinite PEC cylinder computed with the same numerical model.

Comparing the results shown in 10 it can be seen that the mushroom EBGs modeled in this study have a larger bandwidth than the split-ring EBGs at higher frequencies and large curvature. However, using a complete 3-D EBGs structures and optimized split-ring elements with multiple split-rings diameters, we can achieve band-gap at the desired frequency range also for relative flat surfaces bandwidth. We should also remember that our main focus here is to investigate if the split-rings are able to perform their function on curved surfaces, as it will be shown in the next section.

## 5. Results for Curved surface EBGs ( $3 < ka < 5$ )

We have run several simulations to evaluate the performance of mushroom EBGs and split-ring EBGs for curved surfaces. From our investigations it emerges that at lower frequencies, i.e. for  $3 < ka < 5$ , the high impedance-surfaces fail to perform, (Figure 11a), and it is, therefore, necessary to introduce a different EBG structure for antenna purposes. Figure 11b demonstrates that, indeed, the proposed inner-cross split-ring structures work extremely well when the radius of curvature is small compared to the wavelength (lower frequencies). In other words, for strong curvatures, i.e. for  $3 < ka < 5$ , the split-ring EBGs outperform the mushroom EBGs in the lower frequency range.

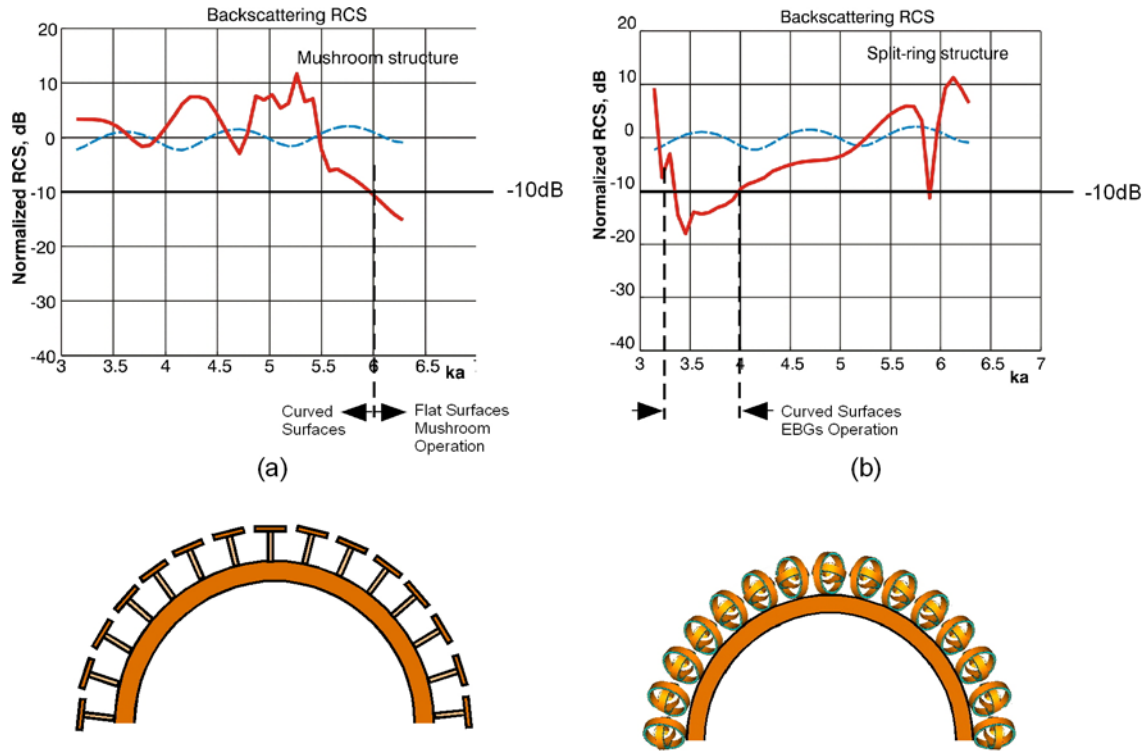


Figure 11. (a) Normalized backscattering RCS (thick solid line) for the mushroom structure as a function of  $ka$ . The dashed line is the RCS of an infinite PEC cylinder computed with the same numerical model (b) Normalized backscattering RCS (thick solid line) for the split-ring structure as a function of  $ka$ . The Split-Ring structure modeled in this study works well for  $3.3 < ka < 4.0$ . However, the bandwidth of operation can be further enlarged to  $3.25 < ka < 5.5$  by split-ring size optimization, as it will be demonstrated in the following.

In the case analyzed here the area of operation is still narrow. However, the structure can be designed to achieve wider  $ka$  with RCS below -10 dB with proper ring diameter distribution.

## 6. Enlarging the EBGs bandwidth

### 6.1 EBGs narrow bandwidth

One drawback of any EBG structure is the inherent narrow bandwidth. However, for the proposed 3D EBGs it is possible to significantly enlarge the proposed EBGs bandwidth in the GHz range beyond the theoretical value, by designing each split-ring to resonate at different frequencies. A simplified example is shown in Figure 12.

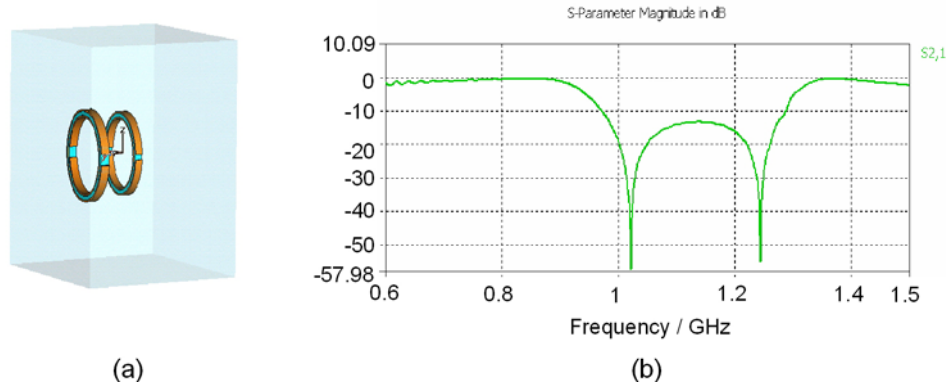


Figure 12. (a) Two split rings of different dimensions. The larger ring is 11 cm in diameter and the smaller ring is 10 cm. The larger ring is 13.2 mm in width and smaller ring is 12 mm. The distance between the rings was set at 6 cm. (b) S<sub>21</sub> (transmission coefficient) parameter for the two combined rings of Figure 8a. The absorption bandwidth achieved is 315 MHz (0.973 GHz – 1.288 GHz).

We simulated two split rings of different dimensions resonating at two adjacent frequencies. We simulated the TE<sub>10</sub> mode. The cavity presented a TE<sub>10</sub> cut-off frequency at about 0.5 GHz.

One split ring shows a very narrow bandwidth, but two rings of different sizes can extend the bandwidth significantly. Therefore careful Inner Cross-Split Ring Resonator design and specific periodicity of the complete structure can provide the desired bandwidth from 1 GHz to 1.5 GHz.

## 6.2 Obtaining Wide Bandwidth with Hybrid Solutions

It is possible to further broaden the bandwidth of EBG structures by introducing a hybrid design [13]. A schematic embodiment of such solution is shown in Figure 13.

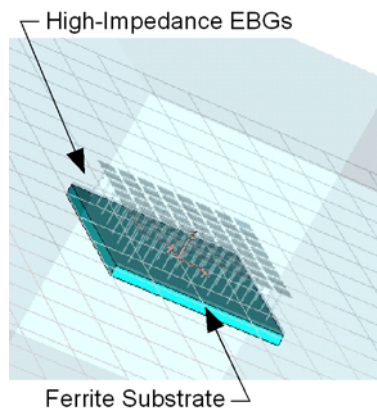


Figure 13. High-impedance EBG surface with ferrite substrate simulated using CST microwave studio.



The hybrid ground plane works by using the ferrite absorber component to absorb the antennas back radiation in the lower frequency band (200-950), while the EBG structure component of the design is used to provide operability at higher frequencies from 1300 MHz up to 2150 MHz or from 2100 MHz up to 3500 MHz, depending on the geometry adopted. Therefore the bandwidth of operation of the EBG/Ferrite hybrid structure is larger than what it is provided by either the ferrite absorber or the EBG structure alone. A summary of frequency bandwidth and resonance performance for 3 EBG/Ferrite hybrid design from [13] is provided in Table 2.

Table 2. Hybrid Ground Plane Bandwidth Performance Comparison [13]

TABLE II  
HYBRID GROUND PLANE BANDWIDTH PERFORMANCE COMPARISON

		Ferrite Operation Region	EBG Operation Region	Hybrid Ground Plane Operation
1 <sup>st</sup> Design Version	Frequency Range	170MHz – 1.28GHz	1.28GHz – 2.15GHz	170MHz – 2.15GHz
	Bandwidth	7.5:1	1.7:1	12.6:1
2 <sup>nd</sup> Design Version	Frequency Range	170MHz – 1.39GHz	1.39GHz – 3.8GHz	170MHz – 3.8GHz
	Bandwidth	8.2:1	2.7:1	22.4:1
3 <sup>rd</sup> Design Version	Frequency Range	170MHz – 2.1GHz	2.1GHz – 3.5GHz	170MHz – 3.5GHz
	Bandwidth	12.4:1	1.7:1	20.6:1

## 7. Reduction in Size of EBGs Using Split Rings

An additional significant result emerged from our study: the proposed split-ring EBG structure is 2.5 times smaller in volume, and 3.2 time smaller in surface, than the equivalent high-impedance mushroom EBG structures, allowing convenient integration in curved surface Army systems, either body armor, ground vehicle, or UAV.

This is an important discovery, since miniaturization is always desirable as the communication apparatus becomes more sophisticated and the physical space becomes prohibitive. We have compared the unit cell size of the two EBG structures: the high-impedance surfaces and the simplified inner-cross split rings. The results are shown in Figure 14.

The size reduction of the occupied *volume* achieved with the split-ring structure is approximately 2.5 times. The unit cell area (*surface*) is 3.2 times smaller. Furthermore, our studies suggest that it is possible to further reduce the size of the split-rings by modifying the width of the rings and the gap. The figure suggests that more split-rings unit cells can fit in the same surface area, and therefore our proposed technology can achieve superior performance enhancement effects.

Figure 15 shows the results of the numerical experiment described above. It is seen that the split-ring surface has a considerably lower first bandgap frequency for a single element occupying the same surface area. On the other hand, we can achieve same frequency resonance with a smaller split ring structure, as shown in Figure 14.

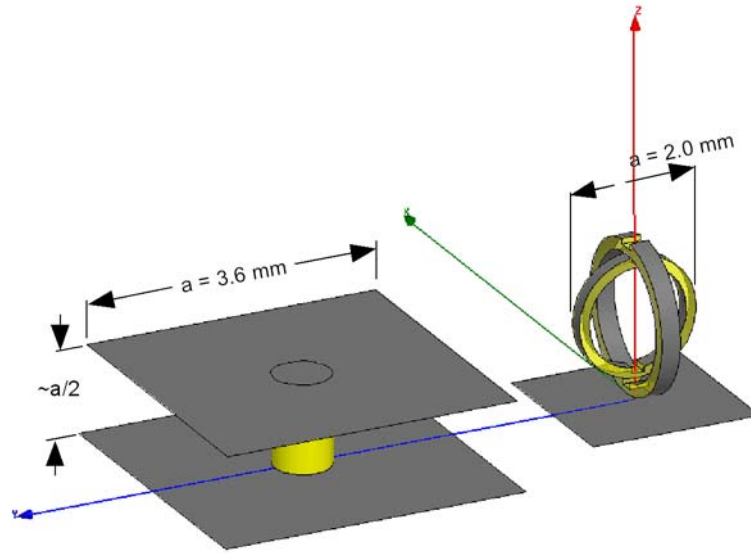


Figure 14. Two EBG elements - a high-impedance structure element and a simplified split-ring element - to scale. Both elements ensure the bandgap at the *same* frequency in the GHz range.

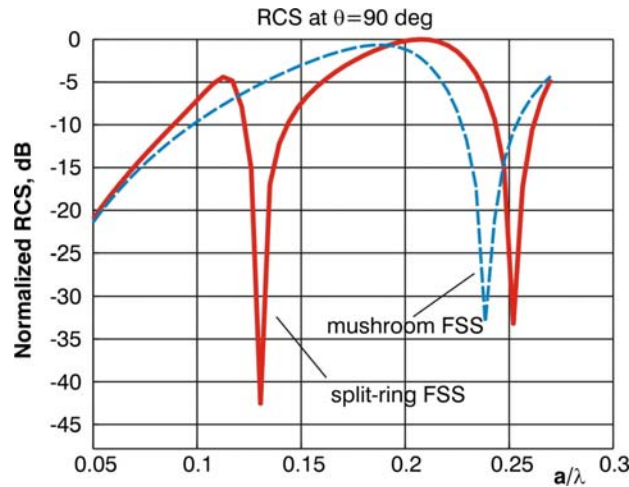


Figure 15. Normalized bistatic RCS at  $\theta = 90$  deg (the “surface wave” RCS) as a function of the frequency/wavelength for a FSS with the fixed unit cell size  $a \times a$ . Dashed curve – mushroom FSS surface; solid curve – split-ring surface FSS.

Based on these bandgap estimates, Table 3 reports on approximate unit cell linear dimensions for some frequencies of interest. These sizes are necessary to ensure the bandgap and surface wave suppression. It is believed that the superior behavior of the 3D split-rings could further be improved using the proper embedding materials and geometry optimization.

Table 3. Unit Cell Dimension  $a$  Necessary for Surface Wave Suppression at Certain Frequencies of Interest

Frequency, GHz	Mushroom unit cell - dimension $a$ , cm.	Split-ring unit cell - dimension $a$ , cm.
1.0	0.72	<b>0.39</b>
1.5	0.48	<b>0.26</b>
2.0	0.36	<b>0.20</b>
2.5	0.29	<b>0.16</b>

Thus, the linear dimension reduction for the split ring under study is approximately given by the factor of **1.85**. This factor is valid for any frequency of interest, indeed. One should emphasize that the occupied surface area

$$S = a \times a \quad (4)$$

and the occupied volume

$$V = a \times a \times h \quad (5)$$

per split-ring element are also quite different for two element types. For the mushroom element investigated in this study,

$$h \approx 0.4a \quad (6)$$

but, for the split ring element,

$$h \approx 1.0a \quad (7)$$

Even though the relative height of the split ring might appear larger, the total occupied volume will still be smaller, due to a smaller overall linear dimension  $a$ . Equations (4)-(7) and Table 3 result in Table 4, which summarizes the data on the volume occupied by one FSS element.

Table 4. Occupied Volume Necessary for Surface Wave Suppression at Certain Frequencies of Interest

Frequency, GHz	Mushroom unit cell - occupied volume, cm <sup>3</sup>	Split-ring unit cell - occupied volume, cm <sup>3</sup>
1.0	0.149	<b>0.059</b>
1.5	0.044	<b>0.018</b>
2.0	0.019	<b>0.008</b>
2.5	0.010	<b>0.004</b>

The reduction in the size of the occupied volume for the present split ring geometry is approximately given by the factor of **2.5**. This factor is valid for any frequency of interest. To visualize the relative element size, Figure 14 shows two FSS elements - the mushroom and the split ring, which ensure bandgap at the *same* frequency.

## 8. IC-SRR (3D EBGs) Manufacturing

A possible procedure for machining a large batch of the 3-D Inner-Cross Split-Ring EBGs unit cell is described in this section. We can build three long dielectric cylinders of radius each equal to the inner split ring radius (Figure 16a). The radius of the rings can vary between 1 mm and 1 cm, depending on the frequency of resonance and the particular design and properties. We can coat them with a metal layer (Figure 16b), etching away a thin stripe that will represent the split of the rings. We can coat the metal with a thicker layer of dielectric material/foam of thickness equal to the gap between rings couples (Figure 16c). We can then coat them again with a metal layer (Figure 16d), etching away a thin stripe on the opposite side than the first one of (Figure 16b). The final step would be slicing the cylinder in a large batch of N split-rings of equal diameter d, and width, w (Figure 16e).

The split rings can then be placed in a monomer solution and it is feasible to use ionic forces to align the three cylinders along the three axes in the same solution for the whole batch. The tolerance for orthogonality between three orthogonal sets of rings is quite large: a split-ring has bandgap behavior along the ring plane. We have estimated that a 30° angle error in alignment for a single ring would produce 85% efficiency for the bandgap performance (proportional to  $\cos \alpha$ ). For a single 3-D inner-cross unit, the bandgap performance is best along the three Cartesian axes and intermediate in between. However, for any incidence angle the surface efficiency would be at least 71% for each ring. If the three axes are not perfectly aligned the bandgap behavior will be along the three non-orthogonal axes. However, when a large number (~100 to 1000) of unit cells are distributed in the ferrite/Kevlar composite with random orientation, the total effect will be isotropic for the overall structure. Therefore, the random distribution and orientation of the unit cells serves two very important purposes: improve the isotropic behavior of the structure, and simplify the manufacturing process.

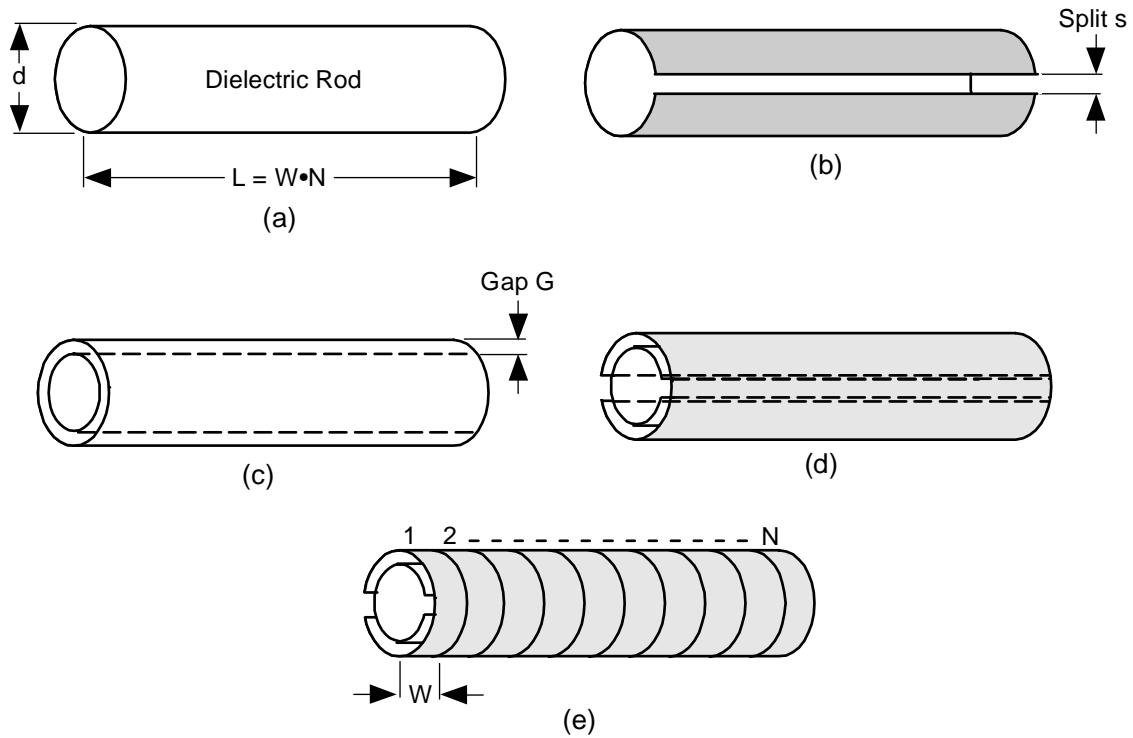


Figure 16. (a) One of three dielectric cylinders of radius equal to inner ring and length  $L = \text{split-rings width} \times \text{number of rings manufactured}$ . (b) Metal depositing and gap etching. (c) Coating with a dielectric layer as the distance between each ring couple,  $G$ . (d) Second metal depositing and gap etching. (e) Each of the three cylinders sliced to provide a large batch of split-rings of equal diameter.

The composite mold can be a  $<10$  mm thick structure in which the split-rings spheres will be embedded. There will be tens to a hundreds of these spheres periodically embedded in the mold (Figure 17a and 17b). The composite mold will present several periodical semi-spherical cavities where the sphere will be inserted with random orientation. The quasi-isotropic behavior of these structures will make it easier to fill the voids with randomly oriented spheres. A sealant to avoid air in the structure can be injected at this stage. The half mold containing the sphere will be then covered with the second half mold of composite ferrite/Kevlar materials.

However, for bulk structures (5-10 layers), a random distribution of one axis split rings of different ring sizes, multiple resonances, and multiple inclinations, would provide the structure good isotropic properties, while simplifying the manufacturing process. Considering that the single element can be few millimeters in diameter for operation at few GHz, a bulk structure can be just 1-2 cm thick and have already strong isotropic behavior.

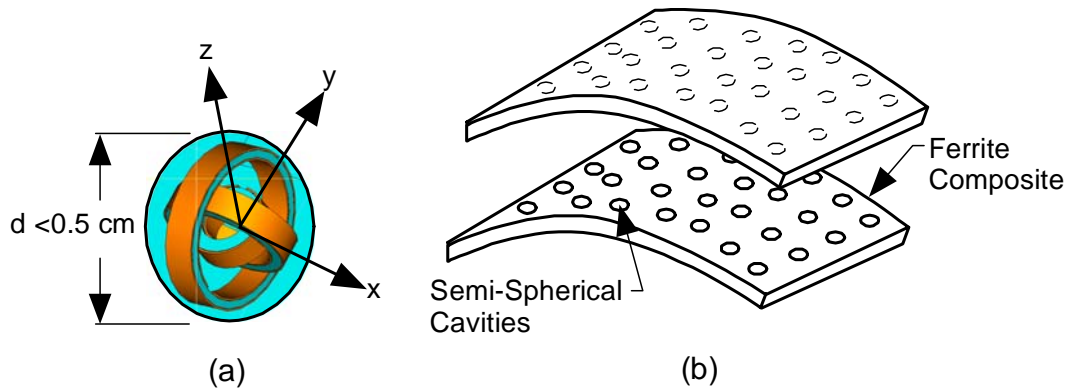


Figure 17. (a) Dielectric Sphere containing the 3D EBG inner-cross split-rings unit cell element. The typical size of such sphere will be  $< 0.5$  cm for GHz frequencies of operation. (b) Ferrite/Kevlar composite mold containing the randomly oriented 3D EBG inner-cross split-rings unit cell elements of Figure 16a.

## 9. Conclusions

We have proven the feasibility of using the proposed 3-D structure for curved surfaces antenna applications. The main points demonstrated in this paper can be summarized as follows:

- Inner Cross-Split Ring Resonable EBG structures work effectively for curved surfaces.
- Classic EBGs (High-Impedance surfaces) are applicable only to flat surfaces or surfaces that have large radius of curvature compared to the wavelength (at higher frequencies).
- IC-SRR EBGs perform better than classic EBGs (High-Impedance surfaces or Mushroom structures), especially when the curvature is strong (small) compared to the wavelength of operation (at lower frequencies).
- IC-SRR EBGs, (as any EBG or FSS metamaterial) are typically narrow bandwidth. However, we have demonstrated that using a hybrid EBG/ferrite metamaterials, we can achieve the Army desired wide bandwidth, covering a frequency range between 400 MHz and 1500 MHz.
- The proposed IC-SRR EBGs unit cells are at least 2.5 times smaller than the classic EBGs, allowing more compact overall structures.
- Because of their smaller size, it is possible to allocate more IC-SRR EBGs unit cells in the same available curved surface, further enhancing the overall structure performance and simplifying manufacturing. The compact size allows, also, placing the unit EBG components in strategic locations, such as in between the elements of an antenna array for mutual coupling reduction.

## 10. Acknowledgement

This ongoing work is being supported by Army (Phase I SBIR Contract No. W15P7T-07-M201). The authors wish to thank Prof. S. Makarov and Dr. W. Agassounon for the help with EM simulations.

## 11. References

- [1] Yablonovitch E. and T.J. Gmitter, "Photonic Band Structure: the face-centered-cubic case", *J. Optical Society Am. A*/Vol. 7, No. 9/September 1990.
- [2] Clavijo S., R. Diaz, W. McKinzie, "Design methodology for Sievenpiper High-Impedance Surfaces: An Artificial Magnetic Conductor for Positive Gain Electrically Small Antennas.
- [3] Sievenpiper, D. L. Zhang, R. F. Jimenez-Broas, N. G. Alexopolous, and E. Yablonovitch, "High-Impedance Electromagnetic Surfaces with a Forbidden Frequency Band," *IEEE Trans. Microwave Theory Techniques*, vol. 47, no. 11, Nov. 1999, pp. 2059-2074.
- [4] Yang F., Y. Rahamat-Samii, "Microstrip antennas integrated with Electromagnetic Band-Gap (EBG) Structures: A Low Mutual Coupling Design for Array Applications", *IEEE Transactions on Antennas and Propagation*, Vol. 51, No. 10, October 2003
- [5] Hao T., G. Faulker, C. Stevens, D. Edwards, "Comparison of simulation and measurement for 1-D metamaterial devices", *Optical Security Systems, Proceedings of the SPIE*, Volume 5955, pp. 176-184, 2005.
- [6] Radkovskaya A., M. Shamonin, C.J. Stevens, G. Faulkner, D.J. Edwards, E. Shmamonina, and L. Solymar, "Resonant Frequencies of a Combination of Split-Rings: Experimental, Analytical and Numerical Study", *Microwave and Optical Technology Letters*, Vol. 46, No.5, September 5, 2005.
- [7] Pendry J.B., A.S. Holden, D.J. Robbins, and W.J. Stewart, "Magnetism from Conductors and enhanced non-linear phenomena", *IEEE Trans. MTT* 47, 2075-2084, 1999.
- [8] Sauviac B., C.R. Simovski, and S.A. Tretyakov, "Double split-ring resonators. Analytical modeling and numerical simulations", *Electromagn* 24, 317-338, 2004.
- [9] Gay-Balmaz P. and O. J.F. Martin, "Efficient Isotropic Magnetic Resonators", *Applied Physics Letters*, Volume 81, Number 5, 939-941, July 2002.

- [10] Chen X., T. M. Grzegorzczak, B. Wu, J. Pacheco, J. A. Kong, "Robust method to retrieve the constitutive parameters of metamaterials". *Physical Review E* 70, 016608, 2004.
- [11] Balanis, C.A., *Advanced Engineering Electromagnetics*, Wiley, New York, pp. 606-609, 1989.
- [12] Harrington, R.F., *Time-Harmonic Electromagnetic Fields*, McGraw Hill, New York, pp. 233-235, 1961.
- [13] Bell J.M., M. F. Iskander, J.J. Lee, "Ultrawideband Hybrid EBG/Ferrite Ground Plane for Low-Profile Array Antennas", *IEEE Transactions on Antennas and Propagation*, Vol. 55, No. 1, January 2007.